F U N D A M E N T A L A S P E C T S O F
A L L O Y S M E L T I N G I N
A D C A R C F U R N A C E

------✂------

Rodney Trevor Jones

PhD

2015

FUNDAMENTAL ASPECTS OF ALLOY SMELTING IN A DC ARC FURNACE

Rodney Trevor Jones

A thesis submitted to the Faculty of Engineering and the Built Environment, University of the Witwatersrand, Johannesburg, in fulfilment of the requirements for the degree of Doctor of Philosophy

Johannesburg, 2015

DECLARATION

I declare that this thesis is my own unaided work. It is being submitted to the Degree of Doctor of Philosophy to the University of the Witwatersrand, Johannesburg. It has not been submitted before for any degree or examination to any other university. Much of the information presented in this thesis was obtained during the course of my employment in the Pyrometallurgy Division at Mintek in Randburg.

17 June 2015

DECLARATION

I declare that this thesis is my own unaided work. It is being submitted to the Degree of Doctor of Philosophy to the University of the Witwatersrand, Johannesburg. It has not been submitted before for any degree or examination to any other university. Much of the information presented in this thesis was obtained during the course of my employment in the Pyrometallurgy Division at Mintek in Randburg.

17 June 2015

ABSTRACT

DC arc furnaces have been applied to a number of smelting processes, including the reductive smelting of chromite ore fines to produce ferrochromium, the smelting of ilmenite to produce titania slag and pig iron, the recovery of cobalt from non-ferrous smelter slags, stainless steel dust smelting, battery recycling, and nickel laterite smelting.

The recovery of base metals and platinum group metals (PGMs) in a reductive smelting process is a function of the recovery of iron (which indicates the extent of reduction). A recovery equation has been developed that is characterised by a single parameter ($K\gamma$) for each metal that can either be fitted empirically to the data, or expressed in terms of the equilibrium constant and the ratios of the activity coefficients involved.

The DC arc furnace has been modelled electrically as an arc in series with a layer of slag. The voltage is non-linear with respect to the current. Equations have been developed (and confirmed by measurement) to describe how the arc voltage varies as a function of arc length and current. The voltage distribution across a molten slag bath requires the solution of Laplace's equation for a geometry that includes the depression in the molten slag caused by the impingement of the arc jet. Aspect ratios of the arc depression were determined photographically.

Equations have been developed for the calculation of the mean residence time in a continuously-fed batch-tapped furnace, and this has been illustrated using a novel graphical depiction. The mean residence time is directly proportional to the tap-to-tap time, and is increased by increasing the volume of material retained in the furnace between taps.

The ConRoast process treats dead-roasted nickel sulfide or PGM concentrates by reductive smelting in a DC arc furnace, where an iron-based alloy is used to collect the valuable metals. This process results in much lower sulfur dioxide emissions, the ability to accept high chromite contents, and improved furnace containment. The ConRoast process has been demonstrated by smelting 50 000 tons of PGM-containing feed materials at Mintek over a period of operation of about five years.

This thesis is dedicated to my family.

Thank you for your patience and understanding.

ACKNOWLEDGEMENTS

I am grateful to many present and former colleagues at Mintek for sharing their ideas, commenting on mine, and acting as a sounding board during the development of much of the work presented here. There are too many to mention all by name, but I would like to particularly thank Tom Curr, Nic Barcza, Quinn Reynolds, Isabel Geldenhuys, Glen Denton, and Steve McCullough for their input. This work would not have been possible without the assistance of the teams of people who have worked on numerous pilot-plant campaigns over almost three decades. Their work, and the data generated from it, provided the raw material for developing the theories that form the basis of this work.

Thanks are also due to Professor Hurman Eric for being willing to undertake the supervision of this thesis, and for his guidance and friendship.

CONTENTS

LIST OF FIGURES

LIST OF TABLES

1 INTRODUCTION

This thesis deals with fundamental aspects of alloy smelting in a DC arc furnace. It aims to elucidate and improve the understanding of a number of facets of this technology, and to show how they can be applied to a particular novel process. In order to properly introduce the subject, it is necessary to have a clear understanding of what is meant by a DC arc furnace, and what is meant by alloy smelting.

1.1 Principles of a DC Arc Furnace

DC arc furnaces have been known by various names over the years. In this thesis, a 'DC arc furnace' refers to a pyrometallurgical vessel that comprises a cylindrical steel shell with either a domed or a flat base, and a roof that is typically conical. It is lined inside with a refractory material, in order to contain the molten materials being processed. The furnace usually has a central vertical graphite (cathode) electrode (sometimes more than one, but that is not the specific focus of this thesis), and an anode imbedded in the hearth in the lower portion of the furnace. It is usual that the molten metal in the furnace is in electrical contact with the anode. Energy is supplied to the furnace by means of an open plasma arc that impinges on the upper surface of the molten material.

The arc in a DC (direct current) furnace is a sustained high-velocity high-temperature jet, driven by electromagnetic acceleration – the Maecker effect (Maecker, 1955) – in the constricted region near the arc's root on the (cathode) electrode surface. The arc is generated by the interaction between the fluid flow, the thermal field, and the electromagnetic fields.

The self-constricting electromagnetic forces keep this supersonic super-heated plasma jet reasonably coherent.

A DC reactor is used to stabilize the arc further. A reactor, also called an inductor, and sometimes known as a choke, is a device for introducing inductive reactance into the electrical circuit. All three terms describe a coil of insulated wire – having a low resistance and high inductance. A reactor opposes changes in electric current passing through it, by developing a voltage across it proportional to the rate of change of the current. When the current flowing through an inductor changes, the time-varying magnetic field induces a voltage in the conductor, according to Faraday's law of electromagnetic induction, which opposes the change in current that created it. In this way, the reactor stabilizes the current.

Furthermore, the surface of the molten bath (or at least a portion of the surface in the arc-attachment zone) is open, *i.e.*, essentially uncovered by unreacted feed material.

1.2 Alloy Smelting

Smelting is the metallurgical process of extracting metals from their ores by heating to extreme temperatures in a hearth or furnace where melting or fusion of the products takes place. However, smelting involves more than just 'melting the metal out of its ore'. Most ores contain chemical compounds of metals bound together with other elements, such as oxygen (as an oxide) or sulfur (as a sulfide). To produce the metal, these compounds have to undergo chemical reactions. Many non-gaseous impurity elements or compounds ('gangue') are removed in the form of molten slag.

Smelting reactions typically require the presence of either an oxidizing agent (such as the oxygen in air) or a reducing agent (such as the carbon in charcoal or coke). In the case of sulfide ores, oxygen is added to the ores, and the sulfur is removed as sulfur dioxide gas. Copper has been produced this way since about 6000 – 5000 BC, and nickel and platinum are also commonly produced from sulfide ores. In the case of oxide ores, it is common to use a carbonaceous reductant (widely used because of cost considerations) to react with the oxygen from the ore, removing this impurity as a gas (either carbon monoxide or carbon dioxide). Chromite is a good example of an oxide ore (that contains oxides of iron and chromium), and a ferrochromium alloy (mixture of metals) can be produced by the high-temperature reaction of this with carbon.

Reductive smelting is the term given to the process involving the reaction between a metal oxide feed material and a reducing agent. Alloy smelting refers to reductive smelting that has a mixture of metals as its product. This type of process almost always requires high temperatures (typically above 1500°C) and the supply of much energy. The temperature of the alloy needs to be high enough to allow it to be tapped from the furnace in a liquid state, and the slag also needs to be sufficiently fluid for tapping. The process temperature also needs to be high enough for the change in free energy of the reduction reactions to be sufficiently negative so as to favour the production of the metals. It is often the case that electric smelting is the only practical way of reaching the extremely high temperatures required.

For present purposes, smelters can be divided into those that use electrical power and those that do not. Non-electric smelting vessels, such as blast furnaces, flash furnaces, bath furnaces, reverberatory furnaces, aluminothermic reactors, and converters, are not covered here at all. The

focus of this work is only on electric smelting, and, within that category, only direct current (DC) smelting.

1.3 Importance of DC Arc Furnaces

Pyrometallurgy is a vital part of the economy of many southern African countries. A 'List of Southern African Smelters' is available on the Internet (Jones, 2005-2014).

Aside from their widespread use in the steel industry (for melting steel scrap or direct reduced iron), DC arc furnaces have been used for various smelting applications over the past thirty years. This started as a solution to the specifically South African problem of how to deal with chromite ore fines, but DC arc furnace technology has subsequently been applied to a number of other areas of national and international importance. This technology has become important to the production of a number of commodities of key importance to the South African economy, including ferro-alloys, base metals, and platinum group metals (PGMs).

The DC arc furnaces used for smelting applications discussed in this thesis represent over 800 MW of installed capacity.

Smelters are usually very capital-intensive plants, and have high running costs. An improved understanding of the design and operation of DC arc furnaces should lead to higher productivity and greater efficiency of energy usage.

Open-arc open-bath DC furnaces (described in greater detail in later chapters) have a number of advantageous properties, and are increasingly being applied in the metallurgical industry. However, there remain many

misunderstandings about the technology (Jones *et al.*, 2011), and some of these misunderstandings (for example, the need for hollow graphite electrodes) have important cost implications. It is hoped that this thesis will assist in improving the understanding of these very useful furnaces.

1.4 Outline of the Thesis

Chapter 2 focuses on 'Applications of DC arc smelting furnace technology'. A history of DC arc furnaces is presented, providing the context and reasons for the development of this technology. For example, an explanation is provided for why early DC arc smelting furnaces were fed through hollow graphite electrodes, and reasons are given why this might not be necessary (as it has been found that close feeding around the arc has essentially the same result, while saving on the cost of electrodes). The main focus of the chapter is on the actual applications of DC arc furnaces. These include: chromite smelting, ilmenite smelting, cobalt recovery from non-ferrous slags, stainless steel dust smelting, battery recycling, nickel laterite smelting, and the ConRoast process. Also mentioned are two processes that have been developed and piloted, but not yet commercialised: zinc fuming, and the Mintek Thermal Magnesium Process.

Chapter 3 covers 'Recovery of base metals and PGMs'. This chapter covers the theoretical development of an equation (the $K\gamma$ recovery equation) that relates the recovery of various metals to the extent of reduction, as indicated by the recovery of iron to the alloy phase in reductive alloy smelting processes. The effect on the shape of the recovery curve of various values of the controlling parameter is shown. Examples are given of the application of this equation to various processes including: cobalt recovery by slag cleaning, ferronickel smelting, PGM

smelting, and converting. The $K\gamma$ recovery equation requires a single parameter that can either be fitted empirically to a set of experimental data, or can be calculated from the equilibrium constant and the individual activity coefficients for all of the species taking part in the exchange reaction. For the cobalt recovery process, as an example, a critical review of the literature was carried out to ascertain the values of the activity coefficients, especially that of cobalt oxide in slag.

Chapter 4 investigates 'DC arcs and electrical aspects'. The nature of the DC arc is discussed, and this leads to the electrical modelling of the steady-state arc. The interaction of the arc with molten slag is studied theoretically as well as photographically. Electrical models of the molten slag bath are presented, and the non-linear electrical behaviour of DC arc furnaces is discussed. An approach is presented for the scale-up and electrical design of DC arc furnaces. A set of quintic equations have been derived that describe the arc voltage in terms of arc resistivity, arc length, and current; and bath voltage in terms of slag bath resistivity, slag bath depth, and current. This applies to a 'sufficiently wide' furnace, with a typical slag density, and an arc depression having a value that was obtained photographically. Some results from high-speed photography of arcs are presented, and there is some discussion of how these photographs confirm the results of dynamic modelling of arc behaviour.

Chapter 5 looks at some aspects of 'Residence time'. A mathematical description is presented of the factors influencing the residence time distribution in continuously-fed batch-tapped furnaces. A novel graphical method is introduced for the depiction of the residence time distribution in this type of furnace. Applications are shown where the model is used to scale-up with constant residence time, and to determine the number of taps needed to change composition.

Chapter 6 examines 'The ConRoast process: A case study'. This process is a good example of reductive alloy smelting in a DC arc furnace. This chapter summarises many years of testing, piloting, and demonstration smelting. It also covers the upstream and downstream elements of the process. The effects on project timing of the world economy, the global recession, and the credit crunch are also discussed.

1.5 Research Methodology and Contribution of Present Study

This study is intended to significantly advance the body of knowledge in the area of reductive smelting processes that take place in DC arc furnaces, by investigating some fundamental aspects of this technology. The importance and significance of this study lies in a number of individual topics that fall within the broader areas of modelling and process design.

Each major chapter presents the relevant background literature and the development of each particular topic in detail. For example, a critical review of the literature has been undertaken especially around activity coefficients for the Co and Fe system (Section 3.5.2) in relation to the recovery of base metals (exemplified by cobalt) in an iron alloy; and with regard to the distribution coefficients of platinum group metals between iron alloys, matte, and slag (Section 6.3.1). The mathematical description of electric arcs (incorrectly published in the literature) has been corrected (Section 4.3) and incorporated into a general model for the electrical design of DC arc furnaces.

Mintek, a South African government-owned minerals research institution, is well known as the 'home' of DC arc furnaces for smelting applications. The author started his working career at Mintek at the same time that the

first commercial application of DC arc smelting was being introduced into the chromite smelting industry, and was personally involved, in various capacities, in all of the industrial applications of DC arc smelting that were developed at Mintek. Initially, his involvement centred on processing the metallurgical data from pilot-plant smelting campaigns. It then progressed to running his own furnace campaigns, and to the thermodynamic modelling of the processes. He spent a great deal of time on the mathematical modelling of various aspects of DC arc furnace technology, and developing methods for furnace and process design. Later, his role changed to that of an inventor of a process (ConRoast), and he was able to make contributions to the process that went beyond the furnace itself to encompass both upstream aspects (such as fluidized-bed roasting) and downstream aspects (such as water atomization of alloys).

1.5.1 Recovery equation

Understanding the chemical (metallurgical) processes taking place inside furnaces has always been key to the understanding of their design and operation. The multi-phase multi-component systems involved in smelting processes have so many variables that it is often difficult to pick out the most important relationships. One of the most important contributions of the work presented in this thesis was the derivation, from first principles, of a relationship between the recovery of a desired metal (such as cobalt or nickel, for example) and the recovery of iron (the fraction of the metal that reports to the alloy, expressed as a fraction of the metal that is present in the feed material). As explained in Chapter 3, this relationship is expressed in terms of a single variable, the value of which is set by the temperature and chemical composition of the system. Data sets from numerous pilot-plant campaigns have been used to validate this model, and it is now used by a number of major international mining companies.

1.5.2 Electrical arc photography and modelling

The electrical specification of the power supply for a DC arc furnace requires a good understanding of the voltage and current ranges that will be required to operate the furnace successfully. If the ranges of voltage and current specified for the transformer are greater than necessary, this can result in a great deal of unnecessary expense, and, if the ranges are too low, the furnace might not be operable at all, or it might allow only a very low throughput.

The author has been involved in many furnace design studies over the years, and this exposed him to various misconceptions that were held

about the operation of DC arc furnaces, and to flaws in the ways furnaces were being designed by engineering companies. These flawed furnace design methods have not been published in the scientific literature, but it became clear that better methods should be developed and formalised. It is also surprising that most operators of industrial DC smelting furnaces have never seen the electrical arcs that are central to the operation of their furnaces. In this case, it is hardly surprising that a number of myths developed about the way in which these furnaces worked.

Electric arcs, including those inside furnaces, have been studied for a very long time. For example, Chapter 4 mentions the work done by Bowman (1969, 1972, 1982, 1990, 1994, 2009) in which he photographed and modelled steady-state electrical arcs in the 1 to 10 kA range. Szekely *et al.* (1983) modelled the energy transfer, fluid flow, and bath circulation in electric arc furnaces. However, there remained a need for a better understanding of the nature of the interaction between the plasma arc and the molten slag bath. As outlined in Chapter 4, the author was able to photograph this interaction and this provided much-needed clarity regarding the geometry of the cavity formed in the area immediately underneath the arc.

These photographs of arcs interacting with molten slag, and the ratios of the dimensions inferred from them, provided the basis for a practical usable electrical model of the arc and the slag bath that can be used for the scale-up and electrical design of DC arc furnaces. Perhaps the most significant contribution in this area was the series of photographs that allowed typical aspect ratios of the arc depression to be determined.

The DC arc furnace has been modelled electrically as an arc (using a customised version of Bowman's model) in series with a layer of slag.

Bowman's model of the steady-state arc describes how the arc voltage varies as a function of arc length and current. The voltage distribution across a molten slag bath requires the solution of Laplace's equation for a geometry that includes the depression in the molten slag caused by the impingement of the arc jet. The aspect ratios of the arc depression, that enabled these calculations to be performed, were based on the photographic work reported here.

Another important contribution to the electrical modelling of DC arc furnaces was to highlight the fact that the voltage is non-linear with respect to the current. This thesis includes examples of calculations that show this clearly.

It should be noted that this early arc photography and modelling work has been extended greatly by Reynolds (2009) in his PhD study on 'Mathematical and computational modelling of the dynamic behaviour of direct current plasma arcs', in which further photographic work has confirmed the results of his dynamic modelling of arc behaviour.

1.5.3 Residence time modelling

In standard textbooks on chemical reactor design, residence time distributions are well defined for batch and continuously stirred reactors. However, a furnace that is fed continuously, but where the liquid slag and metallic products are tapped intermittently, does not fit either of these classifications. A novel graphical depiction of this problem was developed that allowed a residence-time equation (applicable to both the slag and the metal) to be constructed from first principles. The effects of slag and metal tapping intervals, and the fraction of liquid retained in the furnace, have been studied, and are shown to have a significant effect on

the residence time distribution; and this effect can now be quantified by using the equation. The mean residence time is directly proportional to the tap-to-tap time, and is increased by increasing the volume of material retained in the furnace between taps.

The equation is useful for design purposes if one wants to achieve a constant mean residence time when scaling up from a pilot plant to a commercial plant.

During furnace operation, it is sometimes necessary to change the composition of the molten bath (slag and metal), and it is necessary to know how many taps it would take to substantially replace material of the old composition with that of the new. The required number of tapping operations depends strongly on the fraction of material removed during tapping, and this can be calculated using an equation, or be done graphically.

1.5.4 ConRoast process

The author is the first-named inventor on the international patents (Jones *et al.*, 2002) for what has become known as the ConRoast process. This novel process is applicable to the smelting of platinum group metals, as well as to the treatment of nickel sulfide ore concentrates. The idea behind this process initially arose, in 1994, as one of a series of process options being investigated for a particular study. The initial intention was to investigate an environmentally friendly process option that involved dead roasting in a fluidized-bed reactor (to remove the sulfur before smelting and converting), followed by reductive alloy smelting in a DC arc furnace. A techno-economic evaluation of the various process options under consideration showed that this approach appeared to have great promise.

A number of pilot-plant tests were run that showed the effectiveness of this approach, firstly for nickel sulfide smelting, and secondly for the smelting of platinum group metals (PGMs) – especially those concentrates containing significant quantities of chromite.

The ConRoast process treats dead-roasted nickel sulfide or PGM concentrates by reductive smelting in a DC arc furnace, where an iron-based alloy is used to collect the valuable metals. This process results in much lower sulfur dioxide emissions, the ability to accept high chromite contents, and improved furnace containment. The development of this process is documented in Chapter 6. The ConRoast process has been demonstrated by smelting 50 000 tons of PGM-containing feed materials at Mintek over a period of operation of about five years.

The modelling and design of this process relies heavily on the $K\gamma$ recovery equation developed in Chapter 3, as it is based on selective reduction. The intention is to recover as much as possible of the precious metals and base metals to the alloy, while minimizing the quantity of iron that is reduced to the metallic form. In addition, it is very important to leave essentially all chromium dissolved in the slag as CrO. The $K\gamma$ recovery equation provides a very clear framework for this relationship to be clearly understood.

The electrical design of a furnace for the ConRoast process requires the electrical models outlined in Chapter 4, as the slag is of intermediate resistivity (more resistive than titania slag, but less resistive than nickel laterite slag), and the design of the power supply is very important to get right, as there are no existing large industrial installations of the process that would allow the designer to simply rely on present industrial practice.

The residence-time modelling of continuously-fed batch-tapped furnaces, presented in Chapter 5, has also come in useful for the operation of the pilot-plant furnace, as well as for designing the location of the tap-holes of an industrial-scale furnace.

The ConRoast process is widely seen as being very important to South Africa's platinum industry in the coming years, especially as mines move increasingly towards utilising higher-chromium ores.

2 APPLICATIONS OF DC ARC SMELTING FURNACE TECHNOLOGY

2.1 Introduction

The DC (direct current) arc furnace is made up of a cylindrical steel shell that is refractory-lined, with a central vertical graphite electrode that passes through the roof, as shown in Figure 2.1. The anode is imbedded in the hearth at the base of the furnace, and the metal layer is in direct electrical contact with the anode. The slag floats on top of the denser metal layer.

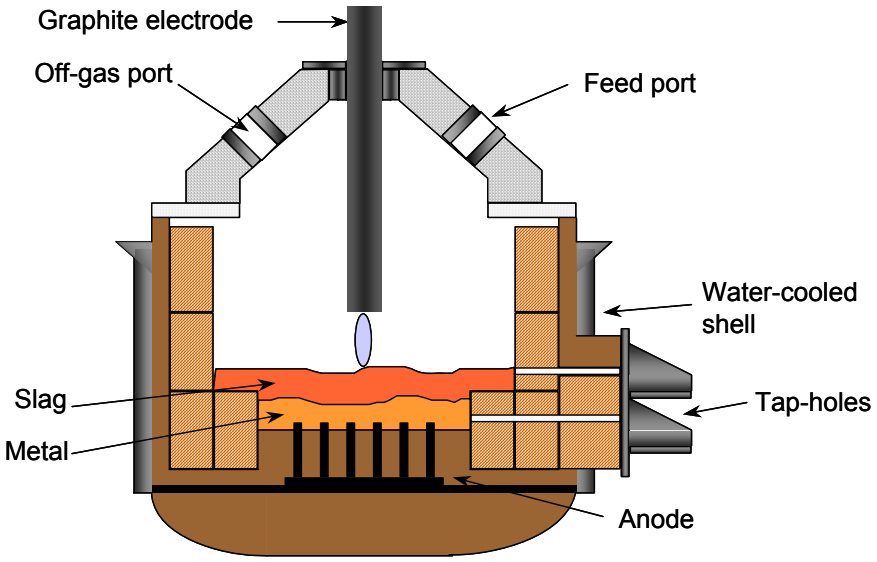

Figure 2.1 Schematic view of a DC arc furnace

Inside the furnace, at its heart, is the plasma arc – a high-temperature ionised gas-like material at a temperature somewhere between 10 000 and 20 000°C. The arc is a highly dynamic phenomenon, resulting in very intense mass and energy transfer, especially in the arc-attachment zone

where the arc contacts the molten slag directly beneath the electrode. The energy required for chemical reactions is supplied by this open plasma arc, and the highly turbulent conditions under the arc promote good mixing and result in a fairly uniform temperature distribution across the molten bath of the furnace.

It is necessary to balance the feed rate and power level, in order to avoid undesirable side reactions (Barcza *et al.*, 1989, 1990). Furthermore, Meihack *et al.* (1987) demonstrated that the rate of loss of energy from the furnace vessel is primarily dependent upon the temperature of the bulk of the molten contents, and does not vary significantly with either feed flux or power flux (as long as the feed rate and power are correctly balanced, according to thermodynamic requirements, in order to maintain a constant temperature).

2.1.1 Classification of furnaces by temperature and ore size

DC arc furnaces are especially useful for the treatment of fine feed materials under conditions where very high temperatures are required. In order to understand the place occupied by DC arc furnaces within the wide range of possible smelting furnace options, it is useful to classify a number of furnace types according to the required operating temperature and the particle size of the feed materials (as shown in Figure 2.2). Given the large number of variables involved in furnace design, clearly there are many possible alternative ways of classifying furnaces. However, the two dimensions selected here (temperature and ore size) serve to illuminate some of the main reasons for many of the principal applications of DC arc furnaces.

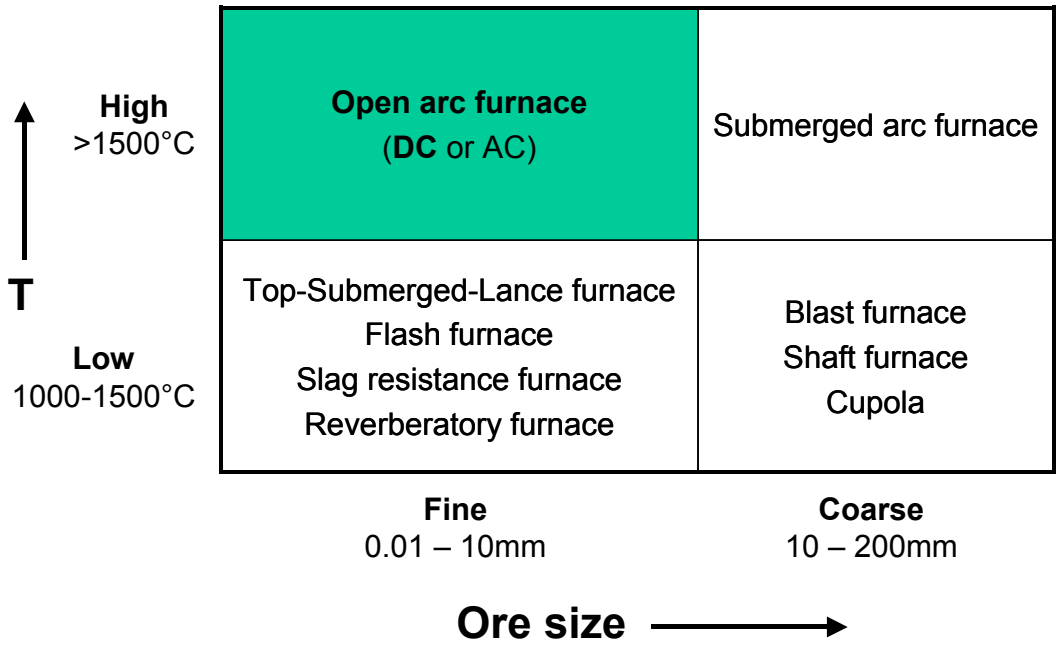

Figure 2.2 Classification of some types of smelting furnaces, based on required operating temperature and the particle size of feed materials

High-temperature operation requires electrical power. Coarse feed materials provide a porous bed that allows the reaction gases to percolate away and escape from the reaction zone. Finer ores and a requirement for very high temperature lead one to the choice of an open-arc furnace (either AC or DC). It should be noted that fine ores allow the use of a fluidized-bed reactor for pre-heating or pre-reduction, and this provides significant energy savings when used in conjunction with a DC arc furnace (Meihack *et al.*, 1987; Dippenaar *et al.*, 1988; Morris *et al.*, 1998).

In the case of open-arc furnaces, DC furnaces have a number of advantages over AC furnaces. For example, in a circular three-phase AC furnace with three electrodes, the arcs repel one another, flaring towards the walls, leading to hot spots on the areas of the side-walls in closest proximity to the electrodes, whereas there is no arc repulsion in the case of the single DC arc. (For that matter, even if two or three cathode electrodes are used in a DC arc furnace, the arcs attract and pull towards each other, as they are, in essence, parallel current-carrying conductors.) DC furnaces

also experience lower electrode consumption. Large AC furnaces suffer from the so-called 'skin effect' where the current is concentrated in the outer periphery of the electrodes. This means that, in large DC furnaces, a higher current can be carried per electrode (or smaller electrodes can be used for the same current) as compared to the AC case. Barcza and Barker *et al.* (2002) pointed out how DC power can overcome some of the constraints imposed on AC submerged-arc furnaces used for ferro-alloy production, namely the current-carrying capacity of the electrodes, and the interaction effect in the control of the electrodes.

2.2 History of DC Arc Furnaces

Contributions have been made by many people to the development of DC arc furnaces (Jones, 2014). The most important of these are outlined below.

2.2.1 Early description of an arc by Humphry Davy

The earliest known written description of a man-made electric arc emanated from Humphry Davy's work in the early 1800s. His early experiments in 1800, only a few months after Volta's introduction of the electric battery, involved the production of sparks during the making and breaking of an electric circuit.

"I have found that this substance [well burned charcoal] possesses the same properties as metallic bodies in producing the shock and spark when made a medium of communication between the ends of the galvanic pile of Signor Volta. The spark is most vivid when the charcoal is hot."
(Davy, 1800)

In his 1812 book, Elements of Chemical Philosophy (Davy, 1812), Sir Humphry Davy provides the first description and diagram (reproduced in Figure 2.3) of the long horizontal arch of flame that gives the arc its name.

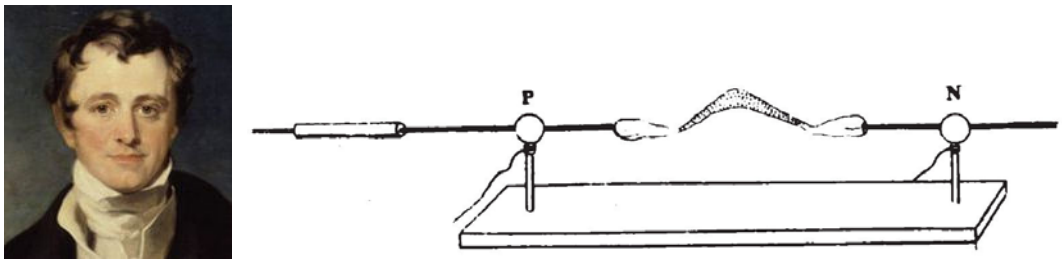

Figure 2.3 Sir Humphry Davy (from a painting by Sir Thomas Lawrence, National Portrait Gallery, London, ~1821) and a horizontal 'arch' electrical discharge, as shown in Davy's 'Elements of Chemical Philosophy' (Davy, 1812)

"When pieces of charcoal about an inch long and one sixth of an inch in diameter, were brought near each other (within the thirtieth or fortieth part of an inch), a bright spark was produced, and more than half the volume of the charcoal became ignited to whiteness, and by withdrawing the points from each other a constant discharge took place through the heated air, in a space equal at least to four inches, producing a most brilliant ascending arch of light, broad, and conical in form in the middle. When any substance was introduced into this arch, it instantly became ignited; platina melted as readily in it as wax in the flame of a common candle; quartz, the sapphire, magnesia, lime, all entered into fusion; fragments of diamond, and points of charcoal and plumbago, rapidly disappeared, and seemed to evaporate in it, even when the connection was made in a receiver exhausted by the air pump; but there was no evidence of their having previously undergone fusion." (Davy, 1812)

2.2.2 DC arc furnace by Sir William Siemens

The idea behind the DC arc furnace has been around for a very long time. Its use for the bulk melting of metals dates back at least to 1878, when Sir William Siemens used a DC arc furnace with a vertical graphite cathode, with the arc transferred to the melt in contact with a water-cooled bottom anode (Siemens, 1878) (shown in Figure 2.4).

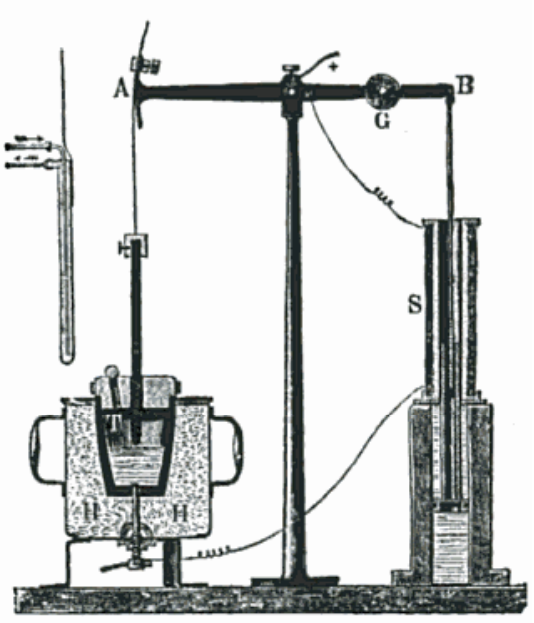

Figure 2.4 Sir William Siemens (from a painting by Rudolf Lehmann, National Portrait Gallery, London, 1882) and the DC furnace he patented in 1878 (Siemens, 1878)

In contrast to this, the first AC electric arc furnace (invented by Paul Héroult) was patented and first operated in La Praz, France, in 1900. The first AC furnace in the USA was installed in 1906 in Philadelphia, and is shown in Figure 2.5.

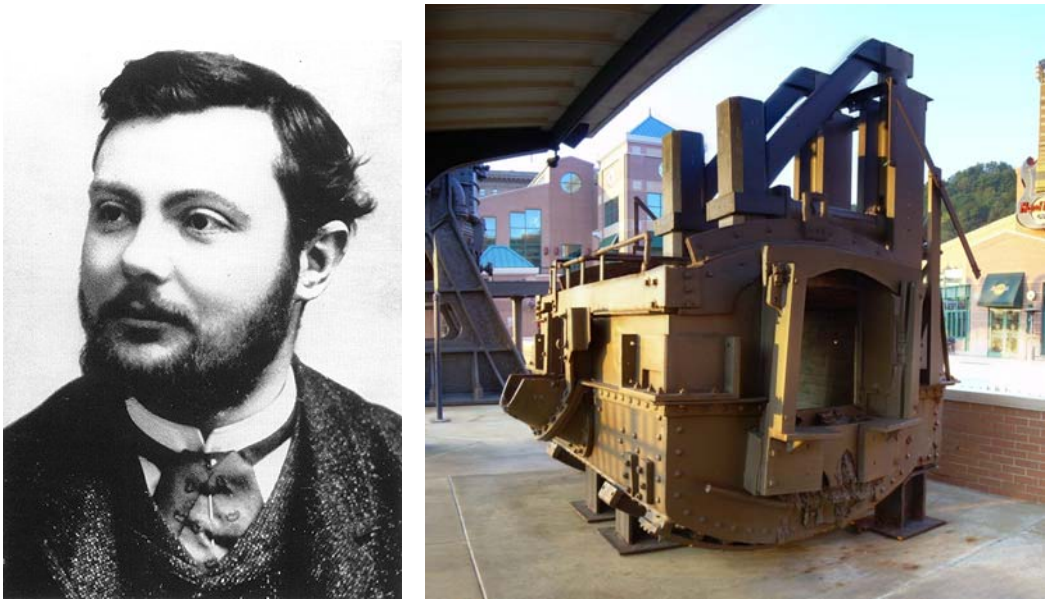

Figure 2.5 Paul Héroult (Alcoa image – used with permission) and the first AC electric arc furnace in USA, 1906 (Philadelphia)

Electric furnace technology became almost entirely AC based thereafter, because of the use of AC for efficient power transmission from large central power stations (following developments by Nikola Tesla and George Westinghouse in 1887 and 1888) and the use of local step-down transformers to supply the high currents required in the furnaces.

2.2.3 DC arc furnaces for steel scrap melting

The industrial use of DC arc furnaces for steel scrap melting was developed largely in parallel with other smelting applications, and is, therefore, discussed separately here. The first modern DC arc furnaces for steel scrap melting started up in 1985 in the USA (Darlington, South Carolina) and France (Trith St-Léger, near Valenciennes in the north-east of the country), with the first DC furnace in Japan (Toyohashi) starting up in 1988 (Hurd & Kollar, 1991). DC operation was seen as having many advantages, but it required the development of low-cost high-power solid-state semiconductor rectifiers before DC furnaces could gain a significant

foothold in the industry. Significant commercialisation of DC furnace technology occurred in the 1990s, when there was a huge demand for DC arc furnaces for steel scrap melting. Around that time, about 80 DC arc furnaces were built in the northern hemisphere.

The global production of steel (currently more than 1500 million metric tons per annum) occurs via two main methods. About two thirds is based on iron ore (involving a two-stage process, using primarily iron ore, coal, and limestone, where ironmaking (the reduction of iron ore to iron) takes place in a blast furnace (BF), and steelmaking (a converting process) takes place in a basic oxygen furnace (BOF)). The remaining one third of steel production is based primarily on recycled steel scrap (where the electric arc furnace (EAF) route uses electricity to melt the steel scrap or direct reduced iron (DRI)). Because steel typically remains in use for decades before it is recycled (and because the use of steel is increasing), there is insufficient scrap available to meet world demand, so iron ore remains widely used.

Steelmaking based on steel scrap requires much less energy and material resources than using iron ore. Compared to the integrated steel production route using iron ore, EAF steelmaking has several advantages, such as significantly lower capital costs (about one fifth of the installed cost per annual ton of production), lower operating costs, a much smaller physical 'footprint', flexibility of raw materials, higher production rates, lower gas emissions, the avoidance of coke production, and significantly lower energy requirements.

A major advantage of electric arc furnaces lies in their ability to accept scrap, DRI, and molten metal in various proportions, as whatever external energy is required can be provided by controlling the electrical power

supplied. Mini-mill steel plants (using electric arc furnaces) also provide the flexibility to produce different grades of steel product. Scrap steel can be re-melted, sometimes together with sponge iron or iron carbide. Because of the smaller production volume, changes can be made much more rapidly. Electric arc furnaces can be rapidly started and stopped, allowing the steel mill to vary production according to demand. Mini-mills can be sited relatively near to the markets for steel products, and the transport requirements are less than those for an integrated mill, which would commonly be sited near a harbour for access to shipping.

Electric arc furnaces also made it possible to achieve the high temperatures needed for the production of high-quality alloyed steel grades.

Essentially, the equipment needed for DC melting has the same configuration as that of a conventional AC furnace. The exceptions are the addition of the bottom electrode (anode), a thyristor rectifier, and a DC reactor (as shown in Figure 2.6), all of which add to the cost of a DC furnace.

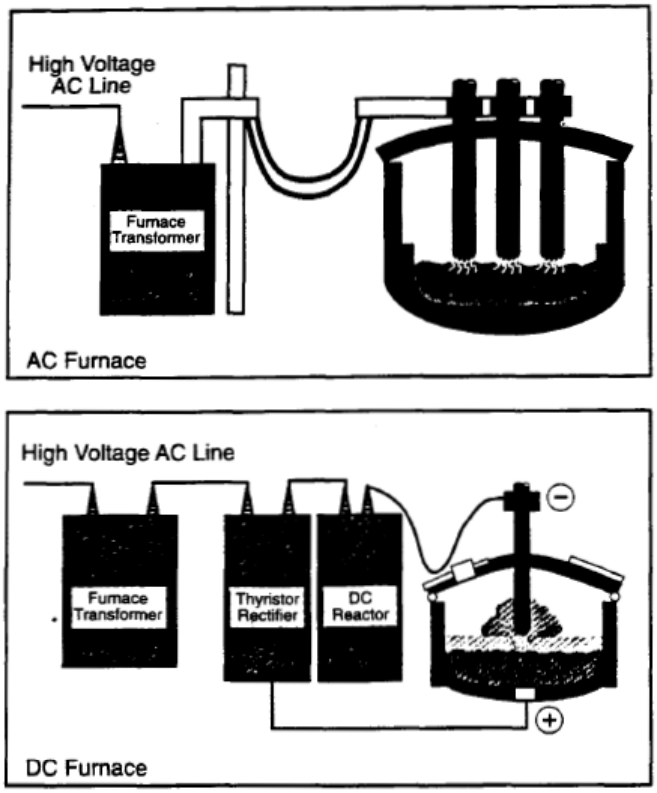

Figure 2.6 Layouts for AC and DC arc furnaces (Hurd & Kollar, 1991)

The conventional AC arc furnace for steel scrap melting operates by means of electric current flowing in three-phase operation from one electrode of three to another through the scrap charge. In the DC arc furnace, the current flows down from the carbon electrode (sometimes more than one), which serves as a cathode, to an anode in the bottom of the furnace.

The use of DC arc furnaces is attractive to EAF steel mill operators for a number of reasons, as summarised by Hurd and Kollar (1991) in Table 2.1.

Table 2.1 AC vs DC furnace advantages (Hurd & Kollar, 1991)

AC Advantages	DC Advantages
• Lower installation costs • No bottom electrode • Higher power rating for bigger heats	• Reduced electrode consumption • Lower lining wear • Bath stirring • Better temperature distribution • Less noise • Less network disturbance • Less energy consumption

Reduced electrode consumption is the major benefit of a DC furnace compared to a conventional three-phase AC furnace. Cost reductions of over 50% in electrode consumption have been achieved (Hurd & Kollar, 1991). Electrode oxidation loss is lower when only one electrode is utilised instead of three. Steady operation of the electrode in the cathode state results in the electrode being cooler. Furthermore, the more stable arc operation in the DC furnace, as compared to the AC furnace, also contributes to reduced electrode consumption.

Some operators of DC furnaces have reported that electricity consumption can be 3 to 5% lower than AC operation. This is ascribed to the fact that current flows down through the charge from the carbon cathode to the furnace bottom anode, not across the top of the charge as in an AC furnace. Steady operation of the electrode in the cathode state also results in less energy loss in this area.

Refractory consumption is lower in DC furnaces. The symmetrical heating pattern in a DC furnace with a single electrode causes less refractory wear on the side-walls of the furnace than is the case with a three-electrode AC

furnace that typically has hot-spots in the areas in closest proximity to the electrodes. The melting of the steel scrap is more uniform in a DC furnace than in an AC furnace, as DC furnaces provide more convection stirring than AC furnaces.

The melting process involves the use of large quantities of energy in a short time, and, in some instances, the process has caused disturbances (flicker and harmonics) in power grids, but this problem is being minimized with the installation of modern furnaces and improved operating practices. There are many ways to reduce the effects of arc disturbances. These are determined by the utility system to which the furnace is to be connected, and they are influenced mainly by the size and stability of the power grid.

DC furnaces for steel scrap melting are favoured especially when the furnace plant is located a long distance from the electrical power generation plant. Through the long transmission line required from power generation to supply the electrical power to the plant site, its short-circuit capacity deteriorates over distance, and hence the grid is more and more prone to disturbance by flicker generated in the arc furnace.

As the electrical utility company needs to deliver clean electrical power to nearby towns or other industrial plants, they often enforce stringent requirements of power quality on all their customers. This requires all flicker and harmonic current originating from the electric-arc operation to be 'cleaned up' on the plant site. The more stable the arc, the less flicker and harmonic current is produced. A strong improvement in power quality on the weak grid is achieved by using DC technology instead of AC. The DC arc furnace operates at a better power factor; switching transients from energizing the furnace transformer can be completely

eliminated; and the flicker seen on the medium-voltage MV-bus is approximately half as severe. There is an approximately 50% reduction in flicker in DC furnaces compared to AC furnaces. The AC arc furnace's current can not be kept fully symmetrical; its power factor is poorer; power on / off is achieved through switching of the furnace transformer; and, while arcing, the AC arc furnace always generates more flicker than a DC arc furnace. This issue becomes more important in cases where the furnace is very big, and where the supplying electrical grid is weak (low short circuit capacity). In areas where the power grid is either weak or unstable, DC is preferred. Reduced voltage fluctuation lessens the problem of flicker, thereby greatly reducing or eliminating the need for costly VAR compensation. A newly built DC furnace might cost more than an AC furnace, but the DC option might be less expensive overall if power correction equipment is required for an AC furnace.

A further advantage of DC furnaces when used for scrap melting is the reduction in acoustic noise relative to AC furnaces.

Offsetting the advantages, capital costs for a DC installation are often higher than for an AC system; however, reduced operating costs can recoup this difference. The introduction of slag foaming technology improved the performance of AC furnaces, as arc immersion in the slag reduces the difference in effects between AC and DC arcs. However, AC and DC arc furnaces both remain widely used for steel scrap melting.

2.2.4 Early use of DC arc furnaces in South Africa

South Africa is very fortunate in having large reserves of chromite. Unfortunately a lot of the 'Transvaal chromites' are highly friable, resulting in large stockpiles of fine ore materials. This posed a particular

challenge to Mintek to provide a solution to this problem. Peter Jochens (shown in Figure 2.7) of Mintek identified 'plasma furnaces' (Hamblyn, 1977) as a possible solution to the 'chromite fines' problem. Mintek and Middelburg Steel & Alloys (now part of Samancor Chrome) conducted smelting trials on Tetronics' pilot transferred-arc plasma furnaces in the UK in 1979/80. These trials were metallurgically successful, in that an alloy of the required composition was produced with a sufficiently high recovery of chromium, but this type of furnace was seen as difficult to scale up to the very large furnaces that were required for the ferro-alloys industry.

Around about the same time, also in the 1970s, ASEA in Sweden developed high-power thyristor rectifiers. Sven-Einar Stenkvist investigated the conversion of AC open arc furnaces to DC, principally for steelmaking. He implemented the idea of using a graphite cathode electrode arcing onto a slag/metal bath as the anode, and devised an electrically conductive hearth and a hollow graphite electrode for finely sized iron ore smelting, where the feed material is fed through the electrode and through the heart of the plasma arc. This is shown in Figure 2.7. Further details are provided by Stenkvist (1984) and Stenkvist & Bowman (1987).

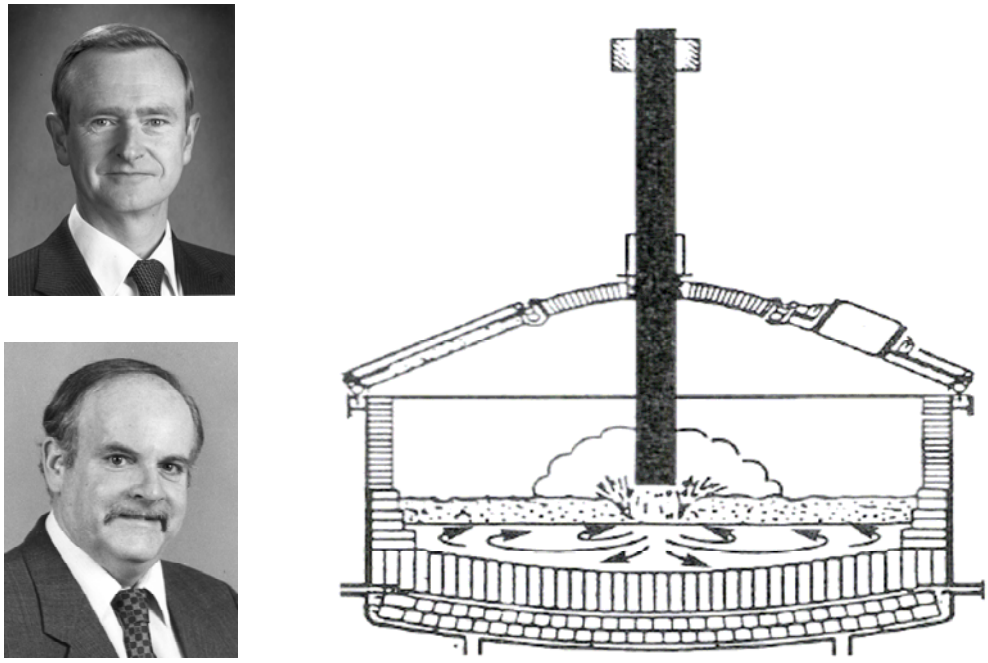

Figure 2.7 Peter Jochens (top left, photograph courtesy SAIMM), Nic Barcza (bottom left, photograph courtesy SAIMM), and the configuration of ASEA's DC arc furnace that was introduced to Mintek (Stenkvist, 1984)

Nic Barcza (shown in Figure 2.7) of Mintek recognised the synergy between the metallurgical process that was proven during the Tetronics testwork, and the scale-up potential of ASEA's DC arc furnace. This is where the application of pre-baked graphite electrodes in a DC arc furnace came about. Mintek built a 1.2 MW DC arc furnace in 1983 to support this development. Since then, that concept has been applied in a number of areas.

The first industrial application of DC arc furnaces for smelting came about when Middelburg Steel & Alloys converted an existing AC furnace at Palmiet Ferrochrome (now Mogale Alloys) in Krugersdorp to a 12 MW DC arc furnace of ASEA design in 1984.

2.2.5 A note about hollow electrodes

There seems to be a persistent misunderstanding about the use of hollow electrodes and stabilising gas in DC arc furnaces, so this subject warrants some clarification.

The first conceptual DC arc furnace for smelting applications (Stenkvist, 1984) was envisaged as using a hollow graphite electrode as a feed chute to place the feed material in the highest temperature zone of the slag surface. In the early 1980s, Mintek interacted with ASEA in Sweden and Lurgi in Germany regarding the ELRED process for iron making. The ELRED process was based on a hollow graphite electrode and this approach offered much greater scale-up potential than the proposed water-cooled plasma torches at that time. In 1985, the first commercial DC-arc smelting furnace treating chromite fines used the hollow graphite electrode feeding arrangement, as did all subsequent DC-arc smelting furnaces built over the next 15 years. It is widely thought that, by feeding through the hollow electrode, the feed materials will also pass through the plasma making up the arc column and thereby be exposed directly to the high temperatures typical of these plasmas, *i.e.*, > 10 000 K. However, it has been shown (Reynolds *et al.*, 2010) that the arc attaches to the electrode in a high intensity spot (~3.5 kA/cm^2) that moves rapidly over the relatively large surface of the graphite electrode tip (the cathode) as well as over the surface of the molten slag surface (the anode), to maintain the lowest resistance path. The arc column tends to move away from the relatively cold and high-resistance feed materials. The high velocity and viscosity of the gas in the arc column make it difficult for solid particles to become entrained into the arc column. Plasma spraying and coating applications usually use a water-cooled plasma torch arrangement whereby the solid particles are injected through the torch assembly into

the region close to the arc attachment spot so that the Maecker (1955) effect can entrain them into the arc column. It is also often assumed that a hollow graphite electrode feed arrangement is essential to avoid large losses of entrained finely sized feed materials to the gas stream leaving the furnace through the off-gas port.

However, it was clear that it would be advantageous to avoid the additional manufacturing cost of a hollow electrode as well as the additional complexity of attaching the feed chute to the top of the electrode column, including provision of an inert gas (usually nitrogen). This gas was required to prevent hot furnace gases from entering the feed system and was also thought to improve the stability of the arc itself.

Consequently, in 1996, Mintek investigated the effects of feeding bag-plant dust through a hollow graphite electrode compared with feeding it through ports in the roof. These ports were located less than 500 mm from the centre of the 200 mm solid graphite electrode. It was found that, even with these very finely sized materials (100% < 20 μm), there were no significant metallurgical differences in smelting behaviour, and the percentage of feed materials reporting to the furnace gas-cleaning plant increased only from 4% to 7%. Subsequent experiments with larger-sized feed materials such as chromite (d_{50} of 0.5 mm) showed an increase in dust losses of less than 1% of the feed material. No negative effect was noticed on the stability of the arc, despite the absence of the nitrogen gas down the electrode.

The first commercial DC arc smelting furnace to utilise solid graphite electrodes and roof feed ports was the 40 MW furnace at Chambishi Metals (discussed later in this chapter) in Zambia in 2001, based on the Mintek pilot-plant testwork with this arrangement (known as side-

feeding). Subsequently, some of the DC furnaces originally installed with hollow graphite electrode feed systems have adopted side feeding, and this trend is expected to continue.

2.3 Smelting Applications of DC Arc Furnaces

2.3.1 Chromite smelting

Mintek began investigating alternative smelting methods for ferro-alloy production in the mid to late 1970s. The growing ferro-alloy industry in South Africa faced the problem of how to deal with the significant quantity of fine material (< 6 mm) that was generated from the friable local chromite ores. In 1976, studies commenced on the possible use of plasma smelting (DC transferred-arc technology), motivated by its potential ability to utilise fine feed materials directly, without costly agglomeration. A further advantage was that the metallurgical and electrical parameters of the smelting process are independent, unlike in a conventional submerged-arc furnace (Jones *et al.*, 1993a, 1993b, 1994).

In 1979, Middelburg Steel & Alloys, now part of Samancor Chrome (Visser, 2006), asked Mintek to take part in tests on plasma smelting at Tetronics in the United Kingdom. After that, Mintek committed itself to the investigation of plasma technology, and to the demonstration to industry of its benefits, particularly the ability to smelt fine materials. Equipment for this purpose was installed in Mintek's pilot bays, and was based initially on a power supply of 100 kVA (and later on one of 3.2 MVA). The first such ferrochromium was produced in a bench-scale DC arc furnace in 1979. The installation of the large experimental furnaces in Mintek's pyrometallurgy pilot bay, Bay 1, demanded an extension of the original building, and, in June 1982, a formal opening ceremony

marked not only the completion of the building operations, but also the inauguration of the larger 3.2 MVA furnace (Levin, 1985), shown in Figure 2.8. The 1 t/h DC arc furnace pilot plant was commissioned in 1984.

Figure 2.8 Mintek's 1 t/h (3.2 MVA) DC arc furnace pilot plant, 1984

As a result of successful initial testwork, Mintek and Middelburg Steel & Alloys undertook a longer-term R&D programme to develop the technology commercially. Based on testwork at 0.3 - 0.5 MW in furnaces 1 – 2 m in diameter, the initial industrial-scale 16 MVA (12 MW) transferred-arc furnace (shown in Figure 2.9) was installed at the Krugersdorp (Palmiet Ferrochrome) plant of Middelburg Steel & Alloys at

the end of 1983 (Kammeyer *et al.*, 1989), then upgraded (around 1987) to 40 MVA (~33 MW) in 1988. An additional 10 MW furnace was later built around 2010 on the same site (for Mogale Alloys).

Chromite is smelted together with some form of carbon to produce ferrochromium, along with slag and CO gas. The DC arc furnace operates with an open-arc, open-bath configuration, so there is no heaped burden through which the reaction gases would need to escape. There is simply a molten bath onto which the fine material is dropped, and it almost immediately assimilates into the molten bath, melting and dissolving into the slag phase where the reactions take place. This furnace does not require coke because there is no burden above the bath so it doesn't require the porosity that would otherwise be needed. This is a very significant advantage, in that it allows the use of inexpensive reductants, thereby avoiding the high cost and relative scarcity of coke.

The power supplied to the DC arc furnace is largely independent of the slag composition, because there is an open electric arc that allows one to adjust the amount of power going into the furnace independently of the electrical resistivity of the slag. This provides extra flexibility and an extra degree of freedom of a change in slag composition unconstrained by electrical properties, so that the chemical activities of the important metals can be changed to achieve higher chromium recovery. A typical increase in chromium recovery could be from about 85% in an AC submerged arc furnace to about 95% in a DC arc furnace – a very significant increase. Slatter (1995) has pointed out that high CaO slags, with conductivities too high for submerged arc furnace operation, can be used for the production of extra-low-sulfur alloys.

In addition, the DC arc furnace has lower electrode consumption.

The DC-arc process allows the use of unagglomerated chromite fines and cheaper, non-coking coal. This furnace technology is regarded as one of the lowest-cost options for the production of ferrochromium.

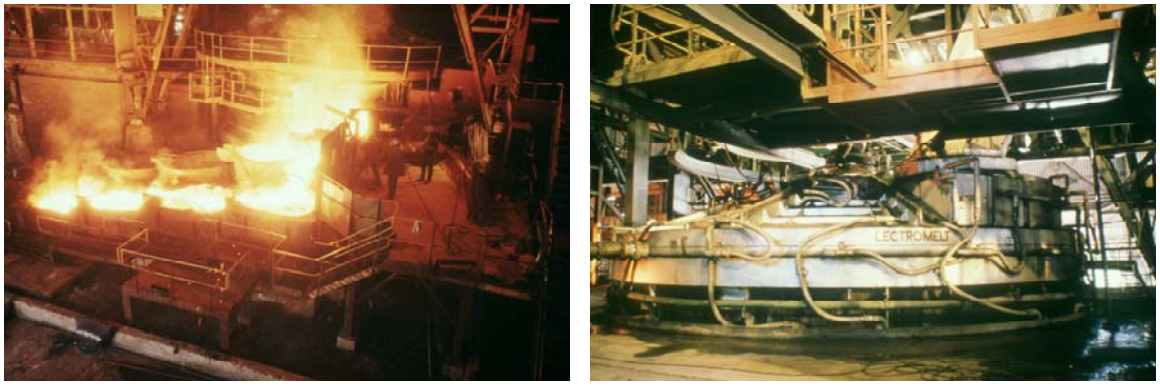

Figure 2.9 First commercial DC arc furnace for ferrochromium at Palmiet Ferrochrome, Krugersdorp

Based on the successful operation of the DC arc furnace for chromite smelting at Krugersdorp, Middelburg Ferrochrome (now part of Samancor Chrome) built a 44 MW (62 MVA) DC arc furnace, the largest of its type, (shown in Figure 2.10) in Middelburg in 1997. This was followed, in 2009, by an additional 60 MW furnace (shown in Figure 2.11) in Middelburg, currently the largest DC arc furnace in South Africa. The 44 MW furnace was subsequently upgraded to 60 MW.

Figure 2.10 Middelburg Ferrochrome built a 44 MW (62 MVA) DC arc Furnace in Middelburg in 1997

Figure 2.11 Samancor Chrome's first 60 MW furnace in Middelburg

Four 72 MW furnaces were constructed by SMS Siemag in Kazakhstan during 2013. Kazchrome (a ferrochromium producer in Kazakhstan) contracted with Mintek in 2007 to undertake smelting testwork. Based on this, and on other design inputs provided by Mintek in 2009, SMS Siemag has built four 72 MW DC arc furnaces in Aktobe, Kazakhstan, and commissioning was scheduled to take place in 2014. Each of these furnaces features an automated online electrode changer for the 75 cm diameter graphite electrodes, and a suspended roof.

2.3.2 Ilmenite smelting

Ilmenite is smelted to produce titania slag (mostly for pigment production) and pig iron. Ilmenite from beach sands in South Africa is of too low a grade to be used directly for the production of pigment or synthetic rutile. Instead, it is smelted to produce a titania slag suitable for the production of TiO_2 pigments. The overall reaction involved is shown as:

$$FeO.TiO_2 + C = TiO_2 + Fe + CO \quad [2\text{-}1]$$

The high electrical conductivity of titania slags (which have a resistivity of 0.025 Ω.cm, according to Bowman (1990)) and the required accurate control of the slag composition effectively rule out the use of conventional submerged-arc technology (where carbon from the electrodes comes into direct contact with the slag) for the smelting of ilmenite. Richards Bay Minerals (RBM) (Williams & Steenkamp, 2006) uses process technology originally developed by Quebec Iron & Titanium (QIT Fer et Titane) of Sorel, Canada, employing rectangular six-in-line graphite-electrode furnaces in open-bath mode with AC open-arc operation.

An alternative to this process, based on single hollow-electrode DC-arc furnace technology, was developed by Mintek and Anglo American Corporation for the Namakwa Sands project. The problem that needed to be solved was to find alternative equipment in which to produce a very conductive slag. Because the slag is so conductive, it is not feasible to obtain sufficient resistive heating in the molten slag, and it is, therefore, necessary to use an open arc. (This is a very different reason for using a DC arc furnace from that requiring it for smelting chromite fines.)

Phase one of the testwork, in 1990, involved four 15 kg batch tests at 30 kW, and showed that the process was feasible, and that a freeze lining was required. Phase two, in 1991, involved smelting two tons of ilmenite, with continuous feeding at 50 kg/h, at a power level of 100 kW. This produced an on-specification slag, and a metal that was high in Ti. Phase three, also in 1991, saw the smelting of 35 tons of ilmenite, fed continuously at 300 kg/h, at power levels of 500 kW (to 1 MW), with on-grade slag and metal produced. Phase four, in 1995, processed 200 tons of

ilmenite at 1 t/h and 1.5 MW, and primarily involved the development of the furnace start-up procedure, process control, and operator training. Following the 0.5 MW pilot-plant testwork in a 1.8 m diameter furnace (shown in Figure 2.12), the first 25 MW DC arc furnace at Namakwa Sands (see Figure 2.13) was constructed in 1994, followed by a 35 MW DC furnace in 1998. The first (25 MW) furnace began production of ilmenite slag and pig iron in June 1995, and the second furnace (35 MW) was brought on line in February 1999 (Gous, 2006).

Figure 2.12 Ilmenite smelting testwork at Mintek

Figure 2.13 Namakwa Sands

Based on that success, without any further testwork being required at Mintek, two further 36 MW DC furnaces (Kotzé, 2006) for ilmenite smelting were built for Ticor SA (see Figure 2.14), near Empangeni, and were commissioned in 2003.

Figure 2.14 Ticor ilmenite smelter, near Empangeni

A further 30 MW furnace was built by Bateman and commissioned for CYMG in China in 2009.

Part of the improvement in understanding that is required for ilmenite smelting was a detailed understanding and modelling of the electrical behaviour of the arc (in terms of the arc voltage as a function of current and arc length). The reason for this is that nearly all of the electrical resistance in the furnace is in the arc, as the slag is highly conductive (as is the metal). (The electrical modelling is covered in Chapter 4.)

2.3.3 Cobalt recovery from non-ferrous slags

A common feature shared by all pyrometallurgical smelting processes is the production of slag. Slag is usually a by-product of metal production,

although there are processes (such as ilmenite smelting, for example) where the slag is the principal product. Many slags contain a significant quantity of heavy metals, the release of which can cause environmental problems. However, the recovery of these metals may make it economic to clean the slags to the point where they are not only safe for disposal, but also where they may be able to be used as products in their own right. Consequently, a great deal of work has been done on the properties of slags (Mills *et al.*, 2011) and on processes for their treatment (Jones, 2004).

One very effective method for the recovery of valuable metals, such as cobalt, from non-ferrous smelting slags, involves treating these waste materials with a carbonaceous reducing agent in a DC arc furnace (a process developed at Mintek since 1988). Mintek has investigated the use of this technology for the recovery of cobalt from copper reverberatory furnace slags, as well as for the recovery of nickel, cobalt, copper, and platinum group metals from furnace and converter slags in plants treating nickel sulphide concentrates. Early pilot-plant testwork at Mintek demonstrated recoveries of 98% for nickel and over 80% for cobalt, at power levels of up to 600 kW.

The technology was further developed by Mintek and Anglovaal Mining Ltd (Avmin) for the recovery of cobalt from the reverberatory furnace slag dump at Nkana in Zambia where about twenty million metric tons of slag had accumulated over about sixty years of smelter operation. (When the copper smelter originally started up, the cobalt was seen as more of a nuisance than a useful metal.)

Simple slag cleaning (by melting and settling out metallic droplets) would not suffice to recover the valuable metals, as a significant portion of the cobalt was present in oxide form dissolved in the slag. What was clearly

needed was a process to recover cobalt from its oxidized form in the slag. In this case, a carbonaceous reducing agent is added to the molten slag to reduce the metal oxides into the metallic state.

Testwork at the 150-250 kW scale was conducted at Avmin's research laboratories, and larger-scale piloting was conducted at Mintek (in partnership with Avmin) in a 3 MW DC arc furnace. Approximately 840 tons of Nkana dump slag (ranging from 0.66% Co) was processed at Mintek at power levels around 1-2 MW in a 2.5 m diameter furnace in 1999. Good overall cobalt extraction was achieved, and approximately 100 tons of cobalt-bearing iron alloy was produced (containing 5 to 14% Co). This testwork demonstrated that the Nkana dump slag could be processed in a DC arc furnace of suitable design, to produce a cobalt-bearing alloy suitable for further hydrometallurgical processing. A relationship was established between the amount of iron reduced and the amount of cobalt recovered to the alloy product (to be discussed further in Chapter 3).

A 40 MW DC arc furnace, designed by Bateman Titaco, was built at Chambishi Metals in Zambia; and power to the furnace was switched on during January 2001 (Jones *et al.*, 2002). This plant is shown in Figure 2.15, and the furnace is shown in Figures 2.16 and 2.17. Notable features of the furnace include an ABB power supply of unusually high voltage, a Concast conductive hearth, and copper cooling of the side-walls. The furnace cooling system was subsequently modified by Hatch.

Figure 2.15 Chambishi Metals, Zambia (40 MW), 2001

This was a very challenging installation, as the metallurgical process had not been carried out industrially before, let alone in a furnace of this type. This was the first commercial DC smelting furnace to use solid electrodes with side-feeding. (A number of furnaces have now changed away from the hollow electrodes that were originally used by ASEA for chromite smelting.) This enabled greater availability for the furnace, in that less time was required for changing electrode sections because no feed pipes had to be removed first. This approach also resulted in lower electrode consumption because of the diminished wear from the inside of the electrode.

The Chambishi furnace recovered a great deal of cobalt from slag, and was eventually able to operate at design capacity, but has recently ceased operation because of economic pressures. The story of the Chambishi plant is told in greater detail by Jones *et al.* (2001, 2002), Nelson *et al.*

(2004), and Barnes and Jones (2011). Further information on the development of the process has been documented by Jones *et al.* (1996), Jones (1998), and Jones & Deneys (1998).

Figure 2.16 Slag-tapping end of the Chambishi 40 MW furnace

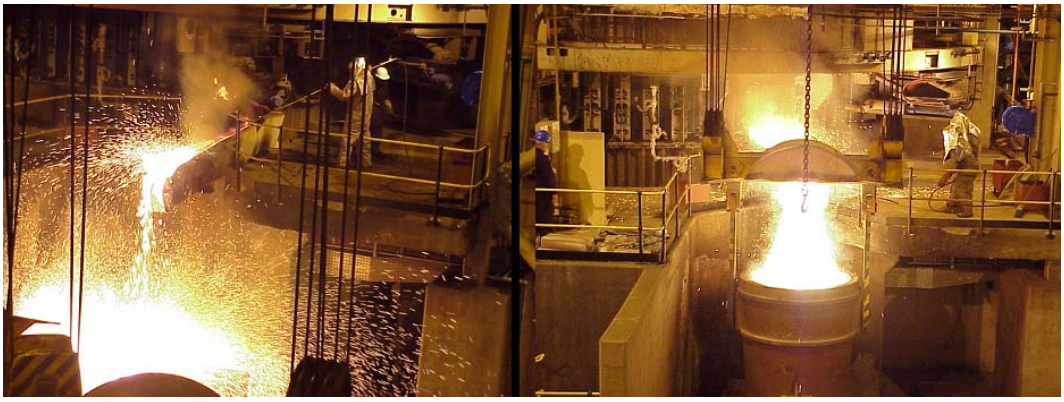

Figure 2.17 Alloy-tapping end of the Chambishi 40 MW furnace

2.3.4 Stainless steel dust smelting

Steel-plant dusts of many different types contain hazardous heavy metals. This can be seen as either a problem or as an opportunity, or both. The disposal of these materials is problematic because of the precautions that need to be taken to avoid contaminating the environment with the heavy metals that might pollute groundwater if not properly contained. However, these metals are valuable, and a DC arc furnace can be used to

recover metals such as chromium and nickel, and produce a slag that can be safely disposed of. The DC arc furnace is well suited to this application because it handles very fine feed materials well, without the need for costly agglomeration, and is able to be operated under the reducing conditions that are required.

Steel-plant dusts are extremely fine, and are therefore difficult to treat. Mintek has developed the Enviroplas process (using DC arc furnace technology) for the treatment of solid wastes from the metallurgical industry (including both carbon- and alloy-steel dusts) without requiring agglomeration. The process has the following benefits:

- Valuable metals such as zinc are concentrated in the vapour phase, and can be condensed directly from the furnace off-gases.
- The recovery of alloying elements such as chromium, nickel, and molybdenum in the hot metal exceeds 90%.
- The resulting innocuous slag can be safely disposed of, as it meets the specifications for disposal without requiring expensive containment.

Mintek has successfully processed about 1700 tons of AOD/EAF dust on a toll-treatment basis, in order to recover the contained chromium and nickel. The metal produced contained 18 per cent Cr, and 6 per cent Ni. All slag samples tested conformed to US EPA regulations for disposal. The chromium and nickel recovery to metal, on a once-through basis without recycling secondary dust generated during the testwork, was 92 and 94 per cent respectively.

The process has been adapted for operation on an existing 40 MVA (32 MW) DC arc ferrochromium furnace at Mogale Alloys in Krugersdorp.

2.3.5 Battery recycling

Mintek designed and built a furnace for a battery recycling company, called Batrec (see Figure 2.18), in Switzerland in 2008. This is a small furnace, 2.5 MW, and treats 5 000 tons of recycled batteries per annum, and produces zinc and ferromanganese.

Figure 2.18 Batrec battery recycling plant in Switzerland

2.3.6 Nickel laterite smelting

Laterites and other oxidized nickel ores constitute a very important part of worldwide nickel reserves. In the conventional production of ferronickel from these ores, much fine material is produced which cannot readily be accommodated directly in existing three-electrode or six-in-line AC furnaces. DC arc furnace technology allows ore particles less than 1 mm in size to be treated directly, thereby improving the overall recovery of nickel without the need for expensive agglomeration techniques. Because of the high moisture content of laterites, the ores need to be dried and calcined before smelting. A further saving in energy consumption is achieved by pre-reducing the ores.

Mintek has been working on the production of unrefined ferronickel from nickel-containing laterite in DC arc furnaces since 1993. In this process, calcined lateritic material is fed, together with a carbonaceous reducing agent, to the central region of the molten bath of a cylindrical DC arc furnace. A wide compositional range of nickel laterites can be smelted in this way. The flexible operation of a DC arc furnace (especially its lower dependence on electrical properties of the slag, because of open-arc operation, in addition to the ability to run at an optimum slag temperature, due to the open-bath mode of operation) allowed for the successful treatment of ores with a SiO_2/MgO ratio between 1.2 and 3.0, as well as ores containing up to 30 per cent by mass of iron (which tends to cause unwanted slag foaming in a conventional immersed-electrode furnace). A frozen lining can be maintained between the molten bath and the refractory lining, in order to minimize refractory wear (especially at high SiO_2 contents).

The smelting of nickel laterite to produce ferronickel was piloted at Mintek (Lagendijk & Jones, 1997) from 1993 to 2006, using a wide variety of feed materials. Figures 2.19 and 2.20 show Mintek pilot-plant furnaces that were used for laterite smelting testwork.

Figure 2.19 Nickel laterite smelting testwork at Mintek

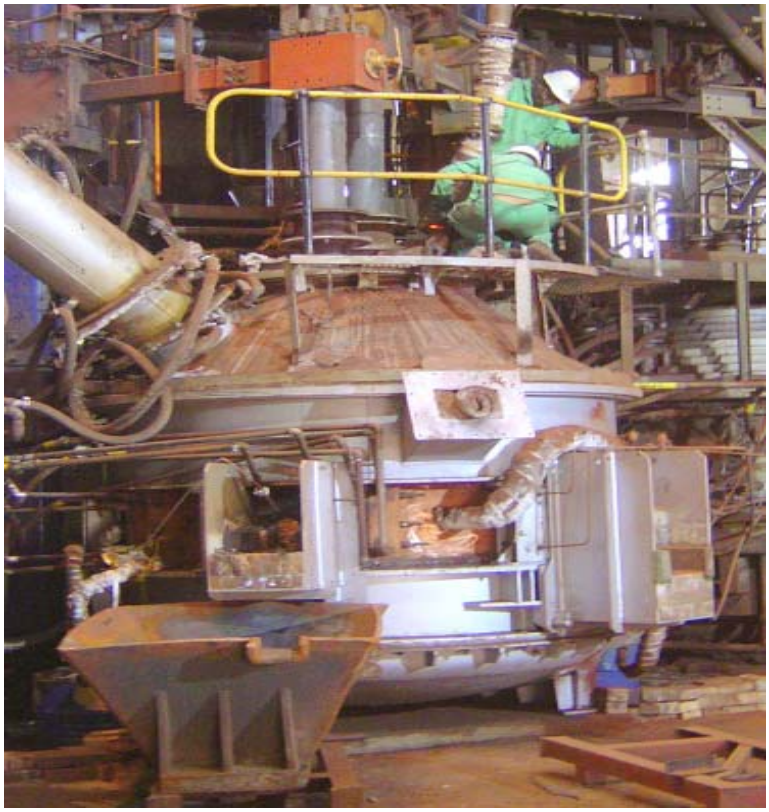

Figure 2.20 A twin-electrode DC arc furnace used for laterite smelting at Mintek

The first commercial application of the DC FeNi process was a 12 MW DC arc furnace (shown in Figure 2.21) (Naude & Shapiro, 2010) in Orsk in the Southern Urals, Russia, commissioned in September 2011.

Figure 2.21 A 12 MW DC arc furnace in Orsk, Southern Urals, Russia

The largest application of DC arc furnace smelting technology is the Koniambo Nickel project in New Caledonia – a greenfield joint venture partnership between Société Minière du Sud Pacifique (SMSP) and Glencore Xstrata. The process is based on milled ore, fluidized beds, and two twin-electrode 80 MW DC arc furnaces, with cyclone pre-heaters. Each 71 cm graphite electrode has a separate 40 MW power supply (transformer and rectifier). The smelting testwork for this project was carried out at Mintek in the late 1990s. The Koniambo ferronickel smelter (shown in Figure 2.22), aims to produce 60 kt/a of Ni in FeNi from one of the world's largest and highest-grade nickel laterite deposits. The smelter commissioning began in 2012, and the first metal from the furnace was produced in April 2013 (Mining Journal, 2013).

Figure 2.22 The Koniambo smelter in New Caledonia

2.3.7 ConRoast

The ConRoast process treats sulfide concentrates by roasting (for sulfur removal), followed by reductive smelting in a DC arc furnace, where an iron-based alloy is used to collect the valuable metals. This process can be used for the treatment of nickel sulfide ores as well as those containing platinum group metals (PGMs). In the case of PGM smelting, the

ConRoast process addresses the three big challenges, namely the sulfur problem (SO_2 emissions), the chromium problem (from the use of UG2 chromitite ores), and the containment problem (avoiding furnace failures).

The ConRoast process is aimed at being a very different smelter, using a DC arc furnace for alloy smelting (from oxide) instead of matte (sulfide) smelting. Sulfur is removed at the beginning of the process (as a steady SO_2 stream to an acid plant, for example), by dead-roasting the concentrate. The PGMs and valuable base metals are collected in an iron-based alloy, which is even more effective than matte in collecting PGMs. (The distribution coefficients for PGMs in an iron alloy relative to slag are even greater than the distribution coefficients for PGMs in matte relative to slag; as discussed in Section 6.3.1.) This flexible PGM processing route can handle a wide range of feeds, as it has no need for much Ni and Cu (or S) in the ore, as Fe is the collector. The reducing conditions in the furnace (and high temperatures, if required) allow much higher levels of Cr_2O_3 in feed (> 5%) without causing a problem with spinel precipitation. The iron is subsequently removed either by converting, or with a few modifications to the base metals refinery.

Roasting removes sulfur (98% elimination of S in a fluidized bed has been demonstrated) and other impurities very effectively. Roasting and smelting removed most (70 – 100%) of the minor impurity elements: As, Bi, Mn, Pb, Se, Te, and V. Alloy smelting collects PGMs very well, resulting in very barren slags – consistently less than 1 g/t PGM in slag, with < 0.3 g/t PGM in slag being demonstrated often. If iron removal from the product alloy is to be done hydrometallurgically (in a process similar to that used at Chambishi Metals), the final levels of C, Si, and Cr in the alloy can all be brought down to less than 0.05% by ladle refining. Water atomization can be used to produce very fine particles (< 100 μm)

that leach rapidly. A high-grade high-recovery clean PGM concentrate (> 60%) was produced.

The sulfur problem: The ConRoast process involves a cleaner approach to the smelting of sulfide ore concentrates than the matte smelting and converting that is traditionally used. The dead-roasting (in preparation for the smelting step) is a continuous process that is done in a well-sealed fluidized bed vessel, and is therefore less environmentally damaging in terms of SO_2 emissions to the atmosphere, let alone to the immediate working environment in the smelter. The feed material is thus oxidized and the furnace is able to operate in a normal reductive smelting mode.

The chromite problem: The presence of high amounts of chromite in a furnace poses a number of problems to the operation, because of the highly stable spinel structure of the chromite crystal. It is very difficult to tap the furnace if much chromite is present. It forms accretions inside, and forms an intermediate layer between the slag and the matte, preventing good collection and settling. By changing to more reducing conditions in the furnace, one can move away from having the insoluble and refractory chromite spinel ($FeO.Cr_2O_3$) towards having CrO that dissolves readily in the slag.

The containment problem: The containment problem is particularly challenging when having to deal with a matte with a very low liquidus temperature, and a slag with a high liquidus temperature in the same furnace vessel. PGM smelting typically operates with very high quantities of slag relative to the matte or alloy, so there is limited opportunity to change the slag composition significantly by adding fluxes. In order to keep the slag molten and sufficiently fluid, the temperature required unfortunately can result in a highly superheated matte that penetrates

refractories very easily and is not readily solidified. By changing from matte to an iron-based alloy, this has a similar liquidus temperature to that of the slag, making the problem of containment much easier to manage.

The ConRoast process has been demonstrated by smelting 50 000 tons of PGM-containing feed materials at Mintek over a period of operation of about five years. This large-scale smelting at Mintek (shown in Figure 2.23) involved the processing of up to 2 000 tons per month, using a clean process that produces an alloy product (typically less than 10% of the mass of the feed material), a by-product slag (that meets the criteria for safe disposal, or could be used as a by-product for purposes such as concrete aggregate, road fill, or shot blasting), and clean gas emissions (after passing through a bag-house, SO_2 scrubber, and stack). The initial work entailed four years of reductive alloy smelting of revert tailings (low sulfur, high chromium, otherwise virtually 'untreatable' material) in a 1.5 MW (3.0 m diameter) furnace, where about 37 000 tons of revert tailings material was smelted, with a maximum rate of 47 tons per day. The furnace ran very reliably. At this scale of operation, the demonstration was a very convincing one, as well as producing sufficient product to make the process economically profitable in its own right.

Subsequent work involved the upgrading of the furnace to 3 MW (4.25 m diameter), and this furnace was first tapped in October 2008. Two six-month campaigns of reductive matte smelting (where some iron and other oxides are reduced to metal, but there is sufficient sulfur present to form a matte product) in the 3 MW DC arc furnace were undertaken, where the feed was a 75:25 mixture of high-chromium concentrate and converter slag, and 12 000 tons was smelted, with a maximum rate of 66 tons per day. A commercial 5 MW DC arc furnace has been announced, but not yet built.

Figure 2.23 1.5 MW and 3 MW DC arc furnaces at Mintek

Part of the increased understanding and huge amount of data that came out of this work led to the development of a very useful model for predicting the recoveries of various metals as a function of the iron recovery which is just a proxy for the extent of reduction in the furnace. This relationship between the recovery of nickel, cobalt, and even chromium is shown as a function of iron recovery in Chapter 3. This allows one to predict the behaviour of any new feed material that is introduced into the furnace.

2.3.8 Zinc fuming

In this application, the metal product is obtained in the vapour phase instead of as a molten alloy.

There are numerous residue materials that are classified as hazardous waste because of their lead content, but contain sufficient zinc to be worth treating further. Mintek has undertaken considerable work on the

treatment of lead-blast-furnace slags, steel-plant dusts, and leach residues. A technically viable process has been demonstrated for lead-blast-furnace slags (Schoukens *et al.*, 1995), which involves the feeding of a molten stream of slag into a DC arc furnace where carbon is added and zinc vapour is produced. The zinc vapour is then absorbed in an ISP lead-splash condenser (that is actually more of an absorber than a condenser). Unfortunately, this process has not yet been implemented industrially, because of commercial reasons.

A 2 t/h pilot plant, including a lead-splash condenser, was commissioned in 1994, and piloted at Mintek from 1994 to 1998. The intention was to simulate a fuming furnace that was fed by a molten stream of slag (typically from a lead blast furnace). To do this, it was necessary to use two furnaces, with the first functioning simply as a pre-melter. The primary 'fuming' furnace carries out the reduction reactions and fumes off the zinc vapour. The vapour leaves the furnace and passes through a carefully designed cross-over duct that needs to keep the temperature above about 1000°C, in order to avoid the reversion of zinc vapour to zinc oxide.

Figure 2.24 shows the 5.6 MVA DC arc zinc fuming furnace pilot plant at Mintek. The condenser is the large rectangular unit in the back left corner of the floor.

Figure 2.24 5.6 MVA DC arc zinc fuming furnace pilot plant at Mintek

Figure 2.25 shows molten slag flowing from the pre-melter into the fuming furnace in the 5.6 MVA DC arc furnace pilot plant at Mintek.

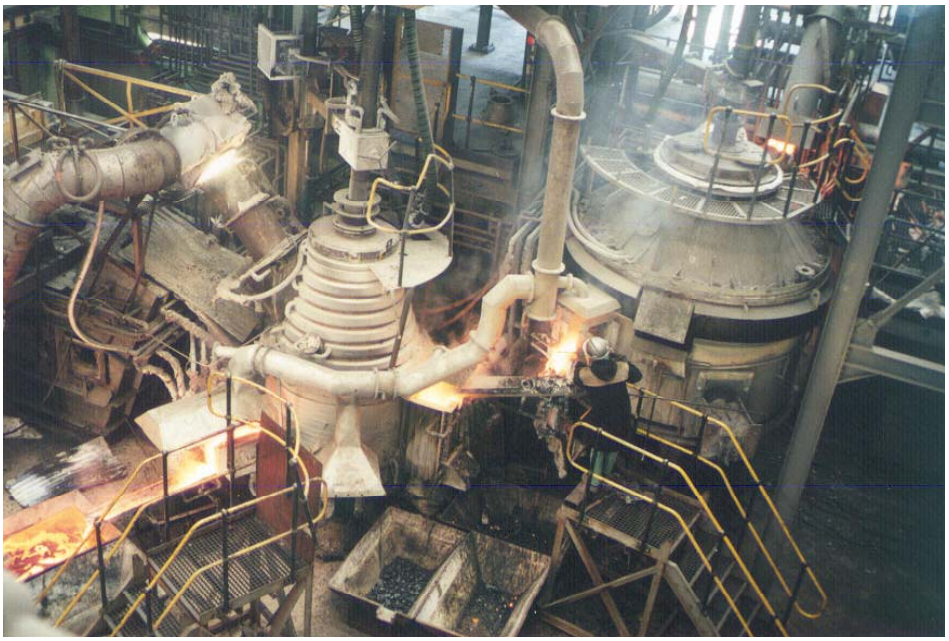

Figure 2.25 Molten slag flows from the pre-melter into the fuming furnace in the 5.6 MVA DC arc furnace pilot plant at Mintek

The process was able to recover about 98% of the zinc metal via fuming and condensation. Some work was also done on the packed-bed distillation of the zinc to 99.5% Zn purity.

An interesting further development of this process was studied by Deneys *et al.* (1997) where cobalt was recovered in an iron alloy, in conjunction with a zinc fuming process for the treatment of one particular lead-blast-furnace slag.

2.3.9 Mintek Thermal Magnesium Process

Magnesium is an important component of light alloys used in the aerospace and transport industries, but continuous production of the metal requires the use of more sophisticated technology than for most other metals.

Thermal production of magnesium, at normal atmospheric pressure, was demonstrated in the late 1980s by Albert Schoukens at Mintek. Initial testwork was carried out in a DC arc furnace at a scale of 50 to 100 kVA. This work eventually led to the development of the Mintek Thermal Magnesium Process (MTMP). Mintek's use of an open DC arc for the production of magnesium vapour provides the freedom to operate at 1700°C or more. The higher temperature provides a greater choice of slag composition, and, therefore, permits a wider choice of feed materials and their proportions. Atmospheric pressure (instead of under a vacuum as in the conventional process) can be used at this temperature, thereby avoiding batch operation and allowing scale-up beyond 10 MW units. By avoiding vacuum conditions, there is reduced leakage of air and consequent re-oxidation of magnesium.

The MTMP is based on DC open-arc smelting of calcined dolomite (dolime) at atmospheric pressure in the presence of ferrosilicon (Figure 2.26). As such, the process is not constrained by the electrical resistivity of the slag, and allows the furnace to be operated at relatively high voltage. The volatilized magnesium is captured as liquid metal in a surface condenser, which permits periodic tapping of the crude magnesium. Doing so, in conjunction with conditions at atmospheric pressure, makes possible the operation of a large-scale facility 'continuously' (or semi-continuously). The Mintek Thermal Magnesium Process has resulted in the production of high-purity magnesium metal. This process has lower capital costs, and is economically viable on a much smaller scale than the conventional electrolytic process.

The process is a more continuous one (designed to run for more than 72 hours at industrial scale), although periodic cleaning is required to remove accretions from ducts. Longer operation means less downtime, therefore higher availability and lower production costs. There is greater ability to scale up, which also lowers production costs. Lower impurity levels result in lower refining costs.

The past few years have seen an increased focus on the condensing aspect of the process, and there have been some significant developments on this front. Some key results include:

- Produced Mg at atmospheric pressure
- Condensed Mg as a liquid
- Tapped crude liquid Mg on line
- Mg quality better than industry average
- Produced over a ton of Mg so far.

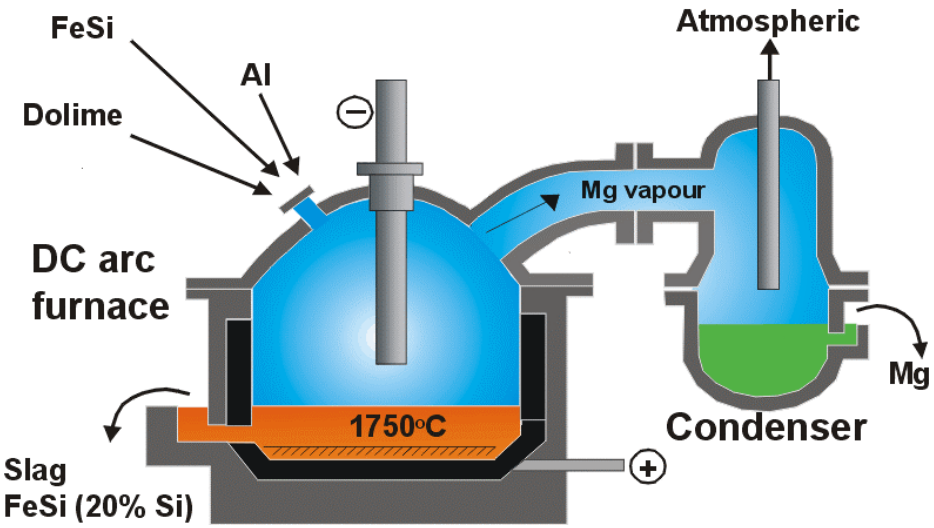

Figure 2.26 Mintek Thermal Magnesium Process – simplified diagram

Figures 2.27 to 2.29 show the magnesium furnace in operation, as well as its products.

Figure 2.27 Sampling a molten stream from the DC arc furnace for magnesium production

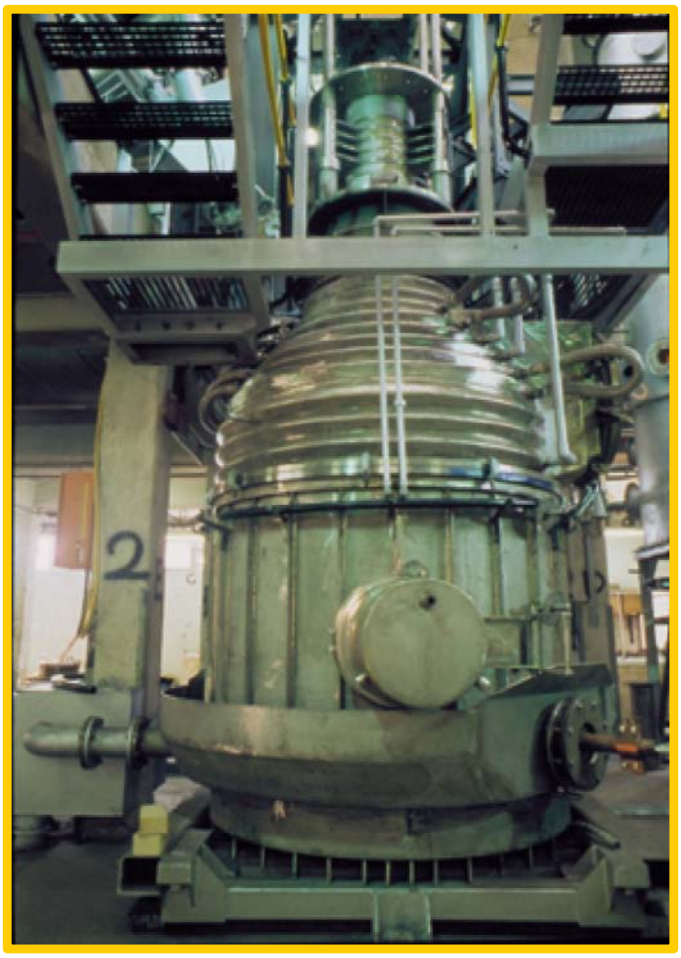

Figure 2.28 DC arc furnace for magnesium production

Figure 2.29 Ingots of magnesium produced in a DC arc furnace at Mintek

2.4 Conclusions

DC arc furnaces have some important benefits. They are good at accommodating finely sized feed materials (because of the open bath). They do not require coke or char (no burden porosity required). DC arc furnaces can treat feed materials with a wide range of composition (because of the extra degree of freedom coming from power being supplied by an open arc); this allows choice of chemistry for metallurgical benefit. These furnaces are geometrically simple and elegant, thereby reducing uneven wear on side-walls, and leading to lower costs. The direct-current operation reduces electrode consumption, and provides a directed arc jet and good mixing.

However, there are some drawbacks. Thermal efficiency is decreased by the hot off-gas leaving the furnace (unless some of this energy is recovered). The absence of a burden does not allow for the capture of volatile species.

Apart from extensive use in the steel industry, it is only in the past few decades that DC arc furnaces have been used for smelting processes, where the feed materials are predominantly non-metallic and significant chemical reactions are involved. Mintek's Pyrometallurgy Division has been fortunate enough to be involved in the industrial-scale commercialisation of roughly one major application of this technology per decade, and has become well known internationally for its work on DC arc furnaces. This started with the smelting of chromite ore fines to produce ferrochromium in the 1980s, and was followed by the smelting of ilmenite to produce titania slag and pig iron in the 1990s. In both of these cases, the process chemistry was well known and the products were familiar (albeit with some minor variations), even though the type of

furnace was novel at the time. A further example was the use of a DC arc furnace to recover metals (principally cobalt) from non-ferrous smelting slags early in the 2000s. In this case, a new process was carried out in a 'new' piece of equipment to produce a somewhat unfamiliar intermediate product. This, therefore, required testing and demonstration at quite a large scale. Since then, there has been commercial application of processes for stainless steel dust smelting and battery recycling. Nickel laterite smelting was commercialised in the 2010s. Table 2.2 lists the DC arc furnaces used for smelting applications.

Table 2.2 DC furnace installations

Process	Year	Furnaces
Steel		> 80 DC furnaces, up to 175 MW
FeCr	1985	10MW, 30MW, 60MW, 60MW, (4 x 72MW)
TiO2	1994	25MW, 30MW, 35MW, 36MW, 36MW
Co	2001	40MW
Stainless steel dust	2004	32MW
Battery recycling	2008	2.5MW
FeNi	2011	12MW, (2 x 80MW)

DC arc furnaces are well suited to reductive smelting processes (*e.g.*, FeCr, TiO_2, FeNi), but less so in the case of processes involving a gaseous intermediate such as SiO, or those with a low-melting (super-heated) product.

DC arc furnaces are not a panacea for all metallurgical problems, but are very well suited to a number of reductive smelting processes where they have been applied successfully in a number of industrial contexts, and many further applications are expected.

3 RECOVERY OF BASE METALS AND PGMS

3.1 Introduction

A number of pyrometallurgical processes involve reductive alloy smelting using a carbonaceous reducing agent. These processes include the smelting of chromite to produce ferrochromium, the smelting of nickel laterite ores to produce ferronickel, the recovery of base metals from slags, and the recovery of platinum group metals (PGMs) via collection in iron alloys. When carbon is added to the molten bath in a furnace, the oxides of the various metallic elements reduce to different extents, at a given level of carbon addition, in order to minimize the Gibbs free energy of the system within the constraints of mass conservation. This allows some metallic elements to concentrate preferentially into an alloy phase, while others (whose oxides have more negative standard free energies of formation) remain predominantly in the slag in oxidized form. This selective reduction behaviour allows a reasonable degree of separation (of one element from another) to take place during smelting. It is well known that an increase in the amount of the reductant added to the furnace results in increased quantities of the various metallic elements that report to the alloy that is produced, but it would be very useful for the design of such smelting processes to have an equation that described this behaviour quantitatively. This chapter deals with the development of such an equation that relates the recovery of individual metals to the recovery of iron, in terms of a single parameter that can either be derived from thermodynamic data or be empirically fitted to experimental and plant data. This equation may be used for process design calculations over a range of feed material compositions, and is particularly useful for

calculating the degree of reduction that is required to achieve a particular level of recovery of the metal of interest.

Mintek is in the fortunate position of doing work in support of a great variety of industrial processes (Jones & Curr, 2006), and this provides a wider range of operating data than is readily available at a single operating plant elsewhere. In particular, Mintek has applied DC arc furnace technology to many alloy smelting processes, and it has been found that this type of furnace provides relatively consistent alloy and slag compositions, usually fairly close to chemical equilibrium conditions, because of the largely uniform temperature and the well mixed nature of the melt in the furnace that is stirred effectively by the vigorous action of the open electric arc impinging on the surface of the slag. The stirring is sufficient to promote coalescence of small alloy droplets, but not so intense as to keep many droplets in suspension in the slag.

3.2 Theoretical Development of the $K\gamma$ Recovery Equation

In most of the ores and concentrates under consideration in this chapter, iron oxide is present as either the dominant or one of the most common reducible oxides. For this reason, and in deference to the dominant position of iron in the world of metallurgy, the otherwise arbitrary decision is made to express the recoveries of the metals of interest in relation to the recovery of iron. This is merely a convenient choice of reference.

For the purposes of developing an equation that describes the recovery of metals, the relationship between Co and Fe is considered here, purely as an example of this type of reaction. (This specific example is discussed in greater detail in Section 3.5.) However, the same principles can be applied

to other base metals too. The equation development below builds on and extends earlier work (Jones *et al.,* 2002) that was specifically focused on cobalt recovery.

In the chosen example system, the interchange between Co and Fe can be seen by studying the liquid-liquid reaction between the oxides in the slag and the metals in the alloy:

$$CoO + Fe \leftrightarrows Co + FeO \qquad [3\text{-}1]$$

At equilibrium, the degree of separation between Co and Fe can be indicated by the equilibrium constant, *K*, which is strictly a function of temperature only.

$$K = \frac{a_{Co} \cdot a_{FeO}}{a_{CoO} \cdot a_{Fe}} \qquad [3\text{-}2]$$

The activities *a* may be expressed in terms of activity coefficients γ and mole fractions *x*.

$$K = \frac{\gamma_{Co}\, x_{Co} \cdot \gamma_{FeO}\, x_{FeO}}{\gamma_{CoO}\, x_{CoO} \cdot \gamma_{Fe}\, x_{Fe}} \qquad [3\text{-}3]$$

Although the standard states of each of the constituents of the reaction have not been listed explicitly (to avoid detracting from the generality of the form of the equation, and in the interests of keeping the equations as clear as possible), it is important to note that the numerical values of the equilibrium constant and the activities and activity coefficients can vary according to the choice of standard states. It is obviously important that there is consistency in the choice of standard states, if individual values

for K and γ are to be used. (There is further discussion of this matter for the Fe-Co system in Section 3.5.)

For the purpose of clarity in the development of subsequent equations, the ratio of the activity coefficients of these four chemical species in solution may be lumped together, as defined in Equation [3-4]. Individual activity coefficients may be obtained from the literature.

$$\gamma = \frac{\gamma_{CoO} \cdot \gamma_{Fe}}{\gamma_{Co} \cdot \gamma_{FeO}} \qquad [3\text{-}4]$$

In using γ, the ratio of the activity coefficients, rather than the individual activity coefficients themselves, we would like to make the assumption that γ, in a given system, is not a strong function of composition, so that we may derive a simple expression to show the relationship between the recovery of Co to the alloy and the recovery of Fe to the alloy. [This assumption is seen to be reasonable in at least some of the major systems of interest, and is considered in greater detail for the iron and cobalt system in Section 3.5. For example, Belton *et al.* (1973) studied the equilibrium between liquid iron-cobalt alloys in terms of the Richardson model of ideal silicate mixing, and one of the consequences of this model is that $\gamma_{CoO} / \gamma_{FeO}$ should be independent of composition. Liu and Grimsey (1997) point out that the activity coefficient ratio $\gamma_{FeO} / \gamma_{CoO}$ would be expected to remain relatively constant for these chemically similar oxides. In the geological literature, Holzheid *et al.* (1997) found that the activity coefficients of FeO, NiO, and CoO in a high-temperature silicate melt were independent of partial pressure of oxygen and temperature over the range of 1300 to 1600°C, and were not affected by fairly wide variations in composition. In the case of iron being the major metal, its activity coefficient will be close to unity, and if the other non-ferrous metallic

element is dilute the assumption of a constant activity coefficient is not unreasonable.] In any case, the utility of the final equation will be tested by how well it fits actual data over a wide range of compositions.

From Equations [3-3] and [3-4]:

$$K\gamma = \frac{x_{Co} \cdot x_{FeO}}{x_{CoO} \cdot x_{Fe}} \qquad [3\text{-}5]$$

The simplicity of the stoichiometric coefficients of Equation [3-1] (and more particularly the fact that the number of moles in the slag and the number of moles in the alloy both remain constant) allows the equation above to be expressed in terms of numbers of moles:

$$K\gamma = \frac{n_{Co} \cdot n_{FeO}}{n_{CoO} \cdot n_{Fe}} \qquad [3\text{-}6]$$

Note that the above equation may also be expressed in terms of mass percentages, simply by taking into account a conversion factor to allow for the ratios of the molecular masses. Equation [3-7] provides an alternative method for generating a value for $K\gamma$ if measured compositions are available.

$$K\gamma = 0.988\left(\frac{\%Co \cdot \%FeO}{\%CoO \cdot \%Fe}\right) \qquad [3\text{-}7]$$

If the amounts of cobalt and iron initially present in the feed (in both metallic and oxide form) are denoted by a superscript zero, the following mass balance equations may be written.

$$n_{Co} = n_{Co}^0 + n_{CoO}^0 - n_{CoO} \qquad [3\text{-}8a]$$

$$n_{Fe} = n_{Fe}^0 + n_{FeO}^0 - n_{FeO} \qquad [3\text{-}8b]$$

Recoveries R_{Co} and R_{Fe} may be defined as follows:

$$R_{Co} \equiv \frac{n_{Co}}{n_{Co}^0 + n_{CoO}^0} \qquad [3\text{-}9a]$$

$$R_{Fe} \equiv \frac{n_{Fe}}{n_{Fe}^0 + n_{FeO}^0} \qquad [3\text{-}9b]$$

Combining Equations [3-8] and [3-9]:

$$n_{CoO} = (1 - R_{Co})(n_{Co}^0 + n_{CoO}^0) \qquad [3\text{-}10a]$$

$$n_{FeO} = (1 - R_{Fe})(n_{Fe}^0 + n_{FeO}^0) \qquad [3\text{-}10b]$$

Substituting Equations [3-9] (re-arranged) and [3-10] into [3-6] gives:

$$K\gamma = \frac{R_{Co}(n_{Co}^0 + n_{CoO}^0) \cdot (1 - R_{Fe})(n_{Fe}^0 + n_{FeO}^0)}{(1 - R_{Co})(n_{Co}^0 + n_{CoO}^0) \cdot R_{Fe}(n_{Fe}^0 + n_{FeO}^0)} \qquad [3\text{-}11]$$

This simplifies to:

$$K\gamma = \frac{R_{Co}(1 - R_{Fe})}{R_{Fe}(1 - R_{Co})} \qquad [3\text{-}12]$$

Equation [3-12] is re-arranged to give:

$$R_{Co} = \frac{K\gamma \cdot R_{Fe}}{1-(1-K\gamma)R_{Fe}} \qquad [3\text{-}13]$$

As shown in Section 3.5, it is certainly possible to calculate a value for $K\gamma$ from published theoretical data (if this is available for the particular system of interest), but this would apply only to an equilibrium system exactly the same as that under consideration. Conditions in a DC arc furnace do indeed often approach equilibrium conditions, but not always perfectly. The complex multi-component systems in real industrial processes are often modelled somewhat imperfectly by thermodynamic relationships derived from systems with fewer components. Furthermore, published data often relate to conditions different from those under consideration. It may sometimes be more useful to use the form of the theoretically derived equation, and to fit the model to actual plant data. Values of $K\gamma$ may be found by fitting Equation [3-13] to experimental data – for example, by using a least-squares minimization technique. For illustrative purposes, the curve in Figure 3.1 below shows a value of $K\gamma$ = 14. (A comparison will be shown later in this chapter between the model and experimental data.)

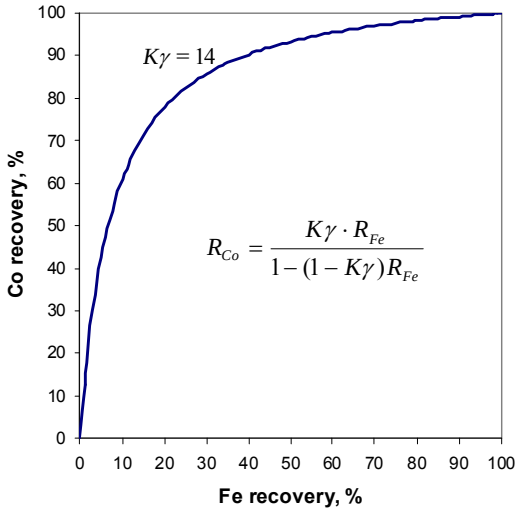

Figure 3.1 Illustrative relationship between Fe recovery and Co recovery to the alloy

3.3 Effect of Various Values of $K\gamma$ on the Shape of the Recovery Curve

The symmetrical nature (*i.e.*, the interchangeability of the two *R* terms in the same form of equation) of Equation [3-13] implies that it can be used to describe the recoveries of both elements that are more 'noble' (easier to reduce) than iron, and those that are less so. The more 'noble' the element, the higher the value of $K\gamma$. Figure 3.2 shows the effect of various values of $K\gamma$ on the shape of the recovery curve for a hypothetical element X. It can be seen from this set of curves that the higher the value of $K\gamma$, the closer the curve is to the top left. A value of 1 for $K\gamma$ yields a straight line, and can be seen as plotting the recovery of Fe against itself. Values of $K\gamma$ less than 1 generate curves closer to the bottom right. A pair of curves with reciprocal values of $K\gamma$ exhibit symmetry involving reflection across the '$K\gamma = 1$' line.

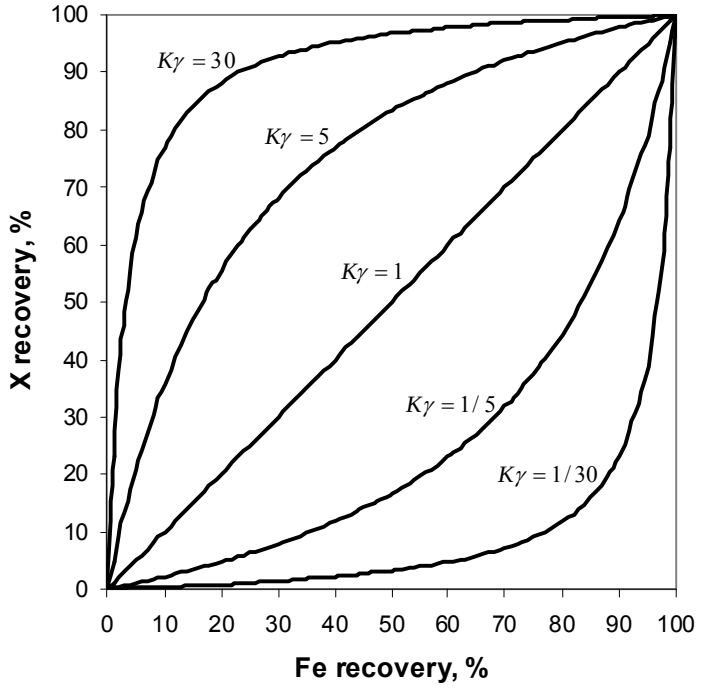

Figure 3.2 Recovery curves with different values of $K\gamma$

Moderate values of $K\gamma$ result in curves having a moderate degree of curvature, and it can be expected that such curves may be usefully fitted to sets of experimental data. Curves having more extreme values of $K\gamma$ (say those above about 50, or those less than about 1/50) will be subject to greater uncertainty as a result of experimental errors, as these will be accentuated in this area. Given that the activity coefficient ratio is unlikely to lie outside the range 10 to 0.1 (or maybe 100 to 0.01 at the most), then it is apparent that the K value would need to be neither very large nor very small if moderate values of $K\gamma$ are to be achieved. The result of this is that the two elements involved in the equilibrium (*e.g.*, Co and Fe) must be chemically very similar. Therefore, this relationship might be expected to work well for elements close to iron in the periodic table, such as Cr, Mn, Co, and Ni. If a reference other than iron is used, then the relationship could apply to other metals too.

3.4 Non 1:1 Stoichiometry of Reactions

The $K\gamma$ recovery equation presented here is based on the assumption of a 1:1 relationship in the stoichiometry of the exchange reaction exemplified by Equation [3-1]. This system has the great virtue of simplicity, in that it is possible to study the effect of the recovery of Fe on the recovery of another metallic element without explicitly having to take into account the other materials present (except, of course, to acknowledge the effect of composition on the individual activity coefficients). Additional work has been done to formulate similar equations for reactions of more complex stoichiometry (*e.g.*, Cr_2O_3 and Fe). However, these relationships (in particular, the mass balance expressions) are inherently more complicated in that the recovery relationships depend on all the species present in the system. Unfortunately, this dramatically decreases their utility. An example is provided here to make this clear.

The equations that follow are based on the methodology previously outlined in Equations [3-1] to [3-13]. An illustrative reaction between Cr_2O_3 and Fe can be represented by Equation [3-14], and K and γ follow naturally from this.

$$Cr_2O_3 + 3\ Fe \leftrightarrows 2\ Cr + 3\ FeO \qquad [3\text{-}14]$$

$$K = \frac{a_{Cr}^{\ 2} \cdot a_{FeO}^{\ 3}}{a_{Cr2O3} \cdot a_{Fe}^{\ 3}} \qquad [3\text{-}15]$$

$$\text{Define} \quad \gamma = \frac{\gamma_{Cr2O3} \cdot \gamma_{Fe}^{\ 3}}{\gamma_{Cr}^{\ 2} \cdot \gamma_{FeO}^{\ 3}} \qquad [3\text{-}16]$$

$$K\gamma = \frac{x_{Cr}{}^{2} \cdot x_{FeO}{}^{3}}{x_{Cr2O3} \cdot x_{Fe}{}^{3}} \qquad [3\text{-}17]$$

The complication arises when expressing the mole fractions in terms of the total number of moles present in each phase (slag and alloy), as these do not cancel neatly as they did in the case of a 1:1 stoichiometry.

$$K\gamma = \frac{\left(\frac{n_{Cr}}{n_{alloy}}\right)^{2} \cdot \left(\frac{n_{FeO}}{n_{slag}}\right)^{3}}{\left(\frac{n_{Cr2O3}}{n_{slag}}\right) \cdot \left(\frac{n_{Fe}}{n_{alloy}}\right)^{3}} \qquad [3\text{-}18]$$

$$K\gamma = \frac{n_{Cr}{}^{2} \cdot n_{FeO}{}^{3}}{n_{Cr2O3} \cdot n_{Fe}{}^{3}} \cdot \frac{n_{alloy}}{n_{slag}{}^{2}} \qquad [3\text{-}19]$$

The mass balance relationships follow from Equation [3-14].

$$n_{Cr} = n_{Cr}^{0} + \frac{1}{2} n_{Cr2O3}^{0} - \frac{1}{2} n_{Cr2O3} \qquad [3\text{-}20a]$$

$$n_{Fe} = n_{Fe}^{0} + n_{FeO}^{0} - n_{FeO} \qquad [3\text{-}20b]$$

Recoveries R_{Cr} and R_{Fe} may be defined as follows:

$$R_{Cr} \equiv \frac{n_{Cr}}{n_{Cr}^{0} + \frac{1}{2} n_{Cr2O3}^{0}} \qquad [3\text{-}21a]$$

$$R_{Fe} \equiv \frac{n_{Fe}}{n_{Fe}^{0} + n_{FeO}^{0}} \qquad [3\text{-}21b]$$

Combining Equations [3-20] and [3-21]:

$$\frac{1}{2}n_{Cr2O3} = (1 - R_{Cr})(n^0_{Cr} + \frac{1}{2}n^0_{Cr2O3}) \qquad [3\text{-}22a]$$

$$n_{FeO} = (1 - R_{Fe})(n^0_{Fe} + n^0_{FeO}) \qquad [3\text{-}22b]$$

Substituting Equations [3-21] (re-arranged) and [3-22] into [3-19] gives:

$$K\gamma = \frac{R_{Cr}{}^2 (n^0_{Cr} + \frac{1}{2}n^0_{Cr2O3})^2 \cdot (1 - R_{Fe})^3 (n^0_{Fe} + n^0_{FeO})^3 \cdot n_{alloy}}{2(1 - R_{Cr})(n^0_{Cr} + \frac{1}{2}n^0_{Cr2O3}) \cdot R_{Fe}{}^3 (n^0_{Fe} + n^0_{FeO})^3 \cdot n_{slag}{}^2} \qquad [3\text{-}23]$$

$$K\gamma = \frac{R_{Cr}{}^2 (n^0_{Cr} + \frac{1}{2}n^0_{Cr2O3}) \cdot (1 - R_{Fe})^3 \cdot n_{alloy}}{2(1 - R_{Cr}) \cdot R_{Fe}{}^3 \cdot n_{slag}{}^2} \qquad [3\text{-}24]$$

As shown in Equation [3-24], R_{Cr} is an implicit function of $K\gamma$, R_{Fe}, $(n^0_{Cr} + \frac{1}{2}n^0_{Cr2O3})$, n_{alloy}, and n_{slag}. This makes the relationship nowhere near as useful as in the case for the 1:1 stoichiometry, and so this will not be discussed any further.

3.5 Application to Co Recovery by Slag Cleaning

Cobalt can be recovered by means of carbothermic reduction from non-ferrous slags that typically contain much FeO as well as smaller quantities of cobalt. Mineralogical studies have shown that cobalt is present largely as CoO (strictly speaking, as Co^{2+} ions) in copper reverberatory furnace slag obtained from dumps in Zambia (Jones *et al.*, 2002). The CoO in the

solid slag is associated primarily with Fe_2SiO_4, although analysis by scanning electron microscopy also showed some Fe_2SiO_4 particles with no detectable Co or Cu. Copper in this slag is mainly attributed to the presence of copper-rich sulphides (presumably entrained during converting). A slag-cleaning process involving reductive smelting of the dump slag, using carbon as a reductant, may be used to recover the valuable cobalt into an iron-rich alloy. A metal-slag equilibrium is set up involving an exchange reaction between iron and cobalt (in the alloy) and their oxides (in the slag). The cobalt oxide, and, to a lesser extent, the copper oxide associated with the silicate/oxide phases, is reduced to form metallic Co (and Cu), resulting in the formation of FeO in the slag.

3.5.1 Equilibrium constant, *K*, for the Co and Fe reaction

The chemical reaction between Co and Fe that takes place at the interface between metal droplets and the molten slag at temperatures around 1600°C may be shown as $CoO_{(s)} + Fe_{(l)} \leftrightarrows Co_{(l)} + FeO_{(l)}$ which simply adds the appropriate standard states to Equation [3-1]. Liquid standard states have been used wherever possible. However, in the case of CoO, only solid data was available in the data set used for the calculation of the equilibrium constant. The choice of standard state is arbitrary, as long as the same standard state is used for both the activity coefficient data and the equilibrium constant. The equilibrium constant, *K*, is strictly a function of temperature only. Calculations using FactSage 6.2 thermodynamic software (Bale *et al.*, 2002) are shown in Table 3.1. Over the temperature range of interest (between 1500 and 1600°C), *K* has a value of approximately 20, as calculated by FactSage software.

Table 3.1 The equilibrium constant for the reaction
CoO*(s)* + Fe*(l)* = Co*(l)* + FeO*(l)*
calculated using data from FactSage thermodynamic software

$\Delta G°_r$, kJ	T, °C	T, K	*K*
-41.1147	1400	1673	19.22
-42.5207	1450	1723	19.46
-43.9256	1500	1773	19.68
-45.3276	1550	1823	19.90
-46.7246	1600	1873	20.09

The equilibrium constant for the reaction CoO*(s)* + Fe*(l)* ⇆ Co*(l)* + FeO*(l)* is calculated from the free energy of the reaction using Equation [3-25].

$$K = e^{-\frac{\Delta G_r^0}{RT}} \qquad [3\text{-}25]$$

Within the FactSage software, the free energy of reaction is derived from data from the following sources. CoO*(s)* data is from the JANAF Thermochemical Tables (Stull & Prophet, 1985). Data for Co*(l)* for the temperature range 1768 - 6000 K, and Fe*(l)* for the temperature ranges 298.15 - 1811 - 6000 K, is from the SGTE Data for Pure Elements (Dinsdale, 1991). FeO*(l)* data is from École Polytechnique de Montréal (Pelton *et al.*, 1992).

3.5.2 Activity coefficients for the Co and Fe system

For the calculation of γ, individual activity coefficients may, in principle, be obtained from the literature. However, in practice, in the case of multi-component industrially relevant systems, it is often difficult to obtain

consistent sets of activity coefficient data for the composition ranges and temperatures of interest.

For this cobalt-recovery slag-cleaning process, the intention in this section is to obtain a good enough set of activity coefficient data to calculate $K\gamma$ on a theoretical basis, as an alternative to using pilot-plant data for the empirical fitting of a value for $K\gamma$ to be used in the recovery equation.

Teague, Swinbourne, and Jahanshahi (1998, 2000) and Chen, Zhang, and Jahanshahi (2004) have provided good summaries of a number of studies in the metallurgical literature of the thermodynamic behaviour of cobalt-containing slags. To these can be added a number of studies in the geological literature (Holzheid *et al.*, 1997; Holzheid & Palme, 1998; O'Neill & Eggins, 1999, 2002; O'Neill & Berry, 2006), and some more recent metallurgical work (Derin & Yucel, 2002; Kitamura *et al.*, 2008). A selection of these studies is listed in Table 3.2, where the slag system and temperature range is indicated.

Table 3.2 Data sources for the activity coefficient of CoO in slag

Authors	Slag with CoO	Alloy	Temp. °C	Std state for γ_{CoO}
Smith & Masson, 1971	SiO_2	Co-Pt-Rh	1450-1500	Solid
Wang *et al.*, 1974	FeO-SiO_2(sat.)	Co-Au	1250-1350	Liquid
Yazawa, 1981	FeO-SiO_2 FeO-CaO	Co-Cu	1250	Solid
Reddy & Healy, 1981	Cu_2O-SiO_2	Co-Cu	1250	Solid
Reddy, 1985	FeO-SiO_2-Al_2O_3(sat.)	Co-Cu	1200-1300	Liquid
Grimsey & Toguri, 1988	FeO-SiO_2(sat.)	Co-Au Co-Cu	1250-1350	Solid
Katyal & Jeffes, 1989	FeO-SiO_2 FeO-SiO_2-CaO FeO-CaO	Co-Cu-Fe Co-Cu-Fe Co-Cu-Fe	1255-1378 1260-1370 1255-1350	Liquid
Grimsey & Liu, 1991	FeO-SiO_2-Al_2O_3	Co-Au-Fe Co-Fe	1300	Solid
Grimsey & Liu, 1995	FeO-SiO_2(sat.)	Co-Au-Fe	1300	Solid
Liu & Grimsey, 1997	FeO-SiO_2 FeO-SiO_2-Al_2O_3 FeO-SiO_2-CaO FeO-SiO_2-MgO	Co-Fe Co-Au-Fe Co-Au-Fe Co-Au-Fe	1300 1300 1300 1300	Solid
Holzheid & Palme, 1996	SiO_2-CaO-MgO-Al_2O_3-(FeO)	Co, Ni, Fe-Co-Ni, Fe-Co, Fe-Ni	1305-1600	Solid
Holzheid, *et al.*, 1997	Olivine silicates SiO_2-CaO-MgO-Al_2O_3-(FeO)	Co, Ni, Fe-Co-Ni, Fe-Co, Fe-Ni	1300-1600	Liquid
Teague, *et al.*, 1998			1250-1350	Solid
Pagador, *et al.*, 1997, 1999	FeO-MgO-SiO_2 FeO-CaO-MgO-SiO_2	Ni-Fe Ni-Cu-Fe	1500-1600 1500	Liquid
O'Neill & Eggins, 1999	FeO-CaO-MgO-Al_2O_3-SiO_2-(TiO_2)	Co	1400	Liquid
O'Neill & Eggins, 2002	CaO-MgO-Al_2O_3-SiO_2	Co	1400	Liquid
Teague, *et al.*, 2000	FeO-SiO_2-CaO	Co-Pt-Fe	1300	Solid
Teague, *et al.*, 2001	FeO-CaO FeO-CaO-SiO_2	Co-Pt-Fe Co-Pt-Fe	1300 1300	Solid
Derin & Yucel, 2002	FeO-SiO_2-Al_2O_3	Co-Cu-(Fe)	1400	Liquid
O'Neill & Berry, 2006	CaO-MgO-Al_2O_3-SiO_2	Co	1400	Liquid
Kitamura, *et al.*, 2008	FeO-MgO(sat.)-CaO-SiO_2	Fe-Cu-Co	1300-1600	Liquid

* In this table, 'FeO' refers generically to the presence of iron oxide

Conversion between solid and liquid standard states for CoO

It is conventional in chemical thermodynamics to choose as a standard state, the form of a pure species that is most stable at the temperature of interest, under a pressure of 1 atm. However, this is essentially an arbitrary choice, and different investigators have chosen either solid or liquid standard states for CoO. In this document, pure CoO*(s)* is chosen to be the reference state, and so it is sometimes necessary to convert the CoO*(l)* activity coefficient data to the CoO*(s)* basis. This is done by means of a temperature-dependent correction factor that takes into account the free energy of fusion.

$$\frac{\gamma_{CoO(l)}}{\gamma_{CoO(s)}} = e^{\frac{-\Delta G^0_{fus}}{RT}} \qquad [3\text{-}26]$$

Wang, Santander, and Toguri (1974) investigated the solubility of cobalt in silica-saturated iron silicate slags in the temperature range of 1250 to 1350°C. The standard state of CoO was taken to be that of the pure supercooled liquid metal oxide. Their work is of significance here, as they introduced the thermodynamic data that was used by a number of subsequent investigators to convert between solid and liquid standard states. The free energy of formation of CoO from the elements was calculated using the thermodynamic values recommended by Kubaschewski *et al.* (1967). The enthalpy of fusion of CoO was estimated by assuming an entropy of fusion of 4.5 cal/mol/K (18.8 J/mol/K) based on FeO (as entropies of fusion would be expected to be similar, as FeO, CoO, and NiO have the same NaCl-type lattice structure). Consequently, the enthalpy of fusion of CoO at its melting point (1805°C, *i.e.*, 2078 K) was estimated to be 9351 cal/mol (39125 J/mol). The Gibbs free energy of fusion for CoO is shown in equations [3-27] and [3-28].

$$CoO(s) = CoO(l) \qquad \Delta G^o = 9351 - 4.50\ T \text{ cal/mol} \qquad [3\text{-}27]$$

$$\Delta G^o = 39125 - 18.8\ T \text{ J/mol} \qquad [3\text{-}28]$$

Katyal and Jeffes (1989) reported the activity coefficients of CoO in iron silicate and calcium ferrite slags at temperatures between 1250 and 1380°C. The value of γ_{CoO} of iron silicate slag was reported relative to the pure liquid CoO as the standard state. In order to convert the activity coefficient to have pure solid cobalt oxide as a standard state, they used the data from Wang *et al.* (1974) shown in equation [3-27]. However, they also stated in a footnote "Since writing this, some evidence has indicated that an entropy of fusion of 6.0 cal/mol deg might be more appropriate". Consequently, the enthalpy of fusion of CoO at the same assumed melting point (1805°C, *i.e.*, 2078 K) would then be 12468 cal/mol (52166 J/mol).

$$CoO(s) = CoO(l) \qquad \Delta G^o = 12468 - 6.0\ T \text{ cal/mol} \qquad [3\text{-}29]$$

$$\Delta G^o = 52166 - 25.1\ T \text{ J/mol} \qquad [3\text{-}30]$$

Teague, Swinbourne, and Jahanshahi (1998) used a slightly different value for the melting point of CoO, namely 2103 K (1830°C), from Knacke *et al.* (1991), but still based their figure for the entropy of fusion on the estimate by Wang *et al.* (1974). The resulting Gibbs free energy for the melting of CoO is shown in equation [3-31].

$$CoO(s) = CoO(l) \qquad \Delta G^o = 39580 - 19\ T \text{ J/mol} \qquad [3\text{-}31]$$

Teague *et al.* (1998) point out that Wang's estimated entropy of fusion for CoO seems low when it is compared to that of other inorganic compounds

which have the same NaCl-type structure, such as MgO (Kubaschewski & Alcock, 1979). Although they do not explicitly refer to the footnote in (Katyal & Jeffes, 1989), Teague *et al.* (1998) say that a more likely value is 24 J/mol/K. If a higher entropy value is used, this will result in higher values for the activity coefficient of CoO*(s)*. The assumed higher entropy value leads to equation [3-32].

$$CoO(s) = CoO(l) \qquad \Delta G^{o} = 50472 - 24\,T \ \text{J/mol} \qquad [3\text{-}32]$$

The small difference in melting point between the 1805°C assumed by Wang *et al.* and the 1830°C assumed by Teague *et al.* has very little effect on the magnitude of the free energy of fusion and on the correction factor used to convert the activity coefficient of CoO from the liquid to the solid standard state. However, the marked difference in assumed values for the entropy of fusion has a very significant effect, as shown in Figure 3.3, where equations [3-31] and [3-32] are compared, and equation [3-26] is used to generate the corresponding correction factors. The difference made by the assumed value for the entropy of fusion for CoO is especially pronounced at lower temperatures.

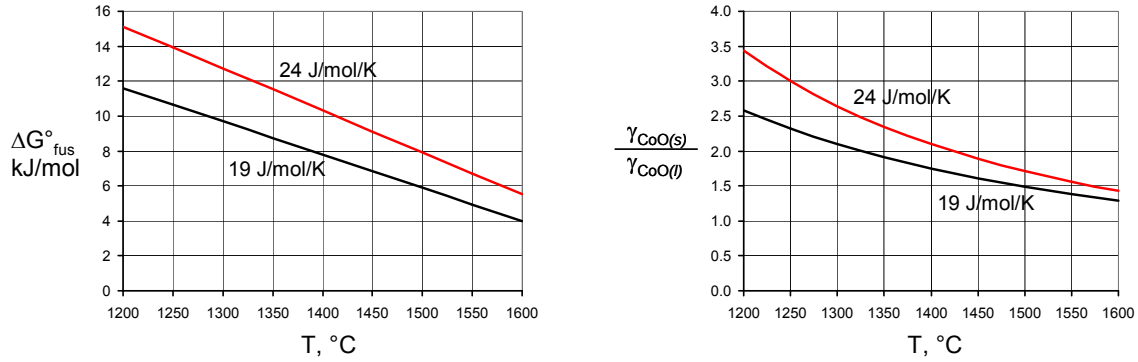

Figure 3.3 Free energy of fusion of CoO as a function of temperature and the assumed value of the entropy of fusion, along with the ratio of $\gamma_{CoO(s)}$ to $\gamma_{CoO(l)}$

The entropy of fusion is not the only value to be assumed by various investigators in converting activity coefficients between solid and liquid standard states. By contrast, Smith and Masson (1971) assumed a value of 9100 cal/mol (38070 J/mol) for the enthalpy of fusion of CoO, although they do not explicitly record their assumed melting point of CoO. However, Belton *et al.* (1973) quote the 38070 J/mol figure in conjunction with a melting point of 2018 K (1745°C). This leads to equation [3-33], which produces very similar values to equation [3-31].

$$CoO(s) = CoO(l) \qquad \Delta G^{o} = 38070 - 18.9\,T \text{ J/mol} \qquad [3\text{-}33]$$

Measurement of activity coefficients for CoO in slags

Smith and Masson (1971) measured activities of CoO in CoO-SiO_2 melts at 1450 – 1500°C, by equilibrating the melts, held in Pt-Rh containers, with atmospheres of known partial pressure of oxygen (from 6×10^{-7} to 3×10^{-3} atm.). Their results were found to be in good agreement with the application of polymer theory to silicate melts, on the assumption of linear chains being formed. They chose to use a standard state of solid CoO, and covered a range of mole fractions of CoO from 0.561 to 0.695 (in the vicinity of the composition of the orthosilicate $2CoO.SiO_2$). The values presented for $\gamma_{CoO(s)}$ increased (with increasing CoO content) from 0.77 to 1.42, with a mean value of 1.16. The activity coefficients of CoO showed very little sensitivity to temperature over the limited range studied. The results are not readily comparable with the other studies presented here, as they pertain to the simple CoO-SiO_2 system rather than to the typical industrial copper and nickel smelting slags that have CoO in dilute solution in silica-saturated iron silicate slags .

Wang, Santander, and Toguri (1974) measured the solubility of cobalt (and nickel) in silica-saturated iron silicate slags in equilibrium with cobalt-gold (and nickel-gold) alloys under controlled partial pressure of oxygen (10^{-10} to 10^{-6} atm.) in the temperature range of 1250 to 1350°C. They explained the solubility of cobalt in iron silicate slags by a simple oxidation process where the solubility increased with increasing partial pressure of oxygen, increasing cobalt content of the alloy, and slightly with increasing temperature. The standard state of CoO was taken to be that of the pure supercooled liquid metal oxide. No activity coefficient values were calculated in their paper, but a later evaluation of their results by Katyal and Jeffes (1989) indicated a value of $\gamma_{CoO(l)}$ of 1.14 in silica-saturated slag, which has an FeO/SiO_2 ratio of 1.3. From Figure 3.3, it can be seen that the correction factors to change from a liquid to a solid standard state could vary between 1.9 and 3.0 depending on the temperature and the chosen basis. This would indicate a possible range of 2.2 to 3.4 for $\gamma_{CoO(s)}$.

Yazawa (1981) calculated values of $\gamma_{CoO(s)}$ of 1.7 in calcium ferrite slags, and 2.0 in iron silicate slags (at 1250°C and p_{O2} values of 10^{-10} to 10^{-7} atmospheres). According to Katyal and Jeffes (1989), these values, when recalculated to liquid standard state values of 0.85 and 0.98 respectively, show good agreement with their work for iron silicate slags, but Yazawa's value for calcium ferrite slag is appreciably lower than theirs.

Reddy and Healy (1981) equilibrated liquid Cu-Co alloys with iron-free cobalt silicate slag at 1250°C, and found that about 99% of the cobalt reported to the slag. The distribution of cobalt between slag and metal is shown in Figure 3.4. The relationship between mole fraction of cobalt oxide and its activity (relative to the pure solid standard state) is shown in Figure 3.5, where the negative deviation from ideality can be seen at lower

concentrations. Grimsey and Liu (1995) have pointed out that the lack of any measurements of partial pressure of oxygen makes it difficult to assess this data. Reddy and Healy reviewed the early literature in the field of equilibria between metal containing cobalt, and slag of various compositions, and found the various authors to be in poor agreement.

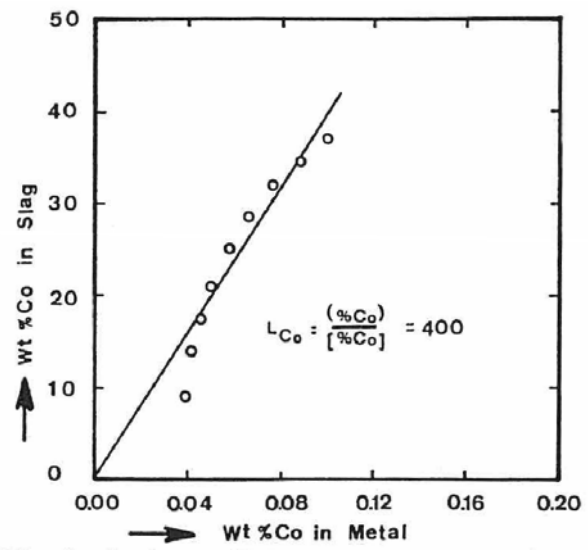

Figure 3.4 The distribution coefficient of cobalt between slag and metal at 1250°C (Reddy & Healy, 1981)

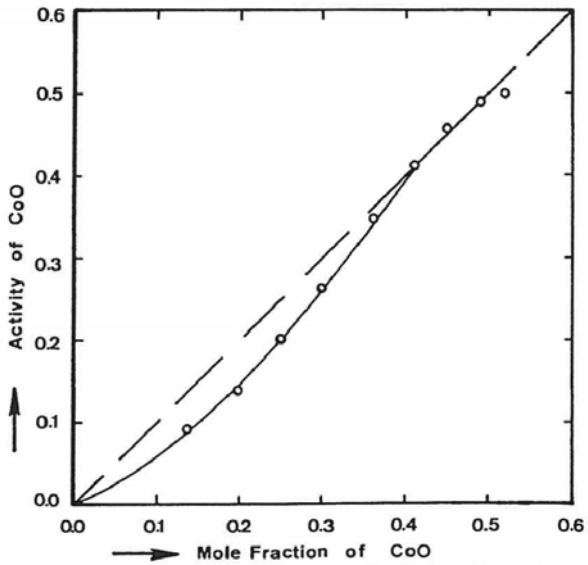

Figure 3.5 Relationship between mole fraction of cobalt oxide and its activity (relative to the pure solid standard state) in copper silicate slag at 1250°C (Reddy & Healy, 1981)

Reddy (1985) equilibrated alumina-saturated iron silicate slags (with an Fe/SiO_2 ratio of 1.34) with liquid Co-Cu alloys at temperatures of 1200 to 1300°C, and reported the infinite dilution activity coefficient of cobalt oxide (relative to the pure liquid) as

$$\ln \gamma^{o}_{CoO(l)} = 19.63 - 0.01298\,T \qquad \text{[where T is in K]} \qquad [3\text{-}34]$$

As pointed out by Grimsey and Liu (1995), this equation implies a relatively large enthalpy of solution for cobalt oxide, as when the data predicted by this relationship are refitted to the usual temperature-dependent form, the resulting expression is

$$\ln \gamma^{o}_{CoO(l)} = \frac{30060}{T} - 19.89 \qquad [3\text{-}35]$$

This gives an enthalpy of solution for cobalt oxide in slag of 249 kJ/mol, which is 7.5 times as high as the 33.1 kJ/mol measured by Grimsey (1988) for nickel oxide (liquid) at infinite dilution in iron silicate slags.

Based on Reddy's work, and converting standard states from liquid to solid, Grimsey and Liu (1991) calculated a value of 0.93 for the infinite dilution activity coefficient $\gamma^{o}_{CoO(s)}$ at 1300°C, compared to their own significantly higher value of 1.94 reported for cobalt oxide in alumina-saturated slag.

The substantial temperature dependence of Reddy's data ($\gamma^{o}_{CoO(l)}$ = 1.67 at 1200°C, and 0.45 at 1300°C), in contrast to that of other studies, indicates that this data may be suspect, as was also indicated by Grimsey and Liu (1995).

In related work, Reddy and Acholonu (1983) determined the activity coefficient of cobalt oxide in alumina-saturated iron silicate slag (with $Fe/SiO_2 = 1.34$) by equilibration with copper-cobalt alloy at 1200 to 1300°C over a range of partial pressures of oxygen. The results showed that $\gamma_{CoO(l)}$ decreases with an increase in oxygen partial pressure and/or temperature.

As pointed out by Derin and Yücel (2002), Acholonu (1983) obtained the following relationships by linear regression.

$$\log \gamma_{CoO(l)} = 11796/T - 7.59 \quad \text{for } pO_2 = 10^{-10} \text{ atm.} \qquad [3\text{-}36]$$

$$\log \gamma_{CoO(l)} = 10707/T - 7.00 \quad \text{for } pO_2 = 10^{-9} \text{ atm.} \qquad [3\text{-}37]$$

$$\log \gamma_{CoO(l)} = 11087/T - 7.35 \quad \text{for } pO_2 = 10^{-8} \text{ atm.} \qquad [3\text{-}38]$$

Acholonu (1983) also found that the activity coefficient of cobalt oxide decreased as the alumina content in the slag increased. This is in contradiction with the results from later workers.

Grimsey and Toguri (1988) built on the work of Wang, Kurtis, and Toguri (1973) as well as Wang, Santander, and Toguri (1974) to derive a relationship that expresses the activity coefficient of cobalt oxide (γ_{CoO}, relative to solid CoO) in silica-saturated fayalite slags as a function of cobalt solubility (wt% Co in slag). Wang *et al.* reported the cobalt contents of contiguous alloys and slags as mole fractions for the alloys, and as wt% Co for the slags. Grimsey and Toguri (1988) provided a relationship between wt% Co and the mole fraction of cobalt oxide in the slag. They combined this with data on cobalt activities in both the Co-Au and Co-Cu systems, to calculate the activity coefficient of cobalt oxide in silica-

saturated slags. Figure 3.6 shows the resulting activity coefficient of cobalt oxide (relative to the pure solid standard state) as a function of the cobalt content of the slag. Cobalt concentrations in the slag up to about 10% by mass are considered here (with one data point over 12%).

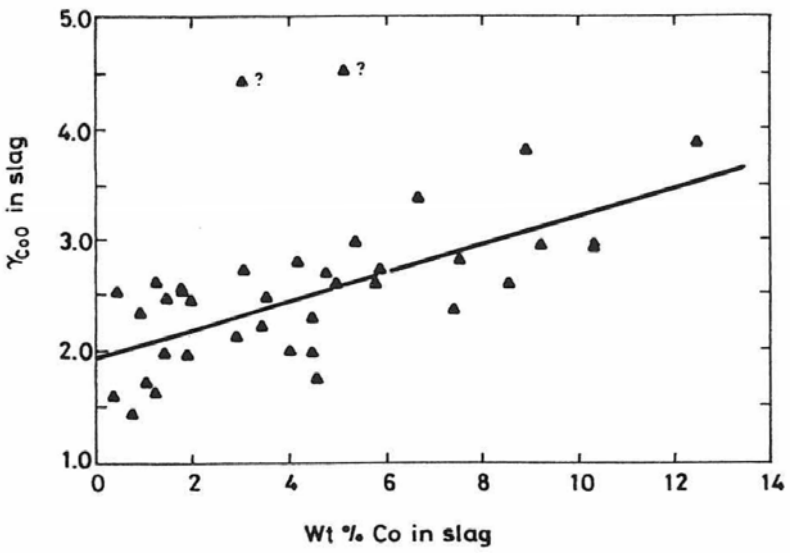

Figure 3.6 Activity coefficient of cobalt oxide (relative to pure solid cobalt oxide) vs wt% cobalt in slag (Grimsey & Toguri, 1988)

According to Grimsey and Toguri (1988), although there is considerable scatter in the data, it appears that, within experimental error, $\gamma_{CoO(s)}$ is not strongly dependent on temperature (within the 1250-1350^{o}C temperature range), and increases as the cobalt content of the slag increases. The straight-line relationship shown in Figure 3.6 was derived from a least-squares fit, and is represented by equation [3-39].

$$\gamma_{CoO(s)} = 1.94 + 0.123 \text{ (wt\% Co in slag)} \qquad [3\text{-}39]$$

Unfortunately, equation [3-39] has been incorrectly printed and interpreted in the review by Chen, Zhang, and Jahanshahi (2004) where it refers erroneously to the wt% of Co in the alloy rather than in the slag.

When applied to an iron silicate slag containing a small amount of cobalt (less than half a percent), $\gamma_{CoO(s)} = 2.0$, in very good agreement with that calculated from the data of Katyal and Jeffes (1989).

Fontana *et al.* (1989) reported the solubility of cobalt in iron silicate slags containing lime that were equilibrated with Cu-Co alloys by levitation at 1350°C and at partial pressures of oxygen between 10^{-10} and 10^{-7} atm. The addition of CaO (up to a certain point) decreases the cobalt and copper content of slags. The activity coefficient of cobalt oxide is increased by the addition of lime. However, actual values of activity coefficients were not calculated, and Grimsey and Liu (1991) have pointed out that the individual effects of silica and calcia were difficult to distinguish. The lack of alloy compositions makes it difficult to assess this data further.

Katyal and Jeffes (1989) used a levitation melting technique to determine the distribution of cobalt and copper between a copper-cobalt alloy equilibrated with iron silicate and calcium ferrite slags at partial pressures of oxygen fixed by CO/CO_2 gas mixtures, and at temperatures from 1250 to 1350°C. The slags used were of compositions similar to those encountered in industrial furnaces, based on 'FeO'-SiO_2, 'FeO'-CaO-SiO_2, 'FeO'-CaO-Al_2O_3-SiO_2, and 'FeO'-CaO systems.

Katyal and Jeffes (1989) reported the activity coefficients of CoO in iron silicate and calcium ferrite slags. The activity coefficient of CoO at high dilution in 'FeO'-SiO2 slags was found to be close to unity. For iron silicate slags relatively close to silica saturation (with around 35% silica), the average activity coefficient of cobalt oxide was reported as 1 (relative to the pure liquid standard state) and independent of the cobalt content of slag up to the maximum of 19%. Some slight decrease in the value of the activity coefficient of CoO was observed as the 'FeO' content of the slag

was increased. A slight increase in CoO activity was found with the addition of CaO. The activity of CoO in calcium ferrite slags was found to be somewhat greater than in iron silicate slags. Katyal and Jeffes (1989) found that the value of $\gamma_{CoO(l)}$ was only a little greater than 1 in slag containing 20% lime by mass. Teague *et al.* (2001) recalculated this to have a value of 2.5 relative to pure solid cobalt oxide as the standard state. They also observed that adding silica to calcium ferrite slag increased the activity coefficient of CoO.

The value of γ_{CoO} of iron silicate slag was reported to be unity relative to the pure liquid CoO as standard state. Chen *et al.* (2004) recalculated this to have a value of 2 relative to pure solid cobalt oxide as the standard state, but felt that this high value of the activity coefficient of CoO could be overestimated due to limitations of the experimental technique used. Katyal and Jeffes (1989) used a levitation melting technique in their experiment, in which the slag was heated by the energy transferred from the metal drop. As the emissivity of the slag layer is larger than that of the metal drop, it is reasonable to expect that there should be a temperature gradient across the slag. Katyal and Jeffes equilibrated 1 g metal with about 85 mg of slag sample in their experiments; in such a case, according to Chen *et al.* (2004), the slag temperature could be 50 to 70°C lower than the reported metal temperature. Under such conditions, the solubility of cobalt in the slag could be underestimated in their study. Therefore, the reported activity coefficient could be overestimated.

Although the primary interest here is in iron silicate slags, it is useful to compare the work done by Katyal and Jeffes on calcium ferrite slags with that of others. Experimental studies on the activity coefficient of CoO in calcium ferrite slags have been reported by Takeda *et al.* (1983), Katyal and Jeffes (1989), and by Teague *et al.* (2001). As part of a study into the

distribution of minor elements between slag and blister copper, Takeda *et al.* (1983) reported the value of the activity coefficient of CoO to be about 1.4 in calcium ferrite slags at 1250°C. Katyal and Jeffes (1989) found the activity coefficient of CoO, referred to liquid CoO, was a little greater than unity in the calcium ferrite slag. Referred to solid CoO, this value of γ_{CoO} was recalculated by Chen *et al.* (2004) to be 2.5. Teague *et al.* (2001) reported a value of 2.1 for the activity coefficient of CoO(*s*) in calcium ferrite slag, which agrees relatively well with the figure of Katyal and Jeffes.

Grimsey and Liu (1991) undertook a study of the solubility of CoO in iron silicate slag at 1300°C, in contact with solid Co-Fe or liquid Co-Au-Fe alloys, at partial pressures of oxygen of 10^{-10} and 10^{-9} atm. Much of the work reported from this study was expanded on in a later publication (Liu & Grimsey, 1997). Although it was later (Grimsey & Liu, 1995) replaced by an improved version, Equation [3-40] was presented to describe the data in Figure 3.7. According to Grimsey & Liu (1991), the apparent slight decrease in activity coefficient with an increase in mole fraction is not statistically significant, and the data are best described by the mean value. The error was calculated at the 95% confidence level, and the equation applies up to 10% cobalt oxide in slag.

For alumina-free iron silicate slags (silica-saturated and silica-unsaturated):

$$\gamma_{CoO(s)} = 0.88 \pm 0.08 \qquad [3\text{-}40]$$

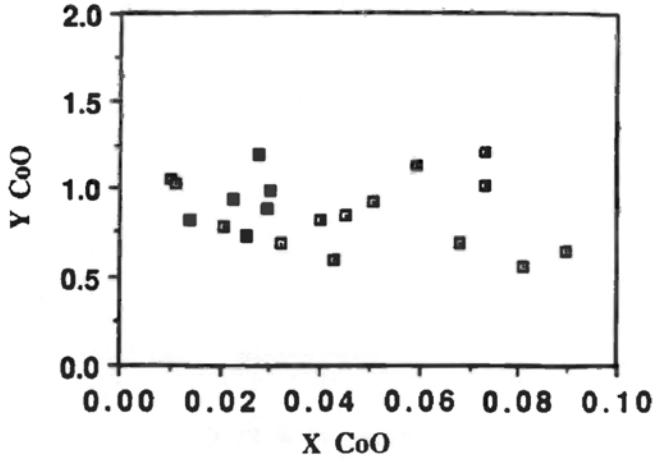

Figure 3.7 Activity coefficient of cobalt oxide (relative to pure solid cobalt oxide) at 1300°C versus cobalt oxide mole fraction in alumina-free silica-saturated iron silicate slag (Grimsey & Liu, 1991)

Equation [3-40] can also be applied to data covering a wide range of silica contents, as shown in Figure 3.8. The activity coefficient of cobalt oxide appears largely independent of silica content down to at least 30% silica.

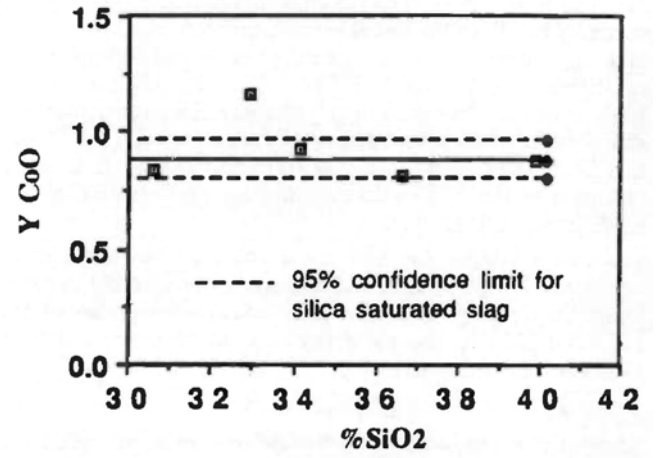

Figure 3.8 Activity coefficient of cobalt oxide (relative to pure solid cobalt oxide) at 1300°C versus silica content in alumina-free silica-unsaturated iron silicate slag (Grimsey & Liu, 1991)

In Figure 3.9, Grimsey & Liu (1991) show the much higher values of cobalt oxide activity coefficients in alumina-saturated iron silicate slags.

For alumina-saturated iron silicate slags:

$$\gamma_{CoO(s)} = 2.07 \pm 0.19 \qquad [3\text{-}41]$$

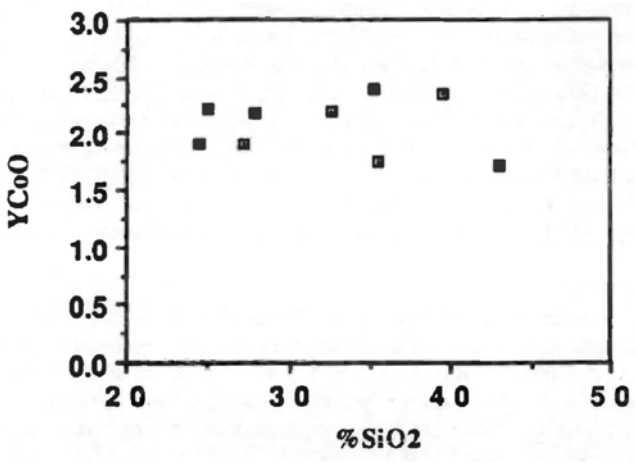

Figure 3.9 Activity coefficient of cobalt oxide (relative to pure solid cobalt oxide) at 1300°C versus silica content in alumina-saturated (13 to 16% alumina) iron silicate slag (Grimsey & Liu, 1991)

Grimsey & Liu (1991) used Equation [3-42] to show the influence of alumina content on the cobalt oxide activity coefficient (applicable to the range of 0 to 21% alumina). This equation was later replaced by an improved version (Liu & Grimsey, 1997) that is presented further on.

$$\gamma_{CoO(s)} = 0.88 + 0.074\ (\text{wt\% } Al_2O_3 \text{ in slag}) \quad \pm 9\% \qquad [3\text{-}42]$$

Grimsey and Liu (1995) studied the solubility of CoO in silica-saturated iron silicate slag at 1300°C, in contact with liquid Co-Au-Fe alloys, at partial pressures of oxygen of 10^{-10} and 10^{-9} atm. The slag-alloy equilibria were studied to provide comparative data for the activity coefficient of cobalt oxide, especially at relatively low concentrations in slag, as these have the greatest industrial relevance. Grimsey and Liu showed that the

solubility of cobalt in the slag increased with an increase in oxygen partial pressure, and with the activity of cobalt in the system, as would be expected. They also found that the activity coefficient of cobalt oxide was constant and independent of cobalt oxide content up to l0% in the slag, and that the magnitude of the activity coefficient was almost half that previously reported for silica-saturated slags but comparable with that reported for alumina-saturated slags and for cobalt oxide dissolved in cobalt silicate. As shown in Figure 3.10, they reported a value of the activity coefficient of CoO, referred to solid CoO, of 0.91 ± 0.09 (at the 95% confidence level).

$$\gamma_{CoO(s)} = 0.91 \pm 0.09 \qquad [3\text{-}43]$$

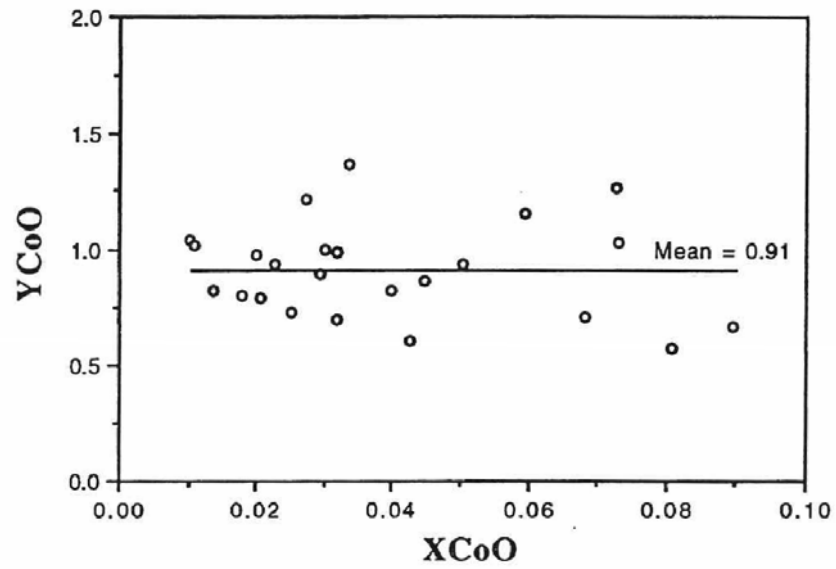

Figure 3.10 Activity coefficient of cobalt oxide (relative to pure solid cobalt oxide) at 1300°C as a function of cobalt oxide mole fraction in silica-saturated iron silicate slag (Grimsey & Liu, 1995)

The constant value for $\gamma_{CoO(s)}$ is clearly an approximation that is valid only for the dilute solution range of the activity curve where Henry's Law is followed, as the activity coefficient is always some function of composition, temperature, and pressure.

The activity coefficient for cobalt oxide as measured by Grimsey and Liu is significantly lower than that calculated from the data of Wang *et al.* (1973, 1974) for silica-saturated slags, or as measured by Katyal and Jeffes (1989) for near-silica-saturated slags, as illustrated in Figure 3.11. However, Grimsey and Liu's value of 0.9 for $\gamma_{CoO(s)}$ is similar to the value of 1.2 obtained by Smith and Masson (1971) for cobalt oxide in cobalt silicate.

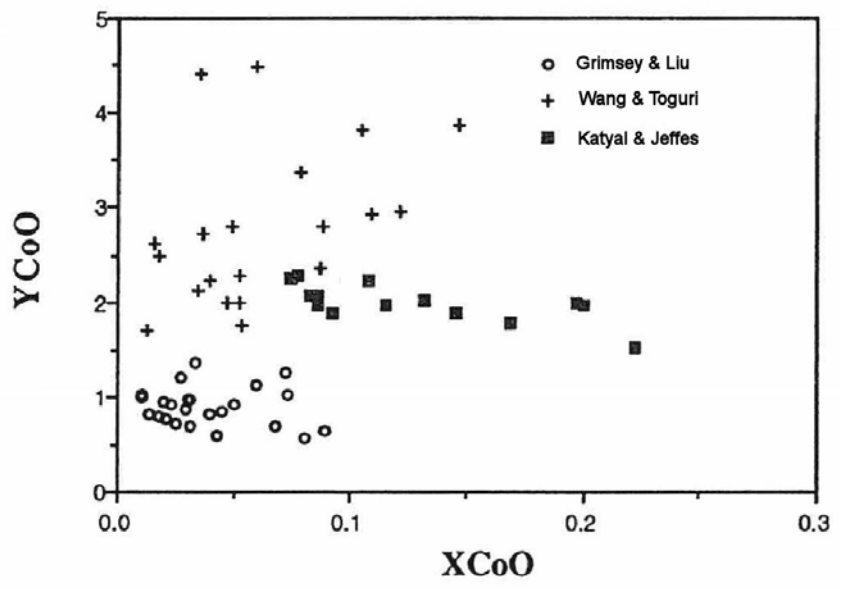

Figure 3.11 Comparison between the work of Grimsey & Liu, Wang & Toguri, and Katyal & Jeffes, showing activity coefficient of cobalt oxide (relative to pure solid cobalt oxide) as a function of cobalt oxide mole fraction in silica-saturated iron silicate slag (Grimsey & Liu, 1995)

Liu and Grimsey (1997) studied the effect of silica, alumina, calcia, and magnesia on the activity coefficient of cobalt oxide in iron silicate slags. Iron silicate slags with varying contents of silica (14 to 43% by mass), or alumina (up to 16%), or calcia (up to 13%), or magnesia (up to 11%) were equilibrated with solid iron alloys or liquid cobalt-gold-iron alloys in cobalt, alumina, or silica crucibles at partial pressures of oxygen of either

10^{-10} or 10^{-9} atm. at 1300°C. The solubility of cobalt oxide was measured in the slags, and the activity coefficient (relative to pure solid cobalt oxide as the standard state) was calculated. The activity coefficient of CoO was found to increase with an increase in either alumina, or calcia, or magnesia in the slag (thereby decreasing the solubility of cobalt in slag), and to decrease with an increase in the silica content of slag. The reason for this is likely to be that the additions of CaO, MgO, and Al_2O_3 to the slag reduced the interactions between the CoO and SiO_2, thus increasing the activity of CoO and decreasing the solubility of cobalt in the slag.

Liu and Grimsey (1997) have discussed the differences between their work and that of others, and have highlighted significant inconsistencies in the published data for the activity coefficient of cobalt oxide. However, their work seems to be consistent with reports of industrial practice where the iron silicate slags are not silica-saturated and the Fe/SiO_2 ratio is an important variable.

The activity coefficient of cobalt oxide for silica-unsaturated alumina-free slags is plotted against silica content in Figure 3.12. This figure shows that the activity coefficient decreases with an increase in the concentration of silica in the slag for the range of 28 to 38% silica by mass. A description of the behaviour of $\gamma_{CoO(s)}$ versus percent silica or mole fraction (x) of silica in the alumina-free slag is given by the following least-squares fitted equations. The fitted lines include the previous data for silica-saturated slags (Grimsey & Liu, 1995) containing 37 to 41% silica, and apply for the range of 30 to 40% silica in slag.

$$\gamma_{CoO(s)} = 1.70 - 0.021 \text{ (wt\% } SiO_2 \text{ in slag)} \qquad [3\text{-}44]$$

$$\gamma_{CoO(s)} = 1.55 - 1.35\, x_{SiO2} \qquad [3\text{-}45]$$

Chen *et al.* (2004) have pointed out that the activity coefficients of CoO(*s*) reported by Liu and Grimsey (1997) and by Teague *et al.* (2000) in silica-unsaturated slags are in good agreement and can be expressed by equation [3-44]. Extrapolating this equation to the silica concentration at saturation (at approximately 40% SiO_2) gives a value of 0.9 for the activity coefficient of CoO(*s*), which agrees with the work by Grimsey and Liu (1995). However, Teague *et al.* (2000) have pointed out that this is in disagreement with the value of 2 for $\gamma_{CoO(s)}$ obtained from earlier studies of silica-saturated slags (Grimsey and Toguri, 1988; Katyal and Jeffes, 1989).

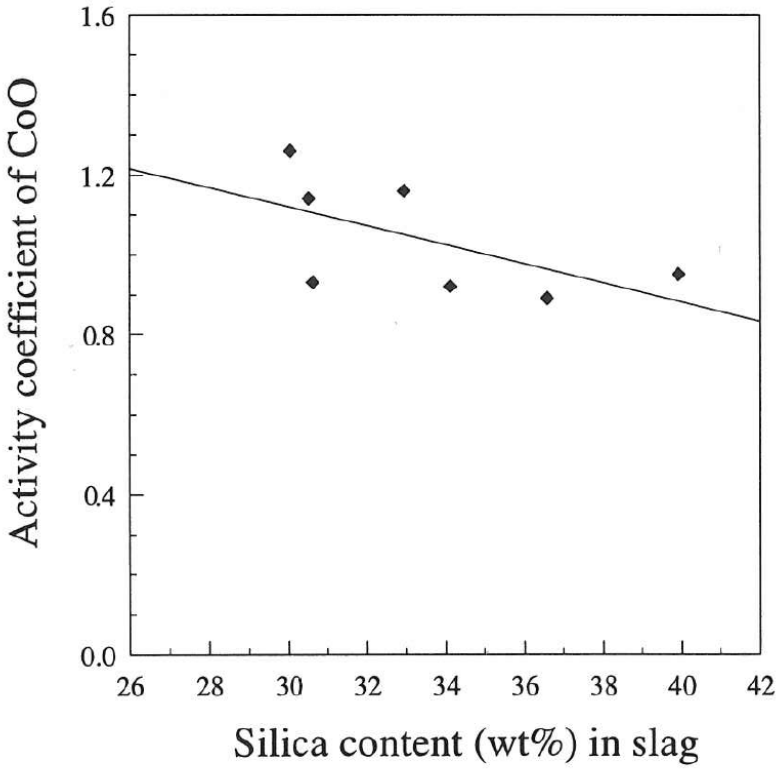

Figure 3.12 The activity coefficient of cobalt oxide (relative to pure solid) at 1300°C as a function of silica content in alumina-free slag (Liu & Grimsey, 1997)

Figure 3.13 shows the activity coefficient of cobalt oxide for alumina-saturated slags containing similar levels of alumina (13 to 16%), versus silica content in the slag. It can be seen that the activity coefficients in alumina-saturated slags are much higher (roughly double) than those in alumina-free slags.

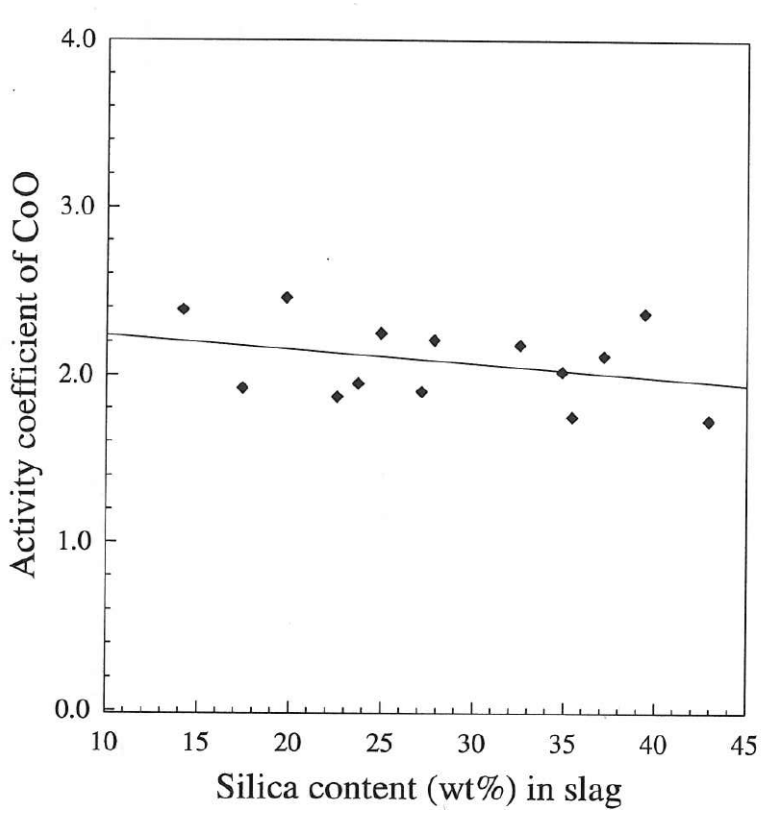

Figure 3.13 The activity coefficient of cobalt oxide (relative to pure solid) as a function of silica content in alumina-saturated slag (with 13 to 16% Al_2O_3) at 1300°C (Liu & Grimsey, 1997)

The effect of alumina content on the activity coefficient of cobalt oxide is shown even more clearly in Figure 3.14, where the activity coefficient increases from 0.9 to about 2.0 as the alumina content increases from zero to about 16% by mass. This data is summarised in the following equations.

$$\gamma_{CoO(s)} = 0.90 + 0.085 \text{ (wt\% } Al_2O_3 \text{ in slag)} \quad [3\text{-}46]$$

$$\gamma_{CoO(s)} = 0.90 + 6.2\, x_{Al2O3} \quad [3\text{-}47]$$

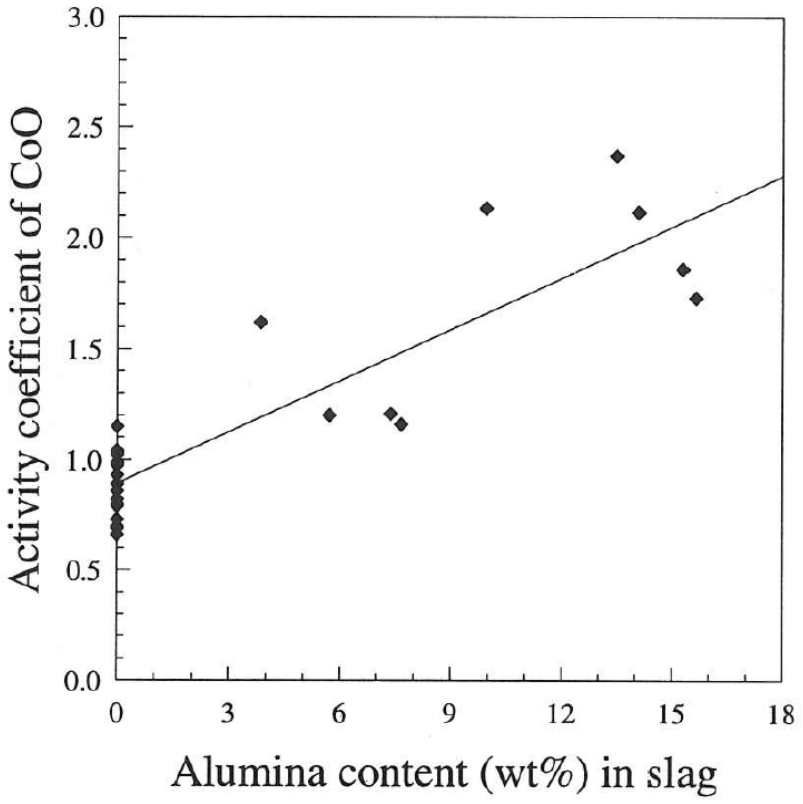

Figure 3.14 The activity coefficient of cobalt oxide (relative to pure solid) as a function of alumina content in silica-saturated slag at 1300°C (Liu & Grimsey, 1997)

Figure 3.15 shows the effect of CaO on the activity coefficient of CoO, and is summarised by the following equations.

$$\gamma_{CoO(s)} = 0.90 + 0.036 \text{ (wt\% CaO in slag)} \quad [3\text{-}48]$$

$$\gamma_{CoO(s)} = 0.90 + 2.9\, x_{CaO} \quad [3\text{-}49]$$

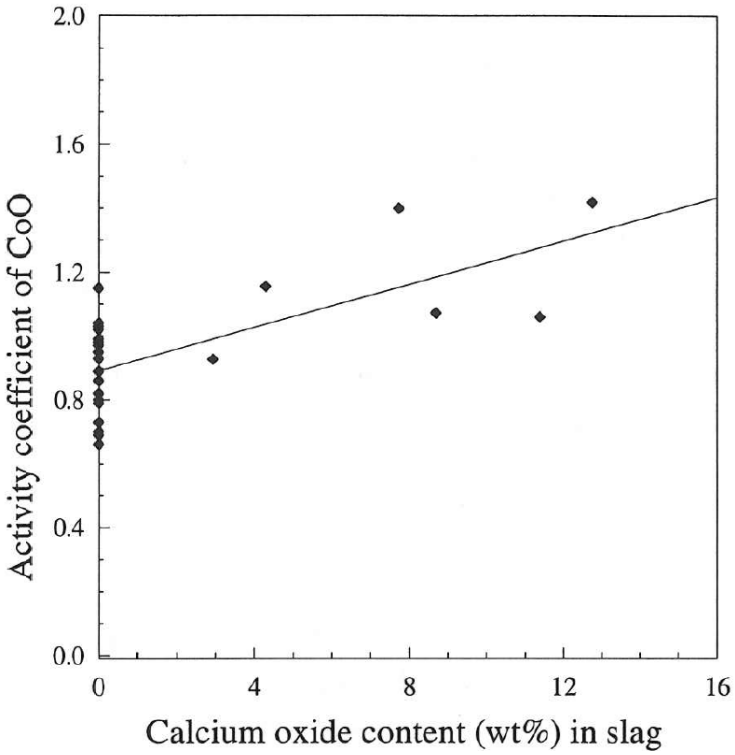

Figure 3.15 The activity coefficient of cobalt oxide (relative to pure solid) as a function of calcia content in silica-saturated slag at 1300°C (Liu & Grimsey, 1997)

Figure 3.16 shows the effect of MgO on the activity coefficient of CoO, and is summarised by the following equations. As there are only three data points for MgO-containing slags, further investigation would be advisable before placing too much reliance on this straight-line relationship.

$$\gamma_{CoO(s)} = 0.90 + 0.13 \text{ (wt\% MgO in slag)} \quad [3\text{-}50]$$

$$\gamma_{CoO(s)} = 0.90 + 7.9\, x_{MgO} \quad [3\text{-}51]$$

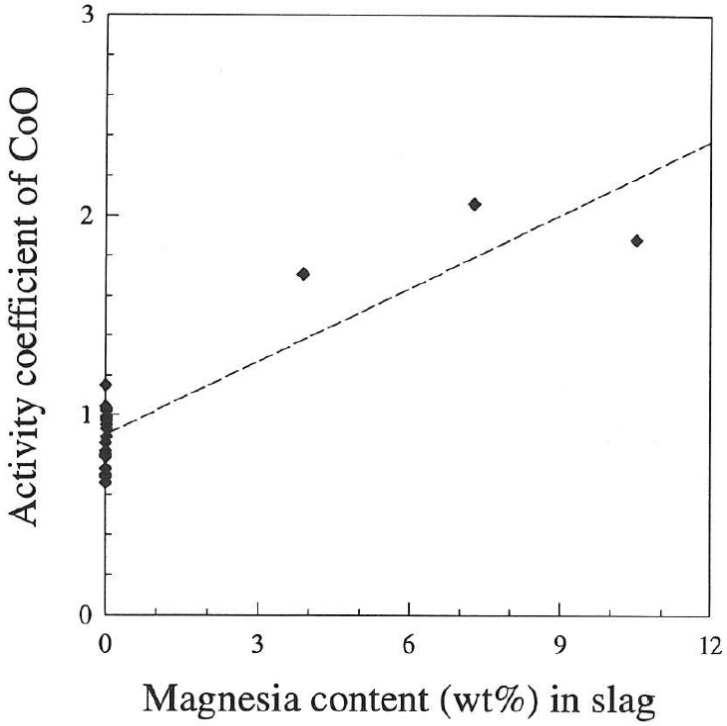

Figure 3.16 The activity coefficient of cobalt oxide (relative to pure solid) as a function of magnesia content in silica-saturated slag at 1300°C (Liu & Grimsey, 1997)

Liu and Grimsey (1997) also pointed out that the ratio between γ_{FeO} and γ_{CoO} would be expected to remain relatively constant for these chemically similar oxides.

Pagador *et al.* (1997) studied the solubility of nickel (as well as minor elements including cobalt) in iron-magnesia-silicate slags equilibrated with Ni-Fe alloy in a MgO crucible under conditions of controlled CO/CO_2 gas mixtures, at temperatures between 1500 and 1600°C. They showed that the distribution ratio (between slag and metal) for cobalt was intermediate between that of iron and that of nickel. No activity coefficients for CoO were calculated.

Pagador *et al.* (1999) have measured the distribution of cobalt between MgO-saturated FeO_x-CaO-MgO-SiO_2 slag and Ni-Cu-Fe alloy at 1500°C (1773 K). Figure 3.17, plotted by Kitamura *et al.* (2008), shows a comparison of the activity coefficients of CoO(*l*) obtained by the research of the two sets of authors. Even though the experimental temperature and the oxygen partial pressure (referred to as oxygen potential by Kitamura *et al.* (2008)) are different, both the results show similar values.

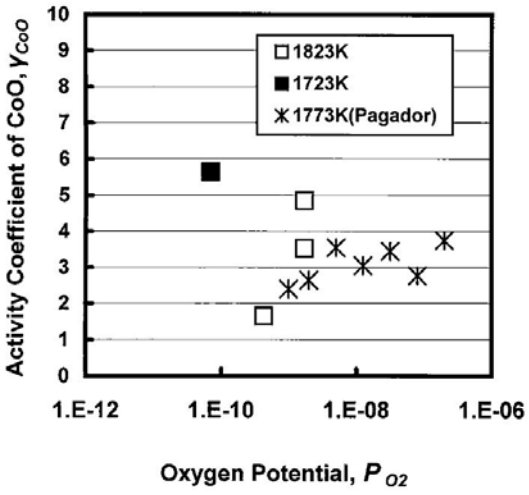

Figure 3.17 Calculated activity coefficient of CoO(*l*) in slag as a function of oxygen partial pressure (Kitamura *et al.*, 2008)

Converting the standard state from liquid to solid at 1500°C, using the values shown in Figure 3.3, it can be seen that $\gamma_{CoO(l)} = 3$ translates to $\gamma_{CoO(s)} = 4.5$ to 5.1.

Holzheid and Palme (1996) investigated the influence of FeO on the solubilities of cobalt and nickel in silicate melts, covering a wide range of temperature (1305 to 1600°C) and partial pressure of oxygen ($10^{-8.1}$ to $10^{-12.6}$ atm.). They reported activity coefficients for CoO(*s*) of 1.60 to 3.79.

Holzheid *et al.* (1997) studied the solubilities and activities of NiO, CoO, and FeO in silicate melts, as a function of temperature, oxidation state, and melt composition. The activity coefficients (relative to pure liquid standard states) of FeO, NiO, and CoO in the silicate melt, calculated by assuming oxides as melt components, were found to be independent of partial pressure of oxygen and temperature (within the range 1300-1600°C). The activity coefficients were not affected by variations in FeO (from 0 to 12% by mass) and MgO (from 4 to 30%) contents, except for a small increase of γ_{CoO} and γ_{FeO} at MgO contents above 20%. The average activity coefficients obtained were $\gamma_{NiO(l)} = 2.70 \pm 0.52$ (77 experiments), $\gamma_{CoO(l)} = 1.51 \pm 0.28$ (76 experiments), and $\gamma_{"FeO"(l)} = 1.70 \pm 0.22$ (57 experiments) relative to the respective pure liquid oxide standard states and simple oxide mole fractions. The activity coefficients do not depend on partial pressure of oxygen, are independent of temperature (in the range 1300-1600°C), and do not depend on FeO and MgO contents of the liquid, with MgO up to about 20%. At higher MgO contents, the FeO and CoO activity coefficients increase with MgO.

Holzheid *et al.* (1997) commented that the values of the activity coefficients are lower in this work than in the work of Holzheid and Palme (1996) because the 1996 work was based on solid standard states, and the 1997 work was based on liquid standard states. It is unfortunately rather difficult to convert the average activity coefficient from the basis of a liquid to a solid standard state, as the original data that has been averaged

comes from experiments undertaken at a wide range of temperatures. Perhaps the best indication can be obtained by taking a liquid-to-solid correction factor for the average temperature of 1450°C from Figure 3.3 which shows a value of about 1.6 to 1.9, signifying a representative value for $\gamma_{CoO(s)}$ of 2.4 to 2.9, corresponding to the stated $\gamma_{CoO(l)}$ of 1.51.

O'Neill and Eggins (1999) studied the effects of melt composition on the activity coefficients of FeO, CoO, and some other species, in CaO-MgO-Al_2O_3-SiO_2 -TiO_2 silicate melts. The work was conducted at 1400°C and 1 bar, and the proportions of the major constituents (CaO, MgO, Al_2O_3, and SiO_2) were varied. They found that the variation of activity coefficients of FeO and CoO (as well as NiO) with melt composition is very limited, and that γ_{FeO} could be represented by a single value for all CaO-MgO-Al_2O_3-SiO_2 compositions to within ±30%, and γ_{CoO} to within ±20%.

Teague, Swinbourne, and Jahanshahi (2000) used the classical metal-slag-gas equilibrium technique to study the thermodynamic activity of cobalt and iron oxides in iron-silicate-based slags (silica-unsaturated, both with and without small additions of lime), under controlled partial pressure of oxygen (3.70×10^{-8} to 2.95×10^{-7} atm.) at 1300°C. Platinum foils were equilibrated with iron silicate slags, and the resulting concentrations of iron and cobalt in the platinum were used, together with a regular solution model of the Pt-Fe-Co system, to calculate the activities of species in the slags, and thus to determine the value of the activity coefficient of CoO as a function of slag composition.

The equilibrium distribution of cobalt between iron-silicate-based slags and Pt-Fe-Co alloys showed that the value of the activity coefficient of cobalt oxide (with respect to pure solid cobalt oxide) in the slag, $\gamma_{CoO(s)}$,

was not dependent on the CoO concentration. The measured activity of cobalt oxide in silica-unsaturated (25% silica by mass) iron silicate slag showed a positive deviation from ideal behaviour for melts with a CoO content of up to 10% by mass. As shown in Figure 3.18, Henry's Law was obeyed for cobalt oxide contents up to a 0.1 mole fraction (approximately 10% by mass), in agreement with previous work (Grimsey and Liu, 1991, 1995; Liu and Grimsey, 1997), and the value of the activity coefficient, $\gamma_{CoO(s)}$, is 1.50.

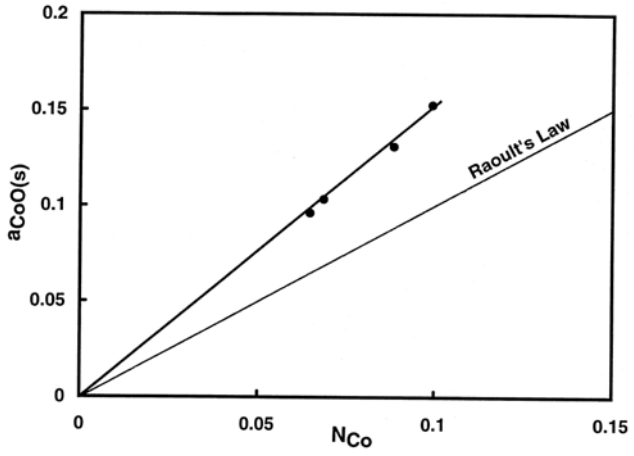

Figure 3.18 Activity of CoO(*s*) as a function of the mole fraction of cobalt oxide in silica-unsaturated iron silicate slags at 1300°C and an oxygen partial pressure of 3.70×10^{-8} atm. (Teague *et al.*, 2000)

The activity coefficient of CoO(*s*) was largely independent of the cobalt oxide content up to approximately 10% by mass, but dependent on the silica and lime content of the slags. At higher silica contents (above 25% silica), the value of the activity coefficient of CoO(*s*) decreased to about unity, and is in accord with other published data on silica-saturated slags. The value of $\gamma_{CoO(s)}$ from a single experiment with an iron silicate slag containing approximately 31 wt% silica under very similar conditions was found to be 1.03, significantly lower than that for the 25 wt% silica slags. Liu and Grimsey (1997) also found that the value of the activity coefficient

of cobalt oxide decreases with increasing silica content in iron silicate slags. Katyal and Jeffes (1989), however, found that the value of the activity coefficient of cobalt oxide did not change significantly with increasing silica content in iron silicate slags, for silica contents in the range 25 to 35% by mass.

The cobalt oxide activity coefficient values from Teague *et al.* (2000) are plotted in Figure 3.19 together with the values from Liu and Grimsey (1997) which are at the same temperature but a lower oxygen partial pressure of 10^{-9} atm. The data are in very good agreement, from which it can be inferred that the value of the activity coefficient of cobalt oxide shows no significant dependence on oxygen partial pressure, over the range represented, in iron silicate slags. This is contrary to the findings of Wang, Kurtis and Toguri (1973). Most significantly, the results strongly support the data of Liu and Grimsey (1997) and thus the value of the cobalt oxide activity coefficient in silica-saturated iron silicate slags (approximately 40 wt% silica) at 1300°C appears to be around 0.9.

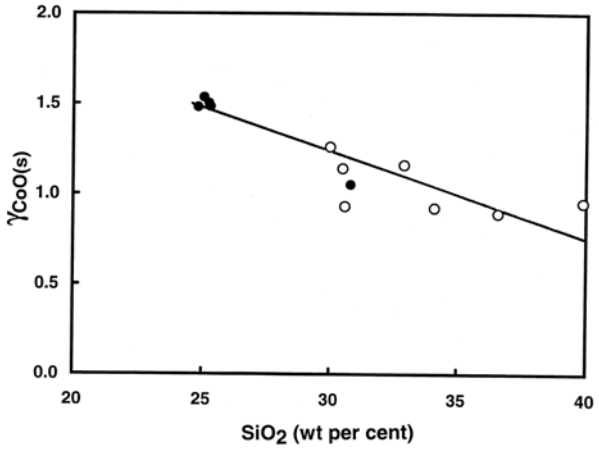

Figure 3.19 Activity coefficient of CoO(*s*) as a function of silica content at 1300°C for iron silicate slags. Solid dots represent work by Teague *et al.* (2000) at an oxygen partial pressure of 3.70×10^{-8} atm. Hollow dots represent the work of Liu and Grimsey (1997) at oxygen partial pressures of 10^{-9} to 10^{-10} atm. (Teague *et al.*, 2000)

The cobalt oxide activity coefficient values from Teague *et al.* (2000) are plotted in Figure 3.20, together with values from Smith and Masson (1971) for the binary CoO-SiO_2 system at 1450°C. Smith and Masson's values are from equilibrium studies with oxygen partial pressures in the range 7.4×10^{-7} to 1.9×10^{-6} atm. Both sets of data are in very good agreement. Other studies have shown that the cobalt oxide activity coefficient shows no significant temperature dependence from 1250 to 1400°C in iron silicate slags (Katyal and Jeffes, 1989; Wang, Kurtis, and Toguri, 1973; Wang, Santander, and Toguri, 1974), and Teague *et al.* (2000) suggest that there may be no significant dependence on oxygen partial pressure over the range 3.8×10^{-8} to 1.9×10^{-6} atm. in these slags. It is inferred that the value of the cobalt oxide activity coefficient is dependent only on the silica content in silicate slags.

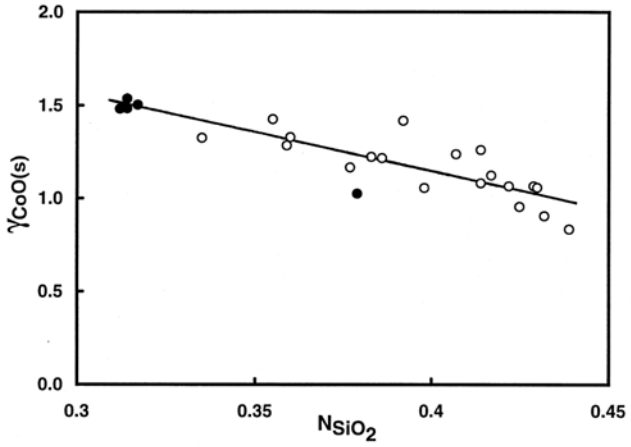

Figure 3.20 Activity coefficient of CoO(*s*) as a function of the mole fraction of silica in iron silicate slags. Solid dots represent the work of Teague *et al.* (2000) at 1300°C and an oxygen partial pressure of 3.70×10^{-8} atm. Hollow dots represent the work of Smith and Masson (1971) at 1723 K and oxygen partial pressures of 1.03×10^{-6} to 7.38×10^{-7} atm. for the CoO-SiO_2 system.
(Teague *et al.*, 2000)

Substitution of silica by lime resulted in an increase of the activity coefficients of both CoO and FeO. Results from varying the concentration

of CaO in the slags show that when the silica content of slag is partially replaced by lime at constant total iron and cobalt oxide content, initially the activities of FeO and CoO increased. Beyond about 5 wt% CaO in the slag, these activities remained constant. This suggests saturation of the melt with another phase, such as a solid solution of magnetite containing CoO.

The value of the activity coefficient of CoO(*s*) for a liquid iron silicate slag containing 4.2 wt% CaO was 1.1. This is higher than the value for CaO-free liquid iron silicate slag, 1.02, at the same temperature and oxygen partial pressure. This dependence is in agreement with the results of Grimsey and Liu (1997), Katyal and Jeffes (1989), and Fontana *et al.* (1989). The value of the activity coefficient of FeO for a liquid iron silicate slag containing 4.2 wt% CaO was 0.83. This is significantly higher than the value for CaO-free liquid iron silicate slag, 0.69, at the same temperature and oxygen partial pressure.

Teague, Swinbourne, and Jahanshahi (2001) undertook a study of cobalt-containing calcium ferrite and calcium iron silicate slags, with the aim of determining the value of the activity coefficient of CoO(*s*) with and without small additions of silica.

Equilibration of cobalt between calcium ferrite based slags and Pt-Fe-Co alloys at 1300°C and an oxygen partial pressure of 1×10^{-7} atm. showed that the value of the activity coefficient of CoO(*s*) was 2.1 and that Henry's Law was obeyed up to approximately 10% CoO by mass. By comparison, that of Katyal and Jeffes (corrected to the solid standard state) gives a value of 2.5. The value of the activity coefficient of CoO (*s*) found in this work is very similar to, but between, the results of Takeda *et al.* (1983) and

Katyal and Jeffes (1989). The activity coefficient of CoO(*s*) was also found to be independent of the lime content of the slag.

The values of the activity coefficients of CoO, FeO, and Fe_2O_3, as functions of silica content, are shown in Figure 3.21. The value of the activity coefficient of CoO increases significantly with silica content, in agreement with Katyal and Jeffes. The addition of silica to calcium ferrite slag was shown to increase the activity coefficient of cobalt oxide up to 4% silica by mass.

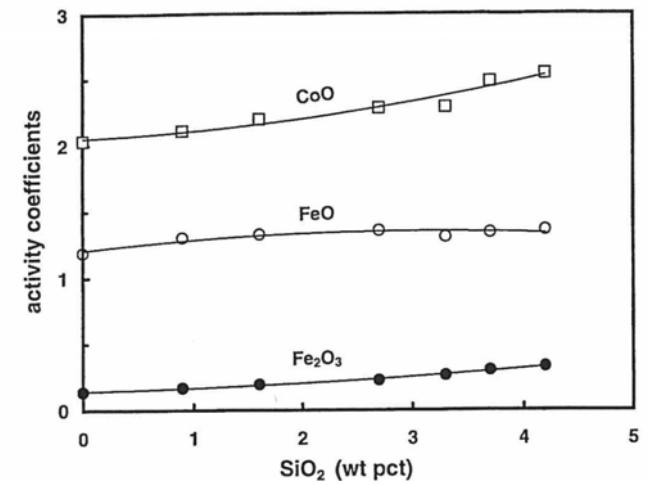

Figure 3.21 Activity coefficients of CoO(*s*), FeO(*s*), and Fe_2O_3(*s*) as a function of SiO_2 content for calcium iron silicate slags at 1300°C, 2.95×10^{-7} atm. of oxygen, and a CoO content of approximately 3% by mass (Teague *et al.*, 2001)

Derin and Yücel (2002) studied the distribution of cobalt between Co-Cu alloys (containing some iron) and Al_2O_3-FeO-Fe_2O_3-SiO_2 slags at 1400°C. They investigated the solubility of cobalt (0.092 to 3.365 wt% Co) in alumina-containing iron silicate slags in equilibrium with cobalt-copper-iron alloys (0.070 to 6.351 wt% Co) at partial pressures of oxygen of 4.5×10^{-10} to 1.1×10^{-8} atm. They found that the activity coefficient of

cobalt oxide in the slag increased with increasing cobalt oxide content in the slag and/or decreasing oxygen partial pressure in the system.

For oxygen partial pressure of 1.1×10^{-8} and 2.4×10^{-9} atm.:

$$\gamma_{CoO(l)} = 0.2731 + 0.2379 \text{ (wt\% CoO in slag)} \quad [3\text{-}52]$$

For oxygen partial pressure of 4.5×10^{-10} atm.:

$$\gamma_{CoO(l)} = 0.1782 + 0.0395 \text{ (wt\% CoO in slag)} \quad [3\text{-}53]$$

These relationships are shown graphically in Figure 3.22.

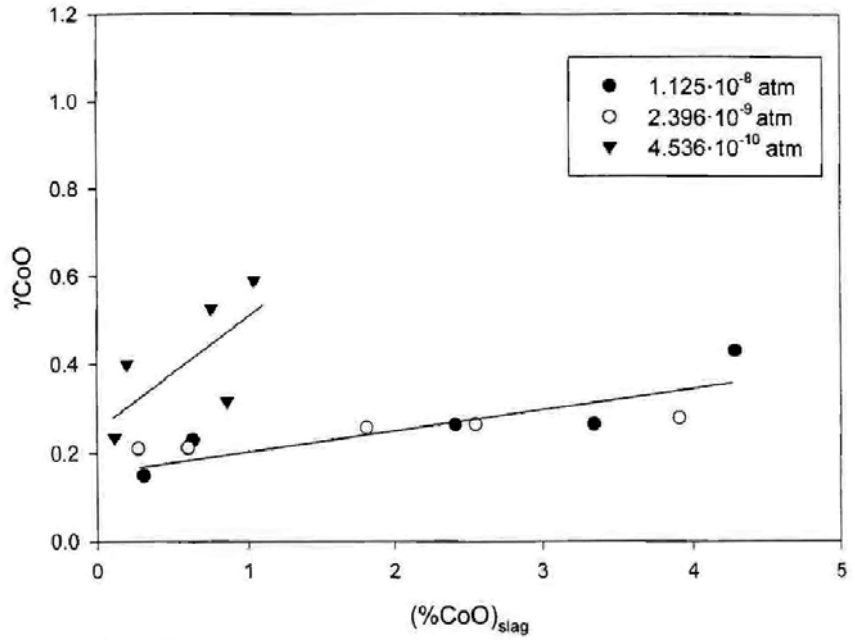

Figure 3.22 Activity coefficient of CoO(*l*) in slag as a function of cobalt oxide content and oxygen partial pressure (Derin & Yücel, 2002))

It can be seen that slags at 1400°C containing very small quantities of CoO under reducing conditions would be expected to have an activity coefficient of cobalt oxide (relative to the pure liquid standard state) of around 0.2 which translates to an activity coefficient of about 0.4 relative to the pure solid standard state. This is a much lower figure than those

from the other studies considered here. Derin and Yücel attempted to explain the difference as resulting from the higher temperature of their study, as well as differences in composition. The substantial temperature dependence (with the activity coefficient of CoO decreasing with an increase in temperature) of data from Reddy (1985) was cited in support of this, although this was seen by Grimsey and Liu (1995) as an indication that Reddy's data might be suspect.

O'Neill and Eggins (2002) investigated the activity coefficients of FeO, NiO, and CoO as part of a study to understand the effect of melt composition on the partitioning of trace elements between metals and silicate melts. The activity coefficients of FeO, NiO, and CoO varied by a factor of two over the same range of melt compositions, but showed no simple dependence on any particular major-element oxide component. However, the activity coefficients of all three components are very highly correlated with each other. This means that the effect of melt composition can be largely eliminated if the ratios of two activity coefficients are used.

O'Neill and Berry (2006), as part of a larger project, studied the activity coefficient of CoO at low dilution in CaO-MgO-Al_2O_3-SiO_2 melts at 1400°C. This study extended the work of O'Neill and Eggins (2002). The standard state used was that of the pure liquid oxide at the temperature of interest. The activity coefficients vary by a factor of two over the range of melt compositions studied, but show no simple correlation with composition. The variation in activity coefficients with melt composition between CoO and FeO is nevertheless highly correlated (as it also seems to be with the oxides of other divalent cations of similar ionic radius), that is, the ratio for γ_{CoO} / γ_{FeO} is effectively constant for all melt compositions. Values of 0.88 to 1.78 are recorded for $\gamma_{CoO(l)}$. From Figure 3.3, the liquid-

to-solid correction factor for 1400°C has a value of about 1.8 to 2.1, signifying a range of values for $\gamma_{CoO(s)}$ of 1.5 to 3.7.

Kitamura *et al.* (2008) investigated the cobalt distribution between MgO-saturated FeO_x-MgO-CaO-SiO_2 slag and Fe-Cu-Co molten alloy. The purpose of their work was to develop a "low-activation" steel containing minimal cobalt, for use in steel-reinforced concrete shielding for nuclear applications. They found that the activity coefficient of CoO decreases with increasing temperature and decreasing slag basicity. They claim that the work done by Grimsey and Toguri (1988), Reddy and Healy (1981), Grimsey and Liu (1995), Pagador, Hino, and Itagaki (1999), and Derin and Yücel (2002) shows that the activity coefficient of CoO (presumably relative to the liquid standard state, although this was not explicitly specified in the paper) was approximately 0.4 for the Al_2O_3-saturated slag, and around 2 for the SiO_2-saturated slag and other slag systems. However, steelmaking process conditions typically involve higher temperature, partial pressure of oxygen, and slag basicity than those used in the case of non-ferrous smelting. As MgO-based refractories are used in steelmaking, a MgO-saturated FeO_x-CaO-SiO_2 system containing 0.2% (by mass) of CoO was selected. The partial pressure of oxygen in the gas atmosphere was controlled by CO-CO_2 gas. The mass percentage ratio of CaO to SiO_2 was varied between 0.8, 1.0, and 1.2. Temperatures varied between 1300 and 1600°C (1573-1873 K). At temperatures below 1450°C, some CaF_2 was used as a flux. Molten samples were quenched after being allowed to reach equilibrium. The activity coefficient of CoO was calculated with the assistance of using values of the activity coefficient of Co in the alloy derived from a modified version of the Margules equations used by Derin and Yücel (2002) for molten Fe-Cu-Co alloys.

$$RT \ln \gamma_{Co} = A_{Cu-Co} X_{Cu}^{\ 2} + A_{Co-Fe} X_{Fe}^{\ 2} + (A_{Cu-Co} + A_{Co-Fe} - A_{Cu-Fe}) X_{Cu} X_{Fe} \qquad [3\text{-}54]$$

In equation [3-54], X is the molar fraction, and A is the interaction coefficient of each binary alloy. The following values of A are used at a temperature of 1673 K: $A_{Co\text{-}Fe}$ = - 8500, $A_{Cu\text{-}Co}$ = 36 525, $A_{Cu\text{-}Fe}$ = 32 446. These values have been modified so that they are in accordance with the observed results for the activity coefficients of cobalt (with respect to pure liquid cobalt as a standard state) in Fe-Co alloy and Cu-Co alloy reported by Oishi *et al.* (1981) and Maruyama and Ban-ya (1978) respectively.

The activity coefficient of CoO in slag can be calculated using the activity coefficient of cobalt and the observed partition ratio. The values for γ_{CoO} (presumably relative to the liquid standard state, although this was not explicitly specified in the paper) varied between 1.23 and 13.45.

Figure 3.23 shows the effect of temperature and slag composition (where basicity, B, equals the mass percentage ratio of CaO to SiO_2) on the activity coefficient of CoO. An inverse relationship between the temperature and the activity coefficient is observed; therefore, an increase in the temperature causes a decrease in the activity coefficient of CoO. However, the slag composition, expressed in terms of basicity, does not seem to have a significant effect on the activity coefficient of CoO.

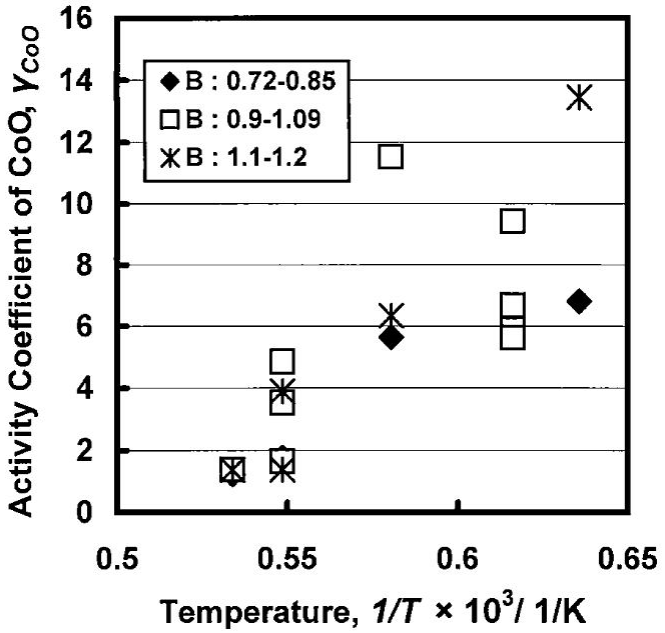

Figure 3.23 Influence of temperature and slag composition on the activity coefficient of CoO(*l*) in slag (Kitamura *et al.*, 2008)

Low-basicity slag has a smaller activity coefficient of CoO compared to that of high-basicity slag. A strong dependence of activity coefficient on temperature is seen, with the lowest value for $\gamma_{CoO(l)}$ of around 1.5 at 1600°C, and the highest value of around 13.5 at 1300°C. On the basis of this result, equation [3-55] was put forward by Kitamura *et al.* to describe the activity coefficient of CoO in slag.

$$\ln \gamma_{CoO} = 8.3283 + \frac{14976.3}{T} + 0.9552\ B \qquad [3\text{-}55]$$

Unfortunately, as confirmed by personal correspondence with Professor Kitamura in July 2014, equation [3-55] is incorrect by many orders of magnitude and should not be used.

Evaluation of various values for γ CoO(*s*)

Much uncertainty remains regarding the values of the activity coefficient of CoO(*s*) in iron silicate slags.

The published data reveal a number of inconsistencies. The data of Wang *et al.* (1973, 1974) indicated a significant effect of cobalt content on the activity coefficient, whereas the data of Katyal and Jeffes (1989) did not. The data of Reddy (1985) indicated a significant effect of temperature on the activity coefficient of CoO, whereas those of Wang *et al.* (1973, 1974) and Katyal and Jeffes (1989) did not.

The numerical values of the activity coefficients also differ substantially. Grimsey and Liu (1995) point out that the data of Wang *et al.* (1973, 1974) yield a value of 1.94 for the infinite dilution activity coefficient relative to the pure solid, which compares well with the average value of 2.0 recalculated from the data of Katyal and Jeffes (1989) for iron silicate slags relatively close to silica saturation (with around 35% silica),but is significantly different from the value of 0.93 calculated from equation [2] of Reddy (1985). The latter value is much closer to the 1.2 measured by Smith and Masson (1971) for relatively high concentrations of cobalt oxide in pure cobalt silicates at higher temperatures.

Derin and Yücel (2002) showed that the activity coefficient of CoO(*s*) was approximately 0.4 for Al_2O_3-saturated slag. This is obviously not applicable to slags with a low alumina content.

The value of 3 for $\gamma_{CoO(l)}$ at 1500°C suggested by the data of Pagador *et al.* (1999) leads to values of 4.5 to 5.1 for $\gamma_{CoO(s)}$. Values up to 13.5 for $\gamma_{CoO(l)}$ (at 1300°C) from the work of Kitamura *et al.* (2008) lead to values of 27 to 36

for $\gamma_{CoO(s)}$. These values are so much higher than those of all the previous workers that they should be disregarded here.

The review by Teague, Swinbourne, and Jahanshahi (1998) revealed significant differences between the reported values for the activity coefficient of CoO(*s*) in iron silicate slags. The studies they reviewed covered the temperature range 1250 to 1350°C, with slags that were mostly silica-saturated, and with oxygen partial pressures in the range 10^{-8} to 10^{-10} atm. Teague *et al.* (2000) have pointed out that the activity coefficient values for CoO(*s*) clustered around either 2 for studies prior to 1990 (Grimsey and Toguri, 1988; Katyal and Jeffes, 1989) or 0.9 for more recent studies (Grimsey and Liu, 1991, 1995). The review concluded that there was insufficient evidence to decide which value was most likely to be correct.

A range of 0.9 to 2 is preferred here for $\gamma_{CoO(s)}$, for present purposes.

Activity coefficient of FeO

Bosworth (1959) studied the activity of ferrous oxide in silicate melts (FeO-SiO_2 and FeO-CaO-SiO_2) at temperatures between 1265 and 1365°C. The standard state that he chose to use was that of pure liquid ferrous oxide. He found that the activity of ferrous oxide appears to be independent of temperature (in the range studied) in the presence of silica alone, but is markedly temperature-dependent in the presence of lime and silica together. Figure 3.24 shows values for $\gamma_{FeO(l)}$ of around 1.2 to 1.7 at a temperature of 1600°C, for CaO:SiO_2 ratios of 1:1 and 1:2.

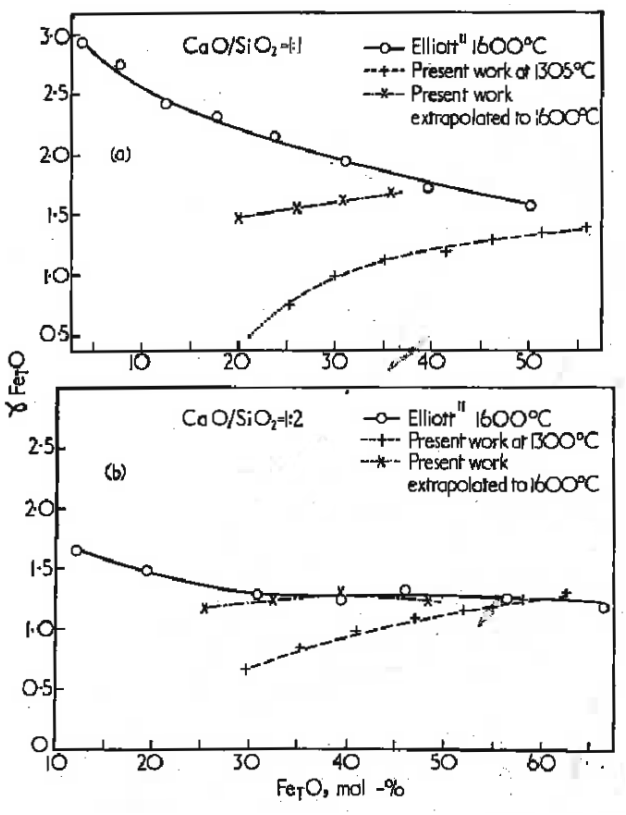

Figure 3.24 Variation of the activity coefficient of FeO(*l*) with composition in the ternary melt FeO-CaO-SiO_2 (Bosworth, 1959)

Holzheid and Palme (1996) investigated the influence of FeO on the solubilities of cobalt and nickel in silicate melts. They found that the activity coefficient of FeO in the melt was close to unity (relative to the pure solid standard state), reflecting nearly ideal behaviour of FeO in the melt.

Holzheid *et al.* (1997) worked with olivine-based silicate melts at temperatures from 1300 to 1600°C, in equilibrium with pure metals or alloys, and obtained values for γ_{FeO} of 1.70 ± 0.22, relative to the pure liquid oxide standard state. They also pointed out that using stoichiometric FeO as the standard state instead of wüstite (denoted here as "FeO") yields slightly higher activity coefficients. In this case, the ratio of $\gamma_{FeO(l)}$ / $\gamma_{"FeO"(l)}$ = 2.02 at 1300°C, 1.94 at 1400°C, and 1.66 at 1600°C.

Teague, Swinbourne, and Jahanshahi (2000) found that the activity coefficient of FeO in iron silicate based slags (at 1300°C and with a partial pressure of oxygen of 3.7×10^{-8} atm.) had virtually no dependence on the CoO content, as shown in Figure 3.25. In this case, $\gamma_{FeO(s)} = 1.0$. If the correction from a solid to a liquid standard state is applied (using an approach analogous to equation [3-26]), then $\gamma_{FeO(l)} = 0.9$.

Figure 3.25 shows the FeO activity coefficient values determined by Teague *et al.* (2000) for lime-free slags containing approximately 25% silica by mass, with increasing cobalt oxide content. Also shown is the value of the FeO activity coefficient for cobalt-free silica-unsaturated iron silicate slag of the same silica content, determined by Schuhmann (1955), at the same oxygen partial pressure and a similar temperature (1350°C). There is very good agreement between the data from the two studies. Teague *et al.* found the value of the FeO(*s*) activity coefficient to be 0.69 in the case of an iron silicate slag containing 31% silica (by mass) and 3% cobalt oxide. This again agrees well with the value of 0.72 from Schuhmann (1955) for iron silicate slag containing 31% silica at the same oxygen partial pressure and a similar temperature. From all of these combined results, it can be seen that the FeO activity coefficient decreases with increasing silica content in iron silicate slags. Teague *et al.* (2000) have pointed out that this is expected because FeO and SiO_2 interact with each other, as shown by the existence of the 'fayalite' compound $2FeO.SiO_2$.

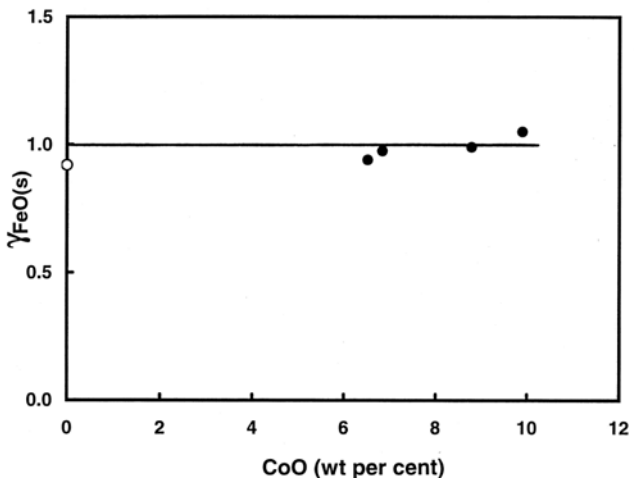

Figure 3.25 Activity coefficient of FeO(*s*) as a function of cobalt oxide content in lime-free iron silicate slags at 1300°C and an oxygen partial pressure of 3.70 x 10^{-8} atm. Solid dots represent work by Teague et al. (2000), and the hollow dot represents work by Schumann (1955) (Teague *et al.*, 2000)

According to Teague *et al.* (2000), it is well established that the activity of FeO is temperature-dependent, and increases with increasing temperature in calcium iron silicate slags. Perhaps differences in temperature provide an adequate reason for some of the variation in the values of $\gamma_{FeO(l)}$ reported here.

Jung, Decterov, and Pelton (2004) undertook a critical evaluation of the phase diagrams and thermodynamic properties of all oxide phases in the FeO-Fe_2O_3-MgO-SiO_2 system. They optimized model equations for the thermodynamic properties in order to reproduce all available data within experimental error limits. The modified quasichemical model was used for the liquid-slag phase. Figure 3.26 shows their calculated activities of FeO (relative to the pure liquid state) as a function of mole fraction at a temperature of 1600°C. It can be seen that the activities are rather close to the corresponding mole fractions of FeO, indicating an activity coefficient close to one. Also shown on the diagram are the results of Kojima *et al.*

(1969) who determined the activity of FeO in FeO-MgO-SiO_2 slags at 1600°C and whose results were consistent with activity coefficients close to unity.

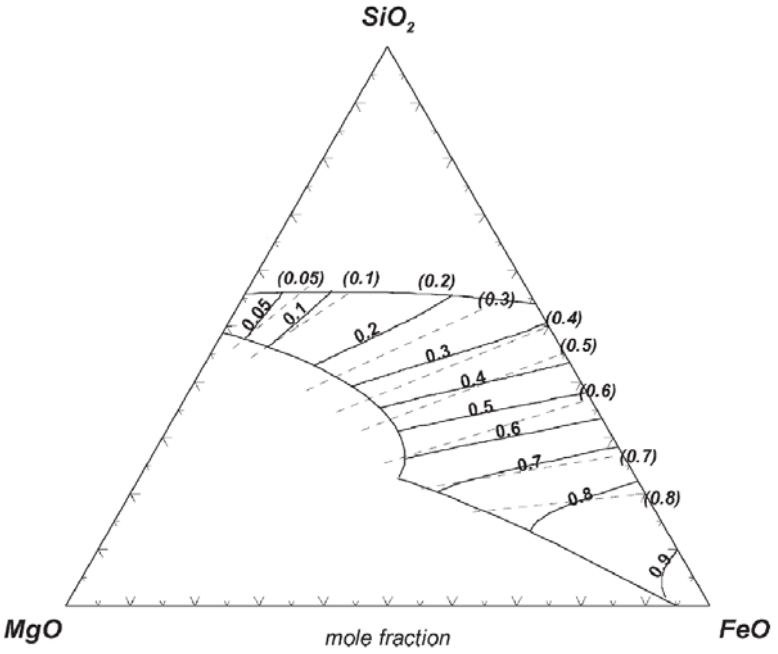

Figure 3.26 Calculated activities of FeO(*l*) in FeO-MgO-SiO_2 liquid slag in equilibrium with metallic iron at 1600°C, with dotted lines showing the results of Kojima *et al.* (1969)
(Jung, Decterov, & Pelton, 2004)

A range of 0.9 to 1.7 is chosen here for $\gamma_{FeO(l)}$, for present purposes.

Activity coefficients of Co and Fe

Hultgren *et al.* (1973) have tabulated activities and activity coefficients (relative to Co(*l*) and Fe(*l*)) for Co-Fe liquid alloys at 1590°C, as shown in Table 3.3 and plotted in Figure 3.27.

Table 3.3 Activities and activity coefficients of Co and Fe in Co-Fe alloys at 1590°C, relative to pure liquids (Hultgren *et al.*, 1973)

x_{Fe}	a_{Fe}	γ_{Fe}	x_{Co}	a_{Co}	γ_{Co}
0.0	0.000	1.590	1.0	1.000	1.000
0.1	0.142	1.416	0.9	0.905	1.006
0.2	0.256	1.282	0.8	0.819	1.024
0.3	0.355	1.183	0.7	0.736	1.051
0.4	0.438	1.095	0.6	0.658	1.097
0.5	0.517	1.035	0.5	0.575	1.151
0.6	0.589	0.981	0.4	0.491	1.226
0.7	0.685	0.979	0.3	0.369	1.230
0.8	0.790	0.987	0.2	0.240	1.199
0.9	0.896	0.996	0.1	0.114	1.136
1.0	1.000	1.000	0.0	0.000	1.051

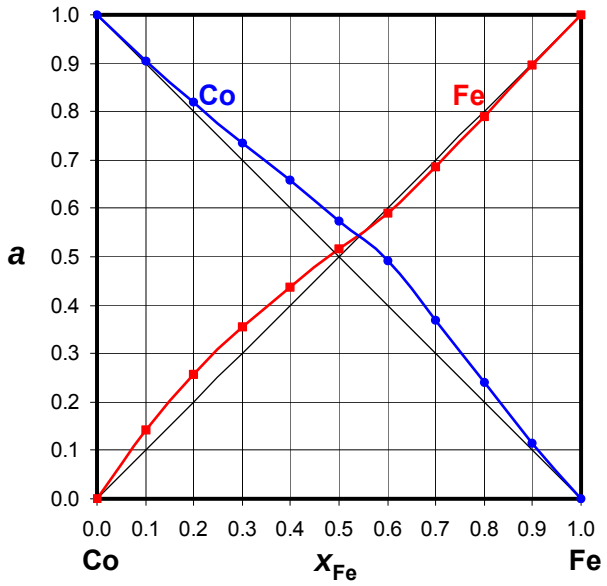

Figure 3.27 Activities of Co and Fe in Co-Fe alloys at 1590°C, relative to pure Co(*l*) and Fe(*l*)
(Plotted from the data of Hultgren *et al.*, 1973)

Pagador *et al.* (1997) commented that activities in the Fe-Co system show nearly ideal behaviour.

Soltanieh (1998) has tabulated the relationship between activities and mole fraction in the Co-Fe system as a function of temperature, between 1200 and 1350°C. The data shows very little sensitivity to temperature.

3.5.3 Calculation of $K\gamma$ from literature values

In the case of recovering cobalt from copper smelting furnace slag by reductive smelting, the product alloy comprises by mass around two thirds Fe, with the remaining Co and Cu being somewhat variable in composition depending on the composition of the feed slag. The slag that is produced typically contains around 50% SiO_2, 24% FeO, 14% CaO, 9% Al_2O_3, 3% MgO, and less than half a percent each of cobalt and copper.

From the preceding discussion:

K = 20

γ CoO(s) = 0.9 to 2.0

γ Fe(l) = 0.98

γ Co(l) = 1.14 to 1.23

γ FeO(l) = 0.9 to 1.7

$$K\gamma = K\,\frac{\gamma_{CoO}\cdot\gamma_{Fe}}{\gamma_{Co}\cdot\gamma_{FeO}} = 8.4\ to\ 38 \qquad [3\text{-}56]$$

3.5.4 Experimental data from Co Recovery pilot-plant work

A set of experimental data from previously reported work on the recovery of cobalt from copper reverberatory furnace slag (Jones *et al.*, 2002) shows a fair degree of scatter and covers mostly the high Co recovery area. This data is shown (using the + symbol) in the upper portion of Figure 3.28.

The scatter is to be expected as the data covers a wide range of experimental conditions, and is based on chemical analyses that have significant uncertainty associated with measurements of CoO in the slag at low concentration. However, some more recent work on the use of a DC arc furnace for cleaning flash furnace slags has provided further data in the low recovery area. This data is shown (using solid dots) in Figure 3.28. The combination of these two sets of data provides convincing evidence that the proposed recovery equation provides a curve of the correct shape to fit the data. The best fit (achieved by minimizing the sum of the squared errors) to the combined data is obtained with a value for $K\gamma$ of about 14.

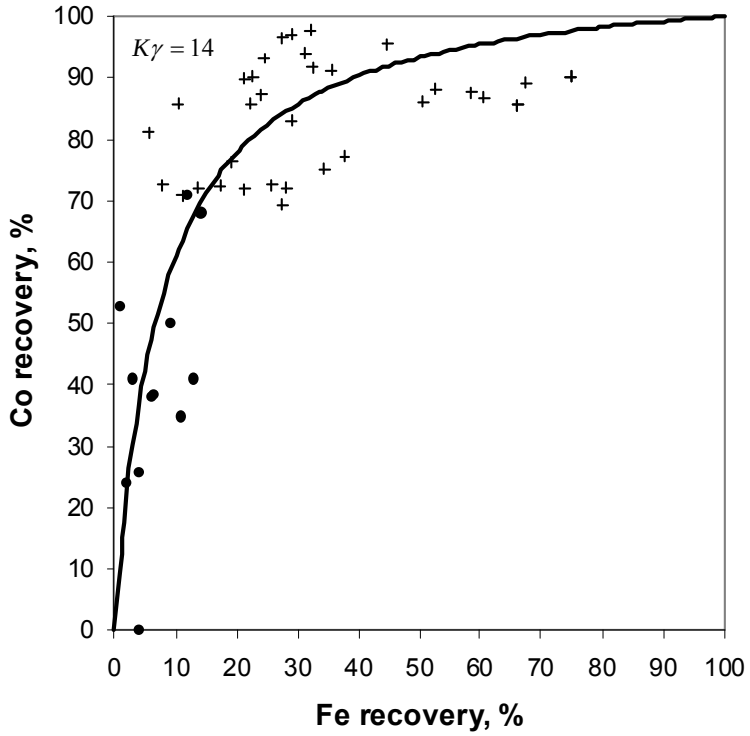

Figure 3.28 Recovery curve for Co ($K\gamma$ = 14) and two sets of data points

Large-scale processes inherently have a great deal of scatter in the data that describes them. However, there is still much practical utility in a

model that allows one to calculate that, for an 80% recovery of cobalt to the alloy to be achieved, the iron recovery needs to be in the region of 25% for this to be the case most of the time. The significant amount of scatter in this data set prevents much more detailed analysis from being done here, other than to say that there is obviously some uncertainty in the best value of $K\gamma$ to be used. A range of $K\gamma$ values from about half to double the chosen value (or say from 6 to 30) would span approximately 70% of the data points. This range is similar to that predicted from literature values in equation [3-56]. More importantly, the implication of this wide a range of $K\gamma$ values is that the corresponding uncertainty in Fe recovery would be from 12% to 40% to generate a Co recovery of 80%. The principal value of this example is that it shows that the model has the correct type of shape to fit the results, but a better-controlled data set would be required for greater certainty in the calculated value of $K\gamma$. Fortunately, the data sets in subsequent examples have much less scatter.

3.6 Application to Ferronickel Smelting (Ni and Cr)

The smelting of nickel laterite ores to produce ferronickel essentially involves a trade-off between recovery and grade. The greater the degree of reduction, the greater the recovery of nickel. However, as an increasing quantity of iron (and some more nickel) is reduced to the metallic state, so the nickel grade is diminished. The $K\gamma$ recovery equation provides a useful tool for quantifying this effect, and for determining a suitable operating point for the ferronickel production process. Once the recoveries of nickel and iron are known, it is a trivial calculation (suitable for a spreadsheet) to calculate the composition (and grade) of the alloy.

The data shown in Figure 3.29 is derived from ferronickel smelting testwork (Geldenhuys & Lagendijk, 2007) carried out in a pilot-scale DC

arc furnace with an operating diameter of 2 m. More than 190 tons of calcined nickel oxide ore was smelted over a period of about 19 days. Three different samples were smelted (denoted by different symbols and colours), each containing relatively low amounts of nickel and iron and relatively high amounts of silica. For two of the samples, dolime was added as flux. In the particular example shown here, there was evidence to suggest that slag-metal equilibrium was not fully attained because of a crusty layer that formed in the furnace, because of the particular experimental conditions employed. Even so, the recovery equation is shown to fit the data well, with a $K\gamma$ value for nickel of about 20.

As a point of comparison, another curve is shown, with a higher value of $K\gamma$ (from a different experimental campaign using different feed materials). It would clearly not be appropriate to merely use a value of $K\gamma$ from a previous ferronickel smelting test, but it would be necessary rather to determine this value experimentally for the particular set of feed materials and operating conditions under consideration. This goes to show the importance of either testwork or wide experience in the selection of an appropriate value of $K\gamma$ to use for characterising the smelting of a particular ore, and the compositions of slag and alloy that arise from it. (The theoretical justification for this is that the ratio of the activity coefficients, γ, does depend to some extent on the slag and alloy composition.)

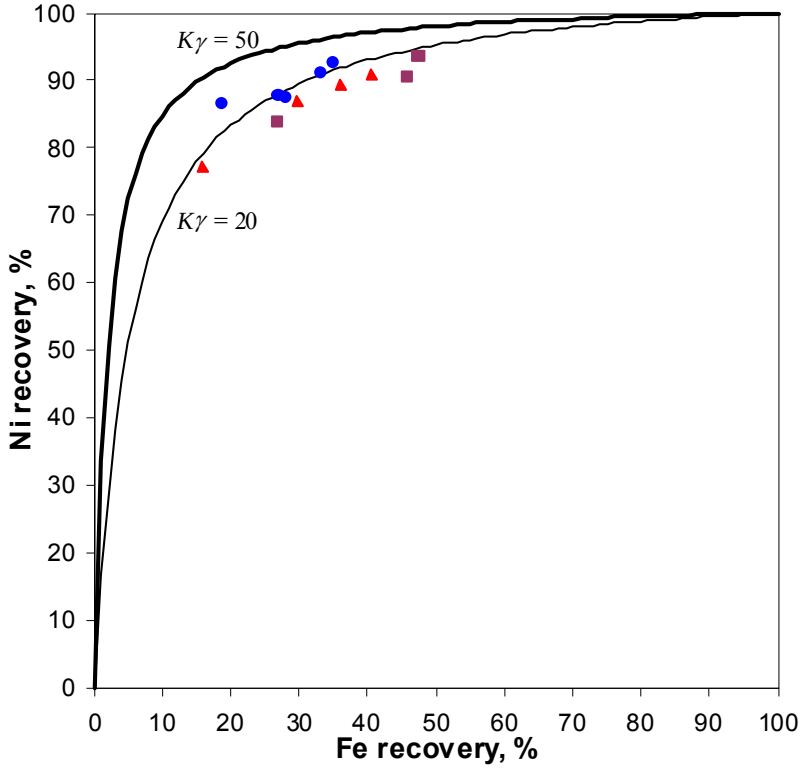

Figure 3.29 Recovery curve example for Ni ($K\gamma$ = 20) in ferronickel smelting, compared to the recovery curve ($K\gamma$ = 50) from another ferronickel test with different feed materials

The recovery of Cr in base metal smelting shows interesting behaviour. Because Cr is 'less noble' than Fe, the curve is the other way around compared to Ni or Co. Figure 3.30 shows numerous data points from laboratory-scale smelting tests carried out on a typical nickel laterite. Tests were carried out on 200 g samples in MgO crucibles in an induction furnace. Because so little metal is produced in these tests, it is quite easy to over-reduce the samples in the attempt to obtain sufficient metal. In this case, the over-reduced tests produced a very wide range of data for plotting the Cr recovery as a function of Fe recovery. A recovery curve with $K\gamma$ = 1/35 provided a good fit to this data. As an additional comparison, a few points are shown (in red) to follow the same curve very closely. These results (red points) came from smelting PGM-containing revert tailings, and each point represents the monthly recovery figure for

the period October 2007 to June 2008 at Mintek. It might seem surprising that the recovery curve fits the Cr data so well, given the earlier comments about the complexities of trying to model a system involving Cr_2O_3. However, under reducing conditions, chromium is most likely to be present in the slag as CrO instead, in which case the recovery equation is most certainly applicable.

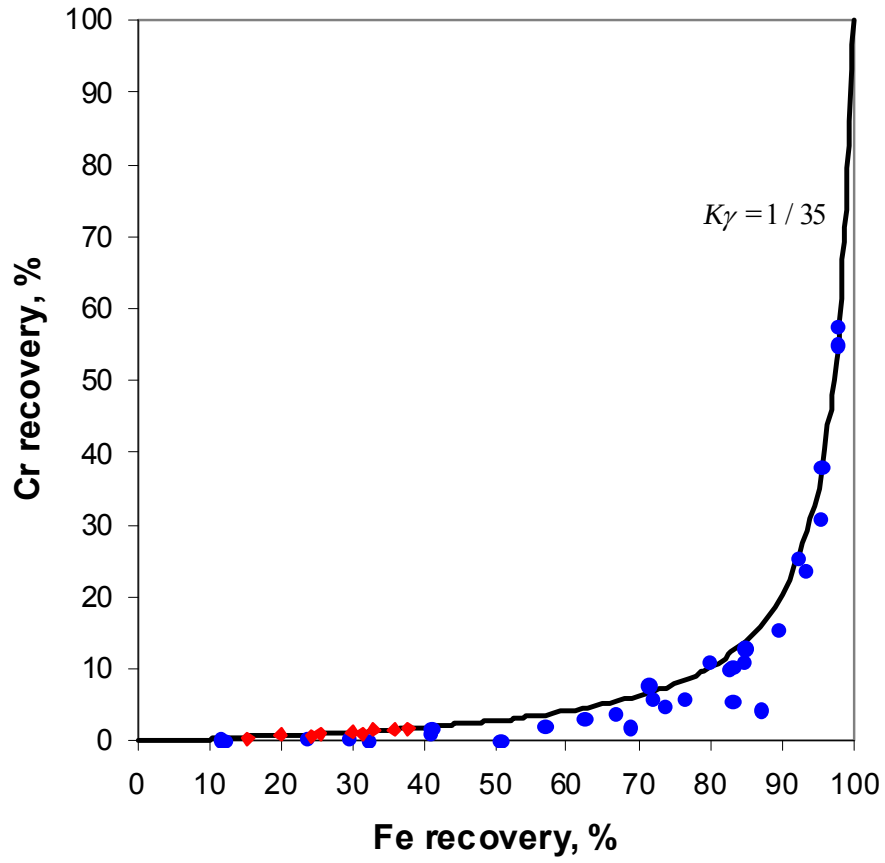

Figure 3.30 Recovery curve for Cr ($K\gamma$ = 1/35) in ferronickel smelting

3.7 Application to PGM Smelting

Mintek's ConRoast process (Jones, 2002; Jones & Kotzé, 2004; Geldenhuys & Jones, 2009) involves smelting low-sulphur concentrates in a DC arc furnace, and collecting the platinum group metals (PGMs) and valuable

base metals in an iron alloy. The intention in this process is to separate the valuable metals from the iron and the gangue constituents present in the slag. The desirable area of operation is clearly somewhere in the region where the recovery of PGMs and valuable base metals is high, and the recovery of iron to the alloy is still reasonably low. This process is also effective at removing chromium (in this context, a deleterious contaminant) by keeping it dissolved in the slag, and away from the alloy product. Figure 3.31 shows the recovery of PGMs, Ni, Co, and Cr as a function of Fe recovery to the alloy. Under the conditions of interest, it is fair to model the Ni, Co, and Cr as interacting with NiO, CoO, and CrO in the slag.

It is not immediately apparent why the PGMs should behave in a similar fashion, as PGMs are often thought of as being extremely unreactive and unlikely to form oxides. However, it has been found that PGM recovery can also be usefully modelled using the $K\gamma$ recovery equation. The PGMs are grouped together for the purpose of recovery modelling, as the quantities are too small, and the analytical techniques too imprecise at low levels, to meaningfully treat them individually. The existence of PGM oxides in slag can be explained by studying the solubilities of various PGMs under conditions of varying partial pressure of oxygen. The valence of the metal ion in the melt may be determined from the experimentally determined slope of the relationship between the log of the concentration of the metal oxide dissolved in the silicate slag and the log of the partial pressure of oxygen. Morita *et al.* (2011) studied the dissolution behaviour of Pt, Ru, and Rh into molten slags, and found that PtO, $RuO_{1.5}$, and $RhO_{1.5}$ are the appropriate forms in which these PGMs dissolve into the slag. The ionic forms were suggested to be PtO_2^{2-}, RuO_2^-, and RhO_2^-. Furthermore, Laurenz *et al.* (2013) conducted experiments with Pd and Ru, where the solubilities of these elements in a slag-like

phase (a picritic melt) were measured as a function of the partial pressure of oxygen in the presence of sulfur. This added to the understanding from previous experiments that platinum group elements dissolve in silicate melts as oxide species, and that their saturation depends on oxygen partial pressure. In that work, palladium exhibited monovalent and divalent oxidation states, and ruthenium was tetravalent. Borisov *et al.* (1994) studied the solubility of palladium in silicate melts, and found a definite dependence on the partial pressure of oxygen. A typical valence state of Pd^{1+} indicates the likelihood of the co-existence of Pd^{0} and Pd^{2+} (*i.e.*, PdO, the most stable of the known palladium oxide species) in solution. Similar calculations have been done for iridium (Borisov *et al.*, 1992) where the iridium solubility in silicate melts is about two orders of magnitude lower than the palladium solubility, and the Ir activity coefficient in iron metal is more than a factor of a hundred below that of Pd in iron metal.

The values of $K\gamma$ obtained here for nickel and chromium are very similar to those used earlier, with a value of $K\gamma$ for Ni of 28 (compared to 20 earlier), and a value of $K\gamma$ for Cr of 1/40 (compared to 1/35 earlier).

The $K\gamma$ recovery equation provides a very clear framework for the relationship between Ni, Cr, and Fe to be clearly understood. This provides a rational basis for the selection of an operating point that allows one to recover as much as possible of the valuable metals to the alloy, while minimizing the quantity of iron that is reduced to the metallic form, in addition leaving essentially all chromium dissolved in the slag as CrO.

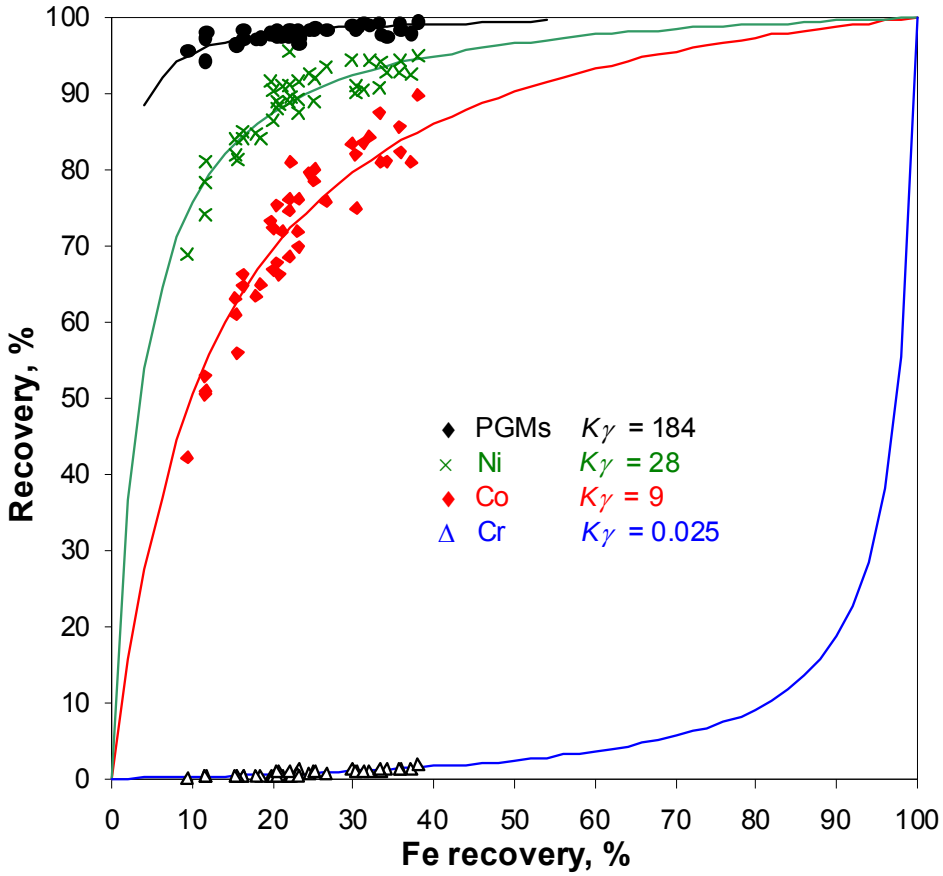

Figure 3.31 Recovery curves for PGMs ($K\gamma$ = 184), Ni ($K\gamma$ = 28), Co ($K\gamma$ = 9), and Cr ($K\gamma$ = 0.025)

3.8 Application to Converting Processes

The $K\gamma$ recovery equation applies also to oxidative converting processes as well as to reduction processes. These two very different types of process are governed by the same chemical reactions, albeit that the one is the reverse of the other. The recoveries of various elements can be plotted against the degree of iron removal from the alloy being converted. This has been well documented by McCullough *et al.* (2008).

An iron alloy containing platinum group metals (PGMs) and base metals was subjected to a pyrometallurgical iron-removal process (by blowing

the molten alloy with either air or oxygen), as a precursor to base metals removal and precious metals refining. The amount of alloy used for each test varied between 0.7 and 5 kg. The alloy charges were contained in alumina crucibles, and were melted using induction heating. Oxygen was introduced into the melt via an alumina tube. Additions of CaO and SiO_2 were made periodically to ensure a low-melting slag, whilst Al_2O_3 was added to the slag to ensure protection of the alumina crucibles. The experimental data for the various converting tests is depicted as deportment of the valuable metal versus the degree of iron removal. Appropriate values of $K\gamma$ were determined by means of curve fitting. Good correlations were found for nickel and cobalt over a very wide range of values for iron removal, as shown in Figure 3.32.

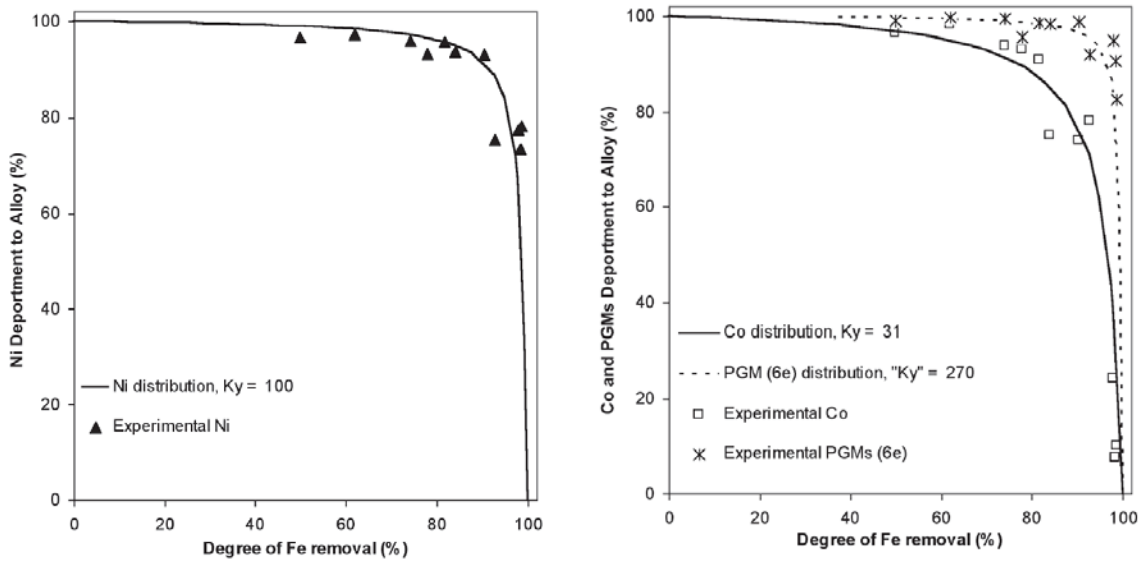

Figure 3.32 Correlation between the degree of iron removal and the deportment of Ni, Co, and PGMs to the alloy. PGMs ($K\gamma$ = 270), Ni ($K\gamma$ = 100), and Co ($K\gamma$ = 31) (McCullough *et al.*, 2008)

Although the numerical values of $K\gamma$ differ somewhat from the case of reductive smelting (not entirely unexpectedly, given that these are

compositionally very different systems), it is clear that the functional form of the $K\gamma$ recovery equation applies well to this system.

3.9 Conclusions

Base metals and platinum group metals can be collected in metallic alloy form, via a wide variety of smelting processes. The recovery, or degree of collection, of the valuable metals is a function of the extent of reduction in the furnace, which, in turn, is indicated by the fraction of iron present in the feed materials that reports to the alloy. An equation has been developed that relates the recovery of various metals (such as Ni, Co, Cr, and PGMs) to the recovery of Fe. This recovery equation (for each metal) is characterised by a single parameter ($K\gamma$) that can either be fitted empirically to the data, or expressed in terms of the equilibrium constant and the ratios of the activity coefficients involved. Data from a number of varied DC arc furnace campaigns is presented to illustrate this behaviour.

The $K\gamma$ recovery equation (Jones *et al.*, 2009) has been found to provide a very useful basis for the design of processes involving the recovery of precious and base metals in DC arc furnaces. The equation produces curves of the correct functional form that are applicable across a very wide range of different extents of reduction. The value of $K\gamma$ to be used can be calculated theoretically, but it is often more effective to fit this value to experimental data obtained from the particular system of interest. $K\gamma$ for a particular metal has a characteristic value that depends on the temperature of operation and to some degree on the composition of the slag and metal system under consideration (as this affects the individual activity coefficients). Process design calculations can be carried out with confidence, knowing that there is good theoretical justification for the form of the equation, and that the single parameter $K\gamma$ is based on

experimental work. The simplicity of the equation has made it straightforward to incorporate into spreadsheet models of various processes, and this is now widely used. The equation clarifies the dependency of the recovery of the valuable metals on the recovery of iron in the furnace, and this allows a furnace operator to control the smelting process more easily and to target the correct degree of reduction.

The multi-phase multi-component systems involved in smelting processes have so many variables that it is often difficult to pick out the most important relationships. One of the most important contributions of this work to the field of reductive alloy smelting was the derivation of the $K\gamma$ recovery equation, from first principles, to show the relationship between the recovery of a desired metal (such as cobalt or nickel, for example) and the recovery of iron (the fraction of the metal that reports to the alloy, expressed as a fraction of the metal that is present in the feed material). Data sets from numerous pilot-plant campaigns have been used to validate this model, and it is now used by a number of major international mining companies.

4 DC ARCS AND ELECTRICAL ASPECTS

4.1 Introduction

At the heart of the DC arc furnace is the plasma arc that provides energy to the furnace (as illustrated in Figure 4.1). It is, therefore, necessary to have a good understanding of the arc itself, as well as how it interacts with the molten material inside the furnace vessel. The inherent persistency and intensity of a direct-current (DC) plasma arc offers some unique advantages for a number of smelting processes (Jones *et al.*, 1993).

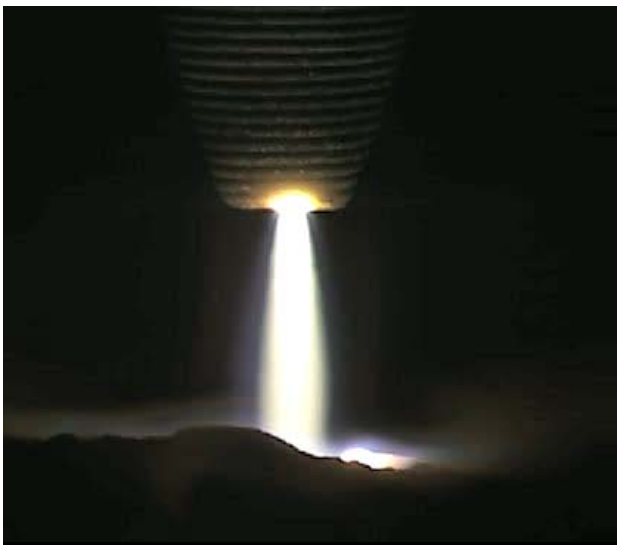

Figure 4.1 Stable arc, 600 A, 5 cm arc length

The stirring caused by the DC plasma arc has been found to be advantageous in terms of mixing fine feed materials into the molten slag bath. At industrial current levels, the velocities in the arc can reach many kilometres per second, and this imparts a significant thrust force to the surface of the molten slag or metal bath beneath. Interaction between the arc jet and the molten bath results in a great deal of turbulent splashing

and mixing, stirring the bath and homogenizing its properties to a large degree.

4.2 The Nature of the DC Arc

DC arc furnaces operate with a graphite cathode positioned above a molten slag and metal bath contained inside a furnace vessel. Initially, the gas between the cathode and the molten material is subjected to resistive heating, but once the temperature of the gas is sufficiently high (above about 5000 K), its constituent molecules and atoms begin to ionise into positively charged ions and negatively charged electrons, giving a neutral but very strongly conductive plasma. The plasma arc, consisting of ionised particles at extremely high temperatures, forms a conducting path between the graphite cathode and the molten bath, and permits electrical current to pass from the furnace electrode through to the furnace bath and complete the circuit.

Flow of the plasma in the arc column is driven very strongly downward by electromagnetic forces, in a jet from the electrode towards the molten bath. According to Stenkvist and Bowman (1987), a DC arc plasma from a graphite cathode provides very efficient transfer of energy from the arc to the anode. This high efficiency is due to the fact that a strong, electromagnetically pumped plasma jet convects most of the power towards the anode. The higher current density near the cathode spot results in self-magnetic compression that accelerates the plasma away from the spot, towards the lower current-density region. Due to the expansion of the current cross-section from the cathode spot along the arc axis, there arises an axial component of the Lorentz force which accelerates the plasma towards the anode. The arc therefore acts as an electromagnetic pump, drawing in gas near the cathode spot and ejecting

it towards the anode. This axial jet tends to stabilise the arc column, in the sense that it remains straight, whereas open arcs are often unstable. The DC arc with stable, unidirectional convection is superior to the AC arc in transferring its energy directly to the anode in a metallurgical process.

Much of the energy from the arc is delivered to a localised area directly beneath the arc, making this a very effective way of heating the process material. At industrial scale, the arc jet can operate at temperatures in excess of 20 000 K and reach supersonic velocities. The power provided by the arc can be controlled by adjusting the arc length and the current.

The open arc provides an additional degree of freedom (compared to a furnace with an electrode immersed in the molten bath) to the supply of energy to the furnace, in that the resistivity of the slag is no longer solely responsible for the dissipation of energy to heat the molten slag. This renders the energy supply nearly independent of slag composition, which may allow the chemical composition of the slag to be optimized for the best recovery of valuable metals (instead of for the required electrical characteristics).

The high-intensity plasma arc emanates from a relatively small attachment area on the graphite electrode, and extends down to the surface of the molten bath. The arc attachment zone, where the arc impinges on the molten slag surface, is highly turbulent and operates at a very high temperature. This promotes very rapid melting, fast reaction kinetics, and effective mixing. The impingement of the arc causes a crater-like depression in the surface of the slag. This is believed by the author to have a significant effect on the distribution of current and temperature in the molten slag, and the voltage drop across the slag (and is discussed in Sections 4.4 and 4.5). The shape and size of this depression has been

photographed by the author, and the resulting information used in a model of the depression.

4.3 Electrical Modelling of the Steady-State Arc

This section summarises work previously published by Bowman and colleagues, then outlines practical measurements made at Mintek and how they can be applied to a usable model of the arc. The intention here is to collect all of the required design equations in one place, and set out a recommended procedure for the electrical design specification of DC arc furnaces.

The steady-state electrical behaviour of the DC arc has been well described previously (Bowman *et al.*, 1969; Bowman, 1972, 1982, 1990, 1994; Jordan *et al.*, 1970; Stenkvist & Bowman, 1987; Bowman & Krüger, 2009). Bowman summarized a large quantity of test data from DC electrical arcs in the 1 to 10 kA range, and verified his model against industrial measurements up to 100 kA. This work provides a description of how the arc voltage varies as a function of arc length and current, for a given set of conditions in the furnace. The model outlined here uses measured and extrapolated arc shapes, fitted to calculated plasma conductivities and estimated temperature profiles, although it does not say much about the highly dynamic nature of the interaction between the plasma arc and the molten slag bath.

The high-intensity plasma arc has been modelled by Bowman as emanating from a relatively small attachment area on the graphite electrode, and extends down to the surface of the molten bath. This is shown schematically in Figure 4.2.

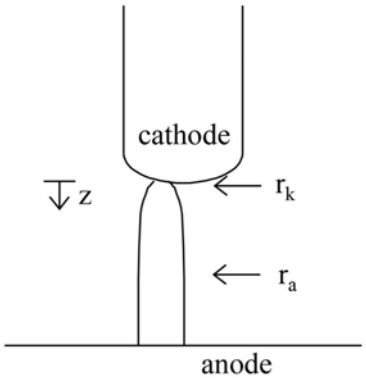

Figure 4.2 Schematic representation of a DC arc

The arc radius, r_a, varies with the distance, z, from the cathode surface. The radius, r_k, of the cathode-spot attachment is determined by the value of the cathode-spot current density, estimated by Bowman (1994) to be around 3.5 kA/cm^2.

Photographs of the arc have been compared by Bowman and colleagues to models of its shape (Bowman *et al.*, 1969; Jordan *et al.*, 1970). These models provide a description of how the arc voltage varies as a function of arc length and current, for a given set of conditions in the furnace.

Equation [4-1], from Bowman's work, describes the shape of the conducting volume of the arc as a function of the distance from the cathode attachment spot. The assumptions include an axi-symmetric arc and no interaction effects at the anode. This equation is incorrectly printed in (Bowman, 1994), and again but with a different error in (Bowman & Krüger, 2009), but has been corrected here by examining the form of the equation that properly fits the figure in the original reference.

$$\frac{r_a}{r_k} = 1 + 2.2\left[1 - \exp\left(-\frac{z}{5r_k}\right)\right] = 3.2 - 2.2\exp\left(-\frac{z}{5r_k}\right) \qquad [4\text{-}1]$$

Figures 4.3 and 4.4 provide an example of the qualitative comparison that was made between actual and calculated arc shapes at Mintek.

Figure 4.3 4 kA arc in air, struck on a graphite block

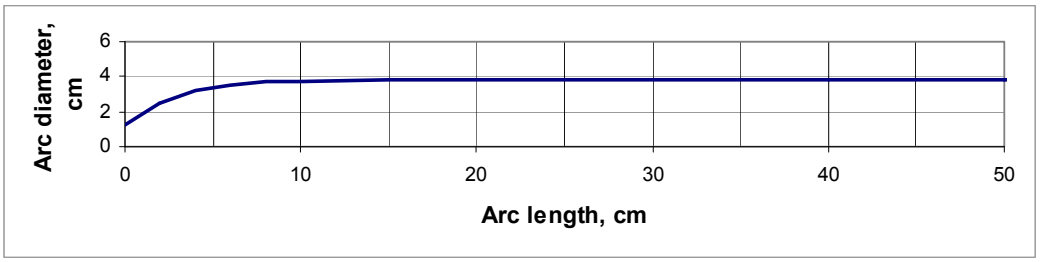

Figure 4.4 Arc diameter versus length for a 4 kA arc

The arc shape function of Equation [4-1] allows the arc voltage to be obtained by the integration shown in Equation [4-2]. Several constants of Bowman's, along with a single variable parameter, the arc resistivity, appear in the arc voltage expression (which is largely proportional to the square root of the current). In Bowman's version of this equation, he uses half of the peak conductivity to represent the average value, as it is assumed to have a parabolic profile. In the version of the equation presented here, the average resistivity (the inverse of conductivity) is used

instead. Variation of the arc resistivity then allows the model to be fitted to pilot- or industrial-plant data. The integration required is:

$$V = \rho_a \cdot \sqrt{I} \cdot \sqrt{\frac{j_k}{\pi}} \cdot \int_{Z=0}^{L/r_k} \left(\frac{r_k}{r_a} \right)^2 dZ \qquad [4\text{-}2]$$

$$Z = \frac{z}{r_k} \qquad [4\text{-}3]$$

where:

V = arc voltage, V

ρ_a = arc resistivity, Ωcm

I = current, A

j_k = current-spot current density, A/cm^2

L = arc length, cm

r_k = cathode-spot radius, cm

r_a = arc radius, cm

z = axial distance from cathode, cm

The final result of this integration is an expression relating the voltage of the arc to its length and current. This is shown in Equation [4-4].

$$V_a = \frac{I\rho_a}{m\pi} \left[-\frac{1}{a^2 + ab} + \frac{1}{a^2 + ab \cdot \exp(mL)} + \frac{\ln(a+b)}{a^2} + \frac{mL}{a^2} - \frac{\ln[a + b \cdot \exp(mL)]}{a^2} \right] \qquad [4\text{-}4]$$

$$a = 3.2 r_k \qquad [4\text{-}4a]$$

$$b = -2.2 r_k \qquad [4\text{-}4b]$$

$$m = \frac{-1}{5 r_k} \qquad [4\text{-}4c]$$

$$r_k = \sqrt{\frac{I}{\pi (3500 A/cm^2)}} \qquad [4\text{-}4d]$$

where:

V_a = arc voltage, V

I = current, A

ρ_a = arc resistivity, Ωcm

r_k = cathode-spot radius, cm

L = arc length, cm

Equation [4-4] is depicted graphically in Figure 4.5, which shows arc voltage as a function of arc length, for a range of different currents, at a given arc resistivity of 0.014 Ωcm (for example).

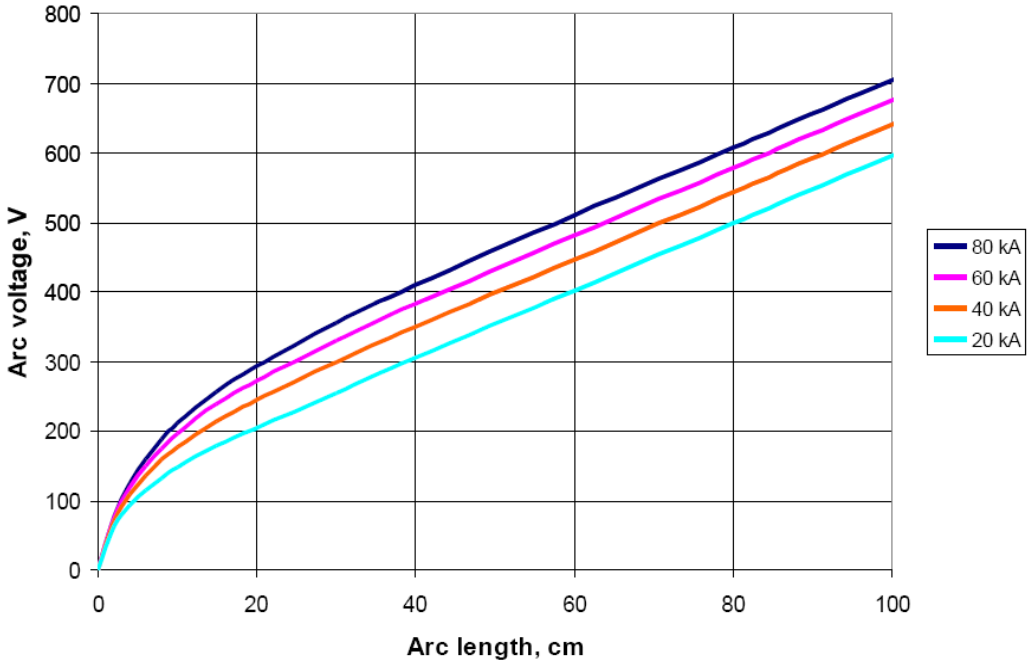

Figure 4.5 Arc voltage as a function of arc length at different currents, for a given arc resistivity of 0.014 Ωcm

Routine measurement protocols have been established in order to obtain values for arc resistivity (and slag resistivity) from the experimental measurements undertaken during pilot-plant furnace campaigns at Mintek (Reynolds & Jones, 2004). Values for arc resistivity are obtained by measuring the voltage while keeping the current constant and varying the

arc length. The value used for the arc resistivity is that which best fits the experimental data. An example of such a data set is shown in Figure 4.6. The arc resistivity varies substantially according to the prevailing gas atmosphere in the furnace. For example, the presence of zinc vapour makes the arc more conductive than carbon monoxide does.

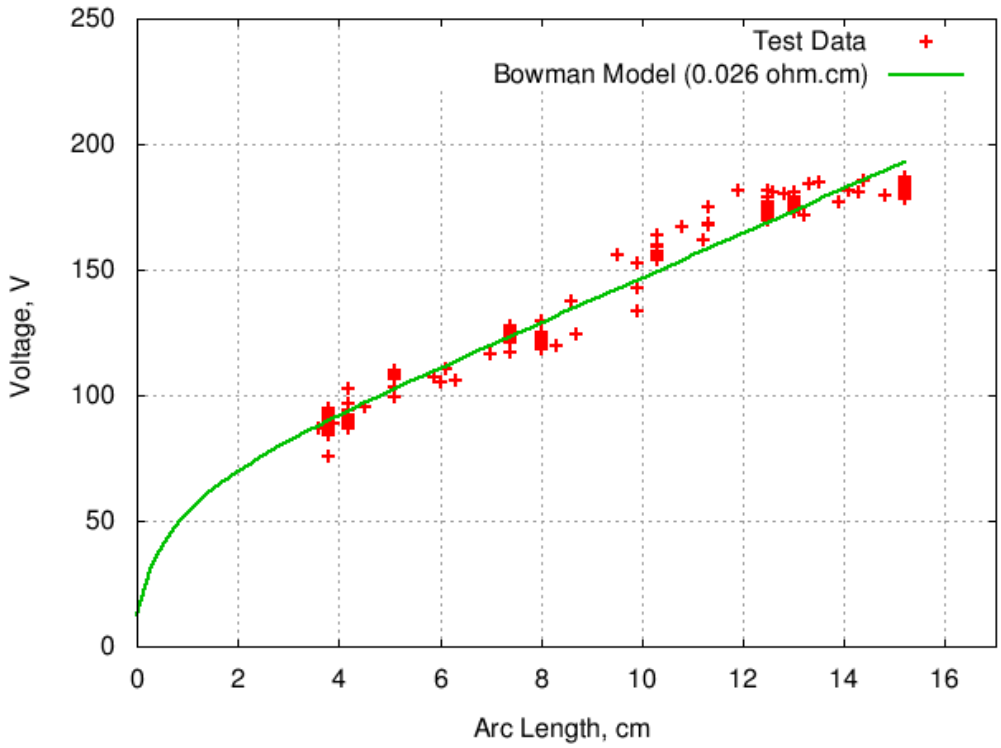

Figure 4.6 Example data set showing the fitting of arc resistivity to voltage measurements as a function of arc length, at constant current

In addition to the verification of the model that was provided by Bowman himself, further confirmation of the validity of the model can be found by noting the good qualitative agreement between the shape of the theoretical curves for voltage versus arc length (as shown in Figures 4.5 and 4.6), and the recently published measured curve for voltage versus arc length obtained from an industrial 60 MW furnace producing ferrochromium, shown in Figure 4.7 (Sager *et al.*, 2010). Publication of this sort of industrial data is extremely rare. Even though the current is not

specified, and no scale is given for the arc length (indicated by the electrode position), this set of data remains valuable.

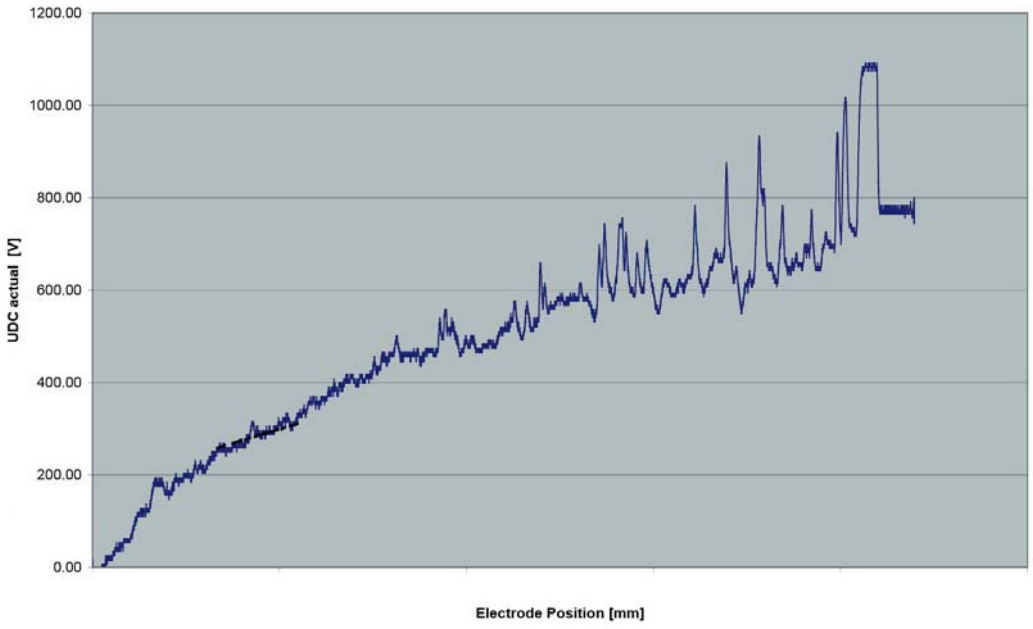

Figure 4.7 Measured arc voltage as a function of arc length at a constant current and fixed DC reactor impedance, obtained from an industrial 60 MW DC arc furnace producing ferrochromium. This figure from Sager *et al.* (2010) is re-published here with permission.

4.4 Interaction of the Arc With Molten Slag

The arc jet is known to be a high-velocity turbulent self-constricted jet (Bowman 1982; Bowman 1990). In the same way that a jet of compressed air can displace water, so it is reasonable to expect that a plasma arc should be able to displace some of the slag onto which it impinges. Of course, the real question is: how much is displaced?

The force generated by the impingement of such a jet on a dense deformable medium can be very significant, even at pilot-plant scale, and tends to create a cavity at such an interface. The arc-attachment zone

(AAZ) at the slag surface is therefore not treated as a flat surface but as a depressed cavity of paraboloidal shape, as suggested by Bowman (1994).

Based on the work of Maecker (1955), Bowman and Krüger (2009) show that the axial force of the arc is proportional to the square of the current, with a constant of proportionality of $(\mu_0/4\pi) \times \ln(r_a/r_k)$, where μ_0 is the permeability of free space (defined as $4\pi \times 10^{-7}$ kg.m.s^{-2}.A^{-2}), and the ratio of the arc radius (r_a) to the cathode-spot radius (r_k) is given by Equation [4-1]. For sufficiently long (*i.e.*, fully developed) arcs, (r_a/r_k) has a value of 3.2, and $\ln(r_a/r_k)$ has a value of 1.16. Bowman (1994) uses this form of the equation to describe the thrust of the arc. This results in Equation [4-5], which shows the thrust of the arc to be proportional to the square of the current. For sufficiently long arcs:

$$T = 0.116\, I^2 \qquad [4\text{-}5]$$

where:
T = arc thrust, N
I = arc current, kA

In an earlier paper, Bowman (1972) used an empirically fitted constant of 0.15 instead of the 0.116 used above, which is the currently accepted value.

Assuming that the shape of the cavity is a paraboloid with radius r and height or depth h, the volume V of the displaced slag may be expressed as:

$$V = \frac{\pi}{2} r^2 h \qquad [4\text{-}6]$$

The thrust of the arc may be equated to the buoyancy force generated by the absence of slag from the cavity (*i.e.*, the volume multiplied by the slag density and gravitational acceleration).

$$0.116\, I^2 = \frac{\pi}{2} \rho\, g\, r^2 h \qquad [4\text{-}7]$$

where:

ρ = slag density, kg/m^3

g = standard gravitational acceleration, 9.81 m/s^2

One further constraint needs to be imposed on these two dimensions, in order to specify fully the size of the cavity, as a function of the arc current. A relationship between *h* and *r* can either be specified *a priori* or fitted to experimental data. It is understood that the depth cannot reasonably be expected to exceed the diameter of the depression in a stable cavity. Visual assessment and measurements from numerous still and video images such as Figure 4.8 allow one to make a quantitative estimate (albeit a somewhat subjective one) of the typical diameter to depth ratio of the arc depression. At least this allows upper and lower bounds to be placed on this ratio, and 6:1 is judged to be the most representative value. The images shown in Figures 4.9 to 4.11 illustrate the different types of depression that may be obtained under different circumstances.

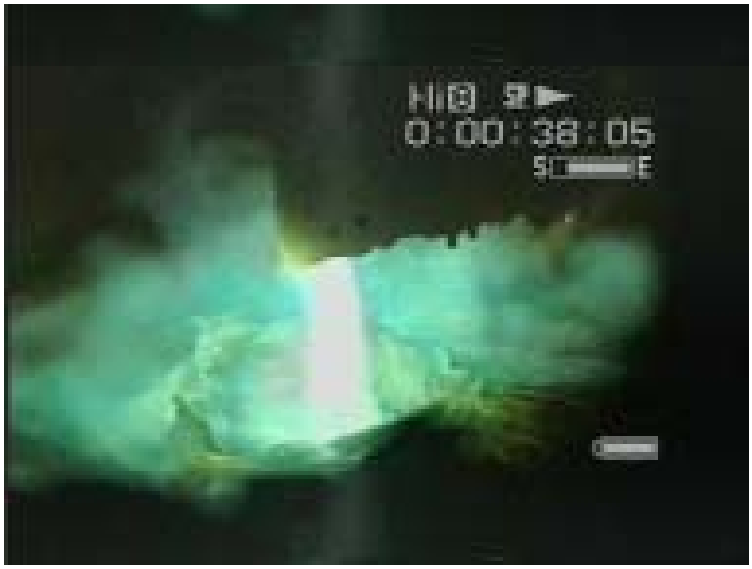

Figure 4.8 Clear image of arc depression at 2.9 kA (Image F00878)

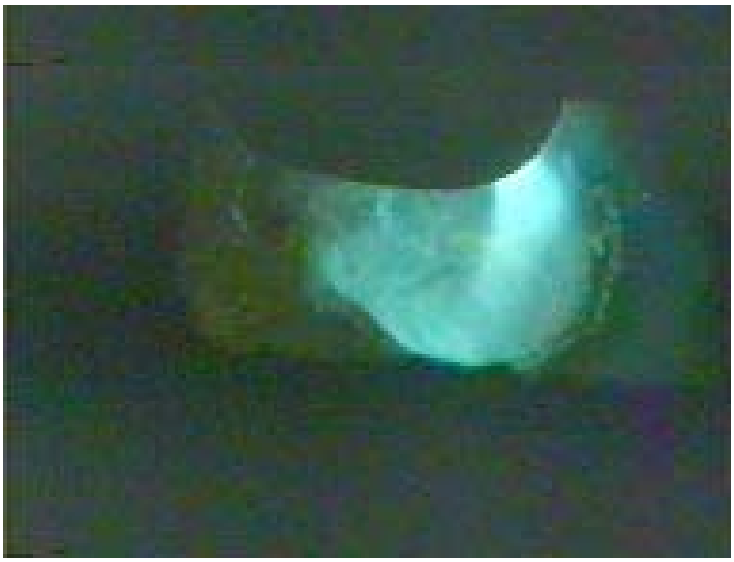

Figure 4.9 Arc depression (Image C0833)

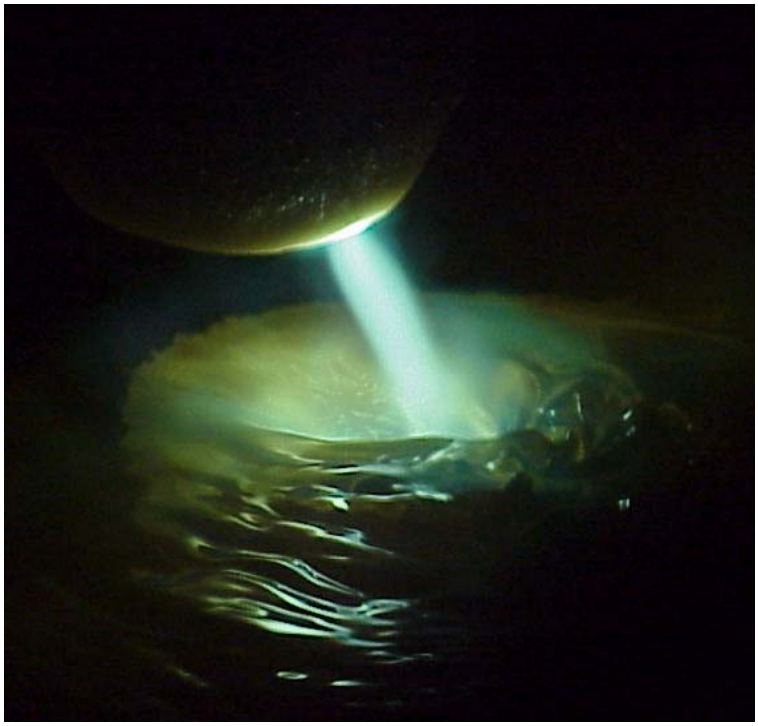

Figure 4.10 'Punched hole' arc depression (Image FL025)

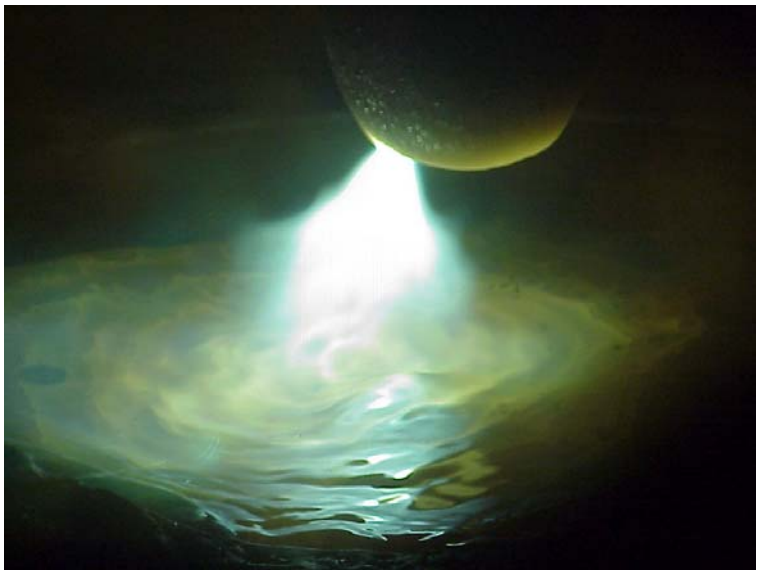

Figure 4.11 'Smeared' arc depression (Image FL028)

According to Bowman (1994), depressions in liquids take about 10 to 100 ms to form. Figure 4.12 shows two depressions existing simultaneously, where the arc has jumped to a new position before the previous depression has had a chance to die away.

Figure 4.12 Two arc depressions existing simultaneously; current = 2.6 kA (Image L00683)

In the past, there has been much speculation about the behaviour of high-current arcs, as some features, such as thrust, depend on the square of the current. Industrial-scale arcs are very difficult (sometimes even dangerous) to photograph, and, in many furnaces, the arc is never visible. Fortunately, video images the author was able to take of the high-current arc in an industrial steelmaking furnace at Charter Steel in Wisconsin showed very similar behaviour (in terms of the type of movement of the arc, the spread of the arc from the tip of the electrode, and the formation of a depression in the slag) to the pilot-scale arcs previously photographed. Some sample images are shown in Figure 4.13.

Figure 4.13 Industrial steelmaking arc at 40 kA, 450 V (Full power is at 70 kA, 550 V)

If we introduce the variable ψ to represent the diameter to depth ratio of the arc attachment zone (the depression in the slag caused by the thrust of the arc), it follows directly from Equation [4-7] that the shape of the cavity is defined by the formulae for the diameter (d_{AAZ}) and depth (h_{AAZ}) in Equations [4-8] and [4-9] respectively.

$$d_{AAZ} = \left(\frac{0.928\psi}{\pi \rho g} \right)^{\frac{1}{3}} I^{\frac{2}{3}} \qquad [4\text{-}8]$$

$$h_{AAZ} = \frac{d_{AAZ}}{\psi} \qquad [4\text{-}9]$$

where:

ψ = diameter to depth ratio = d_{AAZ} / h_{AAZ}

Figure 4.14 shows the dimensions of the arc cavity that is formed, under different assumptions of the diameter to depth ratio. A ratio of 6:1 is based on our assessment of typical arc depressions seen in photographs of arcs from the Mintek pilot plant, and a ratio of 1:1 is the stability limit (Cheslak *et al.*, 1969) for gas jets impinging on liquid surfaces.

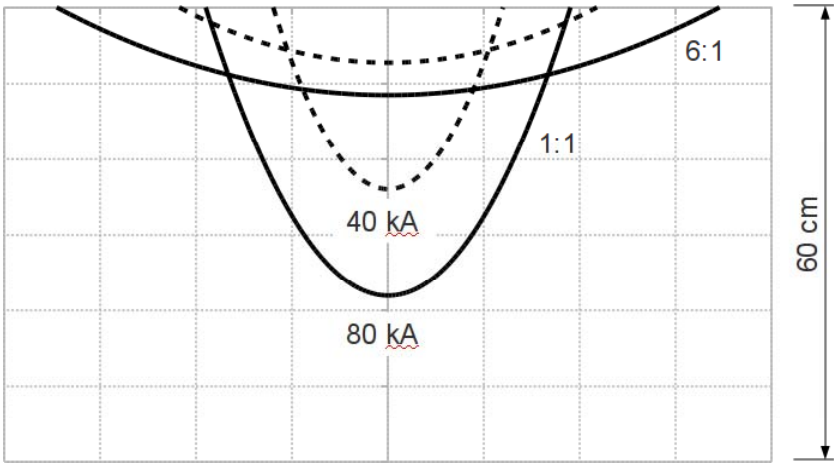

Figure 4.14 Dimensions of the cavity formed by arc jet thrust at different diameter: depth ratios, in the case of a current of 40 kA (dotted lines) or 80 kA (solid lines) and a slag density of 3500 kg/m^3 and thickness of 60 cm

The 1:1 ratio is an extreme case, and the 6:1 ratio is more likely. For slags of reasonable density and moderate depths (typically around 60 cm), it is very unlikely that all of the slag is blown away by the arc, even when the current is very high.

4.5 Electrical Modelling of the Molten Slag Bath

The voltage across the slag bath in a DC-arc smelting furnace can contribute significantly to the overall furnace voltage (especially where the slag is highly resistive), thus impacting on the power supply design and control characteristics of the furnace. A model describing the electrical behaviour of the furnace slag bath has obvious applicability.

It is important to have a relatively accurate prediction of the voltage across the slag before specifying the power supply of a new industrial furnace. An incorrect specification can cause the failure of the process, and an over-conservative specification that will guarantee operation over a wide range of conditions may unnecessarily add significantly to the purchase price of the transformer.

The slag bath would be easy to model electrically if it was known to have a flat surface and a uniform conductivity, and if the potential distribution at the upper surface was well understood. A small zone of constant high potential could be envisaged where the arc impinges on the surface, and a zero potential could be envisaged across the bottom surface of the bath where it is in contact with molten metal across the diameter of the furnace. The Laplace equation (see below) could then be solved to obtain the potential distribution. However, in reality, the impingement of the arc causes a depression in the surface of the slag. This has to be taken into

account in the model, as it can alter the geometrical current distribution quite significantly.

The slag bath in a DC smelting furnace typically behaves as an ohmic conductor, unlike the arc that is extremely non-linear. To model the bath's electrical behaviour with a fair degree of accuracy, a two-dimensional axi-symmetric numerical model is used which describes the variation of the potential (voltage) through the bath. The model requires the solution of Laplace's equation for potential. In Equation [4-10], *r* indicates radial distance from the centre-line, and *z* indicates the vertical position.

$$\frac{1}{r}\frac{\partial}{\partial r} r \frac{\partial V}{\partial r} + \frac{\partial^2 V}{\partial z^2} = 0 \qquad [4\text{-}10]$$

This partial differential equation governs the potential distribution in a material of uniform electrical conductivity, and is solved numerically, using Patankar's (1980) finite-volume method.

Figure 4.15 shows the geometry of the furnace as used by the electrical model. This vertical cross-section showing half of the slag bath in the furnace has AE as the centre-line. Section AB is parabolic in shape, representing the paraboloidal cavity of the arc-attachment zone (AAZ) formed by the impinging plasma arc, where the plasma arc attaches electrically to the surface of the slag. One possible approach to solving the voltage distribution would be to specify the current, *I*, and apply this as a potential-gradient boundary condition across this surface. However, the method actually used for the calculation sets an arbitrary constant-voltage boundary condition on AB (in order to improve convergence of the iterative solution). This voltage is then corrected to its true value, after the calculation, by calculating the current across the lower boundary DE, and

adjusting the arbitrary voltage by the ratio of the calculated to the specified current. Section BC represents the upper surface of the liquid slag, and is taken to be electrically insulating. Section CD represents the furnace side-wall, also assumed to be electrically insulating. Section DE is the interface between the slag bath and the metal pool, which is taken to be at ground or anode voltage, $V = 0$. Section EA is the centre-line of the furnace.

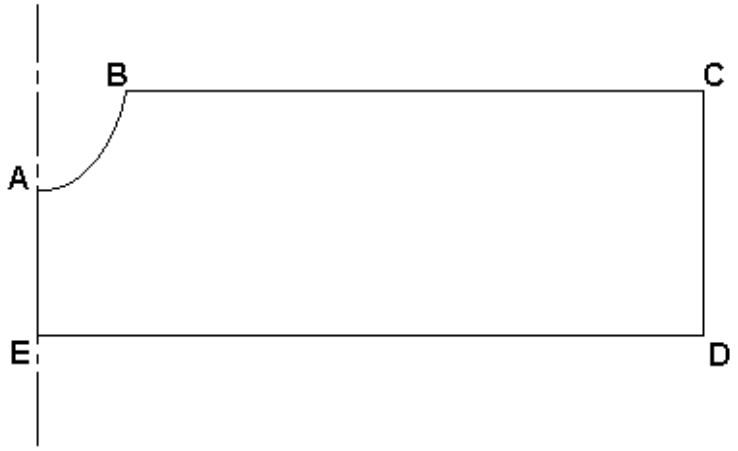

Figure 4.15 Geometry of axi-symmetric furnace bath

The boundary conditions are listed below.

$$\text{AB: } V = \text{constant} \qquad [4\text{-}11a]$$

$$\text{BC: } \frac{\partial V}{\partial z} = 0 \qquad [4\text{-}11b]$$

$$\text{CD: } \frac{\partial V}{\partial r} = 0 \qquad [4\text{-}11c]$$

$$\text{DE: } V = 0 \qquad [4\text{-}11d]$$

$$\text{EA: } \frac{\partial V}{\partial r} = 0 \qquad [4\text{-}11e]$$

For the parabolic cavity, shown as AB, it is required to assume some relationship between the diameter and depth of the depression at a given current. As explained in the previous section, based on a number of

photographs, a ratio of diameter to depth of around 6:1 is assumed. This ratio is fairly pivotal in the behaviour of the potential-theory model of the slag bath, and, as it is a largely empirical number, some further comments are justified. The shape of the depression is affected by two factors—the hydrodynamic stability of the liquid slag in which it is formed, and the motion of the plasma arc. According to Cheslak *et al.* (1969), the large body of experimental and theoretical work that exists in the field of gas jets impinging on liquid surfaces suggests that a ratio less than 1:1 for the depression shape would be unsustainable. In addition, the fact that the arc itself is constantly in very rapid motion over the surface of the slag means that the thrust it produces is 'smeared' over a larger area than just the diameter of the jet. The number of 6:1 provides a good empirical fit to the electrical data while remaining consistent with both the theoretical understanding of arc and gas jet behaviour and the photographic evidence gathered on pilot furnaces operating in the range of 1–10 kA.

A simple analysis of the sensitivity of the model to the diameter to depth ratio for an example furnace is shown in Figure 4.16. In this figure, the calculated furnace voltage is shown as a function of the depression shape (diameter / depth ratio) for an example pilot-scale DC arc furnace (5 kA current, 2 m internal diameter, 30 cm slag depth, 20 cm arc length, 1.0 Ω cm slag resistivity, and 0.0175 Ω cm arc resistivity). The calculated voltage is seen to vary from about 340 V to about 380 V.

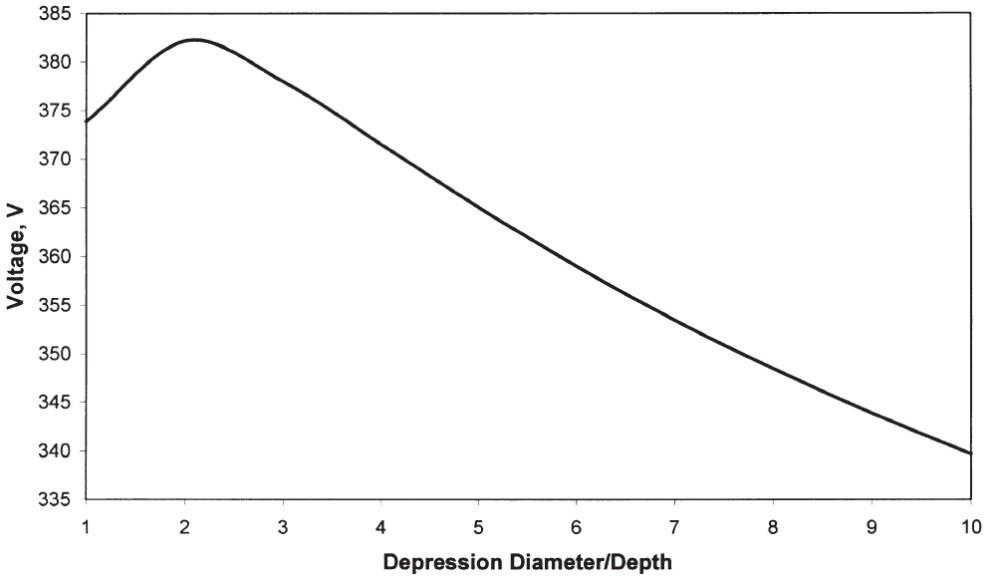

Figure 4.16 Plot of furnace voltage versus depression shape ratio for an example pilot-scale DC arc furnace (5 kA current, 2 m internal diameter, 30 cm slag depth, 20 cm arc length, 1.0 Ω cm slag resistivity, and 0.0175 Ω cm arc resistivity)

To better illustrate the results from the numerical solution of the Laplace equation, Figure 4.17 shows an example calculation of the current distribution in a 60 MW furnace. In this example, it can be seen that the current is strongly concentrated towards the centre of the furnace, with about 10% of the current flowing through the area directly underneath the electrode, most of the current flowing through the central region of the slag bath, and very little current flowing through the outer extremities. This concentration of current in the arc-attachment zone, results in nearly all of the resistive heating taking place in this area.

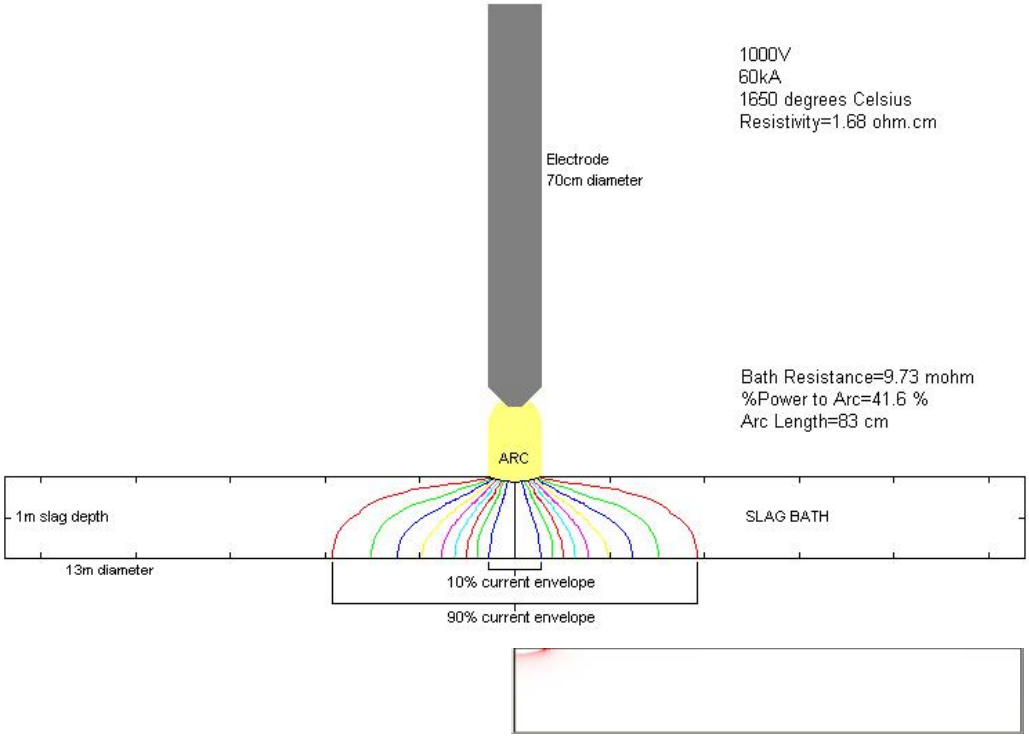

Figure 4.17 Example calculation for a 60 MW furnace, showing the current distribution and the bath power dissipation (with almost all of the resistive heating taking place directly underneath the arc-attachment area)

4.5.1 Effect of furnace diameter

From the current distribution shown in Figure 4.17, it is not surprising that, for all practical (sufficiently wide) aspect ratios, the diameter of the molten slag bath has very little effect on the bath voltage.

Figure 4.18 illustrates the variation of bath voltage with the diameter of the furnace bath, for the case of a current of 10 kA. The slag resistivity is 1 Ω.cm, the bath depth is 50 cm, the usual assumed value of 6:1 was used for the diameter:depth ratio of the arc depression, and the slag density was taken to be 3500 kg/m^3. As the furnace diameter increases, the bath voltage tends towards a fixed value, as less and less current spreads to large radial distances.

In this example, there is less than 0.2% difference in the calculated bath voltage when comparing diameters of 2 m or 4 m, and even if the diameter was 1 m (*i.e.*, in the unlikely case of the depth being equal to the radius) the bath voltage would be only 6.5% greater than if the diameter was 4 m, and a diameter of 1.5 m would increase the bath voltage by about 1% relative to a diameter of 4 m or greater.

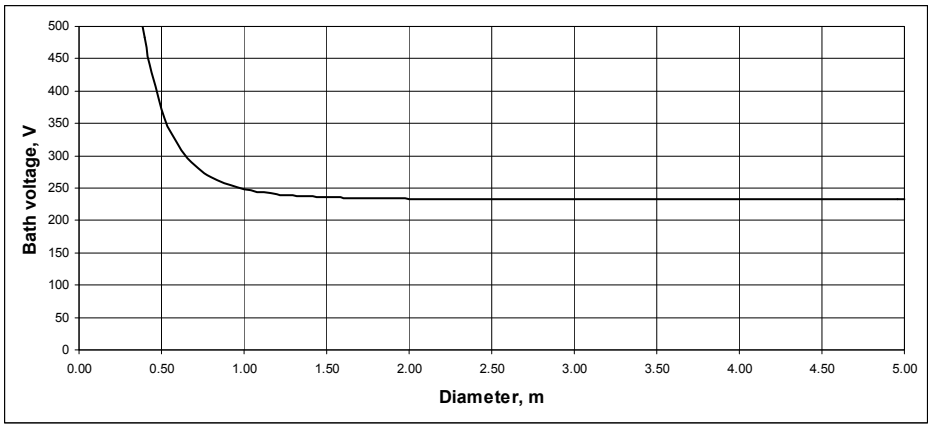

Figure 4.18 The variation of bath voltage with furnace diameter, (slag resistivity is 1 Ω.cm, current is 10 kA, bath depth is 50 cm)

4.5.2 Effect of slag depth

Figure 4.19 shows the variation of bath voltage with slag depth. The slag resistivity is 1 Ω.cm, and the usual assumed value of 6:1 was used for the diameter:depth ratio of the arc depression, and the slag density was taken to be 3500 kg/m^3. At low currents, the bath depth has very little effect on the bath voltage, but the effect becomes more pronounced at higher currents.

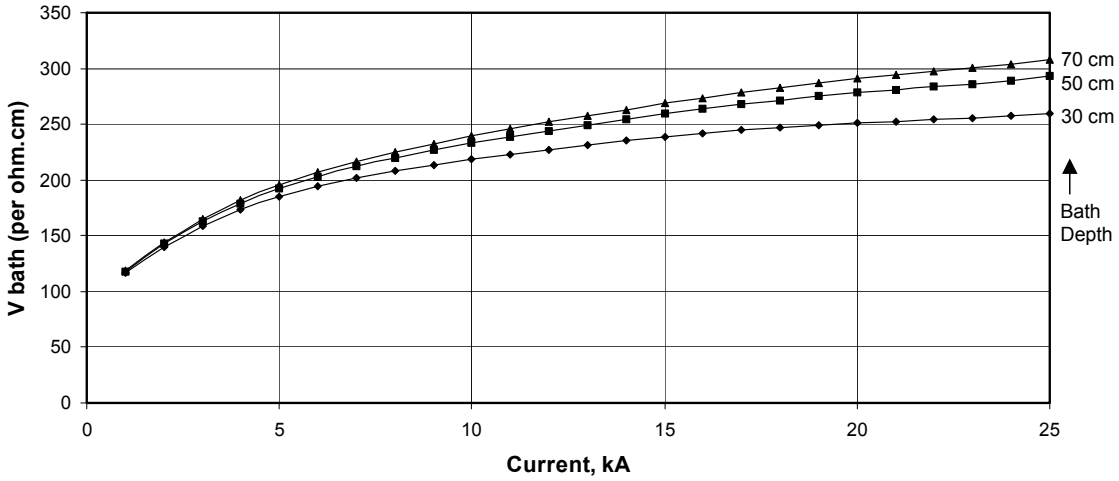

Figure 4.19 The variation of bath voltage with slag depth, for 'sufficiently wide' DC arc furnaces, with a 6:1 diameter:depth ratio of the arc depression, and a slag density of 3500 kg/m^3

4.6 Non-linear Electrical Behaviour of DC Arc Furnaces

The design of DC power supplies for the steel melting industry often makes use of the assumption that the furnace has an approximately constant resistance. This of course leads to a directly proportional relationship between voltage and current. In traditional circuit models, the DC arc is also often presented as a constant-voltage device, showing no dependence on current at all. In contrast to this, our modelling and experimental work has shown that a DC smelting furnace is a more non-linear type of conductor. Figure 4.20 shows an example of the relationship between voltage and current for a range of different arc lengths according to the models developed above.

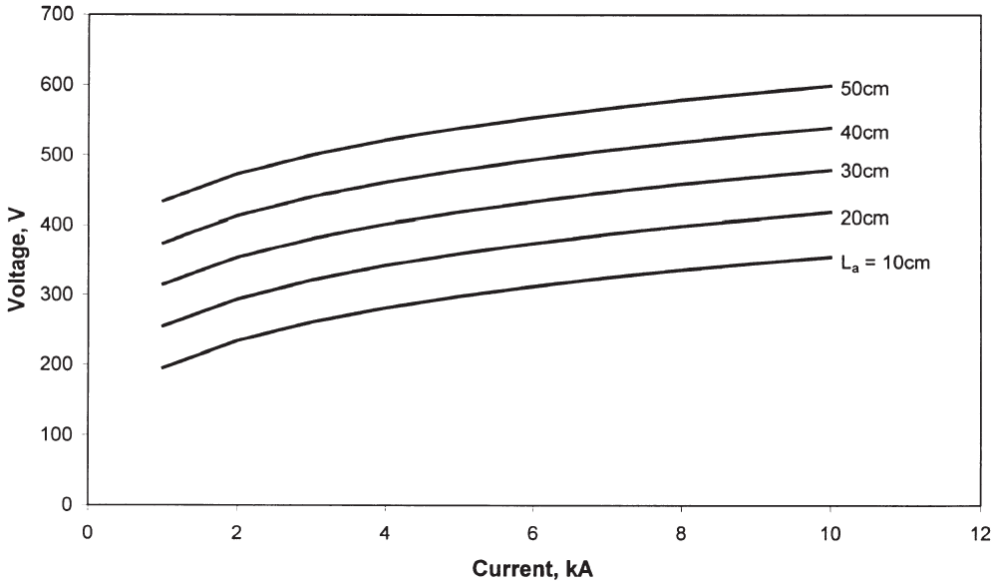

Figure 4.20 Plot of furnace voltage versus current for an example pilot-scale DC arc furnace (2 m internal diameter, 30 cm slag depth, 1.0 Ω cm slag resistivity, and 0.0175 Ω cm arc resistivity)

In summary, the electrical behaviour of a DC arc furnace may be modelled as an arc in series with a layer of slag. The arc has a particular resistivity for a given gas composition and temperature. For example, a value of 0.015 to 0.020 Ωcm is typical for a furnace atmosphere rich in carbon monoxide at a temperature around 1600°C. Following the approach of Bowman (1994), the voltage across the arc is modelled as a function of arc length and current (Jones *et al.*, 2002). The voltage across the slag is calculated by solving the Laplace equations for the assumed geometry of the slag (with the arc depression taken into account) and an assumed distribution of current at the upper surface (Reynolds & Jones, 2004). The slag bath voltage is directly proportional to the resistivity of the slag (which is, in turn, a function of composition and temperature). It is important to note that the voltages across the arc and the slag are both non-linear with current.

Figure 4.21 shows the relationship between voltage (V) and current (I) for a hypothetical 70 MW furnace operating with a fixed slag depth and arc length. The constant-power curve is hyperbolic in shape, resulting from the relationship $P = V\,I$. Constant-resistance lines, resulting from the relationship $V = I\,R$, are shown in the diagram in order to contrast with the calculated shape of the actual relationship between voltage and current. The lowest of the non-linear curves illustrates the behaviour of the arc on its own (*i.e.*, equivalent to a slag with zero resistivity), and the other two curves show the additional voltage resulting from slags of different resistivities (1 and 2 Ωcm respectively).

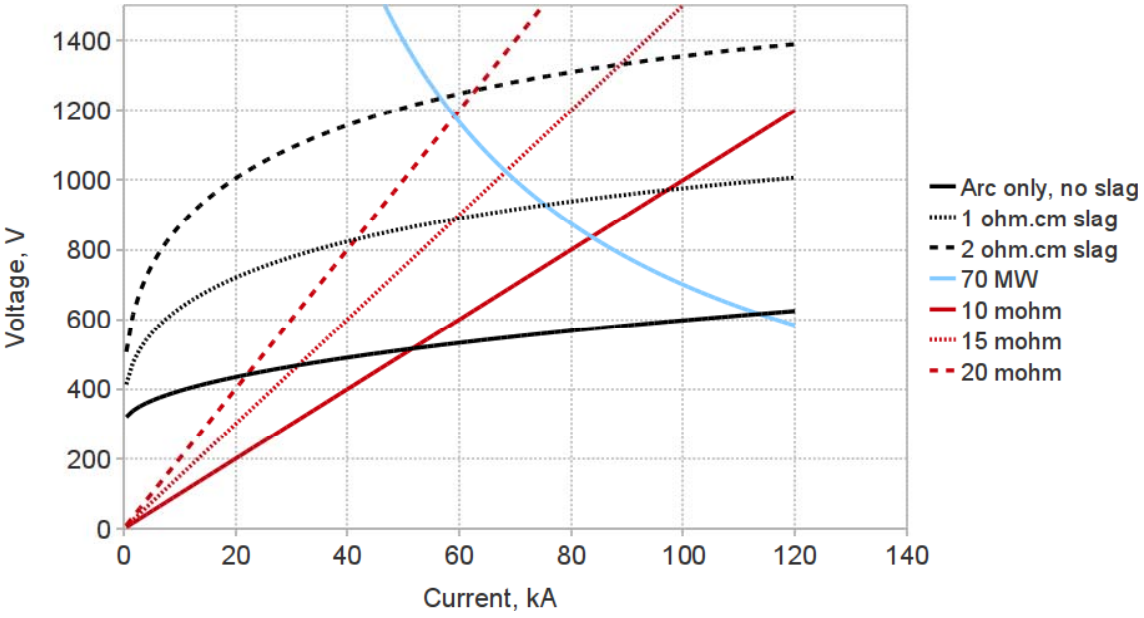

Figure 4.21 The relationship between voltage and current for an industrial-sized furnace operating at a fixed arc length of 50 cm and with a slag depth of 60 cm (for an arc resistivity of 0.0175 Ωcm)

Of course, the ultimate question of whether a DC arc furnace is a constant-resistance device would be answered conclusively by plotting voltage versus current (for a fixed set of conditions including arc length, bath depth, composition, and temperature) for an industrial furnace running from low to high current. The publication of such data is eagerly awaited.

Even though we have argued that the DC arc furnace is not a constant-resistance device, one should also keep in mind that DC arc furnaces are often powered by thyristor rectifiers, which allow for very fast and automatic adjustment to short-term variations in furnace conditions and enable the furnace to be operated at a specific resistance set-point, if this method of control is selected.

4.7 Scale-Up and Design of DC Arc Furnaces

The design of the power supply for a DC arc furnace needs to take into account possible variations in arc length, slag depth, and slag resistivity (which is affected by slag composition and temperature). A number of voltage – current relationships need to be plotted, taking into account the range of variables being designed for, and a suitable operating window can then be specified.

Measurements of arc resistivity and slag resistivity allow one to undertake the calculations necessary to specify the electrical requirements of industrial power supplies for DC arc furnaces. An example of this sort of work is shown in Figure 4.22.

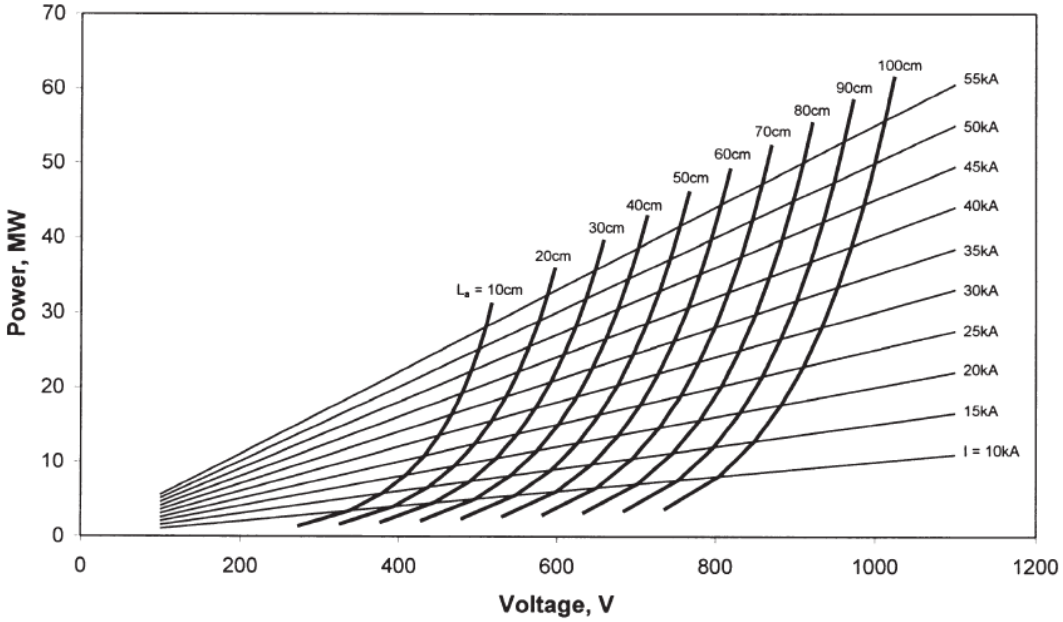

Figure 4.22 P V design plot for an example DC arc furnace (10 m internal diameter, 50 cm slag depth, 1.0 Ω cm slag resistivity, and 0.015 Ω cm arc resistivity)

The theoretical model introduced above has been used extensively to improve the understanding of the operation of pilot-plant furnaces at Mintek, and for the specification of the electrical parameters of a number of industrial furnaces. We have already noted the good qualitative agreement between the shape of the theoretical curves for voltage versus arc length, and the measured curve for voltage versus arc length obtained from an industrial 60 MW furnace producing ferrochromium, shown in Figure 4.7 (Sager *et al.*, 2010).

4.8 Design Equations for Arc and Bath Voltages

We have seen that the bath voltage is a rather complicated function of current and the geometry of the slag bath, including that of the arc depression. The bath voltage needs to be solved numerically, and it is not practical to express the relationship as an analytical solution to the Laplace equation. However, there are some simplifications that can be made to

develop a practical design method. Figure 4.19 showed a series of voltage-current curves where the usual assumed value of 6:1 was used for the diameter:depth ratio of the arc depression, and the slag density was taken to be 3500 kg/m^3 (where these two numbers determine the geometry of the depression in the slag in the arc-attachment zone, relative to the rest of the furnace dimensions). For many furnaces, it is justifiable to assume a 'sufficiently wide' furnace diameter, as shown in Figure 4.18.

In order to model the overall voltage (arc voltage plus bath voltage), it is useful to combine the graph of arc voltage (as a function of current and arc length) with that of bath voltage (as a function of current and bath depth), as shown in Figure 4.23. In both cases, the voltage is directly proportional to the resistivity. The arc voltages are plotted for an arc resistivity of 0.0175 Ω.cm, as this is a typical figure for a wide range of reductive smelting processes where carbon is used as a reductant. The bath voltages are plotted for a slag resistivity of 1 Ω.cm.

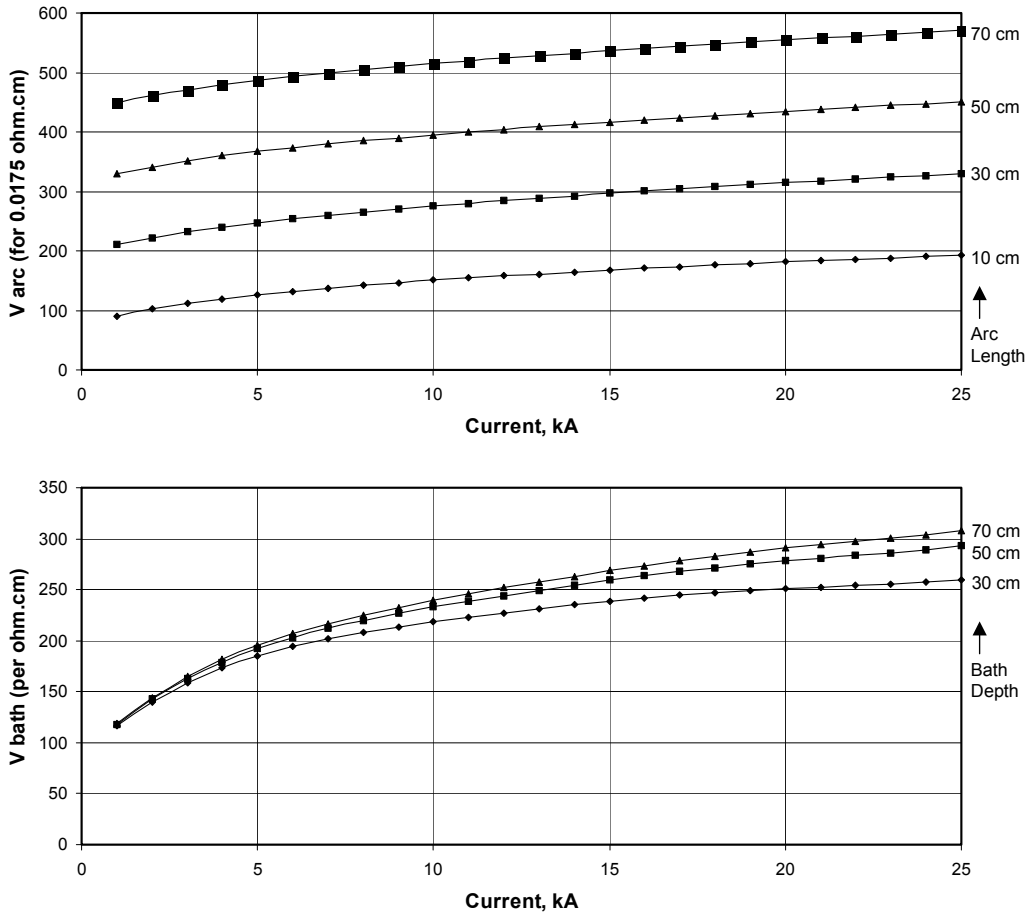

Figure 4.23 Design curves for arc and bath voltages (proportional to resistivity) for 'sufficiently wide' DC arc furnaces, with a 6:1 diameter:depth ratio of the arc depression, and a slag density of 3500 kg/m^3

For the range of currents shown in Figure 4.23 (namely 1 to 25 kA), it has been found that a polynomial of degree five fits each of the curves indistinguishably from those modelled and drawn above. Using quintic regression, and the assumptions listed above (including that of a 'sufficiently wide' furnace diameter), the arc voltage V_a (for an arc resistivity of 0.0175 Ω.cm) and the bath voltage V_b (for a slag resistivity of 1 Ω.cm) can be well represented by Equations [4-12] to [4-18], where I represents current in kA, for the range 1 to 25 kA. As the actual voltages in a particular furnace are directly proportional to the respective electrical

resistivities, it is straightforward to calculate the arc and bath voltages for other values of arc and slag resistivity.

For an arc length of 10 cm:

$$V_a = 77.0 + 14.925I - 1.37451I^2 + 0.086072I^3 - 0.00279I^4 + 0.000036I^5 \quad [4\text{-}12]$$

For an arc length of 30 cm:

$$V_a = 196.6 + 14.804I - 1.26651I^2 + 0.079967I^3 - 0.00262I^4 + 0.000034I^5 \quad [4\text{-}13]$$

For an arc length of 50 cm:

$$V_a = 316.3 + 14.809I - 1.26845I^2 + 0.080270I^3 - 0.00263I^4 + 0.000034I^5 \quad [4\text{-}14]$$

For an arc length of 70 cm:

$$V_a = 435.9 + 14.809I - 1.26844I^2 + 0.080264I^3 - 0.00263I^4 + 0.000034I^5 \quad [4\text{-}15]$$

For a bath depth of 30 cm:

$$V_b = 86.45 + 33.507I - 3.82721I^2 + 0.253611I^3 - 0.00847I^4 + 0.000110I^5 \quad [4\text{-}16]$$

For a bath depth of 50 cm:

$$V_b = 86.67 + 34.747I - 3.78023I^2 + 0.248784I^3 - 0.00828I^4 + 0.000107I^5 \quad [4\text{-}17]$$

For a bath depth of 70 cm:

$$V_b = 86.78 + 35.253I - 3.73702I^2 + 0.243752I^3 - 0.00805I^4 + 0.000103I^5 \quad [4\text{-}18]$$

4.9 Dynamic Modelling and High-Speed Photography of Arcs

A commonly held view is that the arc inside a DC arc furnace is a steady-state phenomenon. In literature on the subject, the arc column is often shown as having a cylindrical, symmetric shape and taking the shortest

path between the end of the electrode and the surface of the molten bath beneath. Many of the mathematical and numerical modelling methods (including the models used in this chapter) used to study plasma arcs also propagate this impression by discarding the time-dependent terms in the governing equations, and using cylindrical coordinate systems which impose symmetry on the system.

Observations of real arcs (as illustrated in Figures 4.24 to 4.28) reveal erratic instabilities and chaotic motion. Sometimes, a helical pattern appears as a precursor to full instability. There are also periods when the arc becomes diffuse and appears to be spread over the entire electrode tip. Clearly, the time-average of this non-steady behaviour has a significant bearing on the properties of the arcs.

Figure 4.24 Arc about to become unstable

Figure 4.25 'Pretzel-shaped' arc in air on a graphite block

Figure 4.26 Diffuse 7 kA arc onto slag

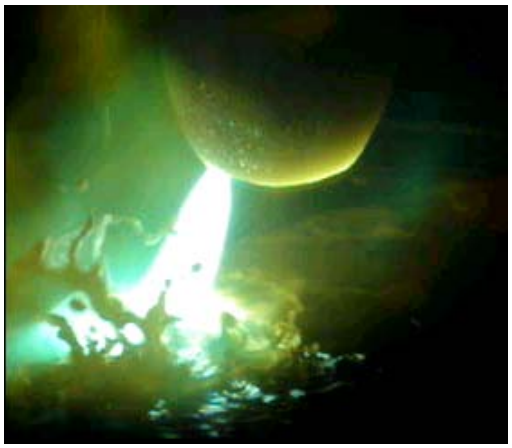

Figure 4.27 Violent splashing at 2 kA (Image L16354)

Figure 4.28 Thicker arc with splashing at 8.1 kA

Additional variables come into play when the arc is enclosed in a hot re-radiating furnace vessel, and when the arc is struck on a molten surface that deforms and splashes. The changing shape of the depression in the liquid surface provides a rapidly changing geometrical arrangement that encourages the arc to move to new, shorter, more conductive paths. In moving to a new position, the arc moves extremely rapidly across the tip of the electrode. Figure 4.29 shows two successive images (one fiftieth of a second apart) in which the arc has moved from one side to the other of a 20 cm diameter electrode.

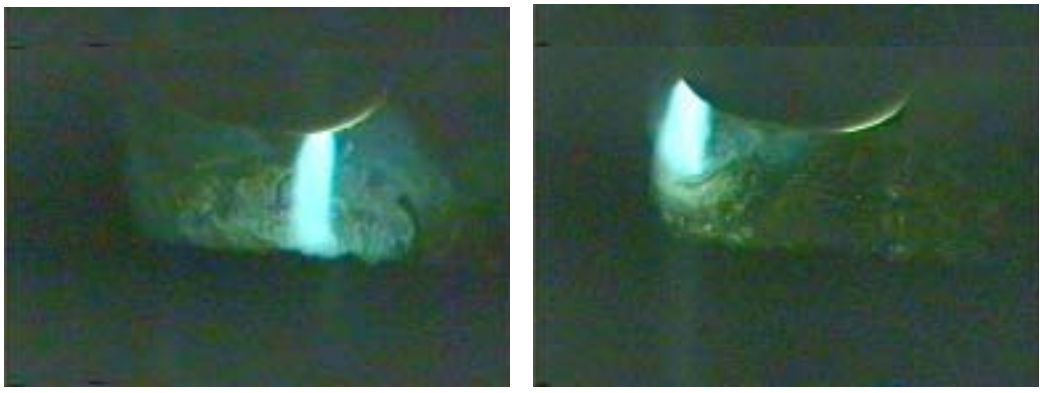

Figure 4.29 Rapid arc movement in two successive images 1/50 s apart (Images C0935 and C0936)

Multiple 'simultaneous' arcs have been observed and recorded (see Figures 4.30 and 4.31), but it would have needed a higher speed camera to ascertain whether these arcs are truly simultaneous or whether they occurred sequentially during the exposure period, which is usually set to less than 1/50 s because of the high intensity of the arc.

Figure 4.30 Two images (a few minutes apart) showing two arcs 'simultaneously' (Images C0792 and C1225)

Figure 4.31 Three 'simultaneous' arcs (total current = 2 kA)

The photographic work presented here includes a number of images taken using a standard digital still camera as well as with a standard camcorder. Welding filters were used to reduce the intensity of the light to manageable levels. The video images were captured at a rate of 25 frames per second (at a resolution of 768 x 576 pixels), but by separating the odd and even scan lines of the interlaced PAL video image, the frame rate was

effectively doubled to 50 frames per second. Much higher filming speeds, with very little delay between successive frames, would be needed in order to capture some of the faster phenomena. High performance digital video cameras may capture images at rates from 1 000 to 60 000 frames per second. This would enable the imaging of phenomena that happen in a millisecond or less to be analysed in detail. Short exposure times permit the digital video camera to capture extremely fast-moving objects on each frame of the video. Classically, high-speed photography used to be performed with the aid of strobe lighting, which gave exposure times down to fractions of a millisecond. With the modern electronics available in high-speed digital video cameras, exposure times of as low as 10 microseconds are available without the need for high-intensity strobes that would otherwise be required to freeze events that are evolving rapidly in time. High-resolution images, up to 1024 x 1024 pixels in size, available in modern CMOS-design digital video cameras, provide sufficient detail for accurate image analysis and tracking of small-scale features from frame to frame.

Early photographic work (Jones *et al.*, 2002) in this area made use of consumer-class photographic equipment, and, due to the extremely short time scales characteristic of plasma arc motion (< 1 ms), much of the detail in the dynamics of the arc motion remained unobserved. These early photographs provided some useful insights, but it became clear that higher shutter speeds and frame rates were required to capture the subtlety and complexity of arc behaviour. More recently, an Olympus iSpeed 3 high-speed digital video camera has been used to capture images of the arc column at between 5 000 and 30 000 frames per second in order to resolve the dynamic behaviour sufficiently. (The camera is capable of capturing images at up to 2 000 frames per second at a resolution of 1280

by 1024, and up to 150 000 frames per second at reduced resolution. In addition, 'shutter speeds' as short as 1 μs can be used.)

This work on high-speed arc photography has been continued to great effect by my colleague Quinn Reynolds (Reynolds & Jones, 2010; Reynolds, 2012b), and has been complemented by dynamic modelling and, more recently, high-speed electrical measurements (Reynolds *et al.*, 2014).

Some excellent dynamic arc modelling work has been done by Reynolds (2009; Reynolds *et al.*, 2010; Reynolds & Reddy, 2011), where the tightly coupled multi-physics nature of the DC plasma arc problem was modelled by deriving then simultaneously solving the mathematical relationships governing the fluid dynamics, energy transfer, and electromagnetic fields occurring in arcs. Reynolds has shown (Reynolds *et al.*, 2010) that plasma arc models developed using explicit time dependence and Cartesian coordinate systems are able to display a wide range of dynamic motion and asymmetric behaviour, with the arc column becoming twisted and deformed into complicated irregular shapes over very short time scales (milliseconds or less). A noteworthy feature of this modelling and photographic work is that it has uncovered a number of features of arc behaviour that were initially thought to be numerical artefacts (because they are not visible to the naked eye) but were later observed and confirmed using high-speed photography.

The results of various tests were compared with the output from an advanced computational model of the plasma arc, with a number of novel phenomena and transition effects being observed in both sets of results. Helical motion and arc length transition effects, anode arcs, transitions between chaotic and pseudo-steady arc behaviour, and arc

extinguishment have been studied (Reynolds & Jones, 2010; Reynolds, 2012b). Some examples of this work are shown in Figures 4.32 and 4.33, although much of the work is beyond the scope of this present thesis.

The simplest form of dynamic motion observed is a regular precession of the arc jet around its attachment point on the electrode. This results in the arc column taking on a helical shape. As the arc length increases beyond a certain transition point, the movement of the arc becomes more chaotic and irregular. Figures 4.32 (a)-(d) show the behaviour of an arc of length 5 cm. Regular helical oscillations of the arc column can be seen, repeating roughly every four frames. The second sequence, shown in Figures 4.33 (a)-(d), show an arc of length 10 cm exhibiting more chaotic, irregular behaviour.

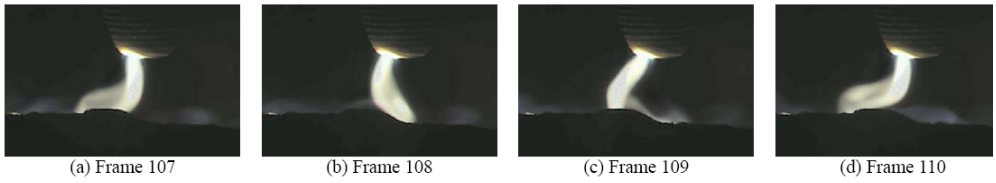
(a) Frame 107 (b) Frame 108 (c) Frame 109 (d) Frame 110

Figure 4.32 Successive frames from a high-speed video sequence showing an arc at 1000 A and 5 cm length, 5000 frames/s, shutter 4 µs

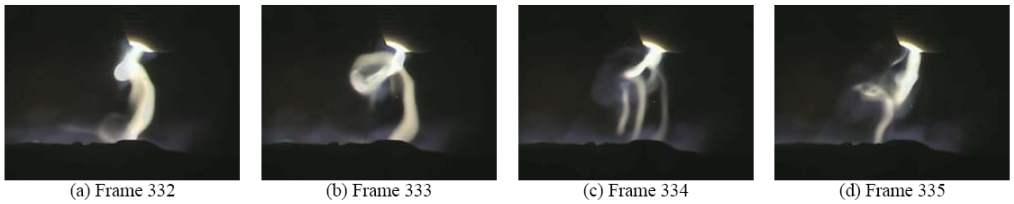
(a) Frame 332 (b) Frame 333 (c) Frame 334 (d) Frame 335

Figure 4.33 Successive frames from a high-speed video sequence showing an arc at 1000 A and 10 cm length, 5000 frames/s, shutter 4 µs

Further photographic and modelling work has also been done on twin-electrode (two graphite electrodes both acting as cathodes) DC smelting furnaces (Reynolds & Jones, 2005) and dual-electrode (one cathode and

one anode) DC furnaces (Reynolds, 2011, 2012a), but this is not included here as the present focus is on furnaces with a single graphite electrode (cathode).

4.10 Conclusions

The power supply is often the item with the longest delivery time when building a furnace, so the voltage and current specifications are often needed at a very early stage of a project. As power supplies are very expensive items, one cannot afford to get the specifications wrong.
The specification of the power supply is one of the principal requirements when an industrial furnace is about to be built, and needs to be in place about twelve to eighteen months before the furnace is to be commissioned. The total power requirement of the furnace is derived from the desired throughput, and the experimentally determined specific energy requirement for the process. The specification of the operating ranges for voltage and current requires a detailed understanding of the scale-up of the furnace design. If the ranges of voltage and current specified for the transformer are greater than necessary, this can result in a great deal of unnecessary expense, and, if the ranges are too low, the furnace might not be operable at all, or it might allow only a very low throughput.

The overall electrical behaviour of a DC arc furnace may be modelled as an arc in series with a layer of slag. In this chapter, equations have been developed (and confirmed by photography and measurement) to describe the electrical behaviour of DC plasma arcs, and the voltage distribution across a molten slag bath.

Based on a corrected version of Bowman's model of arc shape, and his description of the arc voltage (as a function of current, arc resistivity, and

arc length), as well as Maecker's equation for arc thrust, and the Laplace equation for current distribution, an electrical model of the furnace has been constructed that takes into account the arc, the molten slag, and the interaction between them.

A model using measured and extrapolated arc shapes provides a description of how the arc voltage varies as a function of arc length and current. Measurements of voltage as a function of arc length, obtained from an industrial 60 MW furnace producing ferrochromium, provide some confirmation of the validity of this model.

A two-dimensional axi-symmetric numerical model is used to describe the variation of the potential (voltage) through the molten slag bath. The calculation of the voltage distribution across a molten slag bath requires the solution of Laplace's equation for a geometry that includes the depression in the molten slag caused by the impingement of the arc jet. The author was able to provide aspect ratios of the arc depression (based on his photographic work) that enabled these calculations to be performed. The depression in the molten slag caused by the impingement of the arc jet has been photographed to determine a likely range of diameter: depth ratios, and a typical value of 6:1 has been used, showing it to be very unlikely that all of the slag is blown away by the arc, even when the current is very high. These photographs of arcs interacting with molten slag, and the ratios of the dimensions inferred from them, provided the basis for a practical usable electrical model of the arc and the slag bath that can be used for the scale-up and electrical design of DC arc furnaces. In addition to the overall methodology that was introduced for the electrical specification of DC furnace power supplies, perhaps the most significant contribution in this area was the series of difficult-to-obtain

photographs that allowed typical aspect ratios of the arc depression to be determined.

Another important contribution that was made to the electrical modelling of DC arc furnaces was to highlight the fact that the voltage is very non-linear with respect to the current, and that the behaviour is certainly very different from that of a constant-resistance device. Example illustrations of calculations have been presented that show this clearly.

Quintic regression on the numerically calculated results for the bath voltage was used to generate an accurately fitted set of equations to describe the bath voltage in terms of current, slag bath depth, and slag resistivity. Similar equations can be fitted to the arc voltage as well (in terms of current, arc length, and arc resistivity). The resulting set of equations can be used for the practical electrical design of DC arc furnaces.

The photographs and theoretical models introduced here have been used extensively to improve the understanding of the operation of pilot-plant furnaces at Mintek, and have been used for the design of larger furnaces as well. An example application is given in Section 6.11.

5 RESIDENCE TIME

5.1 Factors Influencing the Residence Time Distribution in Continuously-Fed Batch-Tapped Furnaces

There are some processes in which the time spent by the reacting materials in a smelting furnace plays a significant role in determining the extent of the reactions between metal and slag, and influences the degree of settling of metal droplets from a molten slag. Even systems that closely approach chemical equilibrium can require a certain residence time inside the furnace.

In standard textbooks for chemical reactor design, residence time distributions are well defined for batch and continuously stirred reactors. However, there exist many smelting furnaces that do not fit either of these classifications. Here we will focus on producing a mathematical description for the case of a furnace that is fed continuously, but where the liquid slag and metallic products are tapped intermittently. The effects of slag and metal tapping intervals, and the fraction of liquid retained in the furnace, are studied, and are shown to have a significant effect on the residence time distribution.

Previous work (Jones, la Grange, & Assis, 1997) has been done to study the effect of retention time on the degree of cobalt recovery achieved in a slag reduction process. In that work, a method was proposed for the calculation of the mean residence time of the contents of a pilot-plant furnace. Although the method was valid, the contributions of various variables to the residence time were not made sufficiently clear in

equation form. The approach taken in that initial work is extended here (Jones & Reynolds, 2012) for the purposes of providing a more general design or scale-up tool.

The maximum allowable depth of molten material in a given furnace is affected by such factors as the desired batch size (or the size of the ladles) and the pressure of the molten material that the tap-hole and surrounding system can withstand. There may also be some practical limits imposed on the maximum allowable depth of slag by the overall electrical resistance, or by energy transfer considerations. Within these constraints, there might be some scope for choice of tap-hole position. The effects of this choice need to be understood mathematically.

5.2 Mathematical Description

5.2.1 Simplifying assumptions

In real furnaces, the feed material is separated into two phases (such as slag and metal) that may be tapped as separate streams. However, in this chapter, for the purpose of keeping the argument simple and clear, the molten material in the furnace is spoken of as though it was a single phase. This does not diminish the applicability of the resulting equations in any way. In fact, the equations that are developed apply equally to the molten slag or to the molten metal, and can be applied to each of these phases individually.

There are also some circumstances when the equations can be applied to the overall furnace contents as a whole, such as if the metal and slag are tapped at similar times in similar ratios. Alternatively, if the amount of

metal produced is very small, it may be possible to ignore it and apply the equations to the slag on its own.

In the subsequent discussion about the positions of tap-holes, it is assumed that the usual situation applies, where there is a less-dense slag floating on top of a denser metal layer, but this doesn't affect the main argument at all.

The feed rate into the furnace is assumed to be kept constant, *i.e.*, each batch is fed perfectly evenly over the duration of each feeding period. The same quantity of material is fed during each cycle of feeding and tapping. It is assumed that the molten slag and metal inside the furnace are each perfectly mixed. After tapping, the quantity of molten material remaining in the furnace is kept the same every time. Although the fraction of metal tapped from the furnace can be controlled (by choosing when to close the metal tap-hole), the quantity of slag remaining in the furnace is essentially the portion of the slag bath below the level of the slag tap-hole (assuming that the slag is allowed to drain out to this point). The furnace contents at the beginning of a tapping cycle are level with the slag tap-hole, and increase linearly in height during the cycle. Once the tap-hole is opened, the contents are drained down to the level of the tap-hole again.

In practice, the residence time distribution of the slag is often more important than that of the metal, as many reactions take place in the slag layer, as does the settling of metal droplets. There are many cases where the slag behaviour and properties (viscosity, electrical conductivity, freezing behaviour, and aggressiveness towards refractories) are more important to the process design than the metal composition is. The metal often does not play much of a role once it has settled to the bottom of the furnace.

5.2.2 Calculation method

The method for calculating the mean residence time of a semi-continuous batch process is not standard textbook material, and so needs to be outlined here. Given the assumptions previously stated, it is possible to calculate the amount of feed from any particular tap number that is inside the furnace at any given time. From the tap-to-tap time, it is possible to obtain the mean residence time for each portion of feed in the furnace at a given time. Summing the product of the proportions of feed and the respective mean residence times gives the mean residence time for all material in the furnace at a particular time.

To illustrate the method of calculation more clearly, consider the following example, depicted in Figure 5.1. A set mass is fed into the furnace (at a constant feed rate) over a 2-hour time period. This mass is considered to be the initial warm-up mass fed, *i.e.*, no tapping occurs at the end of this stage. This mass has a mean residence time of 1 hour (with a residence time distribution that varies evenly from zero to two hours). The same set batch mass is again fed into the furnace (*i.e.*, feed for tap 1), again at a constant feed rate, over 2 hours. Just before the furnace is tapped, the warm-up feed has a mean residence time of 3 hours, whilst the fresh material fed during tap 1 has a mean residence time of 1 hour. However, since the amount from each feed was identical, the mean residence time of any random particle removed from the furnace is 2 hours. Now, when the same set mass is fed during tap 2, this mass forms half of the total mass in the furnace, and has a mean residence time of 1 hour just before tapping. Also, at this point, the warm-up feed constitutes one quarter of the total mass in the furnace (mean residence time 5 hours), and the feed from tap 1 forms the remaining quarter of the total furnace mass (mean residence

time 3 hours). In this case, the mean residence time of any random particle removed from the furnace is 2.5 hours. Similarly, it is possible to calculate the mean residence time of any particle at any other point in time, and the calculations can be continued until steady state has been reached. This steady-state distribution is the one of primary interest, as the effects of the first few tapping cycles are merely transient.

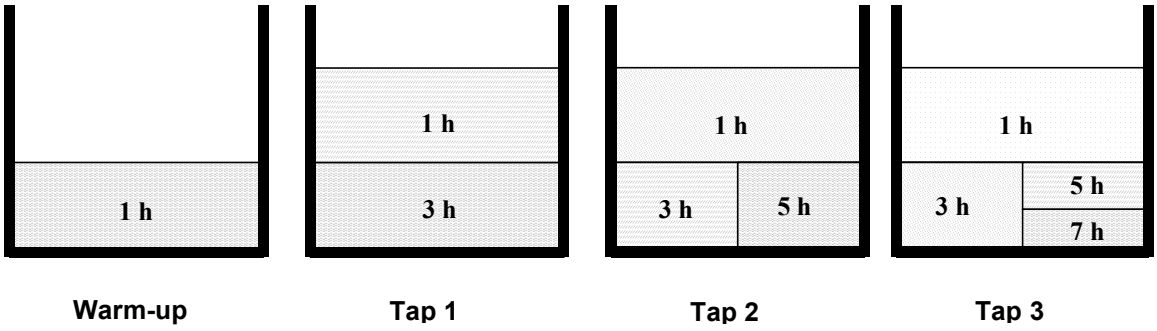

Figure 5.1 Example showing how mean residence times are calculated at the end of each feeding cycle, just before the furnace is tapped

5.2.3 Abstraction of the problem

In order to express this system mathematically, some definitions are required.

t = tap-to-tap time (hours)

n = tap number

$1/f$ = fraction removed during tapping

In considering residence time, one of the key variables in the design of a furnace is the position of the slag tap-hole, as this determines the fraction of molten slag removed during tapping. (This applies particularly to cases where the metal level in the furnace does not change very much.) Figure 5.2 shows the height (s) of the tap-hole above the hearth, in relation to the maximum height of the slag above the hearth level (h). Clearly, the maximum slag level is attained immediately before the furnace is due to

be tapped. The fraction of slag removed during tapping ($1/f$) is shown, in Equation (5-1), as being equal to the amount of slag tapped divided by the sum of the slag tapped plus the slag remaining in the furnace. (This discussion about slag is intended to provide an example to assist in visualising the problem, but the essence of the matter at hand is the fraction of either slag or metal removed during tapping.)

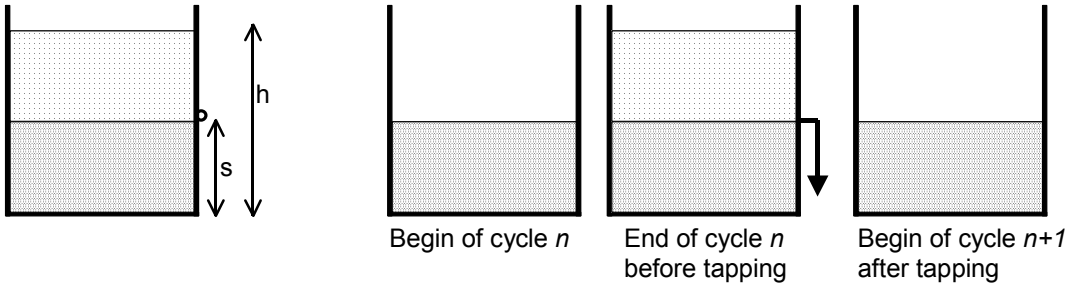

Figure 5.2 Positions of slag level before (s) and after (h) tapping

$$\frac{1}{f} = \frac{h-s}{h} = 1 - \frac{s}{h} \qquad [5\text{-}1]$$

Figure 5.3 shows the relative positions indicated by various values of f and $1/f$.

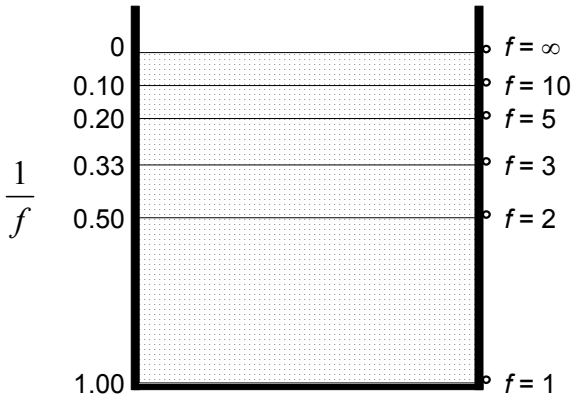

Figure 5.3 Tap-hole positions indicated by various values of f

5.2.4 Example where 1/2 of the material is removed during tapping

Consider the case where one half of the molten material is removed from the furnace, and half is retained inside the furnace each time the furnace is tapped, and the tap-to-tap time is two hours. For the fresh material added during the most recent tapping cycle, the residence time will vary between zero and two hours, with a mean residence time of one hour. Just before the furnace is tapped, this fresh material (with a mean residence time of 1 hour) will make up half of the material inside the furnace. The remaining half will, in turn, have half of that material with a mean residence time two hours longer than that of the fresh material, and so on. This is illustrated diagrammatically in Figure 5.4.

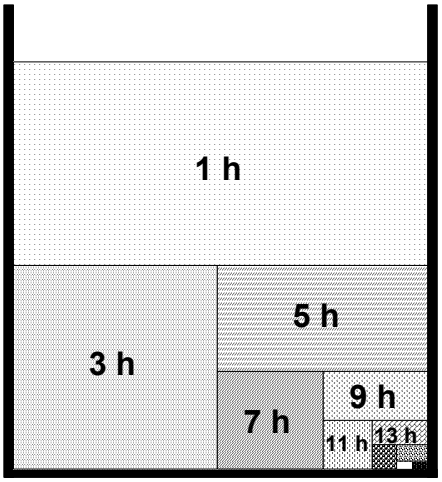

$$\frac{1}{f} = \frac{1}{2}$$

Figure 5.4 A graphical depiction of the 'steady-state' residence time distribution, for a tap-to-tap time of 2 hours, with steady feeding, and half of the material being tapped from the furnace (f = 2)

The overall mean residence time may be expressed as:

$$\text{Mean residence time} = \left(\frac{1}{2}\times 1h\right)+\left(\frac{1}{4}\times 3h\right)+\left(\frac{1}{8}\times 5h\right)+\left(\frac{1}{16}\times 7h\right)+\ldots \qquad [5\text{-}2]$$

Mean residence time (h) =

$$\frac{1}{2}+\frac{3}{4}+\frac{5}{8}+\frac{7}{16}+\frac{9}{32}+\frac{11}{64}+\frac{13}{128}+\frac{15}{256}+\frac{17}{512}+\frac{19}{1024}+\ldots=3 \qquad [5\text{-}3]$$

This can be expressed more concisely as

$$\sum_{n=1}^{\infty}\frac{2n-1}{2^n}=3 \qquad [5\text{-}4]$$

5.2.5 Example where 1/3 of the material is removed during tapping

In this example, also with a tap-to-tap time of two hours, the residence time of feed material added continuously during that period varies between zero and two hours, with a mean residence time of one hour. The fraction of that material that is retained inside the furnace for the next two-hour tap period will have a mean residence time of an additional two hours, *i.e.*, the mean residence time of that portion of material will be three hours. Figure 5.5 shows a graphical representation of the various fractions of the molten material and their respective mean residence times.

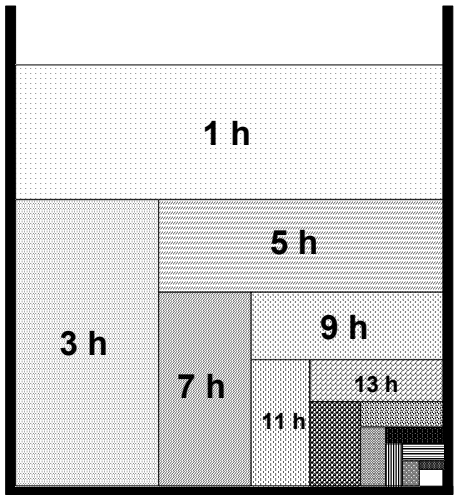

$$\frac{1}{f}=\frac{1}{3}$$

Figure 5.5 A graphical depiction of the 'steady-state' residence time distribution, for a tap-to-tap time of 2 hours, and one third of the material being tapped from the furnace (f = 3)

From the steady-state distribution depicted in Figure 5.5, it can be seen that the fraction of material that has been in the furnace for 1 hour is 1/3. The fraction that has been in the furnace for 3 hours is 1/3 x 2/3 = 2/9. The remaining fraction that has been in the furnace for 5 hours or more is (1 – 3/9 – 2/9) = 4/9. Therefore, the fraction with a mean residence time of 5 hours is 1/3 x 4/9 = 4/27, and so on.

The overall mean residence time may be expressed as:

Mean residence time (h) =

$$\left(1\times\frac{1}{3}\right)+\left(3\times\frac{2}{9}\right)+\left(5\times\frac{4}{27}\right)+\left(7\times\frac{8}{81}\right)+\left(9\times\frac{16}{243}\right)+\ldots=5 \qquad [5\text{-}5]$$

This can be expressed more concisely as

$$\sum_{n=1}^{\infty}(2n-1)\frac{2^{(n-1)}}{3^n}=5 \qquad [5\text{-}6]$$

5.2.6 Generalized expression

The generalized expression for mean residence time may be written as shown in Equation (5-7), and simplified as follows:

$$\text{Mean residence time} = \sum_{n=1}^{\infty} t\left(n-\frac{1}{2}\right)\cdot\frac{(f-1)^{(n-1)}}{f^n} \qquad [5\text{-}7]$$

$$=\frac{t}{f-1}\sum_{n=1}^{\infty}\left(n-\frac{1}{2}\right)\left(\frac{f-1}{f}\right)^n \qquad [5\text{-}8]$$

$$=\frac{t}{f-1}\sum_{n=1}^{\infty}\left(n-\frac{1}{2}\right)\left(1-\frac{1}{f}\right)^n \qquad [5\text{-}9]$$

$$=\frac{t}{f-1}\left[\sum_{n=1}^{\infty}n\left(1-\frac{1}{f}\right)^n-\frac{1}{2}\sum_{n=1}^{\infty}\left(1-\frac{1}{f}\right)^n\right] \qquad [5\text{-}10]$$

This can be simplified further by recognising that this is the sum of a hypergeometric series (of the form $\sum_n nC^n$) plus the sum of a geometric series (of the form $\sum_n C^n$).

$$= \frac{t}{f-1}\left[f(f-1) - \frac{f-1}{2} \right] \qquad [5\text{-}11]$$

This equation simplifies down very tidily to a rather simple result.

$$\text{Mean residence time } R = t\left(f - \frac{1}{2} \right) \qquad [5\text{-}12]$$

This result is shown graphically in Figures 5.6 and 5.7.

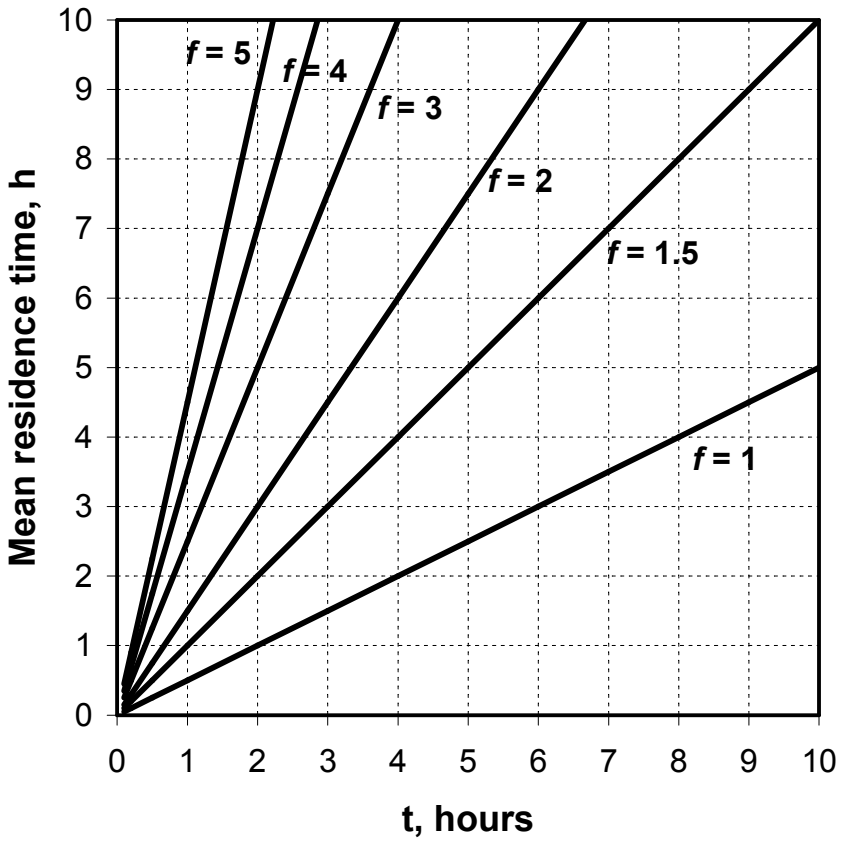

Figure 5.6 Mean residence time shown as a function of tap-to-tap time t for a range of values of f

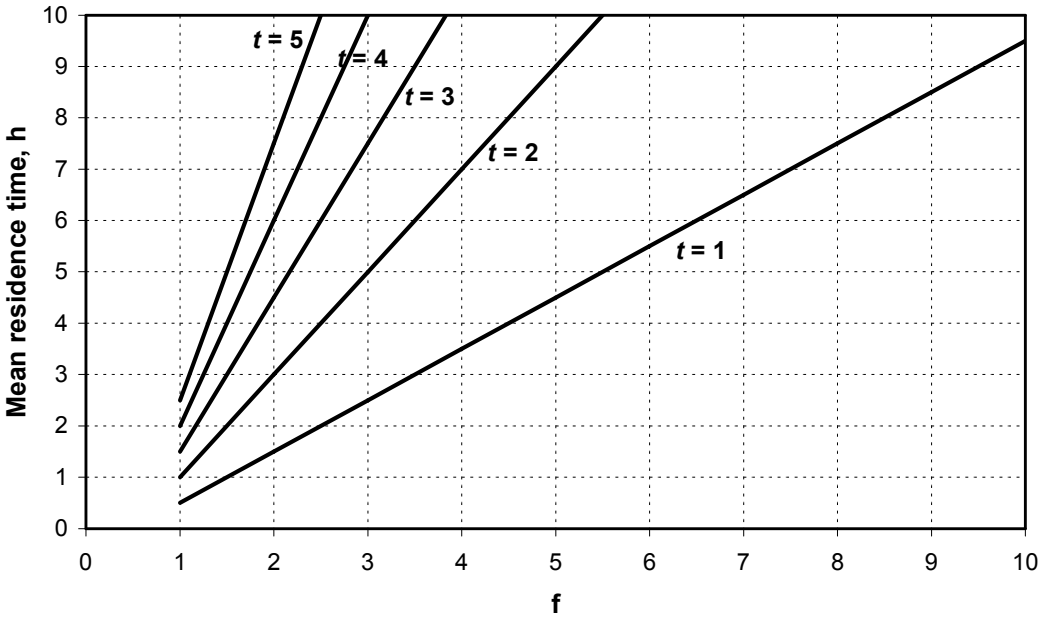

Figure 5.7 Mean residence time shown as a function of f for a range of values of tap-to-tap time t

5.3 Applications

5.3.1 Scale-up with constant residence time

If one wants to achieve a constant mean residence time (of slag or metal) when scaling up from a pilot plant to a commercial plant, there is some flexibility in the choice between the fraction removed during tapping (indicated by $1/f$, and often determined by the tap-hole position) and the tap-to-tap time, t. In Figure 5.8, curves of constant mean residence time (R) are shown as function of f and t.

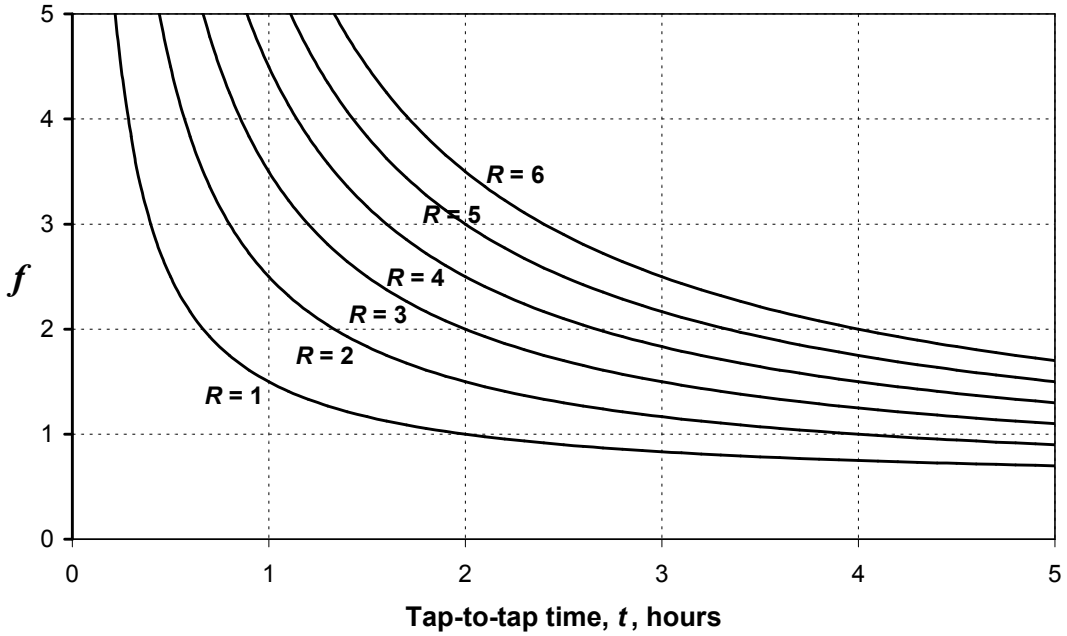

Figure 5.8 Curves of constant mean residence time R (hours), as a function of f and t

An interesting observation from Figure 5.8 (and also Figure 5.6) is that the mean residence time (at steady-state) is equal to the tap-to-tap time when $f = 1.5$, *i.e.*, when two thirds of the molten material is tapped from the furnace each time.

5.3.2 Number of taps needed to change composition

When operating a furnace, it is sometimes necessary to change the composition of the molten bath. For example, a product grade might need to change, or a faulty batch of feed material might need to be worked out of the system. The question then arises as to how many taps it would take to substantially replace material of the old composition with that of the new. This number of taps depends strongly on the value of $1/f$, *i.e.*, the fraction of material removed during tapping. This could be determined graphically by using diagrams similar to those in Figures 5.4 and 5.5, or algebraically using Equation (5-13).

$$\text{Residual fraction after } N \text{ taps} = 1 - \sum_{n=1}^{N} \frac{(f-1)^{n-1}}{f^n} \qquad [5\text{-}13]$$

Figure 5.9 shows the fraction of 'old' material remaining inside the furnace after N taps. For example, if one wanted to ensure that the molten material inside the furnace comprises at least 90% 'new' material, then one would require at least 4 taps for $f = 2$; at least 6 taps for $f = 3$; and at least 11 taps for $f = 5$.

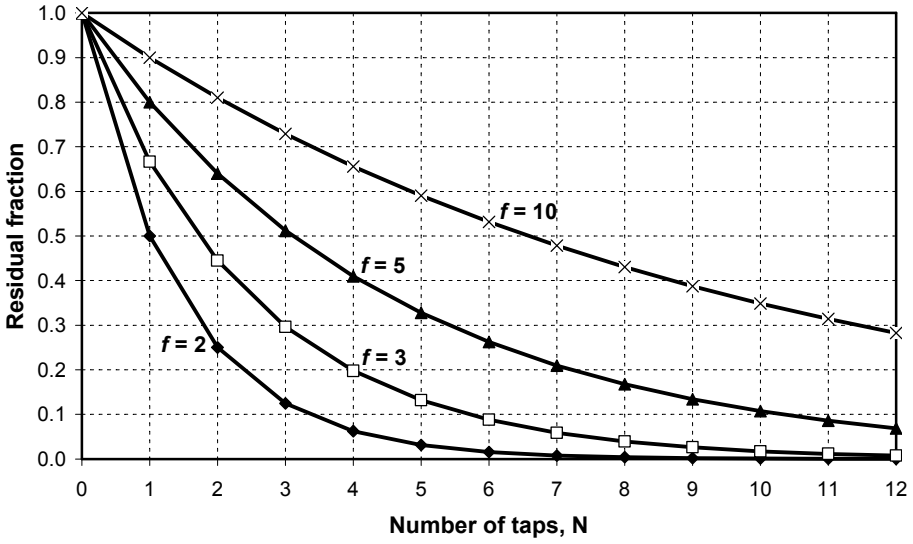

Figure 5.9 The residual fraction of 'old' material left inside the furnace after N taps

5.4 Conclusions

Equations have been developed to allow one to calculate the mean residence time in a continuously-fed batch-tapped furnace, and this has been illustrated using a novel graphical depiction. (The graphical depiction of residence time that was developed allowed the residence-time equation to be derived from first principles.) This was necessary, as many smelting furnaces do not fit the standard textbook classifications of batch

or continuously stirred reactors for which residence time distributions have been well defined. There are some processes in which the time spent by the reacting material in a smelting furnace plays a significant role in determining the extent of the reactions between metal and slag, and influences the degree of settling of metal droplets from a molten slag.

The equations developed apply equally to the slag and to the metal, and can be applied independently to either.

The principal factors influencing the residence time include the slag and metal tapping intervals (where the mean residence time is directly proportional to the tap-to-tap time), and the fraction of liquid retained in the furnace (where the mean residence time is increased by increasing the volume of material retained in the furnace between taps).

The residence-time equation is useful for design purposes if one wants to achieve a constant mean residence time when scaling up from a pilot plant to a commercial plant.

During furnace operation, it is sometimes necessary to change the composition of the molten bath, and it is desirable to know how many taps it would take to substantially replace material of the old composition with that of the new. The required number of tapping operations depends strongly on the fraction of material removed during tapping, and this can be calculated using an equation or graphically.

6 THE CONROAST PROCESS: A CASE STUDY

6.1 Introduction

Commercialisation of a new smelting technology or process is not something that happens very often, and, when it happens, it doesn't happen quickly. Typically, it seems to take about fifteen years from the initial work done in a pyrometallurgical research laboratory to reach full industrial implementation. In Chapter 2, there was a discussion of a number of industrial applications of DC arc furnaces being used for smelting processes where significant chemical reactions are involved. A further application of DC arc furnace technology is poised on the brink of commercialisation – namely the internationally patented ConRoast process (Jones, 2001, 2002; Jones *et al.*, 2002), which can be used for the smelting of both platinum group metals (PGMs) and nickel. This chapter outlines the development of the ConRoast process for PGM smelting (Jones, 2009).

Matte smelting in an electric furnace has been the established route for the treatment of PGM ore concentrates since 1969, when the six-in-line furnace took over from the blast furnace (Mostert & Roberts, 1973). The separation of the base metal sulfides (forming the PGM-containing matte) from the oxide minerals (which make up the slag) is essentially a simple melting operation. However, the products of PGM mining today differ significantly in composition from those of forty years ago, and process changes are required in the smelting of PGM ore concentrates in order to accommodate the increasing amounts of UG2 (chromitite-rich) concentrates that are being produced in the South African Bushveld

Complex. These concentrates contain much higher levels of chromium oxides and much lower levels of base metal sulfides than the previously typical concentrates from the Merensky Reef.

Economic concentrations of PGMs occur mainly within three distinct reefs within the Bushveld Complex: the Merensky Reef, the Upper Group 2 (UG2) Reef, and the Platreef. The Merensky and UG2 Reefs are mined along the Western and Eastern limbs of the complex, while the Platreef is found only along the eastern edge of the Northern Limb. The Merensky Reef and UG2 Reefs are narrow tabular orebodies that extend laterally over hundreds of square kilometres, resulting in vast mineral resources. The Merensky Reef has been the principal source of PGMs since it was first mined in 1925. Although the UG2 chromitite horizon was identified as containing PGMs in the 1920s, it took many years for this reef to be exploited (as the very high chromium content caused problems during the extraction process). Traditionally, the grades were regarded as lower than those of the Merensky Reef, but more recent developments have shown that in many areas the PGM values are higher than in the Merensky Reef. The UG2 Reef has been exploited in its own right only since early 1983. However, with the depletion of shallow Merensky resources, the UG2 Reef (found at a vertical distance of 16 to 400 m below the Merensky Reef) has grown steadily in importance to the point where it now accounts for more than 50% of all the platinum-bearing ore processed in South Africa. Several factors favoured the exploitation of the UG2 Reef: it more than doubles the available PGM reserves; it can be mined through the use of existing facilities; and the chromite is itself a potentially valuable by-product. There is also increasing production of base-metal-rich Platreef ore because of the much lower mining costs that result from open-pit mining methods that can be used on this ore body.

Although the platinum mines of South Africa have traditionally exploited the Merensky Reef of the Bushveld Complex for platinum production, this is becoming increasingly expensive to mine, and much of the new PGM supply is expected to come from UG2 (chromitite-rich with very small amounts of base metals) and Platreef (high base-metal content) ores, which would be metallurgically challenging for traditional 'six-in-line' smelters.

Mintek's ConRoast process was developed to address a number of the shortcomings of the traditional matte smelting process for the production of platinum group metals (Jones, 1999, 2004, 2005; Warner *et al.*, 2007). It controls sulfur emissions by removing sulfur from concentrates prior to smelting. It easily accommodates high levels of chromite by ensuring that the chromium is dissolved in the slag. The concentrates undergo reduction in the furnace, and the PGMs are collected in an iron-rich alloy that has a similar liquidus ('melting') temperature to that of the slag.

Conventional PGM matte smelting requires the presence of a certain quantity of base metal sulfides in order to collect the platinum group metals in a molten sulfidic phase in the furnace. The quantity of chromium oxide in the feed materials is also strictly controlled, in order to avoid the build-up of high-melting chromite spinels. Mintek has developed and successfully demonstrated an alternative process, known as the ConRoast process, which can be used for the production of PGMs using a DC arc furnace. The complete ConRoast process flowsheet (including hydrometallurgical refining) has been described in much detail previously (Jones, 2002) but, essentially, instead of matte smelting, the process is based on alloy smelting of dead-roasted sulfide concentrates in a DC arc furnace. The DC furnace is used to provide the appropriate conditions to generate a small amount of an iron alloy in which PGMs and

base metals are collected, resulting in slag with very low levels of residual PGMs. As the process does not rely on matte collection, there are also no constraints on the minimum quantity of base metal sulfides in the feed material, as the collection of PGMs is done in an iron-rich alloy. The desired degree of recovery of valuable metals is controlled by the addition of a small but variable amount of carbon. The ConRoast process offers advantages in terms of being able to contain SO_2 emissions (by removing essentially all of the sulfur in a continuous enclosed roaster upfront of the smelting), and being able to accommodate a wide variety of feed compositions. The drive towards more environmentally friendly processes remains a strong positive feature of the ConRoast process. A simplified flowsheet is shown in Figure 6.1.

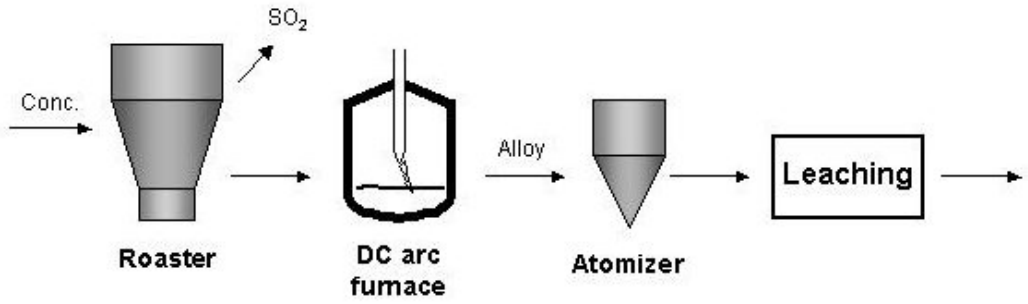

Figure 6.1 Simplified flowsheet for the ConRoast process

6.2 History of the Process and Early Testwork

The development history of the ConRoast process is documented here, in order to show the origins of the process and the thinking behind it. This also serves to illustrate the complexities of the development of an industrial process, and the many factors that play a part along the path towards commercialisation.

As far back as 1994, Mintek was involved in a study that compared a number of pyrometallurgical and hydrometallurgical process routes for the treatment of a nickel-copper-cobalt-PGM concentrate to produce the individual base metals and a PGM-rich residue. During the course of this study, Mintek came up with the concept of a smelting process that involved dead-roasting of concentrate, followed by reductive smelting in a DC arc furnace. An economic comparison showed a significant potential advantage resulting from the simplicity and cost-effectiveness of this process. Furthermore, it was recognised that legislation on emissions of sulfur and other minor elements will get increasingly tougher over time, and a more environmentally-friendly process is needed for the future.

During 1996 and 1997, initial testwork was carried out, under the author's direction, on a nickel sulfide concentrate, first with 500 kg of feed material, then with 30 tons. These tests were very successful, and showed high recoveries of the valuable metals. During 1998, a similar 30-ton test was carried out on a PGM ore concentrate (from a blend of Merensky and UG2 ores), involving dead-roasting in a fluidized bed reactor, followed by smelting in a DC arc furnace. The resulting alloy was treated hydrometallurgically to remove the iron and to separate the base metals from a PGM-rich residue. Again, the results were highly successful. By 2000, the process had been patented by Mintek; over the next few years, patents were granted in a number of countries (Jones *et al.*, 2002). However, the highly conservative PGM industry needed an extended long-term production run to gain sufficient confidence in the process, and this was not easy to achieve because of the very significant cost of roasting sufficient feed material to use for a large-scale demonstration of the smelting process.

A wonderful opportunity came along when a revert tailings material was discovered that was very similar in its characteristics to a dead-roasted concentrate. This material had a low sulfur content, but contained rather high levels of chromite. An initial small-scale smelting test was successfully carried out on this material in 2003. This opened the way for a multi-year demonstration (toll-treatment) smelting campaign at Mintek that began on 1 April 2004, where approximately 37 000 tons of revert tailings was smelted in a 1.5 MW DC arc furnace at a rate of about 1 000 tons per month (Jones & Kotzé, 2004; Geldenhuys & Jones, 2009). This convinced the remaining sceptics that the smelting process worked well. However, there were a number of upstream and downstream aspects to the process that still needed to be demonstrated to a similar level to that of the smelting step.

After the completion of laboratory and pilot-scale smelting testwork, Mintek realised that a partner was required in order to provide the considerable funding that was needed for the purpose of taking the concepts of the ConRoast process, through further development and demonstration, to the point of commercialisation. Numerous presentations were given to all of the established South African PGM producers, as well as to the many emerging PGM miners that were coming onto the scene during a period of great change in the South African mining industry.

The South African Mineral and Petroleum Resources Development Act (MPRDA) came into effect on 1 May 2004. Prior to the implementation of this legislation, the majority of mineral rights (which include mining and prospecting rights) in South Africa were privately held. The MPRDA introduced a fundamental change that brought South Africa more in line with the practice of many mining countries elsewhere where mineral

rights are owned and regulated by the state. Mining companies were required to apply to convert their 'old-order' mining licences and prospecting permits into 'new-order' mining and prospecting rights within a period of five years. When considering the granting of the new rights, the government would take into account a number of factors, including the requirement that at least 26 per cent of the equity of mining companies must be owned by historically disadvantaged South Africans (HDSAs) within ten years. Mining companies were also no longer permitted to hoard vast tracts of unused mining land. This opened up many opportunities for emerging PGM miners to establish their own mines and concentrators, with the intention of empowering the previously marginalized black African people in the country. However, because of the expense of building smelters and refineries, the concentrate would typically still need to be treated by the well-established PGM producers.

An Australian technology development company, Atomaer, recognised the potential of the ConRoast technology, and entered into an agreement with Mintek to fund a three-year (US $15 million) development and demonstration programme in exchange for a ten-year period of exclusive use of the ConRoast process. This agreement was signed on 30 May 2006, with a commencement date of 1 October 2006. The intention was to promote the development and mining of platinum projects for emerging PGM miners in South Africa by providing them access to the ConRoast facility and technology. A black-empowered smelter / refiner (a company with significant ownership and management by black African people) would be established to treat materials from the new independent PGM mines and concentrators. The corporate vehicle for doing this was known as Independence Platinum (Phillips *et al.*, 2006, 2008).

Braemore Resources plc (about 40% owned by Atomaer) acquired Independence Platinum on 20 December 2006, and this entity was renamed Braemore Platinum Smelters. Braemore Resources was initially listed (on 10 March 2005) on the Alternative Investment Market (AIM) of the London Stock Exchange, and was subsequently listed on the JSE on 16 July 2008. Braemore planned to work with various emerging platinum mining companies through technical co-operation, strategic alliances, joint ventures, off-take-, toll-refining-, and marketing agreements.

The story of Atomaer, Independence Platinum, and Braemore Resources (now a subsidiary of Jubilee Platinum) has been told by Phillips *et al.* (2006, 2008).

Clearly, one of the challenges in obtaining off-take agreements is that a mining company will only be willing to commit to providing concentrate to a smelter that is already operating, and a new smelter can only get funds to operate if it can show that it has signed off-take agreements. The way around this impasse was to use the Mintek demonstration furnace to start processing various feed materials on a small commercial scale. While operating the existing plant at Mintek, Braemore planned to establish larger-capacity smelting plants in the Bushveld Complex.

6.3 Description of the ConRoast Process

Dried sulfide concentrate is introduced to a fluidized-bed roaster, where it is exposed to oxidizing conditions at high temperature (above 1000°C), in order to remove essentially all of the contained sulfur as a continuous stream of SO_2 of an appropriate strength for feeding to a sulfuric acid plant. (In the case of low-sulfur feed materials, the gas could instead be scrubbed and neutralized.)

The dead-roasted concentrate is fed hot into a DC arc furnace. This reduces the energy requirement for the smelting process. The DC arc furnace is well known for its ability to handle fine feed materials. The furnace is operated under moderately to quite strongly reducing conditions at high temperature. This avoids the commonly experienced problem of magnetite or chromite spinel build-up in the furnace. (This removes the constraint on the maximum permissible content of Cr_2O_3 in the concentrate, which in turn allows higher PGM recoveries to be achieved in the concentrator.)

The smelting process is alloy-based rather than matte-based, as there is very little sulfur present by this stage of the process. The concentrate is roasted to the extent that no separate sulfur-rich phase is formed during smelting, in addition to the liquid slag and alloy phases. (This removes another constraint on the feed material to be processed, in that there is no minimum quantity of sulfur required. Even weathered oxidized ores can be processed in this way.) By adjusting the amount of reductant fed to the furnace, the amount of alloy produced can be varied, by reducing iron from iron oxide already present in the feed material. (This eliminates yet another constraint on the ore composition, in that there is no minimum amount of nickel and copper required to ensure good collection of the PGMs.) In fact, iron collection of PGMs is even more effective than matte collection (as discussed in more detail in Section 6.3.1). Very clean (barren) slags are produced in the furnace, containing small enough quantities of PGMs that the slags can be discarded, or perhaps sold for purposes such as road-fill or shot-blasting.

The alloy is water-atomized in preparation for further downstream treatment, such as leaching. Prior to the atomization, the molten alloy can

be refined, if required, (to remove small quantities of carbon, silicon, or chromium) in a ladle holding furnace. Although it is possible to use a converter to remove iron from the molten alloy, there is no specific requirement for Peirce-Smith converters or for a converter aisle (thereby eliminating the inherent scheduling problems of this batch process, as well as losses and spillages from the additional handling, and high labour costs). Instead, iron may be rejected from the alloy hydrometallurgically, by precipitation as hematite for example.

The alloy from the furnace differs from the conventional matte feed to the refinery, in that it contains virtually no sulfur, yet contains high amounts of iron. The very fine atomized particles leach very rapidly. An iron-removal step is required prior to the separation of the base metals (Ni, Cu, Co) and the precious metals. Mintek's preferred approach has been based on sulfuric acid leaching, with an atmospheric leaching step for the dissolution of Fe, Ni, and Co, followed by oxidative pressure leaching for the dissolution of Cu. This has resulted in a high-grade PGM concentrate containing exceptionally low quantities of undesirable elements. This PGM concentrate is an eminently suitable feedstock for a precious metals refinery. The ConRoast process achieves very high metal recoveries, and produces high-purity metals, and a clean high-grade PGM concentrate.

6.3.1 Alloy collection versus matte collection of PGMs

Victor Moritz Goldschmidt, one of the founders of geochemistry, developed a classification (Goldschmidt, 1937) of the naturally occurring chemical elements according to their preferred host phases, according to whether they are lithophile ('rock-loving', combining readily with oxygen, mostly ionically or covalently bonded, with an affinity for silicates), siderophile ('iron-loving', dissolving readily in iron or nickel-iron alloys,

metallic bonded), chalcophile ('ore-loving', with an affinity for sulfides, covalently bonded), atmophile ('gas-loving'), or volatile (liquid or gas at ambient surface conditions). The siderophile elements are: Mn, Fe, Co, Ni, Mo, Ru, Rh, Pd, Re, Os, Ir, Pt, and Au (all PGMs are included here). The elements regarded as highly siderophilic are the platinum group elements and Au and Re; these have liquid alloy / silicate partition coefficients (ratio of mass fractions of PGMs occurring in two phases) that are $> 10^4$. The remaining moderately siderophilic elements and some others that may be regarded as barely siderophilic (for example, V and Cr) become more so under strongly reducing conditions. The partition coefficients, usually denoted by D, depend on the compositions of the two liquids, as well as the temperature and pressure. Liu (2000) points out that the variation of D with temperature and pressure is much less than that caused by variations in bulk composition (especially S content). He also found that the partitioning of the platinum group elements is reasonably independent of the concentration of these elements in the alloy phase.

Because PGMs have a low affinity for oxygen, the alloy-silicate and matte-silicate distribution coefficients are typically very large. The task of measuring these distribution coefficients is consequently very challenging, as it entails analysing extremely low concentrations of PGMs, beyond the detection limits of many analytical methods. Even very small entrained droplets of alloy or matte in molten silicate slags can seriously disrupt these measurements. It is to be expected that errors in partition coefficients determined at low PGM contents will be large. According to Barnes *et al.* (1997), errors in platinum group element partition coefficients are of the order of 20 - 50%. For a more extreme example, Lindstrom and Jones (1996) report values for the Ir partition coefficient between solid metal and liquid silicate that vary between 10^6 and 10^{12}.

In order to compare the effectiveness of alloys and mattes for the collection of PGMs, it is necessary to investigate the partitioning between matte and slag, alloy and slag, and then alloy and matte.

Partitioning between matte and slag

The geological or geochemical literature contains numerous studies of PGM distribution coefficients between matte or alloy and silicate phases. Many of these studies were carried out at high pressure (up to 11 GPa) to simulate the conditions in the earth's mantle, but some studies were done at atmospheric pressure too – and these are more relevant to present interests. One such study (Fleet & Stone, 1991) is discussed in more detail later.

PGMs have a clear preference for being in mattes rather than in silicates (oxides). A study of the partitioning of platinum group elements between sulfide liquid and basalt melt (Fleet *et al.*, 1991) has revealed fairly uniform sulfide/silicate partition coefficients with values of the order of 10^3 to 10^4. The partitioning of Pt, Pd, and Ir between immiscible (Fe,Ni)-monosulfide liquid and basalt melt was investigated at 1300°C and at low pressure, over the concentration range 40 to 20 000 ppm of platinum group elements in the sulfide liquid, and over a range of oxygen fugacities. Partition coefficients, D, vary with composition of the sulfide liquid and silicate melt, increasing with a decrease in oxygen fugacity. D_{Pt} and D_{Pd} varied from 2 000 to 20 000, and D_{Ir} varied from 3 000 to 30 000.

Fleet *et al.* (1996) present a summary of the varied partition coefficients between sulfide liquid and basalt melt obtained by various investigators. A few years later, Fleet *et al.* (1999) further measured the partitioning between sulfur-containing liquid metal and a silicate melt. For sulfur

contents of 42.9 atomic % and 46 atomic % (where the mass % would be a lower number), the resulting partition coefficients were D_{Pt} = 1400 to 3600, D_{Pd} = 2900 to 5000, D_{Ru} = 2400 to 4400, D_{Ir} = 1800 to 3200, D_{Os} = 2200 to 3700, and D_{Au} = 900 to 3000 (with the lower values of D occurring at the lower value of sulfur content).

The partition coefficient for Pt between liquid sulfides and silicates remains a subject of some contention. Fonseca *et al.* (2009) studied the partitioning of Pt between matte and a silicate melt as a function of fugacities fS_2 and fO_2 at 1200 and 1300°C. Their results show that the solubility of Pt in mattes increases strongly with increasing fS_2 and decreases weakly with increasing fO_2. These results, coupled with measurements of Pt solubility in silicate melts taken from the literature, allowed them to calculate Pt matte/silicate-melt partition coefficients of between 10^7 and 10^{11} (depending on fO_2 and fS_2), several orders of magnitude higher than previously published values (which they claim to range between 10^3 and 10^9). Their preferred value for conditions appropriate to the Merensky Reef is 10^7, and for the Stillwater Pt-rich horizon is 10^8.

Partitioning between alloy and slag

According to Fonseca *et al.* (2009), the platinum group elements have a high affinity for metallic and sulfide phases and as a consequence are defined as being both chalcophile and highly siderophile elements.

The values of $D_{alloy-silicate}$ for Pt tabulated by Fonseca *et al.* (2009) range from 1.21 x 10^{10} to 4.00 x 10^{12}, and $D_{matte-silicate}$ for Pt ranges from 1.14 x 10^8 to 1.30 x 10^{11}. $D_{alloy-matte}$ for Pt is calculated by dividing $D_{alloy-silicate}$ by $D_{matte-silicate}$ for corresponding data sets; and these values varied from 12 to

792. Early experimental attempts to measure $D_{\text{matte–silicate}}$ of Pt directly are now thought to have been compromised by the presence of 'nanonuggets' in the experimental products. Nanonuggets consist of sub-micron particles of Pt metal and/or Pt-rich sulphides globules that remain suspended in the silicate melt, resulting in an overestimate of the Pt content in the quenched glass, which lead to partition coefficients that may be orders of magnitude too low.

Fonseca *et al.* (2009) also re-iterated that the highly siderophile characteristics of Pt are well accepted, with measured distribution coefficients of Pt between metal and silicate melt as high as 10^{12}, even though the extent to which Pt is chalcophile remains controversial with measured distribution coefficients of Pt between sulfide melt (matte) and silicate melt ranging between 10^3 and 10^9.

Partitioning between alloy and matte

In order to measure the preferred distribution of the platinum group elements to metallic alloys rather than to mattes, it is desirable to measure the partitioning of the various elements between these two phases. One of the classical works on the partitioning of minor amounts of platinum group elements between iron alloy and sulfide was carried out by Noddack *et al.* (1940). Fleet and Stone (1991) pointed out that this work is now known to be suspect due to contamination of the sulfide phases with iron alloy.

Fleet and Stone (1991) investigated the partitioning of minor amounts of all six platinum group elements in the Fe-Ni-S system at 1000°C to 1400°C at low pressure. They reported distinctly different partitioning behaviour for the lighter (Ru, Rh, and Pd) and heavier (Os, Ir, and Pt) elements. The

heavier elements are preferentially concentrated into the alloy phases, while Pd is relatively enriched in sulfide liquids. The behaviour of Pd varies from siderophilic in the presence of iron-rich alloys, to chalcophilic with alloys without much iron. The reported partition coefficients between iron alloys (some containing little or no nickel) and sulfide liquids at 1000°C are greater than 1000 for Pt, Ir, and Os; 30 to 110 for Rh, and 1 to 2 for Pd. The overall affinity for Fe-rich alloy is Os » Ir > Pt > Ru > Rh » Pd. The same study also covered the Ni-S system, where alloy / sulfide partition coefficients of 4 to 220 for Pt, 0.5 to 0.9 for Pd, and 2 to 10 for Rh are reported.

Liu (2000) and Fleet *et al.* (1999) reported on the partitioning of highly siderophile elements (including the PGMs) between solid metal and liquid metal in the Fe-(Ni)-S system at 1000 to 1400°C at low (atmospheric) pressure. Liu pointed out that a sulfur-free liquid metal is similar in chemistry and structure to the corresponding solid metal. It is, therefore, reasonable to use the measured partition coefficients between solid metal and liquid sulfur-containing metal as a good indicator of the partition coefficients between liquid metal and liquid matte.

Fonseca *et al.* (2009), in their work mentioned above, noted that the activities of Pt and Fe in binary solution show a very strong negative deviation from ideality (although their paper refers strangely to "a very strong deviation from Henry's law"). The majority of the (Pt,Fe) alloys obtained in their study fell within the face-centred cubic continuous solid solution (γ-phase) field in the FePt phase diagram, and they extended the work of Gudmundsson and Holloway (1993) to describe the activities of Pt and Fe, using a Redlich-Kister solution model (Redlich & Kister, 1948), as follows.

$$\log_{10}\gamma_{Pt} = X_{Fe}^{\,2}\left[B + C\left(4X_{Fe} - 3\right)\right] \qquad [6\text{-}1]$$

$$\log_{10}\gamma_{Fe} = \left(1 - X_{Fe}\right)^2\left[B + C\left(4X_{Fe} - 1\right)\right] \qquad [6\text{-}2]$$

where γ_{Pt} and γ_{Fe} are the activity coefficients of Pt and Fe respectively, X_{Fe} is the mole fraction of Fe in the metal, and B and C are temperature-dependent constants for the range 1200 to 1400°C. Temperature, T, is in °C.

$$B = 0.0062T - 12.302 \qquad [6\text{-}3]$$

$$C = 0.0017T - 2.565 \qquad [6\text{-}4]$$

Figure 6.2 shows a graphical rendition of equations [6-1] to [6-4] for a temperature of 1400°C.

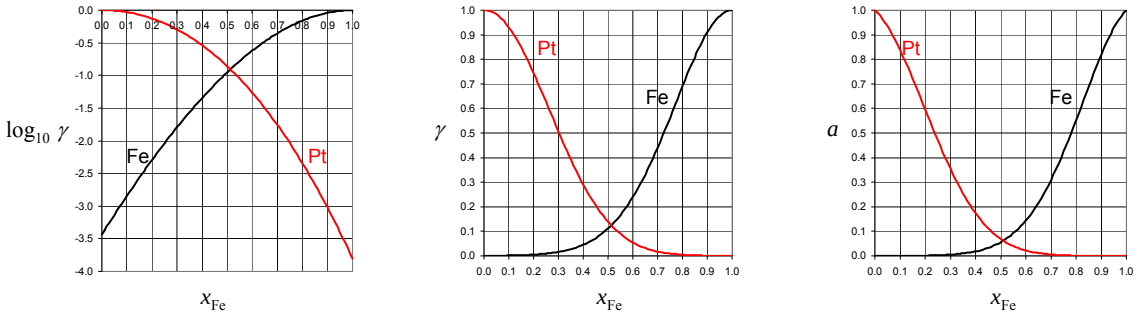

Figure 6.2 Activity coefficients and activities of Fe and Pt in binary solution, plotted from the Redlich-Kister equations of Gudmundsson and Holloway (1993), as modified by Fonseca *et al.* (2009), at a temperature of 1400°C

In the work of Fonseca *et al.* (2009), numerical values for γ_{Pt} varied from 0.009 to 0.79.

Another approach to the estimation of partition coefficients has been to measure the concentrations in Pt-Fe alloy and bulk sulfide particles within a range of mineral samples (Stone & Fleet, 1990). Reported partition coefficients (alloy to sulfide) are > 8000 for Pt, 11 to > 200 for Pd, > 40 for

Rh, and 1 to 20 for Ru. This approach assumes that the sulfide liquid and silicate melt were immiscible liquids in equilibrium with each other, and that the samples analysed are representative of the entire phase.

A patented process (Day & Taylor, 1984) has been developed to recover precious metals by contacting liquid converter matte with an immiscible molten Cu, Ni, or Fe metallic phase. This patent states that "the distribution coefficients of the platinum group metals and gold favour the metallic rather than the matte phase and these elements therefore collect in the metallic phase", even though it does not mention the numerical values of the distribution coefficients.

In metallurgical practice, the limitations to achieving high recoveries of PGMs are not only about the chemical equilibrium compositions, but are linked primarily to forming sufficient collector material (either alloy or matte) and to ensuring coalescence and settling of the droplets through the slag. In the case of traditional sulfide matte smelting, essentially all of the base metal sulfides in the feed material make up the matte product. In the case of an alloy collection process, not only are the distribution coefficients higher than those for matte, but there is an additional degree of control made possible by varying the amount of iron reduction that takes place. If more alloy is needed to achieve the desired level of PGM recovery, it is possible to add some more reductant and produce a greater quantity of alloy.

6.4 Features of the ConRoast Process

The original impetus for the ConRoast process was the development of a more environmentally favourable process route, but, once developed, it became apparent that the process had another significant advantage for

the platinum industry in South Africa, as it was not affected at all by the chrome issues that have caused problems for the traditional 'six-in-line' smelters.

6.4.1 The sulfur problem

Environmental concerns around the platinum industry have focused on sulfur dioxide (SO_2) emissions from traditional PGM smelters (those carrying out matte smelting, usually in six-in-line furnaces), especially on the stray emissions around the mouths of Peirce-Smith converters. Of the sulfur entering a typical smelter, approximately 60% leaves in the converter gases, 20% in the furnace gases, 15% in the converter matte, and 5% in the furnace slag. The furnace gases have an SO_2 content of around 0.4%, which is generally considered too low for efficient recovery. The converter gases, for 70% of the blowing time, have an SO_2 content of more than 4%; the overall gas SO_2 strength varies widely during converter operations (typically from 2.5 to 6%) and leads to erratic acid plant operation as well as expensive acid plant designs (Phillips *et al.*, 2008).

The emission of sulfur dioxide from furnaces and converters is hard to avoid when using a sulfur-based matte-smelting process. However, the ConRoast process does not rely on the presence of sulfur, as it is designed to smelt essentially sulfur-free material in a DC arc furnace, and collects the valuable metals in an iron alloy. Sulfur can be removed, prior to smelting, using a fluidized-bed roaster which is a well-enclosed vessel that produces a steady continuous stream of SO_2 that can be used for the production of sulfuric acid (if the concentration and scale warrant this course of action). Compared to the traditional matte-smelting process, emissions of SO_2 can be orders of magnitude lower if the ConRoast

process is used. The capital costs of acid production can also be reduced markedly.

6.4.2 The chromium problem

The traditional matte-smelting process imposes strict limits on the quantity of chromite (prevalent in the UG2 reef) that can be present in the smelter feed. This constraint restricts the recovery of the PGMs in the production of ore concentrates (in the concentrator plants), as increased losses of PGMs occur together with the rejection of greater quantities of chromite. The ConRoast process eliminates the chromium constraint in smelting and so opens up huge opportunities in the types of materials that can be smelted, and provides an opportunity to significantly enhance the overall process recovery of PGMs (through removing the restrictions in concentrator operations). The ConRoast process solves the chromium problem by making conditions in the furnace sufficiently reducing to allow the chromium oxides to dissolve in the slag.

6.4.3 The containment problem

As the South African platinum producers have moved increasingly to processing ore from the UG2 reef to supplement the previous production from the Merensky reef (Jones, 2005), there have been numerous furnace failures and explosions in the industry. Even though water-cooled copper cooling systems have been introduced in recent years, the highly superheated and corrosive molten matte in traditional smelters is inherently difficult to contain. The ConRoast process is able to use a simple and robust design of furnace, because the melting temperatures of the slag and alloy are close to each other.

6.5 Comparison of Furnace Types

The DC arc furnace offers a number of advantages in the smelting of roasted sulfide concentrates. DC arc furnace technology is seen as the enabling technology to make possible the process described here. The features of DC arc furnaces have been well described previously in this document, so will not be repeated in this chapter.

The application of a DC arc furnace to this flowsheet provides unique advantages, particularly for feeds that contain high amounts of iron oxide that requires much reduction, and for feeds that contain nickel and cobalt which require low oxygen potentials to achieve low slag losses.

A comparison of the characteristics of conventional (usually six-in-line AC, or sometimes circular AC) furnaces and DC arc furnaces highlights the advantages of using a DC arc furnace in this process.

Conventional furnaces

- A conventional furnace has limitations in handling CO gas in the freeboard. Sealing the furnace is very difficult, with multiple electrodes and feed points and a large cavity for the off-gas system. Rather than attempting to seal the furnace, the standard design involves the addition of air to combust the CO in the furnace freeboard and the addition of even more air to temper the combustion product gases. This results in large off-gas volumes, large quantities of dust carryover, and the need to operate fans in a dirty gas environment.
- In reduction smelting, reductants such as coke are mixed into the calcine. The reduction reaction is relatively slow in the conventional smelting configuration of calcine smelting on a slag

bath surface. The power intensity of the furnace, which corresponds to the smelting rate, cannot exceed the reduction reaction rate. This limitation becomes more important as the degree of roast increases and as the amount of reduction increases.

- A calcine bed resting on the slag, or material banked up on the side-walls, can roll over into the slag bath and cause unwanted slag foaming.
- A conventional furnace (a rectangular six-in-line furnace, for example) requires good distribution of feed over the surface of the slag bath. This requires numerous feed points and a complex feed system above the furnace.
- The reduction reaction is dependent on the reductant type. Generally, the need is for fine coke to maximize the reduction reaction rate. Otherwise, coke accumulates at the slag-calcine interface and redirects the furnace power, undesirably.
- The metallized matte or metal that results from reduction smelting has a higher liquidus temperature. This necessitates a higher matte or metal temperature. A conventional furnace has a poor capability to transfer energy in the vertical direction between the slag and matte phases.

<u>DC arc furnaces</u>

- DC arc furnaces are small and intense.
- They have no obvious limit on coke reduction kinetics. The ultimate case of dead roasting and back reduction to alloy is easily possible.
- A wide range of reductants can be used, *e.g.*, anthracite, coal, or coke, of various size ranges.
- DC arc furnaces are easy to seal to contain a CO atmosphere, have little off-gas, little dust, and few feed points.

- They produce hot metal. Temperature control is good, with an even temperature distribution. Having one central electrode avoids the hot spots that AC furnaces experience where electrodes are close to the walls.
- Stable operation is attained by maintaining a constant polarity in the arc. There is also no possibility of short-circuiting by coke between electrodes.
- Electrode consumption is reduced by having fewer electrodes, and not having them immersed in the slag. Because DC electrodes are not subject to the 'skin effect' of AC furnaces where the current is concentrated towards the outer surface of the electrodes, smaller electrodes can be used, as their current-carrying capacity is sufficient. Maintenance is simplified by eliminating the requirement for baking of the electrodes.
- There are structural benefits to having a simpler furnace with only one electrode. Gas sealing is also better.
- The electrical power supply is subject to less harmonics and flicker.

6.6 First 30-ton Test on Nickel Concentrate

As previously described (Jones, 2002), a furnace campaign was carried out in early 1998 using a DC arc furnace with an internal diameter of 1.0 m, connected to a 5.6 MVA power supply. Approximately 26 tons of calcine ('dead-roasted' nickel sulfide concentrate) was processed over a period of 9 days, during which time 83 slag taps were carried out. The metallurgical data presented here is a weighted-averaged summary of the operation during 22 taps under the preferred conditions for producing steady metallurgical performance, *i.e.*, just over a quarter of the campaign. These taps cover a wide range of operating conditions, but the overall average is

considered representative of the steady operation of the furnace during this campaign.

The anthracite addition was approximately 12% based on the mass of calcine fed. (Actual additions were 12.7%, 11.6%, and 12.0% during the three periods summarised here.) Metal was produced at a rate of 250 kg per ton of calcine fed.

Typical operating conditions included feedrates of around 220 kg/h of calcine, power levels around 300 kW (including losses of about 150 kW), voltages between 175 and 250 V, and total power fluxes around 400 to 500 kW/m^2. The specific energy requirement of the process was 760 kWh / t of calcine, excluding losses from the furnace.

Tables 6.1 and 6.2 show the temperatures and compositions of the slag and metal produced during the furnace campaign. Table 6.3 shows the representative composition of the calcine, along with that of the slag and metal products.

Table 6.1 Slag composition during taps of steady metallurgical operation (mass %)

Taps	T, °C	Al_2O_3	CaO	Co	Cr_2O_3	Cu	FeO	MgO	Ni	SiO_2	Fe/ SiO_2
40-46	1481	6.50	2.85	0.11	1.23	0.46	47.33	8.52	0.26	32.78	1.12
49-56	1483	9.18	2.58	0.13	1.23	0.51	48.29	6.22	0.33	31.57	1.19
63-69	1505	7.79	2.42	0.13	1.51	0.48	47.14	5.98	0.29	33.31	1.10
Overall	1489	7.84	2.62	0.12	1.31	0.49	47.61	6.94	0.29	32.51	1.14

Table 6.2 Metal composition during taps of steady metallurgical operation (mass %)

Taps	T, °C	Co	Cr	Cu	Fe	Ni	S	Si
40-46	1470	1.37	0.05	19	33	42	1.3	0.05
49-56	1450	1.47	0.05	19	32	44	1.3	0.06
63-69	1450	1.60	0.05	19	33	42	1.4	0.06

Table 6.3 Representative compositions of calcine, slag, and metal (mass %)

	Calcine	Slag	Metal
Al_2O_3	3.07	7.84	-
CaO	1.43	2.62	-
Co	(0.46)	(0.12)	1.5
CoO	0.59	0.16	-
Cr	-	-	0.05
Cr_2O_3	0.07	1.31	-
Cu	(5.21)	(0.49)	19
Cu_2O	5.87	-	-
CuO	(6.52)	0.61	-
Fe	(32.36)	(37.01)	33
Fe_2O_3	46.27	-	-
FeO	(41.63)	47.61	-
MgO	1.78	6.94	-
Ni	(11.36)	(0.29)	43
NiO	14.45	0.37	-
S	0.78		1.4
Si	-	-	0.06
SiO_2	20.38	32.51	-
Total	95.4	100.0	98.0
Fe/SiO_2	1.59	1.14	-

The recoveries of the valuable elements were calculated based on the analyses shown in Table 6.4. The rest of the compositions and flowrates were calculated on the basis of these numbers.

Table 6.4 Residual contents of metals in slag

	Typical	Best
% Co in slag	0.12	0.09
% Cu in slag	0.49	0.43
% Ni in slag	0.29	0.20
% Fe in metal	33	33

The actual recoveries obtained on this campaign (see Table 6.5) were calculated using both the typical and the best analyses obtained.

Table 6.5 Metal recoveries

	Typical	Best
Co recovery, %	83	87
Cu recovery, %	94	95
Fe recovery, %	25	25
Ni recovery, %	98.3	98.9

Even at the relatively low level of 25% iron recovery (which should ideally be as low as possible), the recoveries of the valuable base metals are very high. This was a very successful outcome of the testwork.

6.7 First 30-ton Test on PGM Concentrate

During 1998, approximately 30 tons of PGM-bearing sulfide ore concentrate was roasted in a fluidized-bed reactor, then smelted in a pilot-scale DC arc furnace (Jones, 2002). The resulting alloy was refined using a blowing operation, then treated hydrometallurgically to produce a high-grade PGM concentrate.

The fluidized bed was operated at approximately 1000°C, and the concentrate was fed at about 140 kg/h. Gas velocities of about 0.4 m/s were used. The residence time was rather low, at approximately 20 seconds per pass. Most of the material underwent two passes through the reactor, with a small quantity passing through three times. The sulfur level decreased from 4.55% S to 0.5% after the first pass (96% elimination of S), and to 0.24% after the second pass (98% elimination), and to 0.13% S after the third pass. During roasting, the impurities were diminished as follows:

S from 4.55% to 0.24% (to 0.13%)
As from 40 to 21 ppm
Se from 60 to 8.8 ppm

Te from 10 to 7.8 ppm

Os from 5.5 to 3.8 g/t

Smelting was carried out in a pilot-scale DC arc furnace. 24 tons of (mostly double pass) dead-roasted concentrate (including 1 ton of triple-roasted material) was processed in a week-long campaign. The furnace was operated at a power level of 300 to 500 kW, which translates to a power flux of 290 to 480 kW/m^2. The average operating temperature was 1650^{o}C. Calcine was fed to the furnace at feedrates of 200 to 300 kg/h, and approximately 5% coke addition was used. No additional fluxes were added. The specific energy requirement of the process was 650 kWh/t of calcine (neglecting energy losses from the furnace shell). (Obviously in a full-scale plant operating with hot feeding of calcine to the furnace, this figure would be less.) The process was operated consistently with less than 1 g/t PGM in slag, and values as low as 0.3 g/t in the slag were demonstrated. The average PGM loss to the slag over the entire campaign was 2.9 g/t.

The compositions of the original concentrate, roasted concentrate, and slag are shown in Table 6.6.

Table 6.6 Analyses of the original concentrate, roasted concentrate, and slag (mass %)

	Al_2O_3	C	CaO	Co	Cr_2O_3	Cu
Original concentrate	4.2	-	4.4	0.06	2.6	1.04
Roasted concentrate	5.4	0.09	4.3	0.06	2.7	1.01
Slag	7.1	0.03	5.2	0.07	2.8	0.13

	FeO	MgO	Ni	S	SiO_2	PGM, g/t
Original concentrate	16.4	20.4	1.91	4.55	42.6	308
Roasted concentrate	16.3	19.9	1.84	0.25	43.3	296
Slag	7.2	24.7	0.10	0.07	51.0	2.9

The overall impurity removal (including roasting and smelting) is shown in Table 6.7, as a percentage of the amount originally present in the unroasted concentrate.

Table 6.7 Impurity removal in roasting and smelting, % of element in feed

As	Bi	Mn	Pb	Se	Te	V
70	87	95	100	95	84	77

Approximately 109 kg of alloy per ton of roasted concentrate was produced in the furnace. Over the campaign, about 2.6 tons of alloy was produced in total. Most of the alloy was tapped in two large batches. (The first alloy tap was diluted somewhat by the initial metal heel in the furnace.) Table 6.8 shows the composition of the alloy, together with the composition of the alloy produced in a laboratory-scale preliminary test (all in mass %). Also shown is the composition of the refined alloy produced by blowing the molten alloy with air, as discussed below.

Table 6.8 Compositions of alloys from 30-ton PGM test (mass %)

	C	Co	Cr	Cu	Fe	Ni	S	Si	PGM
Small-scale test	0.05	0.55	0.27	9.81	70.6	17.1	2.00	<0.05	0.2804
836 kg alloy	1.06	0.33	3.35	7.56	67.7	16.6	0.48	1.34	0.1700
1612 kg alloy	0.97	0.50	2.35	7.43	71.1	15.3	0.97	1.05	0.2646
Refined alloy	0.04	0.6	0.03	13	60	24	0.4	<0.05	0.2609

The alloys produced during the furnace campaign had the following ranges of composition.

C: 0.6 - 1.1%

Cr: 1.6 - 3.35%

Si: 0.76 - 1.34%

The alloy with the worst composition (*i.e.*, from the 836 kg batch) was selected to demonstrate the downstream process on the most conservative basis. In order to lower the quantities of carbon and silicon (and chromium) prior to leaching, it was necessary to blow air into the molten alloy (using a top-blown rotary converter, to simulate the operation of the proposed ladle furnace to be used for this operation). The composition of the resulting refined alloy is shown in Table 6.8. This alloy was water-atomized to a particle size less than 100 μm. The atomized alloy was then used for subsequent leaching tests.

The leaching testwork has been documented elsewhere (Jones, 2002) and is not presented here, as the scope of this thesis is limited to pyrometallurgical aspects of the process.

After hydrometallurgical processing, a final PGM concentrate was produced with the composition shown in Table 6.9.

Table 6.9 Composition of final PGM concentrate after leaching (mass %)

PGM+Au	**Pt**	**Pd**	**Rh**	**Ru**	**Ir**	**Au**
61.4	34.6	12.7	4.3	7.7	1.67	0.61

Fe	**Ni**	**Cu**	**Si**	**Cr**	**Se**	**Te**	**S**	**C**	**As**
3.6	0.27	3.3	1.75	2.5	0.016	0.007	2.0	0.92	0.49

This testwork allowed the following conclusions to be drawn. Roasting removes sulfur (98% elimination of S in a fluidized bed has been demonstrated) and other impurities very effectively. Roasting and smelting removed most (70 – 100%) of the minor impurity elements: As, Bi, Mn, Pb, Se, Te, and V. Alloy smelting collects PGMs very well, resulting in very barren slags; consistently less than 1 g/t PGM in slag, with < 0.3 g/t PGM in slag being demonstrated often. If iron removal

from the product alloy is to be done hydrometallurgically (in a process similar to that used at Chambishi Metals), the final levels of C, Si, and Cr in the alloy can all be brought down to less than 0.05% by ladle refining. Water atomization can be used to produce very fine particles (< 100 μm) that leach rapidly. A high-grade (> 60%) high-recovery clean PGM concentrate was produced.

6.8 Four Months of Testing on Various PGM Feed Materials

It was clearly necessary to demonstrate the ConRoast process on a scale larger than the 30-ton scale, in order to optimize the operation of the furnace, and to make enough alloy product to ensure that steady-state operation had been obtained. Unfortunately, larger-scale demonstration of the process was delayed for a few years because it would be very expensive, because of the requirement for large-scale production of dead-roasted concentrate. Fortunately, there are alternative feed materials that are sufficiently similar that they can be used for extended large-scale demonstration of DC arc smelting in the production of PGMs (Jones & Kotzé, 2004). These materials include medium-grade concentrates that are very high in chromite content and low in sulfur, as well as tailings from a milling-flotation process for the treatment of revert materials from an existing smelter.

In 2004, Mintek was able to successfully treat a wide variety of difficult feed materials that contain low amounts of sulfur and / or high amounts of chromium oxide. A DC arc furnace was used, at power levels up to 1.5 MW, to provide the appropriate conditions to generate an iron alloy that collects PGMs very effectively, leaving extremely low residual quantities of PGMs in the slag. The longest of these campaigns (at that time) was run continuously for more than four months, treating more than

two thousand tons of materials such as low-grade concentrates, revert tailings, and converter slag. The campaigns demonstrated the robustness and versatility of the process, and proved that it is possible to sustainably produce a PGM-containing alloy and discardable slags containing an average of less than 1.4 g/t of PGMs over the entire campaign.

6.8.1 Feed materials

A number of feed materials were tested to establish their suitability for the process. A medium-grade UG2 concentrate (high in chromium, and low in base metal sulfides) was found to work very well indeed when mixed with a small quantity of converter slag (as a source of supplementary iron collector). Smelter concentrate sweepings, even though they have a high sulfur content, also worked well when mixed with varying proportions of converter slag. High recoveries of PGMs were obtained from converter slag, but the grade of the resulting alloy was rather low, as very reducing conditions were used to produce a large quantity of alloy in order to avoid the formation of aggressive furnace slags with a high FeO content. The primary focus of the work then shifted to the treatment of revert tailings (the waste from a milling-flotation process for the treatment of revert materials from an existing smelter), and more of this material has been treated than any other.

The weighted average compositions of the feed materials are presented in Table 6.10. The PGM content was analysed by fire assay, and so represents the approximate total of Pt + Pd + Rh + Au.

Table 6.10 Composition of feed materials, mass %
(PGM listed in g/t for Pt + Pd + Rh + Au)

Feed material	Al_2O_3	C	CaO	Co	Cr_2O_3	Cu	FeO	MgO	Ni	S	SiO_2	PGM	H_2O	Total
Revert Tailings	3.7	0.2	6.0	0.18	2.6	0.3	34.7	10.1	0.99	0.85	34.2	66	2.5	96.3
UG2 Conc.	5.0	0.2	2.9	0.03	4.9	0.2	13.0	22.6	0.44	0.86	44.4	78	-	94.6
Smelter Conc.	3.5	0.4	4.1	0.12	2.0	1.8	22.0	14.3	3.07	7.2	33.5	234	-	92.1
Converter Slag	1.4	0.2	1.9	0.30	2.7	0.8	55.1	3.7	1.51	1.7	30.0	73	-	99.1

6.8.2 Drying of revert tailings

The revert tailings have a clay-like consistency when recovered from the tailings dams. The weighted average moisture content of the delivered material was approximately 19%. After being delivered by bulk side-tipping trucks, the material was loaded by front-end loader into a feed hopper that discharged onto a conveyor belt that fed an electrically-heated rotary kiln that operated at a temperature of up to 550°C. Moisture was removed as steam from the revert tailings, in order to lower the moisture level of the product to approximately 2 per cent (which is the desirable level for feeding to the furnace). The kiln was able to produce over 30 tons per day of bagged dried revert tailings. Any dust that left the kiln together with the steam was captured in a dust scrubber, and the resulting sludge was allowed to settle before being returned to the stockpile of wet material for re-processing.

6.8.3 Furnace operation

The particular furnace used in the work reported here was equipped only with film water cooling on the sidewalls. This placed some constraints on the allowable intensity of the operation, and on the permitted level of aggressiveness of the slag that needed to be contained in the vessel. The furnace was generally operated with slag temperatures between 1550 and 1600°C, and metal temperatures about a hundred degrees cooler than this. Anthracite (with a fixed carbon content of about 74%) was used as the

reducing agent for the process, and, for the most part, no flux was added to the furnace. There was an occasional addition of high-magnesia slag additives (crushed bricks, *etc.*) to supplement the formation of a freeze lining on the side-walls. A high-melting spinel was present in the slag (at the level of a few per cent), and this assisted in the formation of a protective layer of solidified material on the side-walls. The tap-holes performed well, with only two replacements of the alloy tap-hole lining being required over a four-month period. Energy was lost from the shell of the furnace at a rate of up to 450 kW when the furnace was operated at its higher temperatures and power levels. The temperature distribution in the furnace was responsive to such factors as arc length and the state of the upper surface of the molten bath; this allowed the furnace to be well controlled. The furnace slag was highly resistive, which resulted in relatively high-voltage operation.

The operation of the furnace was characterised by the production of very clean (barren) slags much of the time. No appreciable entrainment of alloy in slag was encountered. PGM contents less than the 0.28 g/t detection limit were common, and the weighted average PGM content in slag over the first two months of the campaign was 0.8 g/t. After this, there was a deliberate attempt to operate the furnace under slightly less reducing conditions in order to produce less alloy (therefore higher grade) than was done initially. During the initial smelting of revert tailings, the quantity of alloy produced was equivalent to 11% of the mass of the dried revert tailings fed to the furnace (*i.e.*, about 9% of the mass of the revert tailings as delivered). The maximum daily throughput was 30.5 tons of dried revert tailings. Typical feedrates were around one ton per hour. Very high recoveries of PGMs were obtained.

The recovery curves shown in Chapter 3 give a very good indication of the impact of a moderate decrease in the extent of reduction. In particular, they show that a fairly significant decrease in iron reduction would necessitate only a small lowering of PGM recovery.

Figure 6.3 shows the furnace in operation.

Figure 6.3 Alloy tapping from the 1.5 MW furnace, 16 April 2004
Photograph by Isabel Geldenhuys. Used with permission.

Some aspects of the furnace operation are summarised in Table 6.11. The anthracite addition, and the quantity of alloy, slag, and dust produced are all expressed relative to the mass of the PGM-containing feed material, as are the specific energy requirement of the process (excluding losses from the furnace shell) and the electrode consumption. (Because of the addition of slag additives during the converter-slag-only operation, the percentages

of the alloy, slag, and dust total more than 100% when expressed relative to the converter slag fed to the furnace.)

Table 6.11 Summary of some aspects of the furnace operation, under various conditions

PGM-containing feed	Tons processed	% Anthracite	% Alloy	% Slag	% Dust	MWh/ton	Electrode kg/ton
75% UG2 Conc. + 25% Converter slag	18	4.8	22	60	4.6	0.61	2.9
75% Concentrate + 25% Converter slag	34	3.5				0.53	
50% Concentrate + 50% Converter slag	72	7.6				0.60	
25% Concentrate + 75% Converter slag	30	7.9				0.65	
Converter slag	279	10.8	28	77	2.4	0.76	1.7
Revert Tailings	> 1500	5.0	11	77	4.7	0.70	2.3

UG2 concentrate (high in chromium and low in base metal sulfides) was processed together with a small quantity of converter slag (in a 75:25 ratio by mass). This generated slags very similar in composition to those produced when smelting revert tailings.

As an aside, it is necessary to mention that the iron that is used to collect the valuable metals is typically reduced to the metallic state from the iron oxide that occurs naturally in most PGM-containing feed materials. In cases where the feed materials contain less than the necessary quantity of iron, an additional iron source may need to be added to the furnace feed. Converter slag can be very useful for this purpose, and the use of this material has the added benefit that it obviates the need for recycling slag

to a conventional matte-smelting furnace, and does away with the requirement for a separate slag-cleaning furnace. Because the ConRoast process operates with the addition of some carbon to the furnace, the stable state of the iron oxide is FeO rather than the Fe_3O_4 that causes operational problems in matte smelting.

Smelter concentrate sweepings were also treated in varying ratios together with converter slag, culminating with the treatment of converter slag on its own. Because of the non copper-cooled furnace, a conservative mode of operation dictated that the FeO content of the slag be kept to moderate levels, and this required very strongly reducing conditions when smelting only converter slag. This resulted in too much alloy being produced, and so was not found to be an ideal candidate for this process (except perhaps if run under much less reducing conditions in a copper-cooled furnace). Revert tailings were treated on their own. The weighted compositions of the slags produced in the various modes of operation are listed in Table 6.12. The average slag tapping temperatures for the various conditions were 1559, 1587, 1530, 1509, 1517, and 1554°C respectively. The weighted compositions of the alloy produced during the various periods are listed in Table 6.13, but these are more susceptible to variation, as the amount of alloy produced was small relative to the amount inside the furnace at any time. There wasn't yet sufficient alloy produced to be able to tap during the treatment of the UG2 concentrate, so no alloy composition is reported for this period (although it would be expected to be similar to the alloy produced from revert tailings).

Table 6.12 Slag composition, mass %
(PGM listed in g/t for Pt + Pd + Rh + Au)

Material treated	Al_2O_3	CaO	Co	Cr_2O_3	Cu	FeO *	MgO	Ni	S	SiO_2	PGM	Total
75% UG2 Conc. + 25% Converter slag	4.5	4.4	0.03	4.2	0.07	21.1	20.2	0.11	0.26	43.3	0.6	98.1
75% Concentrate + 25% Converter slag	4.2	5.3	0.06	2.7	0.14	25.4	15.6	0.18	0.51	43.6	0.9	97.7
50% Concentrate + 50% Converter slag	4.2	5.3	0.03	3.7	0.10	21.8	13.2	0.05	0.47	48.6	0.6	97.6
25% Concentrate + 75% Converter slag	3.5	4.2	0.04	3.8	0.13	29.6	9.6	0.06	0.57	48.6	0.6	100.1
Converter slag	3.5	2.6	0.04	5.1	0.13	33.5	12.8	0.03	0.57	41.0	0.6	99.4
Revert Tailings	4.9	7.4	0.04	3.1	0.07	28.0	12.7	0.10	0.34	43.3	1.6	100.1

* Total Fe expressed as FeO

Table 6.13 Alloy composition, mass %
(PGM listed in g/t for Pt + Pd + Rh + Au)

Material treated	C	Co	Cr	Cu	Fe	Ni	S	Si	PGM	Total
75% Concentrate + 25% Converter slag	0.03	0.66	0.20	6.9	61.9	10.3	18.5	0.16	502	98.7
50% Concentrate + 50% Converter slag	0.09	0.74	0.82	4.8	71.4	8.6	12.1	0.10	604	98.7
25% Concentrate + 75% Converter slag	0.05	0.79	0.35	4.6	73.8	11.8	11.8	0.02	500	99.2
Converter slag	0.12	0.96	0.31	3.0	86.2	5.3	4.6	0.16	293	100.7
Revert Tailings	0.12	1.21	0.21	2.1	83.7	8.0	3.7	0.51	459	99.6

Of principal interest in a metal recovery process is the deportment of the various elements to the alloy phase. In the furnace campaign described here, the dust that was produced from the furnace and captured in the bag-house was all recycled back to the furnace. On that basis, as long as the elemental accountability is good, the simplest expression of recovery of a given element is the ratio between the mass of its content in the alloy divided by the combined mass of its content in the alloy and slag. Sulfur has to be treated differently, as we are also interested in how much reports to the gas. The recoveries of various elements of interest are listed in

Table 6.14. (Note that the recoveries reported for the first condition – treating UG2 concentrate – had to be estimated on the basis of feed and slag, rather than alloy and slag, as there was no alloy tapped at that stage.)

Table 6.14 Recoveries of elements to the alloy, % of feed

Material treated	Co	Cr	Cu	Fe	Ni	S	S to gas	PGM
75% UG2 Conc. + 25% Converter slag	85	-	89	50	91	68	25	99.5
75% Concentrate + 25% Converter slag	70	2.2	91	40	93			99.1
50% Concentrate + 50% Converter slag	92	13.0	96	66	99			99.8
25% Concentrate + 75% Converter slag	92	6.9	95	63	99			99.8
Converter slag	90	2.8	88	53	98	59	18	99.4
Revert Tailings	81	1.4	81	36	92	47	23	97.7

6.9 Four Years of Smelting Revert Tailings (1.5 MW)

6.9.1 Demonstrating new technology at large scale

Alternative or new technology inevitably requires piloting and demonstration prior to implementation and this is even more true in the case of pyrometallurgy, as any smelting operation has inherent risks associated with the process and equipment. Large-scale demonstration testwork adds significant value to any project but it is, however, very expensive to demonstrate the smelting step at large scale and for an extended period. The need to address the risks versus the cost of testwork and the availability of suitable feed typically determines the scale and duration of smelting testwork (Geldenhuys & Jones, 2011).

The duration of a typical pilot-plant smelting campaign carried out in Mintek's Pyrometallurgy Division is usually restricted by cost, and the

availability of raw materials, particularly when the feed requires upgrading or pre-treatment (such as roasting or calcining, for example). Generally, a once-off test is commissioned during which a significant quantity of specially prepared feedstock is processed at an appropriate scale. The operational and metallurgical data from these test campaigns are processed and evaluated to provide input into feasibility and, ultimately, design studies.

Although the initial ConRoast testwork was remarkably successful, the process so radically departs from the traditional PGM production flowsheet that large-scale demonstration of the process was inevitably deemed a vital component in the progression towards the ultimate commercialization of the technology. Although Mintek's smelting facilities can process large quantities of feed, currently no pilot facilities are available to produce the large quantities of dead-roasted concentrate on a continuous demonstration basis. Thus, demonstrating the full ConRoast flowsheet on an ongoing basis was not a practical or affordable option. Fortunately, alternative PGM-containing materials with a low sulfur content became available from various sources. These materials were sufficiently similar to dead-roasted concentrates to allow for long-term demonstration of the smelting step of the ConRoast flowsheet. The feed materials included low- to medium-grade PGM concentrates that are high in chromite and low in sulfur, tailings from a milling-flotation process for the treatment of revert materials (also low in sulfur) from an existing smelter, and other PGM-containing wastes or by-products.

Although large-scale testwork on furnaces is very expensive, it is widely acknowledged as being necessary because of the risk of failure of new smelting operations if they are not properly understood. However, if the scale of the work is large enough, it is sometimes possible to make the

testwork pay for itself by utilising the products from the furnace. Recovery of contained metals is a significant economic incentive when treating valuable waste materials from dumps. Remediation of tailings dams or other dumps removes the environmental and economic liabilities typically associated with dumps and also makes valuable land available for more productive uses, whilst processing these materials provides an opportunity to demonstrate the sustainability of DC arc furnace technology to the PGM industry via a continuous, environmentally friendly operation. It is possible to treat all of the material contained in a medium-sized dump over a period of a few years, by running a pilot furnace at a power level of 1 – 2 MW.

6.9.2 From large-scale demonstration testwork to continuous production

Mintek commenced an extensive pilot-plant smelting campaign in April 2004, under the author's direct supervision, initially treating a variety of PGM-containing feed materials and then moving to the treatment of revert tailings. The results from the first 2000 tons processed (over a period of four months) were described in the previous section of this chapter.

The primary focus of the work described here is on the treatment of stockpiled revert tailings (the waste generated by a milling-flotation process used in the treatment of revert materials from an existing smelter). As the testwork progressed, the focus of the continuous smelting operation changed from a research or demonstration operation to a production-oriented operation. As is the nature of any production operation (and perhaps more so for a smaller unit operation), throughput, availability, efficiencies, and process optimization became increasingly important measures.

Between 1 April 2004 and 8 August 2008, Mintek's pilot-plant processed (dried and smelted) over 37 000 tons of PGM-containing feed materials on a toll-treatment basis – demonstrating the sustainability and efficiency of the process over a period of four and a half years (Geldenhuys & Jones, 2009). Various feed materials (including low-grade concentrates, converter slag, and revert tailings) were treated successfully at power levels of up to 1.5 MW in a 3.0 m DC arc furnace, thereby demonstrating the robustness and versatility of the process. Of the total amount processed, 9 500 tons of feed material was smelted for Braemore Platinum Smelters, in a period of just over ten months, resulting in the production of 840 tons of alloy, containing over 16 000 ounces of PGMs on a 4e (Pt+Pd+Rh+Au) basis. The first alloy for Braemore was tapped on 2 October 2007 (shown in Figure 6.4).

Figure 6.4 Alloy tap from Mintek's 1.5 MW furnace, 2 October 2007

Table 6.15 provides a brief summary of the history and the duration of the various campaigns.

Table 6.15 Summary of campaign duration, start-up and end dates, and tonnage processed

	Duration			Ave Power	Feedrate	Reason for shutdown
	From	To	Days	MW	tons/day	
C-1	16-May-2004	15-Aug-2004	92	0.97	17	Facility required for other testwork
C-2	28-Sep-2004	31-Jan-2005	126	1.26	27	Facility required for other testwork
C-3	13-Apr-2005	25-Sep-2005	166	1.35	29	Furnace re-lined after moving
C-4	04-Nov-2005	04-Apr-2007	517	1.39	34	Changed to new client
C-5	29-Sep-2007	08-Aug-2008	315	1.20	30	Decommissioned furnace for upgrade
	Overall		1216	1.29	30	

6.9.3 Operation of the 1.5 MW DC arc furnace

The furnace had separate tap-holes for the removal of alloy and slag. During stable operation, the furnace was fed more-or-less continuously, and tapped intermittently via the dedicated tap-holes, with slag being removed from the furnace approximately every three hours, and alloy tapped about once a day. The slag tap-hole had a water-cooled copper insert, which performed well and rarely required maintenance. The alloy tap-hole performance was good, but the refractory lining generally required a partial replacement every two to three months of continuous operation. Each tap-hole maintenance shutdown typically lasted between 8 and 12 hours, during which time other maintenance on the plant was generally carried out. A weekly maintenance shutdown was also put into practice, in an attempt to improve the overall availability of the furnace, with the primary focus on preventative maintenance.

A single solid graphite electrode was used as the cathode, and the anode at the bottom of the furnace was made up of a number of steel pins that protruded through the refractory hearth to come into intimate contact with the molten alloy. The gas leaving the furnace was combusted and then passed through a bag-house to remove any entrained dust (for continuous recycling to the smelter) before being treated in an SO_2 scrubber prior to discharge through the stack.

The particular furnace used in the work reported here was equipped with film water-cooling on the side-walls, which placed some upper limits on the smelting intensity of the operation. (This was done deliberately to avoid the higher-intensity copper coolers that have failed often in PGM matte smelters elsewhere.) The furnace was operated in such a way as to maintain a freeze lining, and the operational intensity was reduced if the protective layer required reformation. Crushed, high-magnesia bricks were occasionally added to the furnace as a feed material to supplement the formation of the protective solidified layer on the side-walls. The temperature distribution in the furnace was very responsive to such factors as arc length and bath condition. These aspects were usefully monitored, and adjustments were made to arc length and operating intensity to achieve a desired mode of operation depending on the condition of the freeze lining, and process objectives. In this way, the furnace operation was managed by controlling the temperature distribution, especially with regard to the maintenance of the freeze lining.

Overall, the furnace was in production for more than 40 months without any major incidents. The furnace operation became increasingly efficient as the throughput, availability, and process parameters were optimized. A summary of the general process parameters, that is, tons processed, slag

and alloy make, dust carry-over, gross energy requirement, and electrode consumption for each of the five campaigns, is listed in Table 6.16. The alloy make was directly controlled by changing the addition of carbon (in the form of anthracite) to the furnace, and the degree of reduction was controlled (with the aid of the recovery curves introduced in Chapter 3) to achieve the desired optimized PGM recovery. The electrode consumption was good, with an overall consumption of 1.5 kg electrode per MWh.

Table 6.16 Summary of some aspects of the furnace operation, for the five campaigns

No.	Tons processed	% Anthracite	% Alloy	% Slag	% Dust[#]	MWh/ton[*]	Electrode kg[$]/ton
C-1	1 577	5.0	11.3	80	1.4	1.218	1.89
C-2	3 344	3.9	9.3	83	2.5	1.007	1.34
C-3	4 878	3.8	7.9	84	5.0	0.936	1.29
C-4	17 628	2.9	5.5	86	3.0	0.871	1.30
C-5	9 525	3.2	8.9	80	3.6	0.834	1.38
Overall	36 952	3.3	7.3	84	3.3	0.897	1.35

[#] Dust collected and continuously recycled to furnace, expressed relative to mass of PGM-containing feed

[*] Gross energy consumption MWh/ton PGM-containing feed

[$] Electrode consumption expressed as kg graphite per ton of PGM-containing feed processed

Energy consumption (gross) decreased from an average of 1.22 MWh/t in the first campaign to 0.83 MWh/t for the fifth. The lower gross energy consumption was associated with increased throughput and higher equipment availability.

The average gross energy consumption for the months with a throughput exceeding 900 tons was 0.866 MWh/t, while the average for months with less than 900 tons throughput was 1.018 MWh/t. The average throughput per month and estimated thermal efficiencies according to this criterion is summarised in Table 6.17. The figures quoted for 'specific energy

consumption' have taken into account the energy losses from the furnace vessel, and reflect only the energy that is required for the process itself.

Table 6.17 Summary of energy consumption and thermal efficiencies based on throughput

No of months	Throughput	Average monthly throughput	Average Power	Total energy consumption	Specific energy consumption	Thermal efficiency
	tons	tons	kW	MWh/ton	MWh/ton	%
17	< 900	674	1148	1.018	0.634	62
25	> 900	1037	1366	0.866	0.632	73
42	All	895	1286	0.897	0.631	70

Table 6.18 summarises the weighted average chemical composition of the revert tailings treated during the five campaigns. PGM content was analysed by fire assay, with the total reported here (as PGM 4e) representing the sum of the individual values for Pt + Pd + Rh + Au. In general, the chemical composition of the tailings was fairly consistent, although a marked drop in PGM content occurred during the fourth campaign. Upon investigation it was found that the revert tailings dumpsite had been disrupted and contaminated with significant amounts of lower-grade slag. The PGM grade of the feedstock varied significantly during the last two campaigns, and continuous attempts were made to salvage the highest possible grades from the dumpsite by implementing systematic reclamation or selective mining, as well as visual screening of the stocks prior to moving the materials off the dumpsite. Overall, a maximum PGM content of 130 g/t was measured, whilst the grade dropped as low as 6 g/t for a short period during the fourth campaign. The overall weighted average PGM grade for the 36 952 tons processed was 51 g/t.

Table 6.18 Revert tailings composition, mass % (PGM listed in g/t)

Campaign	Al_2O_3	C	CaO	Co	Cr_2O_3	Cu	FeO	MgO	Ni	S	SiO_2	PGM 4e
1	3.65	0.22	6.04	0.17	2.56	0.29	34.7	10.14	0.99	0.84	34.2	64
2	3.76	0.20	6.69	0.18	2.67	0.31	33.2	10.55	1.08	0.86	33.4	72
3	3.51	0.24	6.62	0.17	2.53	0.30	34.0	10.39	1.04	0.76	34.6	61
4	3.79	0.30	6.52	0.13	2.37	0.26	31.5	12.49	0.74	0.72	37.1	39
5	3.74	0.28	6.09	0.14	2.30	0.38	31.8	11.91	1.00	0.78	36.5	58
Overall	3.73	0.27	6.42	0.14	2.41	0.30	32.2	11.79	0.89	0.76	36.2	51

Typically, slag with very low levels of residual PGMs was produced, and no appreciable entrainment of PGM-containing alloy prills in the slag was encountered. The weighted average overall PGM content in the slag was 1.1 g/t, with contents less than the 0.28 g/t analytical detection limit frequently reported. The degree of reduction was controlled by adjusting the carbon addition, generally controlling the reducing conditions to produce the minimum alloy fall whilst maintaining an acceptable recovery of the PGMs. (Anthracite, with about 75% fixed carbon, was utilized as the carbon source.) Although very low levels of PGMs in slag are achievable, a deliberate decision was taken to limit the degree of iron reduction (minimizing alloy fall) whilst marginally compromising on PGM recovery for the sake of minimizing the amount of alloy that would require further downstream treatment. (It is an important feature of the process that it allows this degree of control.) All alloy was re-melted and granulated off-site, and the quantity of alloy impacted directly on the treatment costs. The barren slag was initially returned to the client's own slag stockpile, but, later, the approximately 8 000 tons of slag from the final campaign was crushed and utilized as aggregate or backfill. The slag stockpile at Mintek is shown in Figure 6.5. The weighted compositions of the slags produced during the various campaigns are listed in Table 6.19. The PGM content of the slag was analysed by a fire assay – gravimetric procedure (fire assay fusion followed by cupellation and a gravimetric finish) and so represents the approximate total of Pt + Pd + Rh + Au

(PGM 4e). The average slag tapping temperature was 1585°C, at which temperature the physical properties of the slag were acceptable, and the alloy could be tapped at temperatures within 100°C of the alloy liquidus.

Figure 6.5 Slag stockpile, with gas-cleaning plant in background

Table 6.19 Furnace slag composition, mass % (PGM listed in g/t)

Campaign	Al_2O_3	C	CaO	Co	Cr_2O_3	Cu	FeO	MgO	Ni	S	SiO_2	PGM 4e
1	4.78	0.06	7.46	0.04	3.09	0.07	28.2	12.71	0.10	0.32	43.1	1.55
2	4.75	0.06	7.86	0.05	3.28	0.08	28.8	12.75	0.08	0.32	40.1	1.29
3	4.56	0.07	7.98	0.05	3.08	0.09	31.0	12.34	0.11	0.34	40.1	1.72
4	4.46	0.06	7.33	0.05	2.76	0.10	29.2	14.12	0.12	0.34	41.5	1.00
5	4.06	0.02	6.51	0.03	2.61	0.08	26.5	15.56	0.10	0.34	41.5	0.90
Overall	4.41	0.05	7.27	0.05	2.83	0.09	28.7	14.06	0.11	0.34	41.3	1.12

The mass and weighted compositions of the alloy produced are listed in Table 6.20.

Table 6.20 Alloy composition, mass % (PGM listed in g/t)

Campaign	Tons	C	Co	Cr	Cu	Fe	Ni	S	Si	PGM 4e
1	179	0.11	1.23	0.21	2.05	83.7	8.1	3.71	0.49	462
2	313	0.08	1.43	0.18	2.69	79.2	11.0	5.94	0.27	771
3	385	0.10	1.60	0.14	3.07	75.6	12.5	5.78	0.25	880
4	964	0.06	1.48	0.16	3.17	74.8	10.8	6.57	0.24	634
5	846	0.05	1.23	0.19	3.67	77.9	10.5	6.13	0.16	597
Overall	2 687	0.07	1.40	0.17	3.18	77.0	10.8	6.05	0.24	662

The intention in this process is to separate the valuable metals from the Fe and the gangue constituents that are present in the slag. The desirable area of operation is clearly somewhere in the region where the recovery of PGMs and valuable base metals is high, and the recovery of Fe to the alloy is still reasonably low. This is possible, because Co, Cu, and Ni are preferentially reduced over Fe, especially under less reducing conditions. The addition of carbon is therefore one of the primary variables utilized in order to control the selective deportment of the valuable metallic elements to the alloy phase, in order to optimize recovery of PGMs and other valuable metals, whilst minimizing the recovery of Fe to the alloy phase.

The degree of deportment of the various elements to the alloy phase is, of course, of principal interest in any metal recovery process. During the life of the project, a detailed daily elemental mass balance was compiled which provided the detailed deportments of various elements of interest. The recovery of a given element is here expressed as the ratio between the mass of its content in the alloy divided by the combined mass of its content in the alloy and slag. The basis of this assumption is that all dust captured in the bag-house was fully recycled to the furnace, and the overall elemental accountability was good. The recoveries of various elements of interest are listed in Table 6.21. It is important to bear in mind the earlier comment that the operation of the furnace was focused not on

maximum recovery, but on balancing a good recovery with the production of a minimum amount of alloy.

Table 6.21 Recovery of elements to the alloy, % of feed

Campaign	Co	Cr	Cu	Fe	Ni	PGM 4e
1	80.4	1.4	80.4	34.8	92.2	97.7
2	76.7	0.9	78.6	28.0	94.0	98.5
3	74.3	0.6	74.8	21.6	91.0	97.8
4	63.1	0.5	66.5	16.9	84.5	97.5
5	81.3	1.1	82.2	28.7	92.1	98.6

Parameters for the $K\gamma$ recovery equation, described in detail in Chapter 3, were established for the conditions of interest. The recovery, or degree of collection, of the valuable metals is a function of the extent of reduction in the furnace, which, in turn, is indicated by the fraction of iron present in the feed materials that reports to the alloy. The recovery equation relates the recovery of various metals (such as Ni, Co, PGMs, and Cr) to the recovery of Fe. This equation has proved to be a useful tool to model the recovery relationships during smelting, and to predict the required process parameters for new feed materials.

6.10 Operation of the 3 MW DC Arc Furnace

In order to demonstrate (and benefit from) the economy of scale that results from greater throughput, Mintek's pilot-plant smelter was upgraded during August and September 2008 to a (nominally 3 MW) furnace, with a shell diameter of 4.25 m, that was designed to have a capacity that was double that of the previous furnace (*i.e.*, 2 000 tons per month instead of 1 000 tons per month). In addition to the smelting facility upgrade, an industry-standard flash drier replaced the electrically heated kiln previously utilized for drying, and a pneumatic feed system was also added. Figure 6.6 shows the 3 MW furnace in operation.

Figure 6.6 First slag tap from Mintek's 3 MW furnace, 4 October 2008

Various feed materials were smelted in the 3 MW furnace, with a wide variation in composition. The furnace was remarkably tolerant of most variations. There were some feed materials with a very low iron content, and, when these were smelted, it was necessary to ensure that they were blended with other materials with a higher iron content. The process is based on the collection of the valuable metals in an iron alloy, so there obviously has to be sufficient iron present to do this. One good solution is to use a PGM-containing iron source, such as converter slag, as a part of the feed to the furnace.

Unfortunately, some of the materials that arrived for smelting had a sulfur content somewhat higher than was desirable. This resulted in reductive matte smelting taking place.

6.10.1 Reductive matte smelting

Addition of carbon to PGM-containing sulfide concentrates in a furnace results in some of the iron (and other metallic) oxides being reduced to the metallic state. To some degree, the chromium oxides from UG2 concentrates will be reduced to CrO, thereby becoming more readily soluble in the slag. These advantages are similar to those enjoyed by the ConRoast process (where sulfur is removed in a fluidized-bed roaster prior to smelting, and the PGMs are collected in an iron-rich alloy), yet there are significant differences between 'reductive matte smelting' and 'reductive alloy smelting'.

Reductive matte smelting is constrained to produce a sulfur-rich matte product, either for reasons of crushability or for compatibility with an existing downstream process. This negates the advantage of the alloy having a high liquidus (melting) temperature that is compatible with that of the slag; and there is considerably higher risk of the super-heated matte penetrating the refractories and breaking out of the furnace.

The reductive matte-smelting work described here covers two roughly six-month periods of operation of Mintek's 3 MW DC arc furnace, which has a shell diameter of 4.25 m. The four years of reductive alloy smelting of revert tailings in a 1.5 MW DC arc furnace with a shell diameter of 3.0 m, is used as a reference point for the comparison of the more recent furnace campaigns.

It was common practice during the two reductive matte-smelting campaigns to work with a blend of feed materials, typically somewhere around a 75:25 mixture of various high-chromium concentrates to converter slag. The converter slag provided a convenient supplementary source of iron for the process, and resulted in an overall slag composition that was acceptable in terms of liquidus temperature and viscosity, and was not overly aggressive. The compositions of the blended feed for each of the campaigns are shown in Table 6.22. The compositions of the slag and alloy (or matte) products are shown in Tables 6.23 and 6.24. In these tables, the sections marked 'Alloy smelting' refer to the four years of 1.5 MW revert tailings smelting work.

In both cases, for reductive alloy smelting and reductive matte smelting in a DC arc furnace, it is possible to vary the degree of reduction of the iron oxide in the feed to metallic iron. The recoveries of the valuable metals are directly linked to the extent to which iron oxide is reduced to the metallic state. Clearly, the mass of the alloy (or matte) that is produced in the furnace is also directly linked to the extent of iron recovery to the alloy. This allows the operator of the furnace significant flexibility to choose the desired operating point, and allows a trade-off to be made between the recovery of the valuable metals and the quantity of alloy that is produced (which then needs to be treated further). In light of this, not too much should be read into the variations between the residual PGM contents of the slags listed below, as these figures simply reflect the operating choices that were preferred (or specified by the client) at the time.

Table 6.22 Feed composition, mass % (PGM listed in g/t)

	Al_2O_3	CaO	Co	Cr_2O_3	Cu	FeO	MgO	Ni	S	SiO_2	PGM 4e
Alloy Smelting	3.73	6.42	0.14	2.41	0.30	32.2	11.79	0.89	0.76	36.2	51
Oct 2008-Mar 2009	5.17	3.85	0.13	2.45	0.66	24.54	14.26	1.34	1.53	40.46	74
Oct 2009-Mar 2010	3.50	2.80	0.12	2.30	0.82	20.91	18.59	1.50	1.99	40.87	167

Note: PGM 4e = Pt + Pd + Rh + Au

Table 6.23 Slag composition, mass % (PGM listed in g/t)

	Al_2O_3	CaO	Co	Cr_2O_3	Cu	FeO	MgO	Ni	S	SiO_2	PGM 4e
Alloy Smelting	4.41	7.27	0.05	2.83	0.09	28.7	14.06	0.11	0.34	41.3	1.12
Oct2008-Mar 2009	6.38	4.51	0.04	3.00	0.10	18.15	17.51	0.08	0.18	48.18	0.48
Oct2009-Mar 2010	4.15	3.11	0.06	2.59	0.15	20.70	20.96	0.19	0.28	45.81	1.70

Table 6.24 Alloy composition, mass % (PGM listed in g/t)

	C	Co	Cr	Cu	Fe	Ni	S	Si	PGM 4e
Alloy Smelting	0.07	1.40	0.17	3.18	77.0	10.8	6.05	0.24	662
Oct 2008-Mar 2009	0.05	0.94	0.46	5.56	67.18	12.26	11.42	0.18	749
Oct 2009-Mar 2010	0.04	0.83	0.30	10.42	46.31	20.18	19.13	0.17	1968

6.10.2 Campaign 1: October 2008 – March 2009

In the first six months of commissioning, ramp-up, and operation, the new furnace smelted over 6 000 tons of PGM-containing feed material, and produced almost 15 000 ounces of PGMs in alloy form. Table 6.25 shows that, after the initial start-up period, there were four months of operation where the PGM recovery was in excess of 99.5%.

Table 6.25 Mintek's 3 MW furnace production summary for first six months (Oct 2008 – Mar 2009)

	Oct 2008	Nov 2008	Dec 2008	Jan 2009	Feb 2009	Mar 2009	Total
Tons smelted, t	304	814	1 266	1 229	1 349	1 196	6 158
PGM oz (4e) in alloy	622	1 327	3 972	3 400	2 392	3 208	14 920
PGM (4e) in slag, g/t	2.59	0.71	0.33	0.31	0.34	0.28	-
Built-up Recovery*	96.8%	98.9%	99.7%	99.7%	99.5%	99.7%	-

* Built-up recovery = Mass of PGM (4E) in alloy /
(Mass of PGM in alloy + Mass of PGM in slag)

The first campaign in the then-new 3 MW furnace started out with the intention of doing alloy smelting, as before. However, a serious challenge occurred as a result of feed materials arriving with too high a sulfur content (Jones & Geldenhuys, 2010). This resulted in the formation of an alloy with a much lower liquidus temperature than the process is designed to accommodate. The superheated alloy then caused rapid wear of the side-wall refractories, resulting in a leak adjacent to the alloy tap-hole on 27 March 2009. The escaping stream of superheated molten high-sulfur alloy cut through one of the cooling circuits, resulting in a series of metal-water explosions just outside the furnace. This incident was well managed and there were no injuries or burns, but it did cause a three-week shutdown of the furnace while repairs were carried out. The incident highlighted the benefits of operating in a low-sulfur alloy-smelting mode, as about four and a half years of previous incident-free operation were starkly contrasted with a mere six months of operation in high-sulfur mode. This clearly pointed out the limitations of high-sulfur feed materials, and the necessity for a full implementation of the ConRoast process including the roasting step. It had been expedient to simply smelt

the feed materials directly without first installing a roaster, and this worked quite satisfactorily as long as the sulfur content of the feed was low.

6.10.3 Campaign 2: October 2009 – March 2010

A second opportunity to try out reductive matte smelting in the 3 MW DC arc furnace came about almost exactly a year after the first. This time there was a requirement to produce a crushable (rather than granulated) matte product from a range of high-sulfur feed materials.

In order to produce a matte with a close-to-conventional composition, it was necessary to limit the amount of metallic iron that was produced by reduction of iron oxide. This imposed quite a constraint on the operation, as it was also necessary to meet the need for high PGM recoveries.

Because of the ever-present risk of furnace failure caused by super-heated matte, it was prudent to operate the furnace at a lower power intensity (about 60% of what was used for the alloy-based ConRoast process). In this case, a target throughput of 1200 tons per month was used, although constraints on the supply of feed material limited actual throughputs to around 1000 tons per month.

The very high sulfur content of the matte resulted in it having a very low liquidus temperature (relative to that of the slag). The superheated matte has a great propensity for penetrating the refractory lining of the furnace. There was a marked difference between the alloy-smelting and matte-smelting operations, in terms of SO_2 emissions from the furnace, especially in the immediate working environment during slag and matte tapping.

A notable feature of this campaign is that a significant portion (around a quarter) of the PGMs seemed to stay behind in the furnace. This PGM 'lockup' (inventory inside the furnace) continued to increase for a number of months. At the conclusion of this particular smelting contract, it was required to dig out the furnace contents because of the extensive 'lockup' of the valuable alloy / matte product which was believed to have penetrated the refractory lining including the hearth. It was very clear from a visual inspection of the furnace, during the dig-out, that the matte had penetrated the hearth refractory material (normally over one metre thick) almost all of the way to the bottom of the furnace. There was also evidence of matte penetration between refractory bricks in the side-walls.

The DC arc furnaces that were used for the testwork were lined with refractory bricks similar to those used in conventional matte smelting furnaces, although the hearth design of the DC arc furnace is quite different.

6.10.4 Comparison of reductive alloy smelting and reductive matte smelting

Some highlights of the comparison between the various campaigns are shown in Table 6.26. Most noteworthy is the increase in the sulfur content of the feed material, from 1.5% to 2.0% (compared to much lower average 0.76% S content in the previous four-year alloy-smelting series of campaigns). The higher-S feed resulted in alloys containing averages of 11% and 19% S (and a maximum of 24%) for the two reductive matte-smelting campaigns.

Table 6.26 Summary of main features of the furnace campaigns

	Alloy Smelting	**Oct 2008 – Mar 2009**	**Oct 2009 – Mar 2010**
Duration	~4 years	6 months	6 months
Tons smelted	~37 000	6158	5793
Highest tons/day	47.1 (=1430 t/m)	65.8 (=2000 t/m)	47.2 (=1440 t/m)
Mass of Alloy / Mass of Feed, %	7.3	10.0	6.5
Mass of Slag / Mass of Feed, %	84	82.0	94.2
%S in feed	0.76	1.53	1.99
%S in alloy, average	6.1	11.4	19.1
%S in alloy, maximum	N/A	15.6	23.9
% Cr_2O_3 in feed	2.4	2.5	2.3
Mass Cr in alloy / Mass of Cr in feed, %	0.5 – 1.4	2.8	1.2
PGM recovery, % Alloy / (Alloy + Slag)	99	99	99
PGM retention in furnace = 1 – ((Alloy + Slag) / Feed)	Not directly comparable with other two campaigns	-2%	23%
Furnace integrity	No failures in four years of operation	Tap-hole leak after six months	No failure, but extensive matte penetration of refractories
Corrosion of steelwork	No significant corrosion	Off-gas area	Corroded upper side-walls and off-gas area
SO_2 emissions from furnace	Very low	Significant	High

Testwork at Mintek has shown that reductive matte smelting in a DC arc furnace is able to accommodate the smelting of high-chromium feed materials by means of using carbon as a reductant to ensure the solubilisation of chromium oxide in the slag. However, because of the high sulfur content of the feed materials to the furnace, the major challenges of furnace integrity and sulfur emissions remain, using this approach.

The use of a smelting approach that is a hybrid of matte smelting and reductive alloy smelting is akin to the idea of trying to 'cross a chasm using small steps'. It is better to choose which side of the chasm you would like to be on and then to fully embrace all aspects of that option.

The preferred solution to the problem of smelting UG2 concentrates involves roasting of the concentrates to remove most of the sulfur prior to smelting, followed by reductive alloy smelting in a DC arc furnace. This process is unconstrained by the amount of chromium present in the feed, is much environmentally cleaner in terms of sulfur emissions, is much less prone to failure of furnace containment, and achieves very high recoveries of PGMs. The resulting alloy can be treated further either hydrometallurgically, or pyrometallurgically by converting to remove the iron to produce a product very similar to a conventional converter matte.

6.11 Furnace Equipment Design Specifications

The smelting step of the ConRoast process has been demonstrated at power levels around 1.5 MW and 3 MW. The most likely scale for the first industrial implementation of this process is around 5 to 10 MW. For this reason, consideration is given here to the design specifications for a range of furnace sizes, each separated by a factor of two in power.

6.11.1 Power, throughput, and diameter for the DC arc furnace

At each scale of operation, the throughput of PGM-containing concentrate is determined by the power available to the process. The specific energy requirement (SER) of the smelting process (the energy required to transform the feed materials at 25°C to the product streams at the

temperatures at which they leave the furnace) is typically around 0.63 MWh per metric ton of concentrate (Geldenhuys & Jones, 2009). In addition to this, some of the supplied energy is lost from the outside of the furnace vessel. The thermal efficiency of the furnace (the ratio of the energy that is used by the process itself to the total energy supplied to the furnace) generally increases as the size of the furnace gets larger. The exact value of the rate of energy loss from the furnace vessel depends on the surface area and local energy fluxes in each area, and so is a function of the detailed mechanical design of the furnace. However, typical values can be used to give a very good indication of the throughput of the furnace. At the low end, a thermal efficiency of 70% has been measured (Geldenhuys & Jones, 2009), and this is expected to be around 85% at the high end.

6.11.2 Electrical design of the power supply for the DC arc furnace

The electrical specifications for the furnace transformer and rectifier have been calculated using the methods outlined in Chapter 4.

The electrical characteristic curves for the various sizes of furnace have been generated by calculating the sum of the arc voltage and bath voltage at each value of the current. The arc voltages are calculated using Bowman's model, with an arc resistivity of 0.0175 Ωcm (which is an experimentally determined typical value for processes that produce CO gas). The bath voltages are calculated from a solution of the Laplace equations (using Mintek's *BathVolt* software) for the distribution of potential in the molten slag bath (with an assumed value of 6:1 for the diameter:depth ratio of the arc depression, based on photographs). The bath voltage is directly proportional to the electrical resistivity of the slag.

The Current-Voltage graph shown in Figure 6.7 shows the constant power curves for 1.25, 2.5, 5, and 10 MW, as well as the characteristic behaviour of the furnace voltage (a combination of arc and bath voltages) in terms of the operating current. The expected slag resistivity is 2 Ωcm, but the furnace needs to be able to accommodate a range of feed materials, so curves are also shown for slag resistivity values of 1 Ωcm and 3 Ωcm. For each value of slag resistivity, a range of practical arc lengths (10 cm to 50 cm) is also shown. The voltage and current limits have been chosen, for each scale of operation (power level), to ensure that there is a practical and feasible region of operation for the full range of slag resistivities under consideration (even if the full range of arc lengths is not available at the extreme values of slag resistivity). For example, in the case of the highest chosen power level, the furnace power supply must provide 10 MW of power to the furnace, and needs to have a maximum voltage of 1000 V and a maximum current of 18 kA. The red dots on the diagram (halfway between the extremes) indicate the expected normal operating point of the power supply at each of the four nominal power levels.

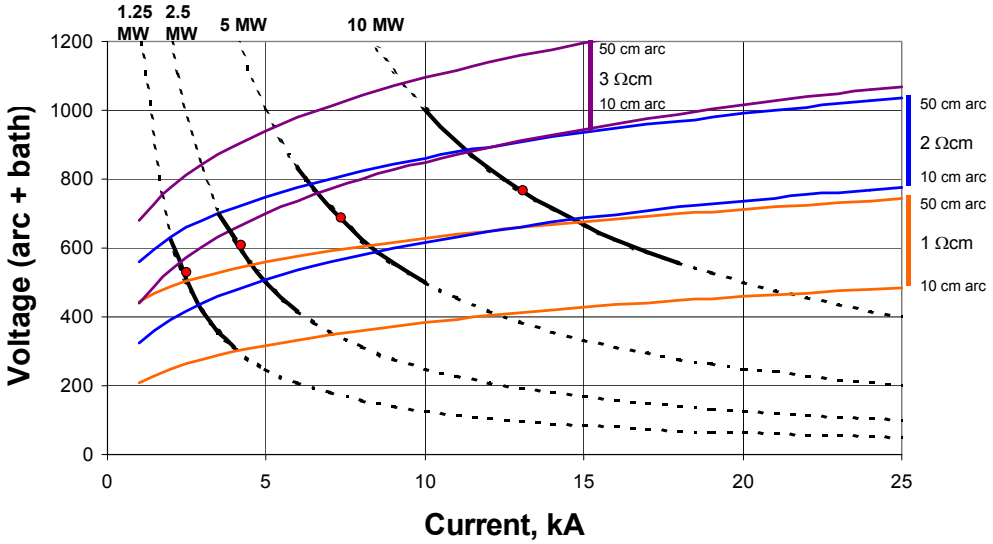

Figure 6.7 Electrical characteristic curves for various DC arc furnaces

It was explained in Chapter 4 that the bath voltage is a rather complicated function of current and the geometry of the slag bath, including that of the arc depression. However, the modelled functional relationship between current and bath voltage remains almost exactly the same in each of the four cases considered here. In each case, the same assumed value of 6:1 was used for the diameter:depth ratio of the arc depression, the slag density was taken to be 3500 kg/m^3, and the slag depth was taken to be 50 cm.

As was shown in Section 4.5.1, for all practical (sufficiently wide) aspect ratios, the diameter of the molten slag bath has very little effect on the bath voltage. As the furnace diameter increases, the bath voltage tends towards a fixed value, as less and less current spreads to large radial distances. For example, there is less than 0.2% difference in the calculated bath voltage when comparing diameters of 2 m or 4 m.

Using quintic regression, and the assumptions listed above (including that of a 'sufficiently wide' furnace diameter), the bath voltage V_b for a slag depth of 50 cm and with an electrical resistivity of 1 Ω.cm can be well represented by Equation [6-5], where I represents current in kA, for the range 1 to 25 kA. As the bath voltage is directly proportional to the electrical resistivity of the slag, it is straightforward to calculate the bath voltage for other values of slag resistivity.

$$V_b = 86.67 + 34.747\,I - 3.78023\,I^2 + 0.248784\,I^3 - 0.00828\,I^4 + 0.000107\,I^5 \quad [6\text{-}5]$$

6.11.3 Tap-hole spacing

The positioning of the slag and alloy tap-holes depends on a number of factors. The alloy tap-hole needs to be as low as possible, in order to

minimize the quantity of valuable alloy retained in the furnace. The level of the alloy in the furnace is expected to remain relatively constant, fluctuating by only a few mm per hour, as only a small quantity of alloy is produced (typically about 10% of the mass of the concentrate fed), and the relative density of the alloy is high (around 7), about twice that of the slag. The slag tap-hole is positioned to control the minimum depth of slag in the furnace, as it is usual to drain the slag from the furnace to the level of the slag tap-hole during the tapping operation.

In order to promote steady electrical operation of the furnace, the slag layer should be thick enough to ensure that the arc does not penetrate directly through the slag to the alloy. In the cases considered here, the current has a maximum value of 18 kA, and this is associated with a typical arc cavity depth of about 4 cm, and a maximum of 14 cm. It would perhaps be advisable to have a minimum slag depth that is double the maximum arc cavity depth. From this perspective, a minimum slag depth of 30 cm is recommended.

In earlier batch tests that were done on related alloy-collection smelting processes in DC arc furnaces (Jones, Hayman, & Denton, 1996), it was found that very high metal recoveries were achievable if the retention time of the slag (after completion of feeding) was around two hours or more. This is not a hard-and-fast rule, but is a good indication that the desirable mean residence time of the molten slag in the furnace should be three hours or more. In addition to this guideline, practical operating constraints dictate a tap-to-tap time of one to two hours, depending on the desired slag-tapping batch size. It is possible, using the method developed in Chapter 5, to calculate the mean residence time of the molten slag in the furnace. Equation [5-12], repeated below as [6-6], expresses the

mean residence time in terms of the tap-to-tap time, t, and the fraction of slag removed during tapping ($1/f$).

$$\text{Mean residence time } R = t\left(f - \frac{1}{2}\right) \qquad [6\text{-}6]$$

As shown in Table 6.27, the quantity of slag generated in the furnace is approximately 8 cm per hour (across a wide range of scales of operation). Calculations have been carried out for tap-to-tap times of one, two, and three hours, representing the range of normal operation and taking into account the possibility of delayed tapping.

For t = 1 h: 8 cm of slag tapped; slag depth = 30 - 38 cm; $1/f = 8/38$; $f = 4.8$
Mean residence time R = 4.3 hours

For t = 2 h: 16 cm of slag tapped; slag depth = 30 - 46 cm; $1/f = 16/46$; $f = 2.9$
Mean residence time R = 4.8 hours

For t = 3 h: 24 cm of slag tapped; slag depth = 30 - 54 cm; $1/f = 24/54$; $f = 2.3$
Mean residence time R = 5.3 hours

In each case, the mean residence time is more than sufficient to ensure full reaction and good settling of the droplets of alloy produced.

6.11.4 Summary of ConRoast furnace design specifications

Table 6.27 presents a summary of the furnace design specifications that have been discussed in Section 6.11. These include those related to power and throughput, as well as the furnace diameter and its relation to the specified power intensity. The electrical design is summarised, as is the tapping configuration.

Table 6.27 Summary of ConRoast furnace design specifications: 1.25 - 10 MW

Furnace power, MW	**1.25**	**2.5**	**5**	**10**
Specific energy requirement, MWh/t	0.63	0.63	0.63	0.63
Thermal efficiency	70%	75%	80%	85%
Hourly throughput of concentrate, t/h	1.39	2.98	6.35	13.49
Overall plant availability	90%	90%	90%	90%
Equipment capacity utilization	90%	90%	90%	90%
Operating hours per year	7096	7096	7096	7096
Annual throughput of concentrate, kt/a	9.855	21.118	45.051	95.734
Power intensity, kW/m^2	250	250	250	250
Internal diameter, m	2.5	3.6	5.0	7.1
Shell diameter, m	3.0	4.1	5.5	7.6
Arc resistivity, Ω.cm	0.0175	0.0175	0.0175	0.0175
Arc length, cm	10 - 50	10 - 50	10 - 50	10 - 50
Molten slag resistivity, Ω.cm	1.0 - 3.0	1.0 - 3.0	1.0 - 3.0	1.0 - 3.0
Molten slag depth, cm	35 - 50	35 - 50	35 - 50	35 - 50
Molten slag density, t/m^3	3.5	3.5	3.5	3.5
Maximum design voltage, V (Insulation components to be designed for this voltage)	660	750	850	1000
Normal operating voltage, V (90% of the time)	520	600	700	750
Maximum design current, kA (High-current conductors to be designed for this current)	3	6	10	18
Normal operating current, kA (90% of the time)	2.4	4.2	7.1	13.3
Furnace transformer rating, MVA (Maximum V x Maximum I)	2.0	4.5	8.5	18
Slag tapping temperature, °C	1600	1600	1600	1600
Alloy tapping temperature, °C	1500	1500	1500	1500
Slag tap-hole diameter, mm	100	100	100	100
Alloy tap-hole diameter, mm	50	50	50	50
Mass of slag per 10 cm of depth, t	1.8	3.5	7.0	14.0
Tons of slag produced per t of concentrate	0.9	0.9	0.9	0.9
Slag production, cm/h	7.1	7.7	8.2	8.7
Tons of alloy produced per t of concentrate	0.1	0.1	0.1	0.1
Alloy production, cm/h	0.40	0.43	0.45	0.48
Height difference between slag and alloy tap-holes, cm (centre to centre)	30	30	30	30
Slag tapping interval, h	2	2	2	2
Slag mass per tap, t	2.5	5.4	11.4	24.3
Alloy tapping interval, h	24	24	24	24
Alloy mass per tap, t	3.3	7.1	15.2	32.4
Mean residence time of slag, h	5.2	4.9	4.7	4.5

6.12 Testing of Other Parts of the Process

The DC arc furnace cannot be investigated in isolation from the other components of the ConRoast process. In order to demonstrate the full process, a number of other steps also had to be piloted. These included drying, roasting, atomization (or granulation), converting, various hydrometallurgical options, and carbonyl processing of the alloy by chemical vapour metal refining (CVMR). Some of these are described in further detail below.

6.12.1 Roasting for sulfur removal

Roasting of sulfide concentrates has been practised for centuries. Oxidative roasting of pyrite (FeS_2) is a standard way of producing sulfuric acid. In many base metals plants, roasting is used on an industrial scale, *e.g.*, for the production of zinc, copper, and nickel, even tin, molybdenum, and antimony. In many cases, the roasting operations take place in conjunction with one or more leaching or smelting operations. Roasting is used in order to capture some of the sulfur present in the concentrates produced from sulfidic ores. The general approach used in sulfide roasting is to oxidize some (or all) of the sulfur, and treat the resulting SO_2, most commonly producing sulfuric acid in an acid plant. Other options for recovery of sulfur include the production of elemental sulfur, or liquid SO_2.

Modern roasting processes (since about 1960) usually use fluidized-bed reactors, which are energy-efficient, and have a high productivity because of their favourable kinetic reaction conditions and excellent mass transfer. The SO_2 content in the off-gas is typically 8 to 15% by volume.

Roasting may be used to prepare sulfide concentrates for subsequent pyrometallurgical or hydrometallurgical operations. For pyrometallurgical processing, the usual purpose of roasting is to decrease the sulfur content to an optimum level for smelting to a matte. Partial (oxidizing) roasting is accomplished by controlling the access of air to the concentrate; a predetermined amount of sulfur is removed, and only part of the iron sulfide is oxidized, leaving the copper sulfide (for example) relatively unchanged. Total, or dead, roasting involves the complete oxidation of all sulfides, usually for a subsequent reduction process. (For hydrometallurgical extraction, roasting forms compounds that can be leached out.)

The roasting process has several effects:
a) Drying the concentrates
b) Oxidizing a part of the iron present
c) Decreasing the sulfur content by oxidation
d) Partially removing volatile impurities; for example, arsenic
e) Preheating the calcined feed with added fluxes (for example, silica or limestone), in order to lower the energy requirement of the downstream process.

There are many modern pyrometallurgical processes (flash smelting, for example) in which roasting is not a separate step, but is combined with matte smelting. Flash furnaces (such as those developed by Outokumpu or Inco (now Vale), for example) employ sulfide concentrate burners that both oxidize and melt the feed, and are used extensively in the copper industry. Autogenous bath smelting (as used, for example, in the Isasmelt or Ausmelt furnaces) is another alternative that is also used. Here a lance blows air or oxygen, together with concentrates and reductant, into a

molten bath, and the energy released by the oxidation of the sulfur provides much of the required energy for the smelting process.

Environmental concerns have highlighted the need to lower the emissions of sulfur from smelters treating sulfidic raw materials. These emissions emanate primarily from the furnaces and Peirce-Smith converters, either as fugitive emissions or as process gases vented up a stack. It should be noted that the typical low concentration (1 to 2%) of SO_2 in the off-gas from many furnaces is too low for effective acid production.

A common trend in nickel sulfide smelting in recent years has been to eliminate as much as possible of the iron sulfides (usually pyrrhotite) during the milling and flotation stages, in order to minimize the sulfur input to smelters.

Dead roasting, *i.e.*, close to 100% sulfur removal, has the benefit of removing essentially all the sulfur at the beginning of a smelting process, thereby avoiding the sulfur emission problem from the smelter. Furthermore, in comparison with the intermittent nature of SO_2 produced in a converting operation, a steady and almost optimum SO_2 content of off-gas from a roaster requires a smaller and less expensive acid plant.

Small-scale roasting (and subsequent smelting) tests on a range of PGM concentrates have been completed at Mintek. Pilot-plant roasting testwork, under the direction of the author, has been carried out successfully by Technip (Eccleston & White, 2008) in the USA, and by Outotec (Hammerschmidt, 2008) in Germany, in order to demonstrate the viability of the roasting process and to obtain sufficient engineering data for the design and costing of the full-scale equipment. The scale of operation considered for the fluidized bed roaster design was for a plant

capable of processing at least 360 000 tons per annum of PGM-containing sulfide concentrates (potentially a mix of UG2 and Platreef concentrates). It was necessary to operate the roasting process at around 1000°C. The roasting testwork clearly demonstrated that it is possible to decrease the total sulfur content of a PGM ore concentrate from about 7% to as low as 0.3% in the cyclone product, with 0.4% as a weighted average of the cyclone and bag-house products.

The demonstration roasting of 300 tons of PGM-bearing flotation concentrate (containing about 7% sulfur) in Germiston, South Africa was also completed, in preparation for further smelting testwork using this material.

6.12.2 Water atomization of alloys

The ConRoast process produces an iron-rich alloy. After tapping the alloy from the furnace, it needs to be produced in a physical form that is conducive to further processing. Water atomization or granulation of the molten alloy can be used for this purpose. Granulation was routinely carried out on much of the alloy produced from the Mintek smelter. However, water atomization can be used as an effective intermediate step between the production of a molten alloy from a smelting furnace and a leaching operation (or even for pneumatic conveying into a pyrometallurgical converter). This is especially appropriate for alloys that are not readily crushable. Very fine particles can be produced by the impingement of high-pressure water jets on a molten alloy stream. The use of very fine material as a feedstock for the leaching process allows for considerable savings in residence time, reactor volume, and lower power consumption for stirring. Testwork was carried out at Atomizing Systems Ltd (Dunkley *et al.*, 2008) in the UK that successfully demonstrated the

production of fine powders, with particles as small as 20 microns that are very suitable for further hydrometallurgical processing. The relationship between the pressure of the water jets and the size of the resulting particles is such that the mean particle size can be halved by doubling the water pressure (over the range of conditions of interest). A pressure of 100 bar resulted in a mean particle size (d_{50}) of 44 μm.

6.12.3 Converting of alloys

The alloy product from the DC arc furnace requires iron removal. The two principal options that have been explored are to do this either pyrometallurgically (by converting) or hydrometallurgically (by leaching). A comprehensive leaching test programme has been undertaken, and a conceptual design has been prepared for a hydrometallurgical pilot plant. (The hydrometallurgical work is not included in the scope of this thesis.)

Small-scale converting tests of the PGM alloy have been conducted at Mintek (McCullough *et al.*, 2008). Significant iron removal has been demonstrated in a laboratory-scale converting process, in which oxygen was bubbled through the liquid alloy, where it was possible to change the distribution of sulfur between the alloy, slag, and gas phases by changing the CaO content of the slag. Some preliminary pilot-scale converting work has also been done at Mintek, resulting in a product very similar to that produced in conventional Peirce-Smith converters in the PGM industry. A few conceptual designs of various converting options have been prepared. Plant-scale trials have been successfully conducted where alloy was co-converted with conventional matte.

The laboratory-scale and pilot-scale converting work reported above was all based on converting as a batch process. However, there are good

reasons for considering a continuous process for larger-scale converting work. A continuous reactor would be preferred to a batch reactor, as this is easier to schedule and operate, and this will also provide a single alloy composition instead of one that changes during the course of the converting operation. A batch process could see the composition of the melt change from a high-iron alloy to that of a matte, over the duration of the converting cycle. However, a continuous process would operate with a steady composition, *i.e.*, that of the final product. Having to contain molten material of a single composition would prolong the life of the refractory lining of the vessel, in comparison with having to deal with an ever-changing composition.

A stationary non-tilting vessel is envisaged for the continuous converter. This is a mechanically simple option, which is expected to be more robust and reliable than having to operate a high-temperature device with moving parts. The converter should have separate tap-holes, at different elevations, for removing the slag and the converted alloy. Slag will be tapped more often than the converted alloy.

A top-blown vessel is envisaged. A number of lance designs are available for use. The non-consumable Sirosmelt lance, as used in Ausmelt and Isasmelt furnaces, is among the most industrially proven designs. Praxair's Coherent Jet oxygen lance has been used successfully in copper furnaces and steel-making furnaces. Another possibility would be to use an oxy-propane gas jet, as is used in Mintek's existing top-blown rotary converter (TBRC); or the lance design from the Kaldo furnace could be used. As a simple alternative, even a scaled-up version of the lab-scale oxygen delivery system could be used, namely a consumable hollow alumina tube immersed in the melt.

Given that the oxidation of iron is highly exothermic, it will be possible to supply the converter with a feed of solid granulated alloy. This would effectively decouple the operation of the smelting furnace from that of the converter, and would allow a stockpile of material to be used as a buffer to ensure steady operation of the converter. An energy balance calculation over the converter shows that it would be possible to control the temperature of the converter by using a mix of air and oxygen-enriched air. The solid alloy can also act as something of a coolant for the very exothermic iron oxidation reaction.

6.13 Economic Considerations

As can be seen from the number of publications about the ConRoast process that emanated in 2008, the technical development of the process was largely completed just before the world economic crisis came to the fore that year. The lack of investor confidence, and shortage of capital or credit, significantly delayed the commercialisation of the ConRoast smelter that was envisaged at that time. This provided a clear message that technical progress does not exist in isolation from world economic considerations. The world's recessionary conditions have curtailed a number of otherwise promising mining projects because of the low availability of credit, the significant decline in the platinum price, and the strengthening rand (for an industry that incurs its costs in rands, but earns its revenues in dollars). If companies can survive the 'interesting times' in which we are living, they will be well poised for significant growth when the economy improves in the years ahead.

6.14 Conclusions

The ConRoast process provides a very good case study of a reductive alloy smelting process that takes place in a DC arc furnace.

The ConRoast process treats sulfide concentrates by roasting (for sulfur removal), followed by reductive smelting in a DC arc furnace, where an iron-based alloy is used to collect the valuable metals. This process can be used for the treatment of nickel sulfide ores as well as those containing platinum group metals (PGMs). In the case of PGM smelting, the ConRoast process addresses the three big challenges, namely the sulfur problem (SO_2 emissions), the chromium problem (from the use of UG2 chromitite ores), and the containment problem (avoiding furnace failures).

The ConRoast process is aimed at being a very different smelter, using a DC arc furnace for alloy smelting (from oxide) instead of matte (sulfide) smelting. Sulfur is removed at the beginning of the process (as a steady SO_2 stream to an acid plant, for example), by dead-roasting the concentrate. The roasting is a continuous process that is done in a well-sealed vessel, and is therefore less environmentally damaging in terms of SO_2 emissions to the atmosphere, let alone to the immediate working environment in the smelter. The PGMs and valuable base metals are collected in an iron-based alloy, which is even more effective than matte in collecting PGMs. This flexible PGM processing route can handle a wide range of feeds, as it has no need for much Ni and Cu (or S) in the ore, as Fe is the collector. The reducing conditions in the furnace (and high temperatures, if required) tolerate much higher levels of Cr_2O_3 in feed (> 5%) without causing a problem with the precipitation of insoluble and refractory chromite spinel ($FeO.Cr_2O_3$). The iron is subsequently removed from the alloy either by converting, or with a few modifications to the base

metals refinery to include one of a number of possible hydrometallurgical iron removal steps.

The implementation of the ConRoast process relies heavily on the $K\gamma$ recovery equation that was developed in Chapter 3, as it is based on selective reduction. The intention is to recover as much as possible of the precious metals and base metals to the alloy, while minimizing the quantity of iron that is reduced to the metallic form. In addition, it is very important to leave essentially all chromium dissolved in the slag as CrO. The $K\gamma$ recovery equation provides a very clear framework for this relationship to be clearly understood.

The containment problem is particularly challenging when having to deal with a matte with a very low liquidus temperature, and a slag with a high liquidus temperature in the same furnace vessel. By changing to an iron-based alloy, this has a similar liquidus temperature to that of the slag, making the problem of containment much easier to manage.

The electrical design of a furnace for the ConRoast process requires the electrical models outlined in Chapter 4, as the slag is of intermediate resistivity (more resistive than titania slag, but less resistive than nickel laterite slag), and the design of the power supply is very important to get right, as there are no existing large industrial installations of the process that would allow the designer to simply rely on present industrial practice.

The residence-time modelling of continuously-fed batch-tapped furnaces, presented in Chapter 5, has also come in useful for the operation of the pilot-plant furnace, as well as for designing the location of the tap-holes of an industrial-scale furnace.

The ConRoast process has been demonstrated by smelting 50 000 tons of PGM-containing feed materials at Mintek over a period of operation of about five years. This large-scale smelting at Mintek involved the processing of up to 2 000 tons per month, using a clean process that produces an alloy product (typically less than 10% of the mass of the feed material), a by-product slag (that meets the criteria for safe disposal, or could be used as a by-product for purposes such as concrete aggregate, road fill, or shot blasting), and clean gas emissions (after passing through a bag-house, SO_2 scrubber, and stack). The initial work entailed four years of reductive alloy smelting of revert tailings (low sulfur, high chromium, otherwise virtually 'untreatable' material) in a 1.5 MW (3.0 m diameter) furnace, where about 37 000 tons of revert tailings material was smelted, with a maximum rate of 47 tons per day. The furnace ran very reliably. At this scale of operation, the demonstration was a very convincing one, as well as producing sufficient product to make the process economically profitable in its own right.

Subsequent work involved the upgrading of the furnace to 3 MW (4.25 m shell diameter), and this furnace was first tapped in October 2008. Two six-month campaigns of reductive matte smelting in the 3 MW DC arc furnace were undertaken, where the feed was a 75:25 mixture of high-chromium concentrate and converter slag, and 12 000 tons was smelted, with a maximum rate of 66 tons per day.

Part of the increased understanding and huge amount of data that came out of this work led to the extension of the very useful $K\gamma$ recovery model for predicting the recoveries of various metals (such as nickel, cobalt, and even chromium) as a function of the iron recovery (which is just a proxy for the extent of reduction in the furnace). This model allows one to

predict the behaviour of any new feed material that is introduced into the furnace.

The ConRoast process is widely seen as being very important to South Africa's platinum industry in the coming years, especially as mines move increasingly towards utilising higher-chromium ores.

7 CONCLUSIONS

This thesis has focused on a number of fundamental aspects of DC arc furnace technology, and their application to a particular novel process.

7.1 Applicability of DC Arc Furnaces

DC arc furnaces have some wonderful features. They are good at accommodating finely sized feed materials (because of the open bath). They do not require coke or char (no burden porosity required). DC arc furnaces can treat feed materials with a wide range of composition (because of the extra degree of freedom coming from power being supplied by an open arc); this allows choice of chemistry for metallurgical benefit. These furnaces are geometrically simple and elegant, which reduces costs associated with complex roof designs and uneven wear on side-walls. However, it is important to take cognisance of the effect of the hot off-gas on thermal efficiency (unless some of this energy is recovered), and of the absence of a burden that could otherwise assist in capturing volatile species that might fume off the molten bath.

Apart from extensive use in the steel industry, it is only in the past few decades that DC arc furnaces have been used for smelting processes, where the feed materials are predominantly non-metallic and significant chemical reactions are involved. Mintek's Pyrometallurgy Division has been fortunate enough to be involved in the industrial-scale commercialisation of roughly one major application of this technology per decade, and has become well known internationally for its work on DC arc furnaces. This started with the smelting of chromite ore fines to

produce ferrochromium in the 1980s, and was followed by the smelting of ilmenite to produce titania slag and pig iron in the 1990s. In both of these cases, the process chemistry was well known and the products were familiar (albeit with some minor variations), even though the type of furnace was novel at the time. A further example was the use of a DC arc furnace to recover metals (principally cobalt) from non-ferrous smelting slags early in the 2000s. In this case, a new process was carried out in a 'new' piece of equipment to produce a somewhat unfamiliar intermediate product. This, therefore, required testing and demonstration at quite a large scale. Since then, there has been commercial application of processes for stainless steel dust smelting and battery recycling. Nickel laterite smelting was commercialised in the 2010s.

DC arc furnaces are well-suited to reductive smelting processes, such as those used for treating chromite, ilmenite, and nickel laterite ores, oxidized concentrates, and slags. On the other hand, DC arc furnaces are less well suited to processes involving a gaseous intermediate such as SiO, or those that might bring a low-melting (super-heated) product into contact with a bottom anode.

DC arc furnaces are not a panacea for all metallurgical problems, but are very well suited to a number of reductive smelting processes where they have been applied successfully in a number of industrial contexts, and many further applications are expected.

7.2 Recovery of Base Metals and PGMs

Base metals and platinum group metals can be collected in metallic alloy form, via a wide variety of smelting processes. The recovery, or degree of collection, of the valuable metals is a function of the extent of reduction in

the furnace, which, in turn, is indicated by the fraction of iron present in the feed materials that reports to the alloy. An equation has been developed that relates the recovery of various metals (such as Ni, Co, Cr, and PGMs) to the recovery of Fe. This recovery equation (for each metal) is characterised by a single parameter ($K\gamma$) that can either be fitted empirically to the data, or expressed in terms of the equilibrium constant and the ratios of the activity coefficients involved. Data from a number of varied DC arc furnace campaigns is presented to illustrate this behaviour.

The $K\gamma$ recovery equation has been found to provide a very useful basis for the design of processes involving the recovery of precious and base metals in DC arc furnaces. The equation produces curves of the correct functional form that are applicable across the whole range of different extents of reduction. The value of $K\gamma$ to be used can be calculated theoretically, but it is often more effective to fit this value to experimental data. $K\gamma$ for a particular metal has a characteristic value that depends on the temperature of operation and to some degree on the composition of the slag and metal system under consideration (as this affects the individual activity coefficients). Process design calculations can be carried out with confidence, knowing that there is good theoretical justification for the form of the equation, and that the single parameter $K\gamma$ is based on experimental work. The simplicity of the equation has made it straightforward to incorporate into spreadsheet models of various processes, and this is now widely used. The equation clarifies the dependency of the recovery of the valuable metals on the recovery of iron in the furnace, and this allows a furnace operator to control the smelting process more easily and to target the correct degree of reduction.

The multi-phase multi-component systems involved in smelting processes have so many variables that it is often difficult to pick out the most

important relationships. One of my most important contributions to the field of reductive alloy smelting was to derive the $K\gamma$ recovery equation, from first principles, to show the relationship between the recovery of a desired metal (such as cobalt or nickel, for example) and the recovery of iron (the fraction of the metal that reports to the alloy, expressed as a fraction of the metal that is present in the feed material). Data sets from numerous pilot-plant campaigns have been used to validate this model, and it is now used by a number of major international mining companies.

7.3 DC Arcs and Electrical Aspects

The power supply is often the item with the longest delivery time when building a furnace, so the voltage and current specifications are often needed at a very early stage of a project. The total power requirement of the furnace is derived from the desired throughput, and the experimentally determined specific energy requirement for the process. The specification of the operating ranges for voltage and current requires a detailed understanding of the scale-up of the furnace design. If the ranges of voltage and current specified for the transformer are greater than necessary, this can result in a great deal of unnecessary expense, and, if the ranges are too low, the furnace might not be operable at all, or it might allow only a very low throughput.

Equations have been developed (and confirmed by photography and measurement) to describe the electrical behaviour of DC plasma arcs, and the voltage distribution across a molten slag bath.

A model using measured and extrapolated arc shapes provides a description of how the arc voltage varies as a function of arc length and current. Measurements of voltage as a function of arc length, obtained

from an industrial 60 MW furnace producing ferrochromium, provide some confirmation of the validity of this model.

The overall electrical behaviour of a DC arc furnace may be modelled as an arc in series with a layer of slag. A two-dimensional axi-symmetric numerical model is used to describe the variation of the potential (voltage) through the molten slag bath.

The voltage distribution across a molten slag bath requires the solution of Laplace's equation for a geometry that includes the depression in the molten slag caused by the impingement of the arc jet. I was able to provide aspect ratios of the arc depression (based on my photographic work) that enabled these calculations to be performed. The depression in the molten slag caused by the impingement of the arc jet has been photographed to determine a likely range of diameter: depth ratios, and a typical value of 6:1 has been used, showing it to be very unlikely that all of the slag is blown away by the arc, even when the current is very high. These photographs of arcs interacting with molten slag, and the ratios of the dimensions inferred from them, provided the basis for a practical usable electrical model of the arc and the slag bath that can be used for the scale-up and electrical design of DC arc furnaces. In addition to the overall methodology that I introduced for the electrical specification of DC furnace power supplies, perhaps my most significant contribution in this area was the series of difficult-to-obtain photographs that allowed typical aspect ratios of the arc depression to be determined.

Another important contribution that I made to the electrical modelling of DC arc furnaces was to highlight the fact that the voltage is very non-linear with respect to the current, and that the behaviour is certainly very

different from that of a constant-resistance device. I have presented illustrations of calculations that show this clearly.

The photographs and theoretical models introduced here have been used extensively to improve the understanding of the operation of pilot-plant furnaces at Mintek, and have been used for the design of larger furnaces as well.

7.4 Residence Time

Equations have been developed to allow one to calculate the mean residence time in a continuously-fed batch-tapped furnace, and this has been illustrated using a novel graphical depiction. This was necessary, as many smelting furnaces do not fit the standard textbook classifications of batch or continuously stirred reactors for which residence time distributions have been well defined. There are some processes in which the time spent by the feed material in a smelting furnace plays a significant role in determining the extent of the reactions between metal and slag, and influences the degree of settling of metal droplets from a molten slag.

The principal factors influencing the residence time include the slag and metal tapping intervals (where the mean residence time is directly proportional to the tap-to-tap time), and the fraction of liquid retained in the furnace (where the mean residence time is increased by increasing the volume of material retained in the furnace between taps).

The residence-time equation is useful for design purposes if one wants to achieve a constant mean residence time when scaling up from a pilot plant to a commercial plant.

During furnace operation, it is sometimes necessary to change the composition of the molten bath, and it is necessary to know how many taps it would take to substantially replace material of the old composition with that of the new. The required number of tapping operations depends strongly on the fraction of material removed during tapping, and this can be calculated using an equation or graphically.

7.5 The ConRoast Process

The ConRoast process provides a very good case study of a novel reductive alloy smelting process that takes place in a DC arc furnace. All of the individual fundamental aspects studied in previous chapters have contributed to the development of this process.

The ConRoast process treats sulfide concentrates by roasting (for sulfur removal), followed by reductive smelting in a DC arc furnace, where an iron-based alloy is used to collect the valuable metals. This process can be used for the treatment of nickel sulfide ores as well as those containing platinum group metals (PGMs). In the case of PGM smelting, the ConRoast process addresses the three big challenges, namely the sulfur problem (SO_2 emissions), the chromium problem (from the use of UG2 chromitite ores), and the containment problem (avoiding furnace failures).

The ConRoast process is aimed at being a very different smelter, using a DC arc furnace for alloy smelting (from oxide) instead of matte (sulfide) smelting. Sulfur is removed at the beginning of the process (as a steady SO_2 stream to an acid plant, for example), by dead-roasting the concentrate. The roasting is a continuous process that is done in a well-sealed vessel, and is therefore less environmentally damaging in terms of

SO_2 emissions to the atmosphere, let alone to the immediate working environment in the smelter. The PGMs and valuable base metals are collected in an iron-based alloy, which is even more efficient than matte in collecting PGMs. This flexible PGM processing route can handle a wide range of feeds, as it has no need for much Ni and Cu (or S) in the ore, as Fe is the collector. The reducing conditions in the furnace (and high temperatures, if required) allow much higher levels of Cr_2O_3 in feed (> 5%) without causing a problem with spinel precipitation. The iron is subsequently removed either by converting, or with a few modifications to the base metals refinery.

Selective reduction allows high recovery of PGMs and base metals while keeping the amount of metallic iron relatively low, and retaining almost all of the chromium dissolved in the slag. By changing the reducing conditions in the furnace, one can move away from having the insoluble and refractory chromite spinel ($FeO.Cr_2O_3$) towards having CrO that dissolves readily in the slag. The $K\gamma$ recovery equation that I developed provides a very clear framework for the selective reduction relationships to be clearly understood.

The containment problem is particularly challenging when having to deal with a matte with a very low liquidus temperature, and a slag with a high liquidus temperature in the same furnace vessel. By changing to an iron-based alloy, this has a similar liquidus temperature to that of the slag, making the problem of containment much easier to manage.

The electrical design of a furnace for the ConRoast process requires the electrical models outlined in Chapter 4, as the slag is of intermediate resistivity (more resistive than titania slag, but less resistive than nickel laterite slag), and the design of the power supply is very important to get

right, as there are no existing large industrial installations of the process that would allow the designer to simply rely on present industrial practice.

The residence-time modelling of continuously-fed batch-tapped furnaces, presented in Chapter 5, has also come in useful for the operation of the pilot-plant furnace, as well as for designing the location of the tap-holes of an industrial-scale furnace.

The ConRoast process has been demonstrated by smelting 50 000 tons of PGM-containing feed materials at Mintek over a period of operation of about five years. This large-scale smelting at Mintek involved the processing of up to 2 000 tons per month, using a clean process that produces an alloy product (typically less than 10% of the mass of the feed material), a by-product slag (that meets the criteria for safe disposal, or could be used as a by-product for purposes such as concrete aggregate, road fill, or shot blasting), and clean gas emissions (after passing through a bag-house, SO_2 scrubber, and stack). The initial work entailed four years of reductive alloy smelting of revert tailings (low sulfur, high chromium, otherwise virtually 'untreatable' material) in a 1.5 MW (3.0 m diameter) furnace, where about 37 000 tons of revert tailings material was smelted, with a maximum rate of 47 tons per day. The furnace ran very reliably. At this scale of operation, the demonstration was a very convincing one, as well as producing sufficient product to make the process economically profitable in its own right.

Subsequent work involved the upgrading of the furnace to 3 MW (4.25 m diameter), and this furnace was first tapped in October 2008. Two six-month campaigns of reductive matte smelting in the 3 MW DC arc furnace were undertaken, where the feed was a 75:25 mixture of high-chromium

concentrate and converter slag, and 12 000 tons was smelted, with a maximum rate of 66 tons per day.

Part of the increased understanding and huge amount of data that came out of this work led to the extension of the very useful $K\gamma$ recovery model for predicting the recoveries of various metals (such as nickel, cobalt, and even chromium) as a function of the iron recovery (which is just a proxy for the extent of reduction in the furnace). This model allows one to predict the behaviour of any new feed material that is introduced into the furnace.

The ConRoast process is widely seen as being very important to South Africa's platinum industry in the coming years, especially as mines move increasingly towards utilising higher-chromium ores. The ConRoast process has also been studied as part of the pyrometallurgy curriculum at a number of South African universities.

7.6 The Way Forward

The work presented in this thesis has led to a greater understanding of a number of facets of DC arc furnace technology. However, there are still many areas that would profit from further investigation, by myself and by others. For example, work is currently underway that is intended to mathematically interpret high-speed electrical measurements and use the results to determine the presence or otherwise of arcing behaviour in a furnace. Another area with good possibilities is the interaction between chemical behaviour (especially in the gas phase) and the response of the arc. No doubt, DC arc furnace technology will continue to be used and studied for some time to come.

REFERENCES

Acholonu C.C. (1983) *Distribution of copper, cobalt, nickel between alloys and silica-unsaturated iron slags*, MSc Thesis, Department of Chemical and Metallurgical Engineering, University of Nevada, Reno, 104 pp.

Bale C.W., Chartrand P., Degterov S.A., Eriksson G., Hack K., Ben Mahfoud R., Melancon J., Pelton A.D., & Petersen S. (2002) FactSage thermochemical software and databases, *Calphad*, Vol.26, No.2, pp. 189-228.
http://sgte.org/fact/factsage/FactSage.pdf

Barcza N.A., Curr T.R., & Jones R.T. (1989) Metallurgy of open-bath plasma processes, Invited lecture at the 9th International Symposium on Plasma Chemistry (ISPC-9), Bari, Italy, September 1989.
http://www.mintek.co.za/Pyromet/Files/OpenBath.pdf

Barcza N.A., Curr T.R., & Jones R.T. (1990) Metallurgy of open-bath plasma processes, *Pure & Applied Chemistry*, Vol.62, No.9, 1990, pp. 1761-1772.
http://www.mintek.co.za/Pyromet/Files/OpenBath.pdf

Barcza N.A., Barker I.J., Rennie M.S., & Brereton-Stiles P.J. (2002) The application and scale-up of AC and DC smelting furnaces for ferro-alloys, 60th Electric Furnace Conference Proceedings, Vol. 60, Warrendale, PA: Iron & Steel Society, pp. 425-437.
http://www.mintek.co.za/Pyromet/Files/2002Barcza.pdf

Barnes A.R. & Jones R.T. (2011) Cobalt from slag - Lessons in transition from laboratory to industry, New Technology Implementation in Metallurgical Processes, 50th Conference of Metallurgists of CIM, Montreal, Quebec, Canada, 2-5 October 2011, pp.111-125.
http://www.mintek.co.za/Pyromet/Files/2011Barnes.pdf

Barnes S.-J., Makovicky E., Makovicky M., Rose-Hansen J., & Karup-Møller S. (1997) Partition coefficients for Ni, Cu, Pd, Pt, Rh and Ir between monosulfide solid solution and sulfide liquid and the formation of compositionally zoned Ni-Cu sulfide bodies by fractional crystallisation of sulfide liquid, *Canadian Journal of Earth Sciences*, Vol.34, pp.366-374.

Belton G.R., Suito H., & Gaskell D.R. (1973) Free energies of mixing in the liquid iron-cobalt orthosilicates at 1450°C, *Metallurgical Transactions*, Vol.4, November 1973, pp.2541-2547.

Bodsworth C. (1959) The activity of ferrous oxide in silicate melts, *Journal of the Iron and Steel Institute*, September 1959, pp.13-24.

Borisov A., Palme H., & Spettel B. (1994) Solubility of palladium in silicate melts: Implications for core formation in the Earth, *Geochimica et Cosmochimica Acta*, Vol.58, No.2, pp.705-716.

Borisov A., Palme H., Holzheid A., Spettel B., Dingwell D.B., & O'Neill H.St.C. (1992) The origin of highly siderophile elements in the upper mantle of the Earth: an experimental approach, *Lunar Planetary Science XXIII*, pp.139-140.

Bowman B., Jordan G.R., & Fitzgerald F. (1969) The physics of high-current arcs, *Journal of the Iron and Steel Institute*, June 1969, pp.798-805.

Bowman B. (1972) Convective heat transfer and power balance in high current free-burning arcs, *Electrowarme International*, 30, 1972, B2 April, pp. B87–B93.

Bowman B. (1982) MHD effects in arc furnaces, *Metallurgical Applications of Magnetohydrodynamics*, Proceedings of a Symposium of the International Union of Theoretical and Applied Mechanics, Edited by Moffatt H.K. and Proctor M.R.E., Trinity College, Cambridge, UK, 6-10 September 1982, The Metals Society, London, pp.272-282.

Bowman B. (1990) Effects on furnace arcs of submerging by slag, *Ironmaking and Steelmaking*, Vol.17, No.2, pp.123-129.

Bowman B. (1994) Properties of arcs in DC furnaces, Proceedings of 52nd Electric Furnace Conference, Nashville, Tennessee, 13-16 November 1994, Iron and Steel Society, Warrendale, PA, USA, pp.111-120.

Bowman B. and Krüger K. (2009) *Arc Furnace Physics*, Stahleisen Communications, Düsseldorf, Germany, ISBN 978-3-514-00768-0.

Chen C., Zhang L., & Jahanshahi S. (2004) Review and thermodynamic modelling of CoO in iron silicate-based slags and calcium ferrite-based slags. VII International Conference on Molten Slags Fluxes and Salts, The South African Institute of Mining and Metallurgy, pp.509-515.
http://www.saimm.co.za/Conferences/MoltenSlags2004/509-Chen.pdf

Cheslak F.R., Nicholls J.A., and Sichel M. (1969) Cavities formed on liquid surfaces by impinging gaseous jets, *Journal of Fluid Mechanics*, Vol.36, Part 1, 1969, pp.55-63.

Davy H. (1800) VII. Additional Experiments on Galvanic Electricity, Journal of Natural Philosophy, *Chemistry, and the Arts (Nicholson's Journal)*, London, Vol.IV, October 1800, pp.326-328.

Davy Sir H. (1812) Elements of Chemical Philosophy: Part 1 Vol.1 J. Johnson and Co., St Paul's Church Yard, London, p.85 and Plate III, Fig.18.
https://archive.org/details/elementschemica00davygoog

Day J.G. & Taylor J.R. (1984) Smelting with flux to produce slag and copper matte; oxidation; treatment with copper, nickel, or iron, US Patent 4448604.
http://www.google.com/patents/US4448604

Deneys A.C., Robertson D.G.C., Jones R.T., & Worcester A.W. (1997) Recovery of cobalt from a Viburnum Trend lead blast furnace slag, Proceedings of Nickel-Cobalt 97, Volume II: Pyrometallurgy Fundamentals and Process Development, Edited by C.A. Levac and R.A. Berryman, Metallurgical Society of CIM, 36th Annual Conference of Metallurgists, Sudbury, Canada, 17-20 August 1997, pp. 23-37.
http://www.mintek.co.za/Pyromet/Files/Viburnum.pdf

Derin B. &Yücel O. (2002) The distribution of cobalt between Co-Cu Alloys and Al_2O_3-FeO-Fe_2O_3-SiO_2 slags, *Scandinavian Journal of Metallurgy*, 31, pp.12-19.

Dinsdale A.T. (1991) SGTE Data for Pure Elements, *Calphad*, Vol.15, pp.317-425.

Dippenaar R.J., Barcza N.A., & Jones R.T. (1988) Energy considerations for the melting of DRI as a function of the degree of pre-reduction, Proceedings of the 7th Process Technology Conference, Toronto, Ontario, Canada, AIME, Iron& Steel Society, April 1988.
http://www.mintek.co.za/Pyromet/Files/DRIenergy.pdf

Dunkley J.J., Norval D., Jones R.T., & Chennells P. (2008) Water atomisation of PGM-containing intermediate alloys, Third International Platinum Conference, 'Platinum in Transformation', The Southern African Institute of Mining and Metallurgy, Sun City, 5-9 October 2008, pp.155-159.
http://www.mintek.co.za/Pyromet/Files/2008Dunkley.pdf

Eccleston E. & White J. (2008) Development of roasting parameters for the ConRoast process with low-sulfur feedstock, Third International Platinum Conference, 'Platinum in Transformation', The Southern African Institute of Mining and Metallurgy, Sun City, 5-9 October 2008, pp.149-154.
http://www.mintek.co.za/Pyromet/Files/2008Eccleston.pdf

Fleet M.E. & Stone W.E. (1991) Partitioning of platinum-group elements in the Fe-Ni-S system and their fractionation in nature, *Geochimica et Cosmochimica Acta*, Vol.55, Issue 1, January 1991, pp.245-253.
http://www.sciencedirect.com/science/article/pii/0016703791904152

Fleet M.E., Stone W.E., & Crocket J.H. (1991) Partitioning of palladium, iridium, and platinum between sulfide liquid and basalt melt: Effects of melt composition, concentration, and oxygen fugacity, *Geochimica et Cosmochimica Acta*, Vol.55, pp.2545-2554.

Fleet M.E., Crocket J.H., & Stone W.E. (1996) Partitioning of platinum-group elements (Os, Ir, Ru, Pt, Pd) and gold between sulfide liquid and basalt melt, *Geochimica et Cosmochimica Acta*, Vol.60, No.13, pp.2397-2412.

Fleet M.E., Liu M., & Crocket J.H. (1999) Partitioning of trace amounts of highly siderophile elements in the Fe-Ni-S system and their fractionation in nature, *Geochimica et Cosmochimica Acta*, Vol.63, No.17, pp.2611-2622.

Fonseca R.O.C., Campbell I.H., O'Neill H.St.C., & Allen C.M. (2009) Solubility of Pt in sulphide mattes: Implications for the genesis of PGE-rich horizons in layered intrusions, *Geochimica et Cosmochimica Acta*, Vol.73, pp.5764-5777.

Fontana A., Ilunga M., Mwema M., Segers L., Twite K., and Winand R. (1989) Properties of ferrous silicate slags associated with copper flash smelting and electric furnace processes, *Extraction Metallurgy '89*, Institution of Mining and Metallurgy, London, 10-13 July 1989, pp.147-164.

Geldenhuys I.J. & Jones R.T. (2009) Four years of DC arc smelting of PGM-containing oxide feed materials at Mintek, Pyrometallurgy of Nickel and Cobalt 2009, 48th Annual Conference of Metallurgists of CIM, Sudbury, Ontario, Canada, 23–26 August 2009, pp.415-427.
http://www.mintek.co.za/Pyromet/Files/2009Geldenhuys.pdf
http://www.mintek.co.za/Pyromet/Files/2009Geldenhuys-CIM.pdf

Geldenhuys I.J. & Jones R.T. (2011) What scale should your smelting testwork be done at, and what do you get for the money you spend?, Sixth Southern African Base Metals Conference, The Southern African Institute of Mining and Metallurgy, 18-20 July 2011, Phalaborwa, South Africa, pp.477-492.
http://www.mintek.co.za/Pyromet/Files/2011Geldenhuys.pdf

Geldenhuys I.J. & Lagendijk H. (2007) A twin-cathode DC arc smelting test at Mintek to demonstrate the feasibility of smelting FeNi from calcine prepared from siliceous laterite ores from Kazakhstan for Oriel Resources plc, International Ferroalloys Conference, Infacon XI, New Delhi, India, 18–21 February 2007, pp.781-797.
http://www.mintek.co.za/Pyromet/Files/2007Reinecke.pdf

Goldschmidt V.M. (1937) The principles of distribution of chemical elements in minerals and rocks, The seventh Hugo Müller Lecture, delivered before the Chemical Society on March 17th, 1937, *Journal of the Chemical Society*, pp.655–673.
http://pubs.rsc.org/en/Content/ArticleLanding/1937/JR/jr9370000655

Gous M. (2006) An overview of the Namakwa Sands ilmenite smelting operations, *Southern African Pyrometallurgy 2006*, Edited by R.T. Jones, South African Institute of Mining and Metallurgy, Johannesburg, 5-8 March 2006, pp.189-201.
http://www.pyrometallurgy.co.za/Pyro2006/Papers/189_Namakwa.pdf

Grimsey E.J. (1988) The effect of temperature on nickel solubility in silica saturated fayalite slags from 1523 to 1623 K, *Metallurgical Transactions B*, Vol.19B, April 1988, pp.243-247.

Grimsey E.J. & Toguri J.M. (1988) Cobalt in silica saturated cobalt slags, *Canadian Metallurgical Quarterly*, Vol.27, No.4, pp.331-333.

Grimsey E.J. & Liu X. (1991) The thermodynamics of cobalt dissolution in iron silicate slags, Fifth AusIMM Extractive Metallurgy Conference, Perth, 2-4 October 1991, pp.323-326.

Grimsey E.J. & Liu X. (1995) The activity coefficient of cobalt oxide in silica-saturated iron silicate slags, *Metallurgical Transactions B*, Vol.26B, April 1995, pp.229-233.

Gudmundsson G. & Holloway J.R. (1993) Activity–composition relationships in the system Fe–Pt at 1300 and 1400°C and at 1 atm and 20 kbar, *American Mineralogist*, Vol.78, pp.178–186.

Hamblyn S.M.L. (1977) Plasma technology and its application to extractive metallurgy, *Minerals Science and Engineering*, vol.9, no.3, July 1977, pp.151-176.
http://www.mintek.co.za/Pyromet/Files/1977Hamblyn.pdf

Hammerschmidt J. (2008) The roasting of PGM-ore concentrates in a circulating fluidized bed, Third International Platinum Conference, 'Platinum in Transformation', The Southern African Institute of Mining and Metallurgy, Sun City, 5-9 October 2008, pp.161-167.
http://www.mintek.co.za/Pyromet/Files/2008Hammerschmidt.pdf

Holzheid A. & Palme H. (1996) The influence of FeO on the solubilities of cobalt and nickel in silicate melts, *Geochimica et Cosmochimica Acta*, Vol.60, No.7, pp.1181-1193.

Holzheid A., Palme H., & Chakraborty S. (1997) The activities of NiO, CoO and FeO in silicate melts, *Chemical Geology*, 139 (1997), pp.21-38.

Hultgren R., Desai P.D., Hawkins D.T., Gleiser M., & Kelley K.K. (1973) *Selected Values of the Thermodynamic Properties of Binary Alloys*, American Society for Metals, Metals Park, Ohio, USA, p.662.

Hurd D. & Kollar J. (1991) Direct current electric arc furnaces, Tech Commentary CMP-063, Published by the EPRI (Electric Power Research Institute) Center for Materials Production, Carnegie Mellon Research Institute, Pittsburgh, Pennsylvania, January 1991, pp.1-4.
http://www.yuber.com.tr/teknik/DCArkOcaklari.pdf

Jones R.T., Curr T.R., & Barcza N.A. (1993a) Developments in Plasma Furnace Technology, High-Intensity Pyrometallurgy, The Institution of Mining and Metallurgy, 4 February 1993, London.
http://www.mintek.co.za/Pyromet/Files/PlasmaDev.pdf

Jones R.T., Barcza N.A., & Curr T.R. (1993b) Plasma Developments in Africa, Second International Plasma Symposium: World progress in plasma applications, Organized by the EPRI (Electric Power Research Institute) CMP (Center for Materials Production), 9-11 February 1993, Palo Alto, California.
http://www.mintek.co.za/Pyromet/Plasma/Plasma.htm

Jones R.T., Curr T.R., & Barcza N.A. (1994) Development of plasma furnace technology at Mintek, *Minerals Industry International*, IMM, London, March 1994, pp. 25-31.
http://www.mintek.co.za/Pyromet/Files/PlasmaDev.pdf

Jones R.T., Hayman D.A., & Denton G.M. (1996) Recovery of cobalt, nickel, and copper from slags, using DC-arc furnace technology, International Symposium on Challenges in Process Intensification, 35th Annual Conference of Metallurgists, Montreal, Canada, 24-29 August 1996, pp. 451-466.
http://www.mintek.co.za/Pyromet/Cobalt/Cobalt.htm

Jones R.T., la Grange T.G., & Assis G. (1997) Influence of DC-arc furnace geometry on a 'cobalt from slag' process, Nickel-Cobalt 97, 36th Annual Conference of Metallurgists, Sudbury, Canada, 17-20 August 1997, pp. 3-14.
http://www.mintek.co.za/Pyromet/Files/Geometry.pdf

Jones R.T. (1998) Recovery of cobalt, nickel and copper from slags using DC-arc furnace technology, *Cobalt News* 98/2, April 1998, pp. 3-6.

Jones R.T. & Deneys A.C. (1998) Using a Direct-Current Arc Furnace to recover cobalt from slags, *JOM*, The Minerals, Metals, and Materials Society, Vol.50, No.10, October 1998, pp. 57-61.
http://www.mintek.co.za/Pyromet/Files/CobaltJOM.pdf

Jones R.T. (1999) Platinum Smelting in South Africa, *South African Journal of Science*, Vol.95, November / December 1999, pp. 525-534.
http://www.mintek.co.za/Pyromet/Files/Platinum.pdf
http://www.mintek.co.za/Pyromet/Platinum/Platinum.htm

Jones R.T., Denton G.M., Reynolds Q.G., Parker J.A.L., & van Tonder G.J.J. (2001) Recovery of cobalt from slag in a DC arc furnace at Chambishi, Zambia, Copper Cobalt Nickel and Zinc Recovery conference, SAIMM, Victoria Falls, Zimbabwe, 16-18 July 2001.
http://www.mintek.co.za/Pyromet/Files/Chambishi.pdf
http://www.mintek.co.za/Pyromet/Chambishi/Chambishi.htm

Jones R.T., Denton G.M., Reynolds Q.G., Parker J.A.L., & van Tonder G.J.J. (2002) Recovery of cobalt from slag in a DC arc furnace at Chambishi, Zambia, *Journal of the SAIMM*, Volume 102, Number 1, January / February 2002, pp.5-9.
http://www.mintek.co.za/Pyromet/Files/Chambishi.pdf

Jones R.T. (2001) ConRoast: DC arc smelting of dead-roasted sulphide concentrates, Colloquium: Developments in metallurgical processing in the platinum industry, Rustenburg, South Africa, 14-16 November 2001.
http://www.mintek.co.za/Pyromet/ConRoast/Summary.htm

Jones R.T. (2002) ConRoast: DC arc smelting of dead-roasted sulphide concentrates, Sulfide Smelting 2002, Edited by Stephens R.L. & Sohn H.Y., TMS (The Minerals, Metals & Materials Society), Seattle, 17-21 February 2002, pp.435-456.
http://www.mintek.co.za/Pyromet/Files/ConRoast.pdf
http://www.mintek.co.za/Pyromet/ConRoast/ConRoast.htm

Jones R.T., Barcza N.A., Kaiura G., O'Connell G., & Hannaford A. (2002) Treatment of metal sulphide concentrates by roasting and arc furnace smelt reduction, European Patent Specification EP 1 157 139 B1, 9 October 2002.
(Also patented in many other countries, including South African patent numbers ZA 99/1285, 26 February 1999 and 2001/6720, 31 July 2002; US patent 6,699,302 B1, 2 March 2004; Canadian patent 2,362,294; Russian patent Eurasia 004522; Botswana patent ARIPO AP 1284)
http://www.mintek.co.za/Pyromet/Files/Pat2002ConRoast.pdf

Jones R.T., Reynolds Q.G., & Alport M.J. (2002) DC arc photography and modelling, *Minerals Engineering*, Volume 15, Issue 11S1, pp.985-991. (Presented at Pyromet '02, Cape Town, 11-12 March 2002.)
http://www.mintek.co.za/Pyromet/Files/ArcPhotoModel.pdf

Jones R.T. (2004) Economic and environmentally beneficial treatment of slags in DC arc furnaces, VII International Conference on Molten Slags, Fluxes and Salts, The South African Institute of Mining and Metallurgy, Cape Town, 26-28 January 2004, pp.363-376.
http://www.mintek.co.za/Pyromet/Files/2004JonesSlag.pdf

Jones R.T. & Kotzé I.J. (2004) DC arc smelting of difficult PGM-containing feed materials, International Platinum Conference, 'Platinum Adding Value', The South African Institute of Mining and Metallurgy, Sun City, South Africa, 3-7 October 2004, pp.33-36.
http://www.mintek.co.za/Pyromet/Files/2004JonesConSmelt.pdf

Jones R.T. (2004) JOM World Nonferrous Smelter Survey, Part II: Platinum Group Metals, *JOM*, December 2004, pp.59-63.
http://www.mintek.co.za/Pyromet/Files/2004JonesPGMSmeltingSurvey.pdf

Jones R.T. (2005) An overview of Southern African PGM Smelting, Nickel and Cobalt 2005: Challenges in Extraction and Production, 44th Annual Conference of Metallurgists, Calgary, Alberta, Canada, 21-24 August 2005, pp.147-178.
http://www.mintek.co.za/Pyromet/Files/2005JonesPGMsmelting.pdf

Jones R.T. (2005-2014) List of Southern African Smelters, Pyrometallurgy in Southern Africa.
http://www.pyrometallurgy.co.za/PyroSA/

Jones R.T. & Curr T.R. (2006) Pyrometallurgy at Mintek, *Southern African Pyrometallurgy 2006*, Edited by R.T. Jones, SAIMM, Johannesburg, 5-8 March 2006, pp.127-150.
http://www.mintek.co.za/Pyromet/Files/2006JonesMintek.pdf

Jones R.T. (2009) Towards commercialisation of Mintek's ConRoast process for platinum smelting, Pyrometallurgy of Nickel and Cobalt 2009, 48th Annual Conference of Metallurgists of CIM, Sudbury, Ontario, Canada, 23–26 August 2009, pp.159-168.
http://www.mintek.co.za/Pyromet/Files/2009Jones-ConRoast.pdf
http://www.mintek.co.za/Pyromet/Files/2009Jones-ConRoast-CIM.pdf

Jones R.T., Geldenhuys I.J., & Reynolds Q.G. (2009) Recovery of base metals and PGMs in a DC alloy-smelting furnace, *Journal of the SAIMM*, Volume 109, Number 10, October 2009, pp.587-592.
http://www.mintek.co.za/Pyromet/Files/2009Jones-Recovery.pdf

Jones R.T. & Geldenhuys I.J. (2010) The pros and cons of reductive matte smelting for PGMs, *Minerals Engineering*, Volume 24 (2011), pp.495-498. (Presented at Precious Metals '10, Falmouth, 15-16 June 2010.)
http://www.mintek.co.za/Pyromet/Files/2010JonesMatte.pdf
http://www.mintek.co.za/Pyromet/Files/2010JonesMatte1.pdf

Jones R.T., Reynolds Q.G., Curr T.R., & Sager D. (2011) Some myths about DC arc furnaces, *Southern African Pyrometallurgy 2011*, Edited by R.T. Jones & P. den Hoed, SAIMM, Johannesburg, 6-9 March 2011, pp.15-32.
http://www.mintek.co.za/Pyromet/Files/2011Jones1.pdf

Jones R.T., Reynolds Q.G., Curr T.R., & Sager D. (2011) Some myths about DC arc furnaces, *Journal of the SAIMM*, Volume 111, Number 10, October 2011, pp.665-673.
http://www.mintek.co.za/Pyromet/Files/2011Jones2.pdf

Jones R.T. & Reynolds Q.G. (2012) Factors influencing the residence time distribution in continuously-fed batch-tapped furnaces, 51st Annual Conference of Metallurgists, CIM, Niagara Falls, Canada, 30 September – 3 October 2012, pp.141-149.
http://www.mintek.co.za/Pyromet/Files/2012Jones-RTD.pdf

Jones R.T. (2014) DC arc furnaces - Past, present, and future, *Celebrating the Megascale, Proceedings of the Extraction and Processing Division Symposium on Pyrometallurgy in Honor of David G.C. Robertson*, Mackey P.J., Grimsey E.J., Jones R.T., & Brooks, G.A. (Editors), Wiley, TMS 2014, 16-20 February 2014, San Diego, California, USA, pp.129-139. http://www.mintek.co.za/Pyromet/Files/2014Jones-DCArcFurnaces.pdf

Jordan G.R., Bowman B., & Wakelam D. (1970) Electrical and photographic measurements of high-power arcs, *Journal of Physics D: Applied Physics*, Vol. 3, pp.1089–1099.

Jung I-H., Decterov S.A., & Pelton A.D. (2004) Critical thermodynamic evaluation and optimization of the FeO-Fe_2O_3-MgO-SiO_2 system, *Metallurgical and Materials Transactions B*, Vol.35B, October 2004, pp.877-889.

Kammeyer H.J., Maske K.U., & Pugh G. (1989) Open-bath production of ferrochromium in a DC plasma furnace, Proceedings of the 5th International Ferroalloys Congress (Infacon '89), New Orleans, Louisiana, USA, 23-26 April 1989, vol.1, pp.95-102.

Katyal A. & Jeffes J.H.E. (1989) Activities of cobalt and copper oxides in silicate and ferrite slags, *3rd International Conference on Molten Slags and Fluxes*, Glasgow, Scotland, 27-29 June 1988, Institute of Metals, London, pp.46-55. http://www.pyrometallurgy.co.za/MoltenSlags1988/046-Katyal.pdf

Kitamura S., Kuriyama H., Maruoka N., Yamaguchi K., & Hasegawa A. (2008) Distribution of cobalt between MgO-saturated FeO_x-MgO-CaO-SiO_2 slag and Fe-Cu-Co molten alloy, *Materials Transactions*, The Japan Institute of Metals, Vol.49, No.11, pp.2636-2641. http://www.jim.or.jp/journal/e/pdf3/49/11/2636.pdf

Knacke O., Kubaschewski O., & Hesselmann K. (1991) *Thermochemical Properties of Inorganic Substances*, Springer-Verlag, Berlin.

Kojima V.Y., Inoue M., & Sano K. (1969) Die aktivität des eisenoxyds in FeO-MgO-SiO_2-schlacken bei 1600°C, *Arch. Eisenhuttenwes.*, Vol.40, pp.37-40.

Kotzé H., Bessinger D., & Beukes J. (2006) Ilmenite Smelting at Ticor SA, *Southern African Pyrometallurgy 2006*, Edited by R.T. Jones, South African Institute of Mining and Metallurgy, Johannesburg, 5-8 March 2006, pp.203-214. http://www.pyrometallurgy.co.za/Pyro2006/Papers/203_Ticor.pdf

Kubaschewski O., Evans E.L., & Alcock C.B. (1967) *Metallurgical Thermochemistry*, 4th Edition, Pergamon Press, Oxford.

Lagendijk H. & Jones R.T. (1997) Production of ferronickel from nickel laterites in a DC-arc furnace, Nickel-Cobalt 97, 36th Annual Conference of Metallurgists, Sudbury, Canada, 17-20 August 1997, pp. 151-162. http://www.mintek.co.za/Pyromet/Laterite/Laterite.htm

Laurenz V., Fonseca R.O.C., Ballhaus C., Jochum K.P., Heuser A., & Sylvester P.J. (2013) The solubility of palladium and ruthenium in picritic melts: 2. The effect of sulfur, *Geochimica et Cosmochimica Acta*, Vol.108, 1 May 2013, pp.172–183. http://www.sciencedirect.com/science/article/pii/S0016703713000343

Levin J. (1985) *The story of Mintek 1934-1984*, Council for Mineral Technology, Randburg, 1985.

Lindstrom D.J. & Jones J.H. (1996) Neutron activation analysis of multiple 10-100 µg glass samples from siderophile element partitioning experiments, *Geochimica et Cosmochimica Acta*, Vol.60, No.7, pp.1195-1203.

Liu M. (2000) Laboratory partitioning of siderophile elements in the Fe-(Ni)-S system and their fractionation in iron meteorites and the core of Earth, PhD Thesis, University of Western Ontario, London, Ontario, Canada, June 2000.

Liu X. & Grimsey E.J. (1997) The effect of silica, alumina, calcia and magnesia on the activity coefficient of cobalt oxide in iron silicate slags, 5th International Conference on Molten Slags, Fluxes and Salts '97, Sydney, Australia, 5-8 January 1997, Iron & Steel Society, USA, pp.709-718.
http://www.pyrometallurgy.co.za/MoltenSlags1997/709-Liu.pdf

Maecker H. (1955) Plasmaströmungen in Lichtbögen infolge Eigenmagnetische Kompression, *Zeitschrift für Physik*, Vol.141, pp.198-216.

Maruyama M. & Ban-ya S. (1978) *J. Jpn. Inst. Met.*, 42, pp.992–999.

McCullough S.D., Geldenhuys I.J., & Jones R.T. (2008) Pyrometallurgical iron removal from a PGM-containing alloy, Third International Platinum Conference, 'Platinum in Transformation', The Southern African Institute of Mining and Metallurgy, Sun City, 5-9 October 2008, pp.169-176.
http://www.mintek.co.za/Pyromet/Files/2008McCullough1.pdf

Meihack W.F.A.T., Curr T.R., Barcza N.A., & Jones R.T. (1987) The effect of feed pretreatment on the efficiency of a plasma-arc furnace, Proceedings of the 8th International Symposium on Plasma Chemistry (ISPC-8), Tokyo, Japan, September 1987.
http://www.mintek.co.za/Pyromet/Files/ISPC8.pdf

Mills K.C., Lang Y., & Jones R.T. (2011) Estimating the physical properties of slags, *Journal of the SAIMM*, Volume 111, Number 10, October 2011, pp.649-658.
http://www.mintek.co.za/Pyromet/Files/2011Mills.pdf

Mining Journal (2013) Xstrata's Koniambo produces first nickel, *Mining Journal*, 11 April 2013.
http://www.mining-journal.com/exploration--and--development/xstratas-koniambo-produces-first-nickel

Morita K., Wiraseranee C., Shuto H., Nakamura S., Okabe T.H., & Sano N. (2011) Dissolution behavior of platinum group metals into molten slags, Fray International Symposium, Volume 1: Sustainable non-ferrous smelting in 21st century, Edited by F. Kongoli, 27 November – 1 December 2011, Cancun, Mexico, pp.305-317.

Morris A.E., Deneys A.C. & Jones R.T. (1998) 'Reduction and Melting of DRI', in Direct Reduced Iron, Chapter 13 by Arthur E. Morris, in *Computer Modeling and Analysis of Processes for the Production of DRI*, Edited by Jerome Feinman and Donald MacRae, Iron and Steel Society, 1998, pp. 187-189.
http://www.mintek.co.za/Pyromet/Files/DRI.pdf

Mostert, J.C. & Roberts, P.N. (1973) Electric smelting at Rustenburg Platinum Mines Limited of nickel-copper concentrates containing platinum-group metals, *Journal of the SAIMM*, 1973, 73(9), pp.290-299.
http://www.saimm.co.za/Journal/v073n09p290.pdf

Naude C.P. & Shapiro M.D. (2010) Implementation of the first commercial scale DC smelter for ferronickel production from low grade laterite ores—technology building blocks and lessons learned, *Journal of the Southern African Institute of Mining and Metallurgy*, vol.110, no.12, December 2010. pp.725–732.
http://www.saimm.co.za/Journal/v110n12p725.pdf

Nelson L.R., Sullivan R., Jacobs P., Munnik E., Lewarne P., Roos E., Uys M.J.N., Salt B., de Vries M., McKenna K., Voermann N., & Wasmund B.O. (2004) Application of a high-intensity system to DC-arc furnace production of ferrocobalt at Chambishi, *Journal of the SAIMM*, Vol.104, No.10, October 2004. pp.551–561.
http://www.saimm.co.za/Journal/v104n09p551.pdf

Noddack W., Noddack I., & Bohnstedt U. (1940) Du treilungskoeffizienten der scwermetalle-zweischen eisensufid und eisen, *Zeitschrift Anorgan. Chemie*, Vol.244, pp.252-280.

O'Neill H.St.C. & Eggins S.M. (1999) The effect of melt composition on the activity coefficients of some siderophile element components (FeO, NiO, CoO, MoO_2, MoO_3 and WO_2) in melts in the CMAS system, Ninth Annual V.M. Goldschmidt Conference, 22-27 August 1999, Harvard University, Cambridge, Massachusetts, USA.
http://www.lpi.usra.edu/meetings/gold99/pdf/7214.pdf

O'Neill H.St.C. & Eggins S.M. (2002) The effects of melt composition on trace element partitioning: an experimental investigation of the activity coefficients of FeO, NiO, CoO, MoO_2 and MoO_3 in silicate melts, An experimental investigation of the effect of melt composition on the activity coefficients of FeO, NiO, CoO, MoO_2 and MoO_3 in silicate melts, and its implications for trace element partitioning, *Chemical Geology*, 186, 151–181.
http://www.sciencedirect.com/science/article/pii/S0009254101004144

O'Neill H.St.C. & Berry A.J. (2006) Activity coefficients at low dilution of CrO, NiO and CoO in melts in the system CaO–MgO–Al_2O_3–SiO_2 at 1400°C: Using the thermodynamic behaviour of transition metal oxides in silicate melts to probe their structure, *Chemical Geology*, 231, Elsevier, pp.77–89.
http://people.rses.anu.edu.au/oneill_h/pubs/CG231_77.pdf

Oishi T., Ono K., & Moriyama J. (1981) Thermodynamic study of molten Cu-Co alloys, *J. Jpn. Inst. Met.*, 45, pp.1126– 1129.

Pagador R.U., Hino M., & Itagaki K. (1997) Equilibrium between FeO_x-MgO-SiO_2 slag and nickel alloy, *Proceedings of the Nickel-Cobalt 97 International Symposium - Vol.II, Pyrometallurgy Fundamentals and Process Development*, CIM, Sudbury, Ontario, 17-20 August 1997, pp.63-75.

Pagador R.U., Hino M., & Itagaki K. (1999) *Mater. Trans. JIM*, Vol.40, No.3, pp.225–232.

Patankar S.V. (1980) *Numerical Heat Transfer and Fluid Flow*, Hemisphere Publishing Corporation.

Pelton A.D., Eriksson G., & Wu P. (1992) Coupled optimization of thermodynamic and phase diagram data. See also Wu P. (1992) PhD Thesis, École Polytechnique, Montréal.

Phillips R.E., Jones R.T., & Cramer L.A. (2006) Independence Platinum Limited (IPt) – formation and objectives, International Platinum Conference 'Platinum Surges Ahead', The Southern African Institute of Mining and Metallurgy, Sun City, 8-12 October 2006, pp.231-236.
http://www.mintek.co.za/Pyromet/Files/2006Phillips.pdf

Phillips R.E., Chennells P., & Jones R.T. (2008) Braemore Platinum Smelters: Commercial exploitation of Mintek's ConRoast technology, Third International Platinum Conference, 'Platinum in Transformation', The Southern African Institute of Mining and Metallurgy, Sun City, 5-9 October 2008, pp.141-147.
http://www.mintek.co.za/Pyromet/Files/2008Phillips.pdf

Reddy R.G. & Healy G.W. (1981) Distribution of cobalt between liquid copper and copper silicate slag at 1523 K, *Metallurgical Transactions B*, American Society for Metals and The Metallurgical Society of AIME, Vol.12B, September 1981, pp.509-516.

Reddy R.G. & Acholonu C.C. (1983) Activity coefficient of cobalt oxide in alumina saturated iron silicate slags, *Journal of Metals*, Vol.35, No.12, p.75, 113th TMS-AIME Annual Meeting, Los Angeles, California, USA, 26 February - 1 March 1984.

Reddy R.G. (1985) Solubility of cobalt in copper smelting and refining slags, *Second Congress Cobalt Metallurgy and Uses*, Cobalt Development Institute, Venice, Italy, 30 September - 3 October 1985, pp.89-105.

Redlich O. & Kister A.T. (1948) Algebraic representation of thermodynamic properties and the classification of solutions, *Industrial and Engineering Chemistry*, Vol.40, No.2, pp.345-348.

Reynolds Q.G. & Jones R.T. (2004) Semi-empirical modelling of the electrical behaviour of DC-arc smelting furnaces, *Journal of the SAIMM*, Volume 104, Number 6, July 2004, pp.345-351.
http://www.mintek.co.za/Pyromet/Files/2004Reynolds.pdf

Reynolds Q.G. & Jones R.T. (2005) Twin-electrode DC smelting furnaces – Theory and photographic testwork, *Minerals Engineering*, Volume 9, Issue 3, March 2006, pp.325-333.
http://www.mintek.co.za/Pyromet/Files/2005Reynolds.pdf

Reynolds Q.G. (2009) Mathematical and computational modelling of the dynamic behaviour of direct current plasma arcs, PhD Thesis, University of Cape Town, South Africa.

Reynolds Q.G., Jones R.T., & Reddy B.D. (2010) Mathematical and computational modelling of the dynamic behaviour of direct current plasma arcs, Infacon XII, The Twelfth International Ferroalloys Congress, 'Sustainable Future', 6-9 June 2010, Helsinki, Finland, pp.789-801.
http://www.mintek.co.za/Pyromet/Files/2010Reynolds1.pdf

Reynolds Q.G. & Jones R.T. (2010) High-speed photography and modelling of direct-current plasma arcs, ICHSIP 29, Morioka, Japan, 20-24 September 2010.
http://www.mintek.co.za/Pyromet/Files/2010Reynolds2.pdf

Reynolds Q.G. & Reddy B.D. (2011) Some aspects of dynamic computational modelling of direct current plasma arc phenomena, Proceedings of Coupled Problems 2011, IV International Conference on Computational Methods for Coupled Problems in Science and Engineering, Kos Island, Greece, 20-22 June 2011, Paper no.135, pp.1239-1250.
http://www.mintek.co.za/Pyromet/Files/2011Reynolds-CoupledProblems.pdf

Reynolds Q.G. (2011) The dual-electrode DC arc furnace—modelling insights, *Southern African Pyrometallurgy 2011*, Edited by R.T. Jones & P. den Hoed, SAIMM, Johannesburg, 6-9 March 2011, pp.33-46.
http://www.mintek.co.za/Pyromet/Files/2011Reynolds1.pdf

Reynolds Q.G. (2011) The dual-electrode DC arc furnace—modelling insights, *Journal of the Southern African Institute of Mining and Metallurgy*, vol.111, no.10, October 2011, pp.697–703.
http://www.mintek.co.za/Pyromet/Files/2011Reynolds2.pdf

Reynolds Q.G. (2012a) The dual-electrode DC arc furnace—modelling brush arc conditions, *Journal of the Southern African Institute of Mining and Metallurgy*, vol.112, no.7, July 2012, pp.605–611.
http://www.mintek.co.za/Pyromet/Files/2012Reynolds2.pdf

Reynolds Q.G. (2012b) Plasma arc extinction events – Insights from high-speed photography and modelling, 30th International Congress on High-Speed Imaging & Photonics (ICHSIP30), Pretoria, South Africa, 16-21 September 2012, 8 pages.
http://www.mintek.co.za/Pyromet/Files/2012Reynolds3.pdf

Reynolds Q.G., Hockaday C.J., Jordan D.T., and Barker I.J. (2014) Arc detection in DC arc furnaces, *Celebrating the Megascale*, Proceedings of the Extraction and Processing Division Symposium on Pyrometallurgy in Honor of David G.C. Robertson, Edited by P.J. Mackey, E.J. Grimsey, R.T. Jones, and G.A. Brooks, TMS 2014, 16-20 February 2014, San Diego, California, USA, pp.157-167.
http://www.mintek.co.za/Pyromet/Files/2014Reynolds2-TMS.pdf

Sager D., Grant D., Stadler R., & Schreiter T. (2010) Low cost ferroalloy extraction in DC-arc furnace at Middelburg Ferrochrome, (Infacon 12, Helsinki, 6-9 June 2010), SAIMM Journal, Vol.110, No.12, December 2010, pp.717-724.
http://www.pyrometallurgy.co.za/InfaconXII/803-Sager.pdf
http://www.saimm.co.za/Journal/v110n12p717.pdf

Sano N. & Nakamura S. (1997) The solubility of platinum in molten slags, , 5th International Conference on Molten Slags, Fluxes and Salts '97, Sydney, Australia, 5-8 January 1997, Iron & Steel Society, USA, pp.353-356.
http://www.pyrometallurgy.co.za/MoltenSlags1997/353-Sano.pdf

Schoukens A.F.S., Denton G.M., & Jones R.T. (1995) Pilot-plant production of Prime Western grade zinc from lead blast-furnace slags using the Enviroplas process, Third International Symposium on Recycling of Metal and Engineered Materials, Point Clear, Alabama, 12-16 November 1995, TMS Fall Extraction and Processing Meeting, pp. 857-868.
http://www.mintek.co.za/Pyromet/LBFS/LBFS.htm

Schuhmann R. Jr (1955) Application of Gibbs-Duhem equations to ternary systems, *Acta Metallurgica*, Vol.3, Issue 3, May 1955, pp.219-226.

Siemens W. (1878) English patents, No. 4208 of 1878 and No. 2110 of 1879.

Slatter D.D. (1995) Technological trends in chromium unit production and supply, Infacon 7, Trondheim, Norway, 11-14 June 1995, pp.249-262.
http://www.pyrometallurgy.co.za/InfaconVII/249-Slatter.pdf

Smith I.B. & Masson C.R. (1971) Activities and ionic distributions in cobalt silicate melts, *Canadian Journal of Chemistry*, Vol.49, pp.683-690.
http://www.nrcresearchpress.com

Soltanieh M. (1998) The high temperature thermodynamics of the Ni-Co-S and Fe-Co-S ternary systems, PhD Thesis, University of Toronto, p.93.
http://www.collectionscanada.gc.ca/obj/s4/f2/dsk2/tape17/PQDD_0008/NQ35327.pdf

Stenkvist S-E. (1984) The properties and practical application of the high-power graphite cathode d.c. arc plasma, Proceedings of Mintek 50, Johannesburg, South Africa, 26-30 March 1984, pp.769-775.

Stenkvist S-E. & Bowman B. (1987) High-power, graphite-cathode DC arc plasma – Properties and practical applications for steelmaking and ferroalloys processing, In *Plasma technology in metallurgical processing* (The Iron and Steel Society, AIME) Chapter 8B, pp.103-109.

Stone W.E. & Fleet M.E. (1990) Platinum-iron alloy (Pt3Fe) in kimberlite from Fayette County, Pennsylvania, *American Mineralogist*, Vol.75, pp.881-885.

Stull D.R. & Prophet H. (1985) *JANAF Thermochemical Tables*, US Dept of Commerce, Washington.

Szekely J., McKelliget J.W., & Choudhary M. (1983) Heat transfer, fluid flow, and bath circulation in electric arc furnaces and d.c. plasma furnaces, *Ironmaking and Steelmaking*, Vol.10, No.14, pp.169-179.

Takeda A., Ishiwata Y., & Yazawa A. (1983) *Mater. Trans. JIM*, Vol.24, No.7, pp.518-528.

Teague K.C., Swinbourne D.R., & Jahanshahi S. (1998) Activity coefficient of cobalt oxide in non-ferrous smelting slags – a review, Proceedings Australian Institute of Mining and Metallurgy, No.1, 1998, pp.1-6.

Teague K.C., Swinbourne D.R., & Jahanshahi S. (2000) Thermodynamics of cobalt oxide in iron silicate-based slags, The AusIMM Proceedings, No.1, 2000, pp.66-72.

Teague K.C., Swinbourne D.R., & Jahanshahi S. (2001) A thermodynamic study on cobalt containing calcium ferrite and calcium iron silicate slags at 1573 K, *Met. Trans. B*, Vol.32B, February 2001, pp.47-54.

Visser M. (2006) An overview of the history and current operational facilities of Samancor Chrome, *Southern African Pyrometallurgy 2006*, Edited by R.T. Jones, South African Institute of Mining and Metallurgy, Johannesburg, 5-8 March 2006, pp.285-296.

Wang S.S., Kurtis A.J., & Toguri J.M. (1973) Distribution of copper-nickel and copper-cobalt between copper-nickel and copper-cobalt alloys and silica saturated fayalite slags, *Canadian Metallurgical Quarterly*, Vol.12, No.4, pp.383-390.

Wang S.S., Santander N.H., and Toguri J.M. (1974) The solubility of nickel and cobalt in iron silicate slags, *Metallurgical Transactions*, Vol.5, January 1974, pp.261-265.

Warner A.E.M., Diaz C.M., Dalvi A.D., Mackey P.J., Tarasov A.V., & Jones R.T. (2007) JOM World Nonferrous Smelter Survey Part IV: Nickel: Sulfide. http://www.mintek.co.za/Pyromet/Files/2007NickelSurvey.pdf

Williams G.E. & Steenkamp J.D. (2006) Heavy mineral processing at Richards Bay Minerals, *Southern African Pyrometallurgy 2006*, Edited by R.T. Jones, South African Institute of Mining and Metallurgy, Johannesburg, 5-8 March 2006, pp.181-188. http://www.pyrometallurgy.co.za/Pyro2006/Papers/181_RBM.pdf

Yazawa A. (1981) Extractive metallurgical chemistry with special reference to copper smelting, 28th Congress of IUPAC, Vancouver, August 1981, pp.1-21.